

20000726124

(2)

18 19
AFAPL 76-71-24

LEVEL II

AD A058794

**FLAMEHOLDER COMBUSTION
INSTABILITY STUDY.**

10 R. C. Ernst

PWA-FR-9163

Pratt & Whitney Aircraft Group
Division of United Technologies Corporation
Box 2691, West Palm Beach, Florida 33402

DDC FILE COPY

11 MAY 1976

12 168p.

DDC
SEP 19 1976
FBI

9 Final Report, ~~1976~~ 1 March ~~1976~~ through 30 September ~~1977~~

Approved for Public Release: Distribution Unlimited

15 F33615-76-C-2423

16 3066

17 05

Prepared for

Air Force Aero Propulsion Laboratory
Air Force Wright Aeronautical Laboratories
Air Force Systems Command
Wright-Patterson Air Force Base, Ohio 45433

62203F

292887

78 09 07 002

mt

Reproduced From
Best Available Copy

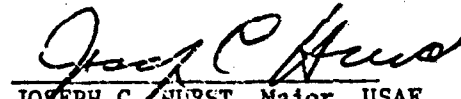
NOTICE

When Government drawings, specifications, or other data are used for any purpose other than in connection with a definitely related Government procurement operation, the United States Government thereby incurs no responsibility nor any obligation whatsoever; and the fact that the Government may have formulated, furnished, or in any way supplied the said drawings, specifications, or other data, is not to be regarded by implication or otherwise as in any manner licensing the holder or any other person or corporation, or conveying any rights or permission to manufacture, use, or sell any patented invention that may in any way be related thereto.

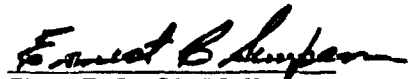
This report has been reviewed by the Information Office (IO) and is releasable to the National Technical Information Service (NTIS). At NTIS, it will be available to the general public, including foreign nations.

This technical report has been reviewed and is approved for publication.


F. N. UNDERWOOD, Captain, USAF
Project Engineer


JOSEPH C. HURST, Major, USAF
Chief, Components Branch

FOR THE COMMANDER


ERNEST C. SIMPSON
Director, Turbine Engine Division

Copies of this report should not be returned unless return is required by security considerations, contractual obligations, or notice on a specific document.

UNCLASSIFIED

SECURITY CLASSIFICATION OF THIS PAGE (When Data Entered)

REPORT DOCUMENTATION PAGE		READ INSTRUCTIONS BEFORE COMPLETING FORM
1. REPORT NUMBER AFAPL-TR-78-24	2. GOVT ACCESSION NO.	3. RECIPIENT'S CATALOG NUMBER
4. TITLE (and Subtitle) FLAMEHOLDER COMBUSTION INSTABILITY STUDY		5. TYPE OF REPORT & PERIOD COVERED Final Report 1 March 1976 to 30 Sept 1977
		6. PERFORMING ORG. REPORT NUMBER FR-9163
7. AUTHOR(s) R. C. Ernst		8. CONTRACT OR GRANT NUMBER(s) F33615-76-C-2023
9. PERFORMING ORGANIZATION NAME AND ADDRESS United Technologies Corporation Pratt & Whitney Aircraft Group Government Products Division West Palm Beach, FL 33402		10. PROGRAM ELEMENT, PROJECT, TASK AREA & WORK UNIT NUMBERS 3066-05-35
11. CONTROLLING OFFICE NAME AND ADDRESS Air Force Aero Propulsion Laboratory (TBC) Wright-Patterson Air Force Base, Ohio 45433		12. REPORT DATE May, 1978
		13. NUMBER OF PAGES 240
14. MONITORING AGENCY NAME & ADDRESS (If different from Controlling Office)		15. SECURITY CLASS. (of this report) Unclassified
		15a. DECLASSIFICATION/DOWNGRADING SCHEDULE
16. DISTRIBUTION STATEMENT (of this Report) Approved for public release; distribution unlimited.		
17. DISTRIBUTION STATEMENT (of the abstract entered in Block 20, if different from Report)		
18. SUPPLEMENTARY NOTES		
19. KEY WORDS (Continue on reverse side if necessary and identify by block number) Flameholder Afterburner Flame Speed Combustion Stability Combustion Efficiency Flame Stability Augmentors Turbofan		
20. ABSTRACT (Continue on reverse side if necessary and identify by block number) A model has been developed which predicts the efficiency and low frequency response of a turbofan augmentor with conventional flameholders. The model evaluates the stability characteristics of the flameholders at low inlet temperature with a model for two-phase fuel flames. The driving potential for low frequency instability is identified with excessive flameholder wake fuel-air ratio. The model is compared to engine experience, available literature and other models with favorable results. The relative stability characteristics of two forced mixing augmentor concepts were examined and the reduction in the dependence of overall efficiency on fuel-air ratio was found to be stabilizing. Recommendations for flameholder design procedures are presented.		

DD FORM 1 JAN 73 1473 EDITION OF 1 NOV 65 IS OBSOLETE

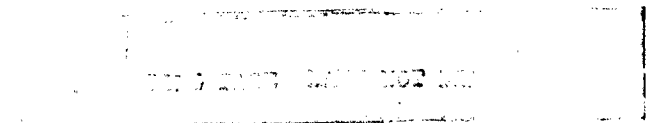
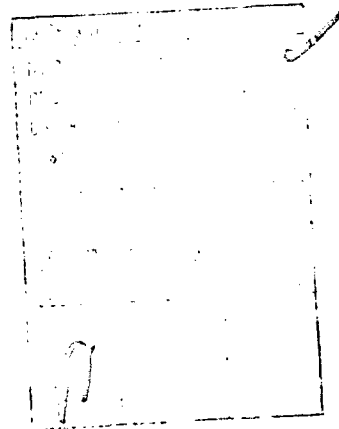
UNCLASSIFIED

SECURITY CLASSIFICATION OF THIS PAGE (When Data Entered)

78 09 07 002

FOREWORD

This final report was prepared in accordance with Contract F33615-76-C-2023, Project No. 3066, Task No. 05, Flameholder Combustion Instability Study. The work was conducted under the direction of Captain F. N. Underwood, Project Engineer, TBC of the Air Force Aero Propulsion Laboratory. The Naval Air Propulsion Test Center cosponsored the contract and was monitored by Mr. W. W. Wagner, the Navy Program Monitor. This report presents the work conducted by Pratt & Whitney Aircraft Group, Government Products Division of United Technologies Corporation, during the period 1 March 1976 through 30 September 1977. R. C. Ernst was the principle investigator under the direction of J. P. Rusnak, the Program Manager for Pratt & Whitney Aircraft Group.



SUMMARY

The principal objective of the Flameholder Combustion Instability Study was to develop an analytical model of the flame stabilization and propagation process in a conventional turbofan engine augmentor and describe the response to low frequency pressure oscillations. The model is to be used for identification of the driving mechanisms of low frequency instability (rumble) in turbofan augmentors.

The program was conducted in two phases. Phase I represented the bulk of the activity and encompassed development of the analytical model and execution of subscale experimental rig testing. Phase II included computerization of the model in a format suitable for analysis/prediction of a turbofan augmentor and comparison of the results with the available literature and engine data. The concepts were also extended to include two novel augmentor types with prediction of their relative stability.

The Phase I model relied on analysis of the individual processes which control the flame stability in low inlet temperature airstreams. Since the fuel is highly liquid, a model was conceived for stabilization in a two-phase fuel spray where the flameholder serves the dual role of controlling both vapor composition and kinetic stability limits. The response is quasi-steady and represents the change in augmentor efficiency with fuel-air ratio and inlet conditions. The model evaluates the various interrelated effects of injector, flameholder and augmentor design. The results of the experimental study were integrated into the analyses. The model predictions are unique in terms of rich limit predictions and flow variable response factors.

The concept was computerized to analyze a turbofan engine and agreed very well with test experience on that engine. The behavioral characteristics were in concert with available data and other models.

The two novel augmentors were found to provide increased stability through a reduction in reliance on fuel-air ratio for flame speed, removal of the liquid vaporization dependence, and increased dynamic stiffness of the piloting source relative to flameholders.

PRECEDING PAGE BLANK NOT FILMED

CONTENTS

<i>Section</i>		<i>Page</i>
I	INTRODUCTION.....	1
	1. Phase I Analytical Approach.....	2
	2. Experimental Approach.....	4
	3. Phase I Results.....	5
	4. Phase II Approach and Results.....	6
II	TECHNICAL DISCUSSION.....	8
	1. Phase I Model Formulation.....	8
	2. Experimental Investigation.....	54
	3. Experimental Program Results.....	74
	4. Phase II — Model Evaluation.....	94
	5. Conclusions and Recommendations.....	117
	APPENDIX A — Test Data.....	119
	APPENDIX B — Equations.....	144

ILLUSTRATIONS

<i>Figure</i>		<i>Page</i>
1	Basic Two-Dimensional Streamtube.....	3
2	Two-Phase Fuel Ducted Flame Model.....	10
3	Ducted Flame Model Linkage Map.....	15
4	Schematic of Wake Mixture Formation.....	16
5	JP-4 Enthalpy Diagram.....	21
6	JP-5 Enthalpy Diagram.....	22
7	Constant Enthalpy Fuel Injection of JP-4 Fuel.....	23
8	Throttling Process, % Vaporized vs Fuel Temperature (JP-4 Fuel).....	23
9	Typical Spray Distribution.....	24
10	JP-4 Droplet Transient Temperature.....	25
11	JP-4 Fuel Wet Bulb Temperature vs Pressure and Gas Temperature.....	26
12	JP-4 Forced Convection Vaporization.....	26
13	Vaporization of JP-4 Fuel Droplets vs Axial Length.....	27
14	Droplet Capture Schematic.....	28
15	Typical B_2 Evaluation Results.....	30
16	Flameholder Surface Vaporization Schematic.....	31
17	Expanded View of Region A Heat Transfer Mechanisms.....	32
18	Finite Difference Solution Procedure.....	34
19	Surface Vaporization vs Fuel Collection Rate for Two Levels of Wake Temperature.....	35
20	Wake L/D vs Blockage Ratio.....	37
21	Wake L/D vs Apex Angle.....	37
22	Wake L/D vs L_{ij} Mach Number.....	38
23	Wake B/D vs Blockage Ratio.....	38
24	Effect of Apex Angle on Wake B/D.....	39

ILLUSTRATIONS (Continued)

<i>Figure</i>		<i>Page</i>
25	Wake Residence Time vs Blockage Ratio.....	39
26	Influence of T_1 on Residence Time.....	40
27	Baffle Stability Correction.....	42
28	Variation in Activation Energy With Inlet Temperature and Equivalence Ratio.....	44
29	Stirred Reactor Kinetic Efficiency vs Loading Rate.....	45
30	Focus of Stirred Reactor Blowout limits.....	46
31	Schematic of Flame Spreading Analysis.....	48
32	Flame Speed for Monodisperse Tetralin Spray.....	50
33	Average Efficiency vs Fuel Air Ratio.....	51
34	Axial Efficiency at Various F/H Widths for 8-in. Duct.....	52
35	Effect of Turbulence.....	52
36	Effect of Wake Reaction Level on Duct Combustion Level.....	53
37	Comparison of Flame Model With Beta Correlation.....	54
38	Flameholder Instability Study Test Rig.....	56
39	Rig Hardware.....	57
40	Inlet Case.....	58
41	Fuel Injection Case.....	59
42	Fuel Spraybars.....	60
43	Spray Direction and Pintel Location With Liquid Fuel Injectors.....	61
44	Combustion Case.....	62
45	Flameholders.....	63
45	Transition Flange.....	64
47	Geometric Nozzle Area Extremes.....	65
48	Nozzle Actuator Assembly.....	66

ILLUSTRATIONS (Continued)

<i>Figure</i>		<i>Page</i>
49	Cross-Sectional View of Kistler Model 606A Installed in a Water Cooled Adapter.....	70
50	Flameholder Skin Thermocouple Locations.....	71
51	Low-Frequency Augmentor Instability Investigation Test Matrix.....	73
52	Flameholder Model Rig Tests.....	74
53	Rumble Rig Combustion Efficiency vs Total Fuel-Air Ratio Peaks Lean.....	77
54	Rumble Break Point Occurs at Predicted Point of Rich Wake Transfer.....	77
55	Overall Combustion Efficiency vs Fuel-Air Ratio.....	78
56	Flameholder Geometry.....	80
57	Combustion Efficiency Data vs Prediction.....	81
58	Laminar Flame Speed for Propane-Air.....	81
59	Run 7.01 Test Analysis.....	83
60	Effect of Heat Addition on Overall Combustion, Efficiency Run 11.02, 35% Blockage Flameholder.....	84
61	Effect of Inlet Temperature on Efficiency.....	86
62	Effect of Velocity on Efficiency.....	86
63	Effect of Inlet Static Pressure on Efficiency.....	87
64	Effect of Static Pressure on Efficiency.....	87
65	Effect of Flameholder Width and Blockage Ratio on Combustion Efficiency.....	89
66	Effect of Apex Angle on Efficiency.....	90
67	Effect of Turbulence Level on Efficiency.....	91
68	Inclined Flameholders vs Normal Location.....	92
69	Drafted Flameholders Efficiency.....	93
70	Effect of Approach Mach Number on Drafted Flameholder Efficiency.....	93
71	Basic Computer Program Logic Diagram.....	96

ILLUSTRATIONS (Continued)

<i>Figure</i>		<i>Page</i>
72	Duct Stream Flameholder Wake Solution.....	98
73	Combustion Model Generalized Geometry.....	100
74	Flame Stability Criteria.....	103
75	The Effect of the JP-4 Mass Velocity on the Eddy Gas Composition for the Natural Gas ($\theta = 0.620$) — JP-4 Flame: H ₂ O, N ₂ and CO ₂ Concentration Profiles.....	104
76	The Effect of the Kerosene Mass Velocity on the Eddy Gas Composition for the Natural Gas ($\theta = 0.620$) — Kerosene Flame: N ₂ and O ₂	104
77	The Effect of the Entrance Air Velocity on the Eddy Gas Composition for the 18×10^{-3} lbm/(in.) ² (min.) JP-4 Wake Flame: H ₂ O, N ₂ , N ₂ and O ₂ Concentration Profiles.....	105
78	The Effect of the Entrance Air Velocity on the Eddy Gas Composition for the 18×10^{-3} lbm/(in.) ² (min.) JP-4 Wake Flame: CO ₂ , CO, and H ₂ Concentration Profiles.....	106
79	F100 Core Stream Efficiency Prediction.....	107
80	F100 Fan Duct Stream Efficiency.....	107
81	Fan Duct Efficiency Near the B.....	109
82	F100 Augmentor Predicted Efficiency vs Fuel-Air Ratio.....	110
83	Effect of Heat Addition on Duct Efficiency.....	110
84	Comparison of Flame Model with Beta Correlation.....	111
85	Swirling Flow Flame Speed vs Conventional Flame Speed.....	113
86	Effect of Augmentor L/D on Combustion Efficiency.....	114
87	Effect of Mach Number on Combustion Efficiency.....	115
88	Comparison of Gas Sample and Choked Nozzle Calculated Efficiencies.....	115
89	Comparison of Gas Sample and Choked Nozzle Calculated Combustion Efficiencies.....	116
90	System Efficiency of the Mechanical Swirler Configuration.....	117
91	System Efficiency Characteristics of the Final Large Pilot Vortex Augmentor.....	117

ILLUSTRATIONS (Continued)

<i>Figure</i>		<i>Page</i>
A-1	Rumble Data for Test Point Number 1 and 2 — Test Number 7.01.....	135
A-2	Rumble Data for Test Point Number 3 — Test Number 11.01.....	136
A-3	Rumble Data for Test Point Number 4 — Test Number 12.01.....	137
A-4	Rumble Data for Test Point Number 4 — Test Number 8.01.....	137
A-5	Rumble Data for Test Point Number 7 — Test Number 8.01.....	139
A-6	Rumble Data for Test Point Number 8 — Test Number 11.01.....	140
A-7	Rumble Data for Test Point Number 9 — Test Number 9.01.....	141
A-8	Rumble Data for Test Point Number 10 — Test Number 10.01.....	141
A-9	Rumble Data for Test Point Number 11 — Test Number 14.01.....	143

TABLES

<i>Table</i>		<i>Page</i>
1	Collection Efficiency vs Droplet Diameter.....	29
2	Flameholder Combustion Instability Study Rig Instrumentation Description	68
3	Revised Test Conditions.....	74
4	Effect of Wake Heat Addition on Efficiency.....	84
5	Program Subroutine Description.....	97
A-1	Experimental Study Rig Data.....	121

SECTION I

INTRODUCTION

The phenomenon of combustion instability has plagued all types of high heat release combustors from industrial furnaces to rocket engines. In general, however, the problem has been most severe in flight propulsion systems such as turbojets, ramjets, and rockets where weight considerations dictate highly efficient structures. In such applications, the pressure, vibration, and heat loads resulting from combustion instability, superimposed on the normal loading, are usually destructive.

In airbreathing engines, high frequency combustion instability problems were first encountered in the early 1950's, and solutions were sought through mathematical modeling and analytical studies directed toward an understanding of the phenomenon. Unfortunately, the computer technology and analytical techniques of 20 years ago proved inadequate, and "cut and try" empirical approaches involving changes in flameholders, combustion chamber shape, fuel injection, velocity profiles, and flame piloting were attempted. Fuel additives and combustion chamber baffles were also tested. Although some of these approaches, notably baffles, produced marginal improvement, the problem was not solved until damping devices in the form of acoustical absorbers (screech liners) were introduced. Screech liners are used routinely, and high frequency instability is no longer regarded as a problem.

Larger and more powerful turbopropulsion systems are presently being designed and developed. Because of the large physical dimensions of augmentors used in these systems, their natural acoustic modes have correspondingly long wavelengths; therefore, combustion instability can occur at very low frequencies, i.e., approximately 200 Hz or less.

The occurrence of instability at lower frequencies makes use of screech liners of conventional design difficult. To obtain adequate damping, the absorbing devices are designed so that the resonant frequency corresponds to the frequency of the expected mode of instability. The required cavity volume is inversely proportional to the square of the resonant frequency; therefore, low frequencies require large volumes. Large cavity volumes can be accommodated by increasing the augmentor envelope, but this produces an unacceptable increase in engine weight.

With the introduction of military augmented turbofan engines, P&WA became involved in the problems of very low frequency instability. The problem of these very low frequencies, called rumble, have been reduced through combined experimental and analytical techniques. This experience has emphasized the necessity to understand the fundamental mechanisms involved in order to formulate a meaningful analytical effort and the necessity to relate this effort to physical hardware and processes.

Mathematical models and analytical studies of low frequency instability have received less attention than studies of high frequency instability and, unfortunately, have not been notably successful. The problems of low frequency instability have been solved or circumvented by empirical methods. For rumble, the development problem is even more expensive and time consuming than for screech since rumble usually occurs only at high altitude, low flight Mach number operation. This requires the extensive use of altitude simulation test facilities to develop a stable augmentor for a turbofan engine.

The main feature which limits the usefulness of many combustion stability models is the absence of a direct correlation between the physical hardware of a real augmentor and combustion stability. Experience has shown that relatively subtle alterations in flameholder geometry can produce profound changes in rumble limits. For a usable design and evaluation tool, the model must be able to relate directly to such geometry changes.

Analytical and experimental studies were conducted to formulate the model necessary to determine the response of an augmentor flameholder to velocity and pressure oscillations typical of low frequency instabilities. The influences evaluated include:

1. Approach velocity, pressure, temperature, and turbulence
2. Flameholder geometry and blockage
3. Fuel distribution and vaporization
4. Heat addition to flameholder wake
5. Inclined flameholder.

Special attention was given to the processes of dynamic flame stabilization in cold airstreams with partially vaporized liquid fuels. This area is one which is unique to turbofan engines and one which has demonstrated the largest influence on the occurrence and severity of rumble.

The experimental studies of the flame stabilization process and the dynamic pressure response of the flameholder and augmentor system were conducted using the existing P₂WA Rumble Simulator Rig. This test rig was specifically designed to investigate the mechanisms involved in rumble.

1. PHASE I ANALYTICAL APPROACH

The approach utilized during Phase I of this program was to formulate a model for the process of flame stabilization and combustion in a turbofan augmentor in terms of basic physical phenomena related to the aerodynamics and thermodynamics of the fuel preparation and combustion processes. By basing the model on evaluations of individual processes which cause the rumble effect, rather than correlating the effect to the overall engine parameters, several significant improvements are available:

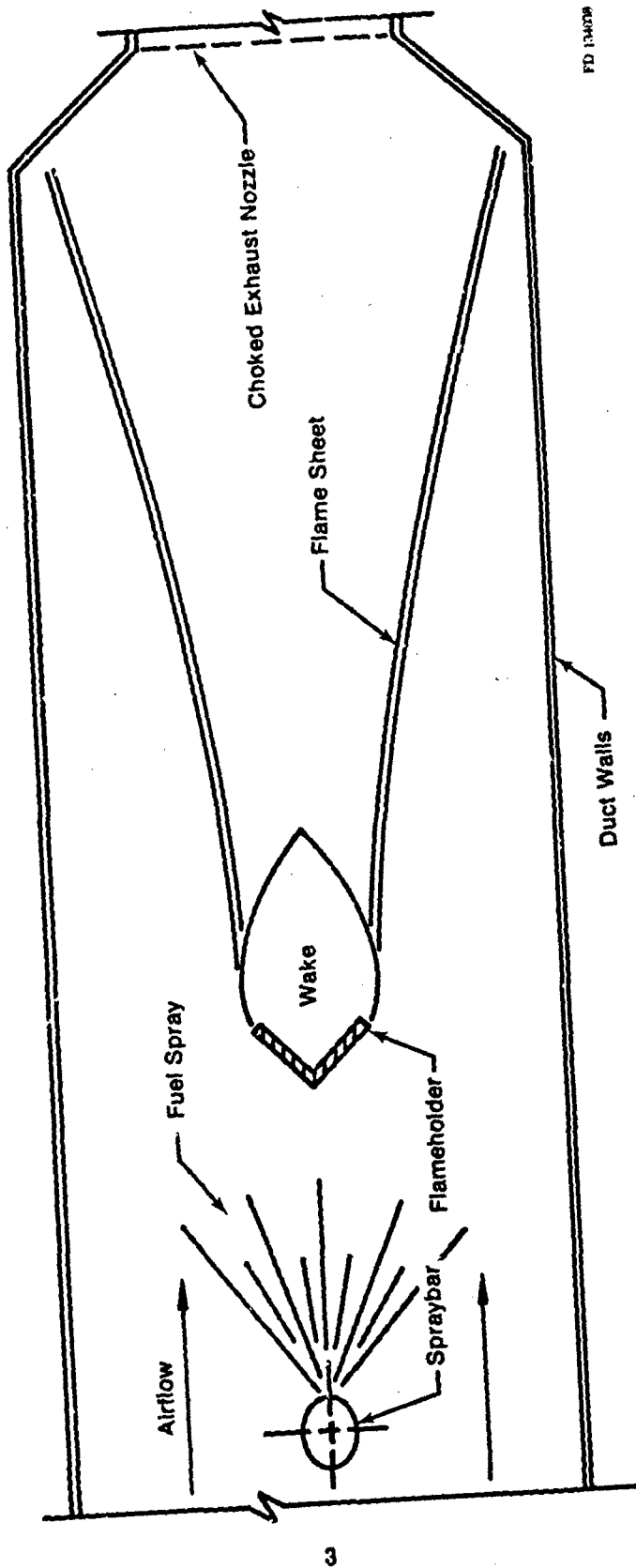
- Increased insight on the fundamental causes becomes available.
- The individual analysis may draw from an experimental data base which fully spans the range of operating parameters where rumble occurs.

The model which has been formulated is a steady-state analysis of the processes which control the stabilization and combustion in the turbofan augmentor. Complete details are presented in Section II of this report. A summary is presented below as an outline of the solution procedure. The model introduces a concept of stabilization in the fan duct section of the augmentor where the process of liquid film vaporization from the flameholder surface is a critical item in controlling the recirculation zone vapor phase fuel-air ratio.

The model analyzes a two-dimensional streamtube (Figure 1) and all comments are related to this streamtube. Since different approaches are taken for the fan and core streamtubes, they are discussed separately.

a. Fan Duct Streamtubes

The effect of inlet air temperatures which are significantly lower than turbine exhaust temperatures is to reduce the liquid fuel vaporization level to a degree where these processes must be closely studied. The degree of vaporization of the droplets of fuel is so low between the injector and the flameholder that the vapor-phase fuel-air ratio is below the lean flammability limit. Since only gaseous species may traverse the shear layers and enter the recirculation zone wake of the flameholder, there would not be sufficient fuel available to provide a stable flame if only droplet vaporization were present.



FD 13409

Figure 1. Basic Two-Dimensional Streamtube

The model proposes that liquid fuel droplets impact the surface of the flameholder in sufficient quantity to form a surface film of liquid phase fuel. This thesis is substantiated by measurements of the flameholder surface temperature in a turbofan engine which revealed significant decreases when the fuel was rejected. The thesis further supposes that this liquid film undergoes partial vaporization due to heat transfer from the reacting wake.

This partial surface vaporization provides the necessary source of vapor-phase fuel to provide a flammable mixture in the wake.

The wake recirculation rate is evaluated from empirical data. The reaction rate within the wake is coupled with the recirculation rate through a stirred reactor analogy to evaluate the wake reaction efficiency and temperature.

Downstream of the wake region, a turbulent flame is initiated in the shear layers and its propagation rate calculated. The flame speed is related to the degree of surface vaporization and wake reaction to account for the local quenching caused by nonvaporized fuel traversing the shear layer zone.

The ultimate degree of flame penetration into the approach mixture determines the streamtube efficiency. Multiple streamtubes are mass averaged to evaluate overall efficiency.

The model consists of separate analyses of each of these processes. Details are presented in Section II.

b. Core Streamtubes

The much higher turbine exhaust gases provide complete droplet vaporization. Thus, the wake fuel-air ratio is assumed to be the same as the total injected fuel-air ratio. As before, the wake recirculation rate is evaluated from empirical data. The same stirred reactor analysis is used to evaluate the wake reaction efficiency. Turbulent flame penetration into the approach mixture is calculated to evaluate the streamtube efficiency.

2. EXPERIMENTAL APPROACH

The experimental approach selected was a systematic evaluation of the influence of various geometric and flow variables under controlled conditions which simulated conventional augmentor operation at high altitude and low flight Mach number. The test apparatus used for this study was the Pratt & Whitney Aircraft Rumble Simulator Rig. This test apparatus is essentially a long duct of 12 in. ID which contains provisions for installing flameholder units, spraybars and viewing ports. It is modularized to allow alterations in upstream length and combustion length. It includes an upstream choked orifice plate to simulate the fan or turbine exit plane and a variable area exhaust nozzle.

The rig is fed airflow from the bleed on a slave JT-4 engine and exhausts through an ejector system. Nonvitiated inlet air is available to temperatures over 600°F and vitiated air to temperatures over 1500°F. Subatmospheric test chamber pressures are possible. A full description of the test apparatus is given in Section II, 2. of this report.

The experimental program was run to evaluate the relative influence of the following parameters on the combustion efficiency and rumble intensity:

- o Fuel-air ratio

- Flameholder geometry
 - Blockage and width
 - Gutter apex angle
- Flameholder to spraybar separation distance
- Drafted flameholder gutters
- Upstream (duct) length
- Combustion length
- Flow variables
 - Static pressure
 - Approach velocity and temperature
 - Free-stream turbulence intensity
 - Fuel vaporization
 - Heat addition to flameholder wake
 - Fuel distribution

These tests were run in two series over a six week period. Fourteen separate configurations were run over a flowrate, pressure, temperature and fuel-air ratio excursion test matrix. Extensive static and dynamic instrumentation was utilized as well as a series of high speed motion pictures.

The basic objective of this approach was to reduce the amount of uncontrolled variables to a minimum and try to limit test changes to one variable at a time.

3. PHASE I RESULTS

The model for flame stabilization and propagation in turbofan augmentors was formulated. The analytical predictions matched the results of the experimental program well. The model correctly analyzed the impact of two-phase fuel on the combustion behavior of the system. The combined analytical and experimental programs produced the following results:

- Augmentor rumble may be treated as a classical combustion stability problem, where the oscillation is driven by the pressure or velocity response of the overall augmentor heat release rate.
- The overall heat release rate is sensitive to variations in velocity and pressure not only through the flame spreading in the free-stream but also through the influence of the flameholder wake region on the downstream flame speed.
- The ultimate level of augmentor efficiency is very sensitive to the nature of the composition and combustion processes in the flameholder near wake region.
- The flameholder wake region composition, i.e., fuel-air ratio, is not necessarily the same as the overall fuel-air ratio and is very sensitive to the exact geometry of the flameholder as well as operating aerothermodynamic conditions.

- The combustion model correctly predicted the influences of the major variables on the overall combustion efficiency, e.g.:
 - Total fuel-air ratio
 - Flameholder approach conditions
 - Vaporization level
 - Flameholder blockage and width
 - Wake heat addition
 - Turbulence level
- The cause of the increased rumble sensitivity with increases in fuel-air ratio and approach flow severity was identified as a decrease in wake reaction efficiency and flame speed.
- The following will, in general, reduce rumble (with the converse true):
 - Wake heat addition
 - Decreased wake fuel-air ratio through flameholder geometry
 - Increased turbulence level
 - Increased fuel vaporization
- In addition, the following produce more severe rumble:
 - Increased spraybar to flameholder separation
 - Increased fuel-air ratio or aerodynamic loading

4. PHASE II APPROACH AND RESULTS

The two tasks performed during Phase II of this contract consisted of computerization and evaluation of the analytical model for combustion in a conventional mixed flow turbofan augmentor and preliminary extension of these concepts to alternative augmentation concepts. Along with this latter task, predictions of the stability of these alternative concepts was performed.

The computerization of the analysis from the Phase I formulations proceeded in a relatively straightforward, if somewhat time consuming, manner. The computer program utilizes a supervisory main with the analysis performed in a subroutine set. This approach allows rapid alteration and improvement on the individual process calculations without disturbing the main program logic.

The computer program will analyze the flame stabilization and propagation process behind a bluff body stabilizer in either the fan duct or core stream zones of a mixed flow turbofan augmentor. Different sequences of subroutines are exercised for these two cases. The lower temperature fan duct analysis performs a two-phase fuel stabilization calculation while the high temperature core stream case is analyzed on the basis of fully vaporized fuel.

The program has been exercised to evaluate its predictions against the results of the experimental program and historical data. Predictions have been made for a turbofan engine augmentor and compared with test experience on that engine development program. The results of these studies are very encouraging in the following manner:

- The behavior of the efficiency versus total fuel-air ratio exhibits the observed sharp rise from the lean limit, peak on the lean side and slower decline until rich blowout.

- The influence of wake heat addition is correct with respect to efficiency increase magnitude and rich limit increase when compared to either test data or engine experience.
- The model predicts augmentor blowout very well when run for the test case engine and compared with development experience.
- The quantitative values and the variation with altitude are in agreement with experience.
- The influence of inlet variables is correct in direction and approximate magnitude.

The efforts under Task II of Phase II were performed on extension to alternate concepts of turbofan augmentor design and evaluation of the possible rumble stability improvement due to these concepts.

Rumble has been identified as the result of the dynamic response of the augmentor efficiency to variations in (in order of sensitivity):

- fuel-air ratio
- pressure
- velocity
- temperature.

For such a situation, rumble may be reduced by any design action which reduces the response of the dynamic efficiency variation to any of these input variables. Such efficiency is essentially a measure of the rate of transverse flame propagation, rumble is reduced by any design or concept variation which reduces the dependence of flame speed on these four variables.

Two alternate concepts of augmentor design have been advanced in recent years. These are the Swirl Augmentor and the VORBIX Augmentor. Both of these attempt to provide forced mixing mechanisms which reduce the response of efficiency to fuel-air ratio dynamic variations. The effect of forced mixing is to remove the sensitivity of transverse flame speed to the local heat release rate (i.e., fuel-air ratio) and replace it with a turbulent mixing function which is primarily a function of the design.

Such an approach will produce an augmentor design which is less prone to rumble. The problems which still exist in these concepts, however, are the piloting response and fuel distribution. In general, severe pilot response to flow variations or severe nonuniformities in fuel distribution will produce higher rumble response characteristics. These topics are treated in Section II.

SECTION II

TECHNICAL DISCUSSION

1. PHASE I MODEL FORMULATION

a. Rumble Mechanism

During Phase I a combustion analysis was generated for the process of stabilization and propagation of flame in the presence of liquid hydrocarbon fuels with conventional bluff body stabilizers. The onset of rumble has been identified as occurring whenever the fuel-air ratio in the colder fan duct airstream exceeds some critical level. This critical level varies with the exact geometry of the flameholder and the operating conditions of the augmentor.

The nature of the feedback mechanism which drives the instability is the classical pressure and velocity response of the heat release mechanism causing variations in the average augmentor exit temperature. These variations result in oscillations in average nozzle inlet pressure through the choked flow relationships for a constant mass flowrate. This results in further oscillations in the flow conditions around the spraying and flameholder region. The relative amplitudes and phase angles are functions of the geometry and operating conditions of the augmentor and fan duct.

This program was directed toward the analysis and modeling of the heat release process in terms of physical geometry and actual operating conditions. The analysis and modeling of the response of the augmentor system to the sensitivity of the heat release process was done in a companion program under Contract F33615-76-C-2024.

The analysis and model for the heat release rate were structured to rely as heavily as possible on analyses of the physical processes of the fuel preparation, flame stabilization and flame propagation. In this manner it was felt that maximum utility of the model would be realized. All too frequently combustion stability models are generated with built-in correlation constants which are generic to one form of combustor only. Whenever a geometry variation is performed there is no guideline for the required change in those constants, and the utility of the model is limited until sufficient experience is obtained. In this model format we have attempted to remove that restriction.

The mechanism of response of the heat release process to variations in pressure and velocity over the spraying and flameholder region is described below with reference to Figure 2.

- A variation in pressure and velocity over the fuel injection spraybar results in a variation in the average air mass flowrate and thus local fuel-air ratio, since the fuel flowrate is essentially constant.
- At the flameholder, the pressure and velocity oscillation results in a variation in the rate of formation of the flameholder wake fuel-air ratio from the available liquid phase fuel.
- The pressure/velocity oscillation also results in a variation in the level of the wake reaction efficiency at the above level of fuel-air ratio. This results in a variation in the rate of initial flame propagation into the approach stream fuel-air mixture.

- The pressure/velocity oscillation also results in a variation in the rate of transverse flame spreading at the local flame speed due to the influences of local pressure and turbulence on flame speed.
- The final result is a variation in the average value of the nozzle inlet temperature due to the combined effects of the previous responses.

This variation occurs at a time delay equal to the transport delay between the sprayings and the nozzle.

This process includes two major mechanisms which cause a response in nozzle inlet temperature to oscillations in augmentor inlet pressure or velocity. The variation in local fuel-air ratio (i.e. axial variation at fixed overall level) causes an axial variation in heat release which is felt as a temporal oscillation in nozzle inlet temperature. Imposed onto this variation is the variation in axially local heat release, at the value of fuel-air ratio, caused by response of the flame-holding process to the pressure or velocity oscillations.

The combustion model required must thus be able to relate the ultimate average of augmentor exit temperature to the local values of operating conditions at the flameholder and fuel injection source as well as to the geometry of the augmentor and flameholder.

b. Combustion Model Philosophy

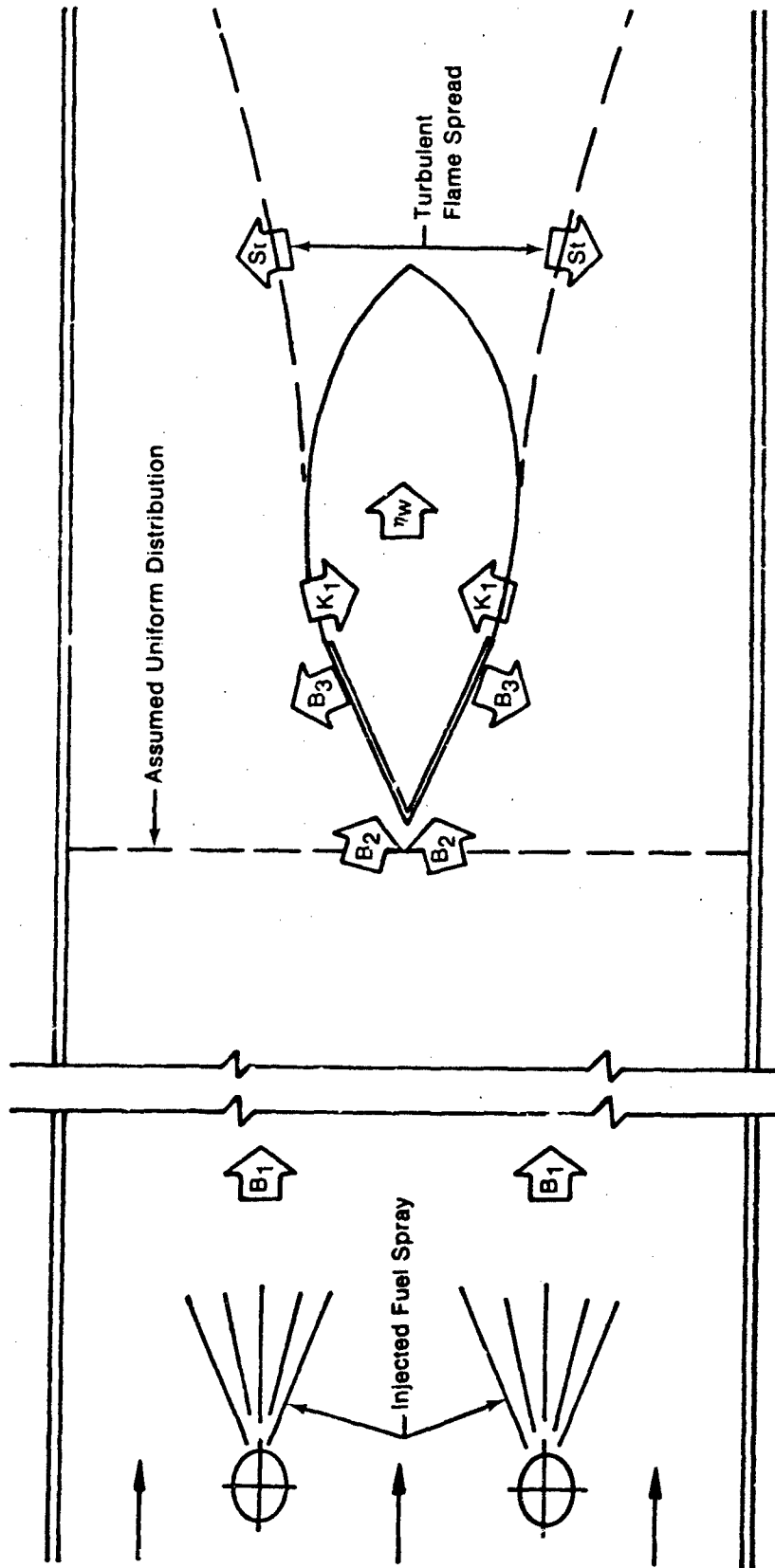
"... it is only rational to begin with an idealization, a simplification, even though we know that to be 'wrong'. We begin with that as a first approximation, then correct for major discrepancies, then for minor discrepancies, then for very minor discrepancies, and so on. Little by little we approach a (possibly unattainable) real 'truth' and in the process develop a precision as tight as necessary for our purposes."

Isaac Asimov, 1969

The basic framework of the model will be described with references to Figure 2. This illustration may be visualized as representing a two dimensional sector of a flameholder array. A full augmentor analysis would require a multistreamtube solution to represent the full flameholder.

The augmentor inlet conditions are known in terms of area, pressure, velocity, temperature, turbulence intensity and vitiation level (if any). The required overall fuel-air ratio and thus fuel flowrate from the spraybar is specified in terms of flowrate versus pressure drop and droplet size and distribution also versus pressure drop. Once specified, the flowrate of fuel or overall fuel-air ratio and duct static pressure will define a droplet size distribution.

At this point of injection a simple enthalpy balance is performed to evaluate the percentage of the fuel which vaporizes due to the adiabatic throttling process of injection from the high-pressure spraying into the low-pressure augmentor. For this, the fuel properties and fuel temperature in the spraying must be known. The fuel flowrate which remains in the liquid phase is placed into 5 or 10 fuel droplet size groups which represent equal mass flowrate distributions of the spray distribution curve for the particular spraying injector.



FD 1344789

Figure 2. Two-Phase Fuel Ducted Flame Model

These fuel droplets are allowed to accelerate with the airstream towards the flameholder with concurrent droplet vaporization. The vaporization analysis utilizes a forced convection model for combined heat and mass transfer. A finite difference scheme integrates the accelerating vaporizing droplet lifetime until either the flameholder plane is reached or the droplet diameter goes to zero. This is performed for each droplet size group. The droplets are treated as spherical for the acceleration and vaporization analysis.

It is at this location, the flameholder leading edge, that the combustion model deviates from classical flameholder or combustion analyses. The classical explanation for the mechanism by which a flameholder functions is that the wake of the bluff body serves as a volume for the reaction of the vapor phase mainstream fuel-air mixture. Ignition of the high-speed mainstream mixture is achieved by the hot wake reaction products in the shear layers aft of the flameholder. The degree of reaction achieved in the wake volume is dependent on the ratio of average residence time to average reaction rate. The reaction rate depends on the entering vapor fuel-air ratio and operating pressure and temperature, i.e. kinetic rate constants.

The problem is that in a relatively cool airstream, such as the 250° fan duct exit temperature, and overall fuel-air ratios which typically react well the degree of droplet vaporization is very low. So low, in fact, that the vapor phase fuel-air ratio at the flameholder is well below the lean flammability limit for JP-type fuels. However, these conditions do produce stable flames in actual burners. Obviously, there is some additional mechanism by which vapor phase fuel is generated and mixed into the flameholder wake.

The mechanism which has been identified for this process is the formation of a liquid film on the surface of the flameholder by impingement of the fuel droplets. This surface film is partially vaporized by the heat flux from the hot wake through the surface of the flameholder into the film. This vaporized fuel enters the recirculation zone through the shear layer and provides the bulk of the vapor fuel for the wake reaction process.

For the purposes of the model, the process of fuel collection on the surface of the flameholder is analyzed as spherical droplet trajectories through the flow field as it moves around the flameholder. The analysis is performed for each of the initial drop size groups utilizing the diameter which remains after the droplet has experienced partial vaporization between the spraybar and the flameholder. This analysis defines the fuel collection rate onto the surface of the flameholder, when integrated over the droplet size groups.

Once the film is established on the surface, the rate of vaporization is analyzed by assuming a Nusselt number form of forced mass transfer driven by the vapor pressure of the film. A combined film heating and vaporization solution is performed as a finite difference analysis along the surface. The heat flux is evaluated from a wake film coefficient and an assumed wake temperature. Since the wake temperature is a function of the fuel vaporization rate and the wake reaction level, an iterative solution is required between this initial guess of wake temperature and the calculated value.

As the finite difference solution proceeds, a certain amount of liquid fuel accumulates which has experienced heating but no vaporization. This fuel is lost to the near field stabilization process but does enter into the far field reaction during turbulent flame spreading. The energy required to raise this fuel from its collection temperature to the final film temperature represents a heat loss from the wake reaction.

For the evaluation of the wake reaction, the wake is treated as a well-stirred chemical reactor operating with gaseous fuel. To perform this calculation, the volume and mass influx rate must be known. These values are produced from published data on the relative size and recirculation rates behind bluff body stabilizers as functions of geometry and operating

conditions. (Specific source references will be given as the analyses are developed in a later section of this report.) These data have been reduced to a series of empirical functions which relate wake volume and recirculation rate to flameholder blockage, geometry, approach flow conditions, and turbulence level.

The reaction efficiency in this known size wake reactor is analyzed assuming that the process proceeds as a single step, second order reaction with the inefficiencies represented as unreacted CO for lean operation or unreacted fuel for rich operation. The entering mass flowrate is balanced against the mass consumption rate at an unknown final level of efficiency. A straightforward solution for the reaction efficiency and thus wake temperature proceeds. Any external heat gain or loss mechanisms are used to adjust the reaction rate and increase or reduce the final reactor efficiency.

At the known level of entering air and droplet vaporized fuel flowrate plus surface vaporized fuel, the iteration is performed as follows:

- Recirculation rate calculated
- Wake temperature assumed
- Surface vaporization calculated
- Wake fuel-air ratio thus known
- Wake reaction level at this f/a calculated
- Wake temperature thus known
- Iterate back through surface vaporization

At this point the wake conditions are known, and the fuel-air ratio distribution around the flameholder is known. The turbulent flame spreading into the free-stream is initiated in the shear layer by the hot wake products. The degree of perfect initiation depends on the excess thermal energy available from these products. Flame initiation is a go or no-go phenomenon and statistical in nature, since a lack of perfect initiation physically results in local regions along the surface of zero ignition. As the temperature of the wake products is reduced, the percentage of the area which fails to ignite increases. As these regions increase in number and size, a greater portion of the heat liberated in those areas which do ignite is transferred into adjacent unlit regions rather than into transverse flame propagation. Since the model is based on uniform flame initiation, this process is observed as a slower rate of flame spreading. To produce this result, the model relates the flame speed to the ideal turbulent value and the wake efficiency level.

The form of the flame spreading model is a thin sheet flame front propagating into a fuel-air mixture at a velocity which was accelerated by the flameholder blockage. The specific analysis for the turbulent flame speed follows Karlovitz, where the turbulent flame speed is related to the laminar flame speed, at the approach conditions and the local fuel-air ratio, and the local value of turbulent velocity. This latter term is evaluated from the turbulence generated by the flameholder and axially decayed in a $10 L/D$ length, based on the width of the effective jet flow between the flameholders, as a function proportional to $x^{-1/2}$. The final value after decay is the free-stream intensity.

An additional term is added to the calculated value of the turbulent flame speed to account for the sensitivity of the reaction rate to integrated efficiency and flame self-turbulence. These terms are modeled as a multiplier whose value depends on the local efficiency and has a value of 1 at zero and 100% efficiencies. The peak value is 2 at 50% efficiency.

The transverse position of the flame front is found by a finite difference integration of the local flame front into the approach flow. Due to the sustaining effect of the local heat release, the approach velocity is axially retained at the value accelerated by the flameholder.

The overall efficiency is found at the nozzle entrance through integration of the flame spreading heat release evaluated from the preceding analyses.

c. Combustion Model Program

The combustion analyses are computerized into one cohesive program which combines the models for the various processes discussed previously under Combustion Model Philosophy. The computerization approach selected is one which utilizes separate subroutines for each of the process sections of the model. Although this approach consumes slightly more computer run time than a full step-by-step calculation procedure it was selected for two reasons:

1. It allows easier alterations to each separate process should changes in any of the local analyses be desired, e.g., a revised reaction kinetics model. This reduces the chances for errors due to unforeseen interactions between sections of the program.
2. The iterative steps required between the wake analysis and the surface vaporization analysis is facilitated if they are isolated in the program.

Written in this manner, a single inlet condition analysis requires only about 10 seconds of CPU execution on the IBM 370-168 computer. The required input consists of a description of the geometry of the streamtube:

- Bloc' age ratio
- Flameholder width
- Flameholder apex angle
- Spraybar to flameholder spacing
- Flameholder to exhaust spacing.

Those parameters which describe the operating conditions are:

- Inlet pressure
- Inlet velocity
- Inlet temperature
- Inlet turbulence intensity
- Fuel-air ratio
- Spraybar fuel pressure
- Spraybar fuel temperature
- Fuel type
- Vitiation fuel-air ratio.

These inputs define the required framework for the analysis. The program organization is shown in Figure 3. The various subroutines perform the analyses as follows:

INJECT	This performs the spray formation and throttling process vaporization analyses.
ACCEL	This evaluates the forced vaporization and acceleration of the droplets between the spraybar and flameholder. Done once per droplet size group.
COLLECT	This evaluates the collective rate of the liquid droplets onto the surface of the flameholder. Performed once per droplet size group.

RECIRC	This evaluates the size of the recirculation zone wake behind the flameholder and the rate of entry of gaseous components into this volume.
B3	This evaluates the rate of vaporization of the liquid film from the surface of the flameholder.
WAKE	For the results of RECIRC and B3, this solves for the wake reaction efficiency and temperature.
FLAME	This performs the solution for the transverse penetration of the turbulent flame from the wake shear layer into the free-stream mixture.

Currently, the input and output reflect the requirements to analyze a single case streamline analysis. The output defines the intermediate results of the various subroutines as well as the heat release profile between the flameholder and the exhaust nozzle. The program is capable of multiple case execution limited only by run time. This capability would be utilized for multiple streamtube analysis and parametric studies. At present, there is no graphics output capability, but it could be added.

d. Analyses and Results

The combustion model as formulated for the rumble mechanism essentially consists of two parts. These are a compositional analysis and a reaction analysis. The compositional analysis defines the manner in which a combustible fuel-air mixture is generated from the injected liquid fuel. The reaction analysis defines the manner in which this mixture actually burns to produce a final level of combustion efficiency.

The analysis for the compositional portion is outlined below for the basic case of a two-dimensional duct with a bluff body stabilizer and liquid fuel injection source. For ease of development of the solutions, the following assumptions were used:

- The injected liquid fuel forms a homogeneously dispersed spray which fills the full cross section of the duct.
- The approach flow field is uniform in the transverse direction, i.e., transverse uniformity of velocity, pressure, and temperature.

Under these assumptions, the form of the compositional analysis was developed. The schematic of the processes is shown in Figure 4.

A certain portion of the injected fuel flowrate experiences flash vaporization during the injection process and forms a uniform flowrate of vapor phase fuel. This fuel flowrate is:

$$\dot{w}_{fv} = \beta_{1T} \dot{w}_f \quad (1)$$

The remaining portion of fuel goes into a liquid droplet spray which undergoes spray vaporization. The vapor flowrate produced by this process is:

$$\dot{w}_{fv} = \beta_{1E} (1 - \beta_{1T}) \dot{w}_f \quad (2)$$

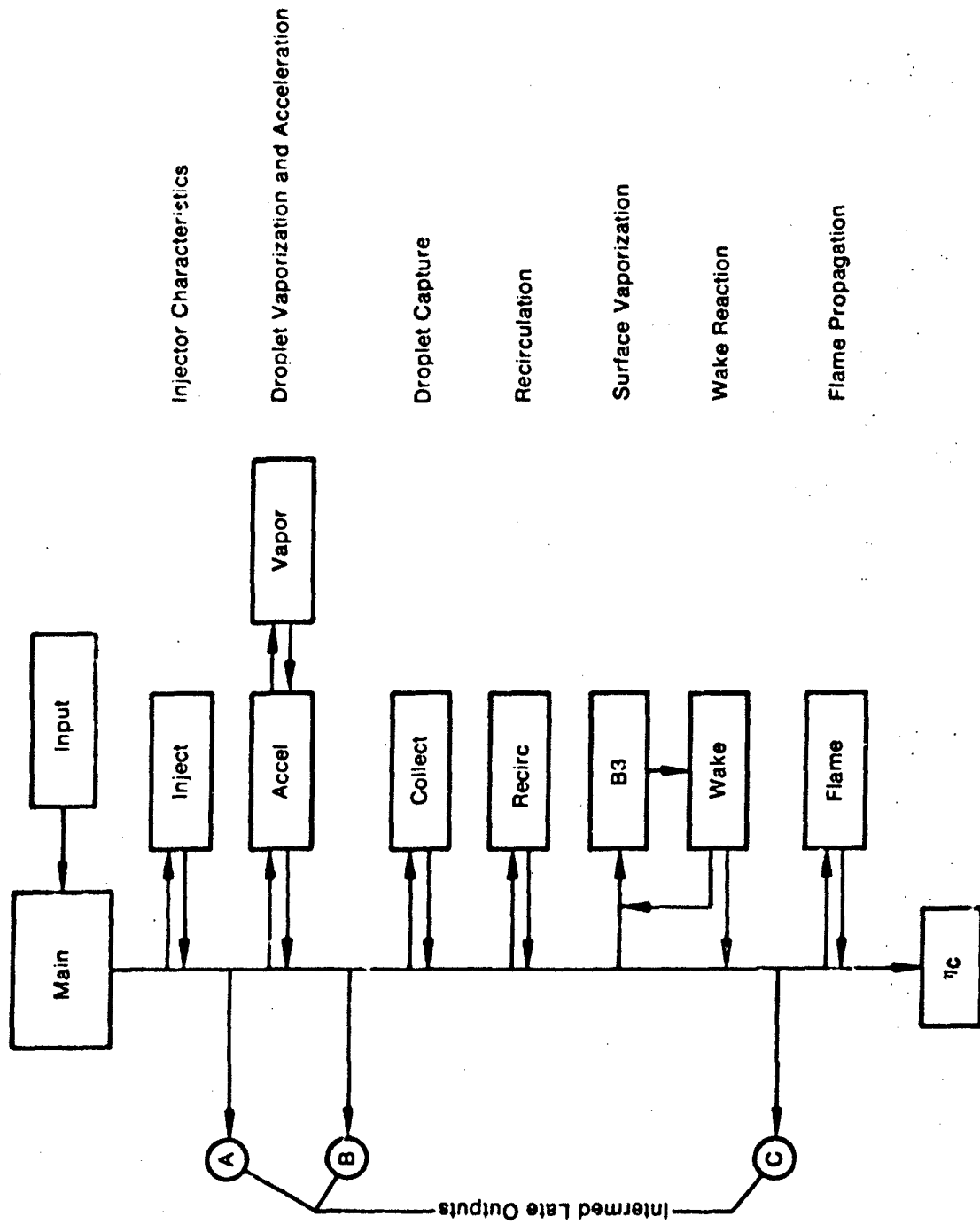
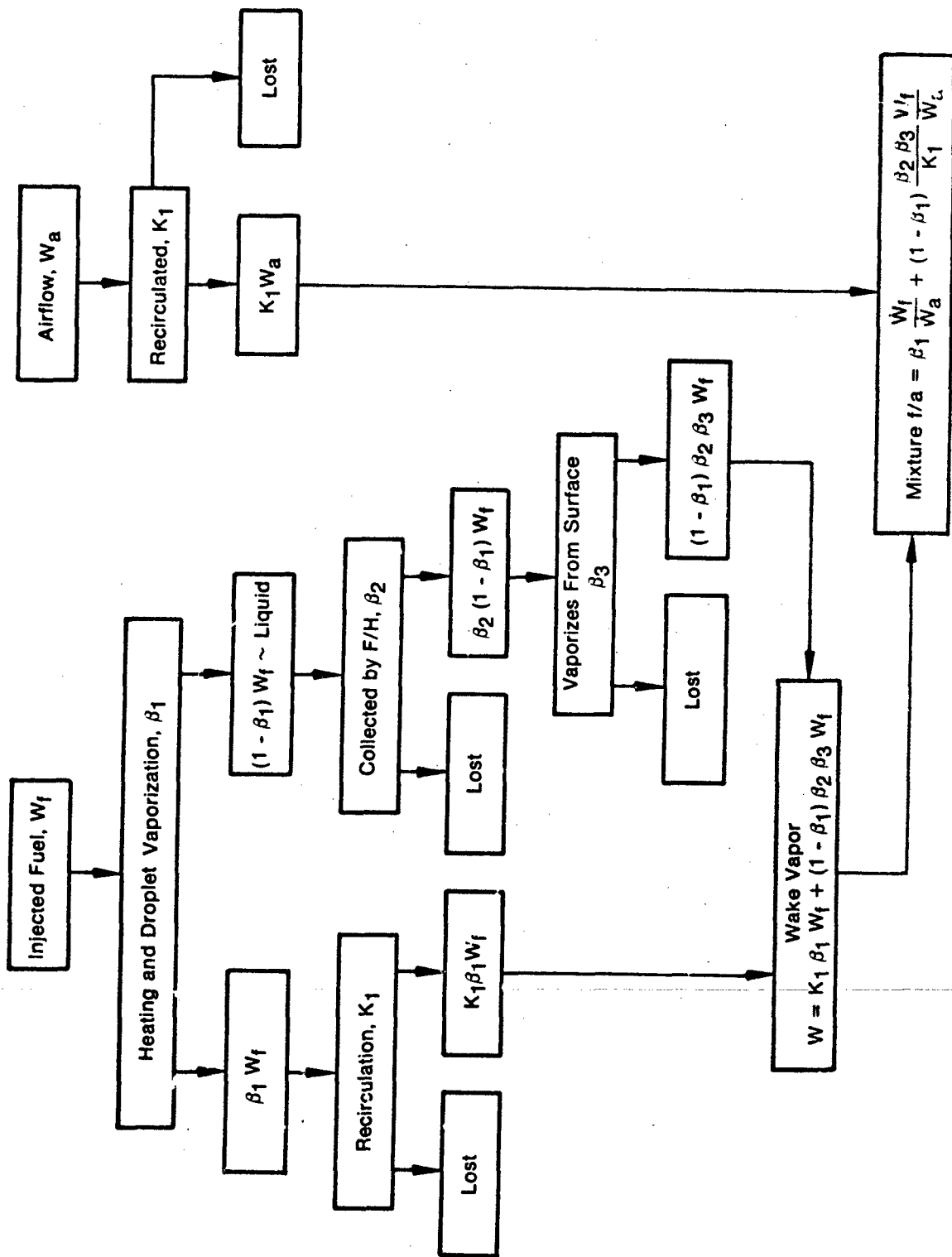


Figure 3. Ducted Flame Model Linkage Map



FD 134041

Figure 4. Schematic of Wake Mixture Formation

Combining these processes into one influence coefficient we may write:

$$\dot{w}_{r_v} = \beta_1 \dot{w}_r \quad (3)$$

We continue to utilize the assumption that the vaporized fuel is homogeneously spread as it is produced. The next processes which are evaluated are those concerned with the formation of the liquid film vaporization rate.

At the flameholder plane, the mixture consists of a flowrate of air (\dot{w}_a), vapor fuel (\dot{w}_{r_v}) and liquid fuel (\dot{w}_{r_l}) defined as:

$$\dot{w}_a = \rho_a VA \quad (4)$$

$$\dot{w}_{r_T} = \theta \dot{w}_a \quad (5)$$

$$\dot{w}_{r_v} = \beta_1 \dot{w}_{r_T} = \beta_1 \theta \dot{w}_a \quad (6)$$

$$\dot{w}_{r_l} = \dot{w}_{r_T} - \dot{w}_{r_v} = (1 - \beta_1) \theta \dot{w}_a \quad (7)$$

This leaves $(1 - \beta_1)$ liquid fuel percentage available. Flowing through the flameholder area, then we have:

$$\dot{w}_{a\Gamma} = \Gamma \dot{w}_a = \Gamma \rho_a VA \quad (8)$$

$$\dot{w}_{r_l\Gamma} = (1 - \beta_1) \theta \dot{w}_a \Gamma \quad (9)$$

$$\dot{w}_{r_v\Gamma} = \beta_1 \theta \dot{w}_a \Gamma \quad (10)$$

The liquid and vapor fuel-air ratios at this point are:

$$(f/a)_v = \frac{\dot{w}_{r_v\Gamma}}{\dot{w}_{a\Gamma}} = \frac{\beta_1 \theta \dot{w}_a \Gamma}{\dot{w}_a \Gamma} = \beta_1 \theta \quad (11)$$

$$(f/a)_l = (1 - \beta_1) \theta \quad (12)$$

A portion of the liquid fuel is now collected and vaporized from the surface. The collection rate of liquid fuel is:

$$\dot{w}_{r_c} = \beta_2 \dot{w}_{r_l\Gamma} = \beta_2 (1 - \beta_1) \theta \dot{w}_a \Gamma; \quad (13)$$

of this amount, β_3 percentage vaporizes from the surface and recirculates:

$$\dot{w} = \beta_3 \dot{w}_{r_c} = \beta_2 \beta_3 (1 - \beta_1) \theta \dot{w}_a \Gamma \quad (14)$$

The prevaporized fuel recirculates at a rate of K_1 percent which passes the blocked area:

$$\dot{w} = \dot{w}_{r_v\Gamma} K_1 = \beta_1 \theta \dot{w}_a \Gamma K_1 \quad (15)$$

Thus the total recirculated vapor fuel flowrate is:

$$\dot{w}_{r_{vw}} = \beta_1 \theta \dot{w}_a \Gamma K_1 + (1 - \beta_1) \beta_2 \beta_3 \theta \dot{w}_a \Gamma \quad (16)$$

The air recirculation rate is K_1 of the flowrate through the blocked area:

$$\dot{w}_{a_w} = \dot{w}_a \Gamma K_1 \quad (17)$$

From Equations 16 and 17, the wake fuel-air ratio in vapor phase is:

$$\phi = \frac{\dot{w}_{f_{vw}}}{\dot{w}_{a_w}} \quad (18)$$

$$\phi = \beta_1 \theta + (1 - \beta_1) \theta \frac{\beta_2 \beta_3}{K_1} \quad (19)$$

$$\frac{\phi}{\theta} = \beta_1 + (1 - \beta_1) \frac{\beta_2 \beta_3}{K_1} \quad (20)$$

Equation 20 relates the wake vapor phase fuel-air ratio to the overall fuel-air ratio and, through the influence coefficients, to the geometric and aerothermodynamic situation under scrutiny. Each of these may now be evaluated from the available body of combustion literature to determine the overall form of the compositional model.

A comment on the implication of Equation 20 is in order here. This equation determines the mixture in the wake which then undergoes reaction to provide the ignition source for the mainstream reaction. As with any stirred chemical reactor, the most efficient process for a fixed volume occurs near the stoichiometric fuel-air ratio. Since the degree of this reaction efficiency strongly influences the overall augmentor efficiency, the fuel-air ratio should be kept near stoichiometric.

If we introduce the following values from the analyses to be presented later:

$$\begin{aligned} \beta_1 &= 0.20 \\ \beta_2 &= 0.75 \\ \beta_3 &= 0.50 \\ K_1 &= 0.25 \end{aligned}$$

we find that Equation 20 yields:

$$\frac{\phi}{\theta} = 0.20 + (0.8) \frac{(0.75)(0.50)}{0.25}$$

$$\frac{\phi}{\theta} = 1.40.$$

Thus, due to the relative fuel concentrating effect of the flameholder, the wake is 40% richer than the overall system. If the overall fuel-air ratio is 0.050, the wake is over stoichiometric at 0.070. Any further increase in fuel flowrate results in a drastic decrease in the wake reaction efficiency due to the increase in wake f/a.

The second portion of the analyses is the wake reaction efficiency and turbulent flame spreading. These analyses will be developed in the following sections.

(1) Fuel Vaporization Before Flameholder

As developed in the preceding analysis, the percentage of the liquid hydrocarbon fuel which vaporizes prior to reaching the flameholder consists of two mechanisms:

The formation of vapor due to the throttling process of injection (β_{1T}).

The evaporation of fuel droplets due to forced convection (β_{1E}).

Thus we define β_1 as:

$$\beta_1 = \beta_{1T} + (1 - \beta_{1T})\beta_{1E}. \quad (21)$$

The process of flash vaporization during the process of injection is treated as an adiabatic flow from a region of high pressure and moderate temperature (within the spraying) to a low-pressure area (in the augmentor). This flow situation is analogous to the expansion valve process and is evaluated from knowledge of the final properties and operating conditions.

The process is evaluated assuming adiabatic expansion from known levels of fuel pressure and temperature within the spraying to a known pressure level in the augmentor. If the spraying pressure is sufficient to maintain the liquid fuel as a saturated liquid, the enthalpy level is defined for the given fuel type as a function of the spraying fuel temperature only.

For adiabatic injection, the final mixture enthalpy equals the saturated liquid enthalpy at T_f . The mixture enthalpy and a known static pressure will define the quality of the injected fuel. This process is readily evaluated from the enthalpy diagram of the particular fuel type. Enthalpy diagrams for JP-4 and JP-5 are shown in Figures 5 and 6.

An expanded diagram of the adiabatic process for JP-4 is shown in Figure 7. This example is for injection of 250°F fuel into a 7.5 psia environment. The parametric results for JP-4 fuel are shown in Figure 8.

The remaining liquid fuel is partitioned into the droplet size groups on a 5 or 10 group equal flowrate basis. For this, the droplet size distribution must be known. Due to the large number of spray systems available to the augmentor designer, no attempt was made to model this droplet formation process. Rather, a distribution function is built into the program which describes the size distribution as a function of the fuel pressure drop. The curve used in the program represents the droplet distributions for variable area pintle spraybars. Figure 9 shows this function.

If 5 size groups are to be used, each one represents 20% of the liquid flowrate. The sizes used in the analysis would be the 10, 30, 50, 70 and 90% diameters. Once these sizes are known, the program performs the solution to the forced convection droplet vaporization between the spraybar and the flameholder.

The basis for the droplet vaporization solution is the form of the Nusselt number devised for spherical droplets by Ranz and Marshall (Reference 1) and subsequently improved by Preim and Heidmann (Reference 2). The assumed forms are:

$$Nu_H = 2 + 0.6 Re^{1/2} Pr^{1/3} \quad (22)$$

$$Nu_M = 2 + 0.6 Re^{1/2} Sc^{1/3} \quad (23)$$

for heat and mass transfer. For the assumption of Lewis No. = 1, i.e., $Pr = Sc$, these become identical. The fuel droplet mass efflux rate is calculated from:

$$\dot{w} = KA_s p_s \ln \left(\frac{p_s}{p_s - p_v} \right) \quad (24)$$

$$K = \frac{Nu D_v MW}{R d_f T_s} \quad (25)$$

During the transient droplet heating period between injection at $T = T_{i_0}$ and achievement of the wet-bulb temperature, the droplet temperature is evaluated from the heat input and the diffusion driven mass efflux. The difference between the heat required to generate the mass efflux and the heat which actually reaches the surface of the droplet is assumed to go towards alteration of the droplet bulk temperature. This assumption is essentially a statement that the droplet internal circulation is sufficiently rapid compared to the thermal input that significant droplet radial thermal gradients do not exist. Although this assumption has been questioned, most notably by Strahle (Reference 3), any errors introduced are quite secondary to errors in evaluation of the droplet film transport properties. Sufficient accuracy and significant numerical simplification is realized by this method.

In evaluation of the net heat flux into the liquid surface, the mass efflux blocking term introduced by Preim (Reference 2) is used. This term evaluates the loss in net flux due to the vapor superheating which occurs as the evolved fuel vapor achieves thermal equilibrium at the free-stream gas temperature. The transient solution proceeds as follows, after evaluation of the fuel mass efflux rate, \dot{w} , from Equation 24.

The thermal film coefficient, h_f , is:

$$h_f = \frac{k Nu_H}{d_f} \quad (26)$$

where Nu_H is from Equation 22.

The net heat flux to the droplet liquid surface, \dot{q} , is calculated with allowance for the thermal blocking due to vaporizing fuel heating (β):

$$\dot{q} = h_f A_s (T_s - T_f) \beta \quad (27)$$

where

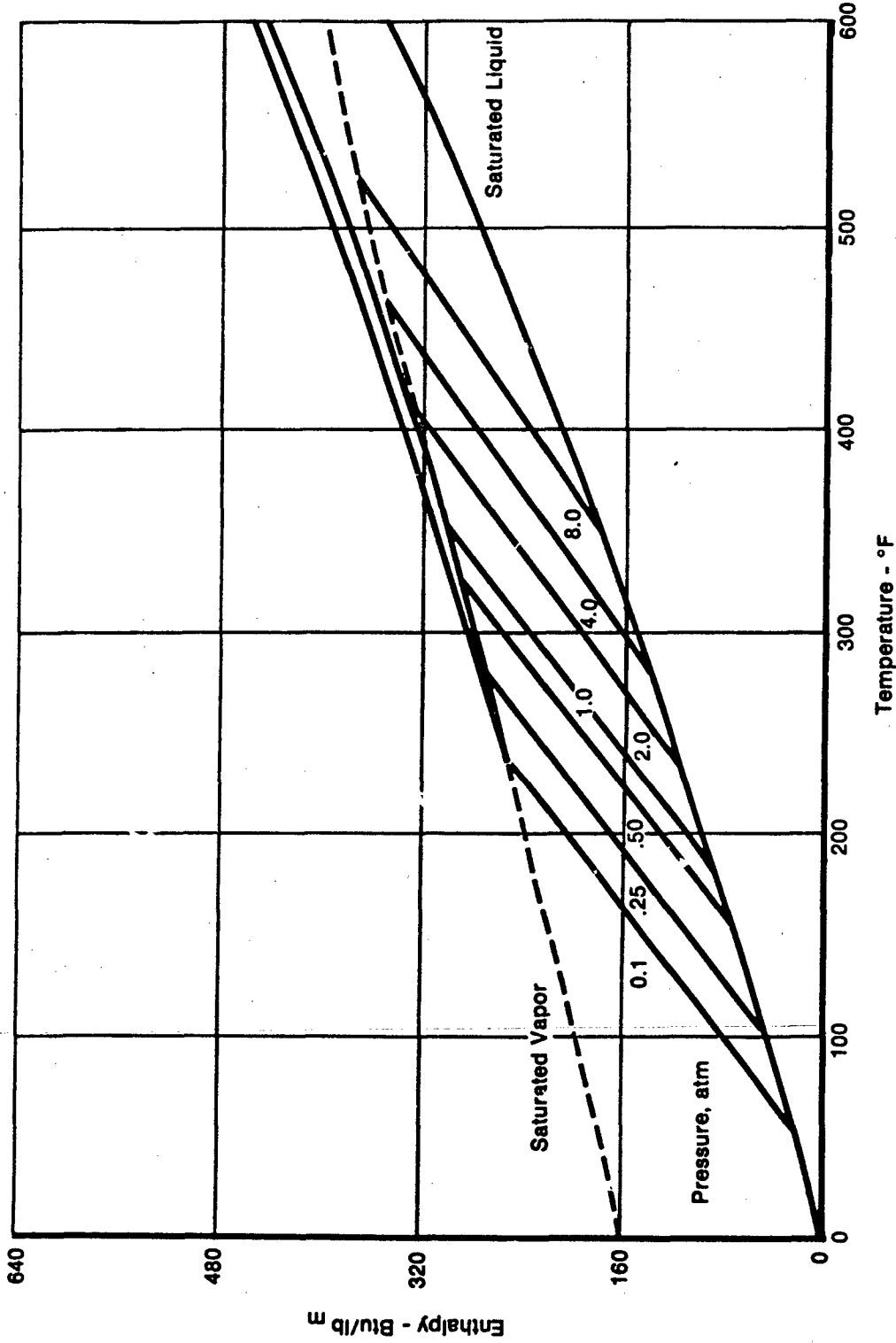
$$\beta = \frac{z}{e^z - 1} \quad (28)$$

and

$$z = Cp_v \dot{w} / \pi k d_f Nu_H \quad (29)$$

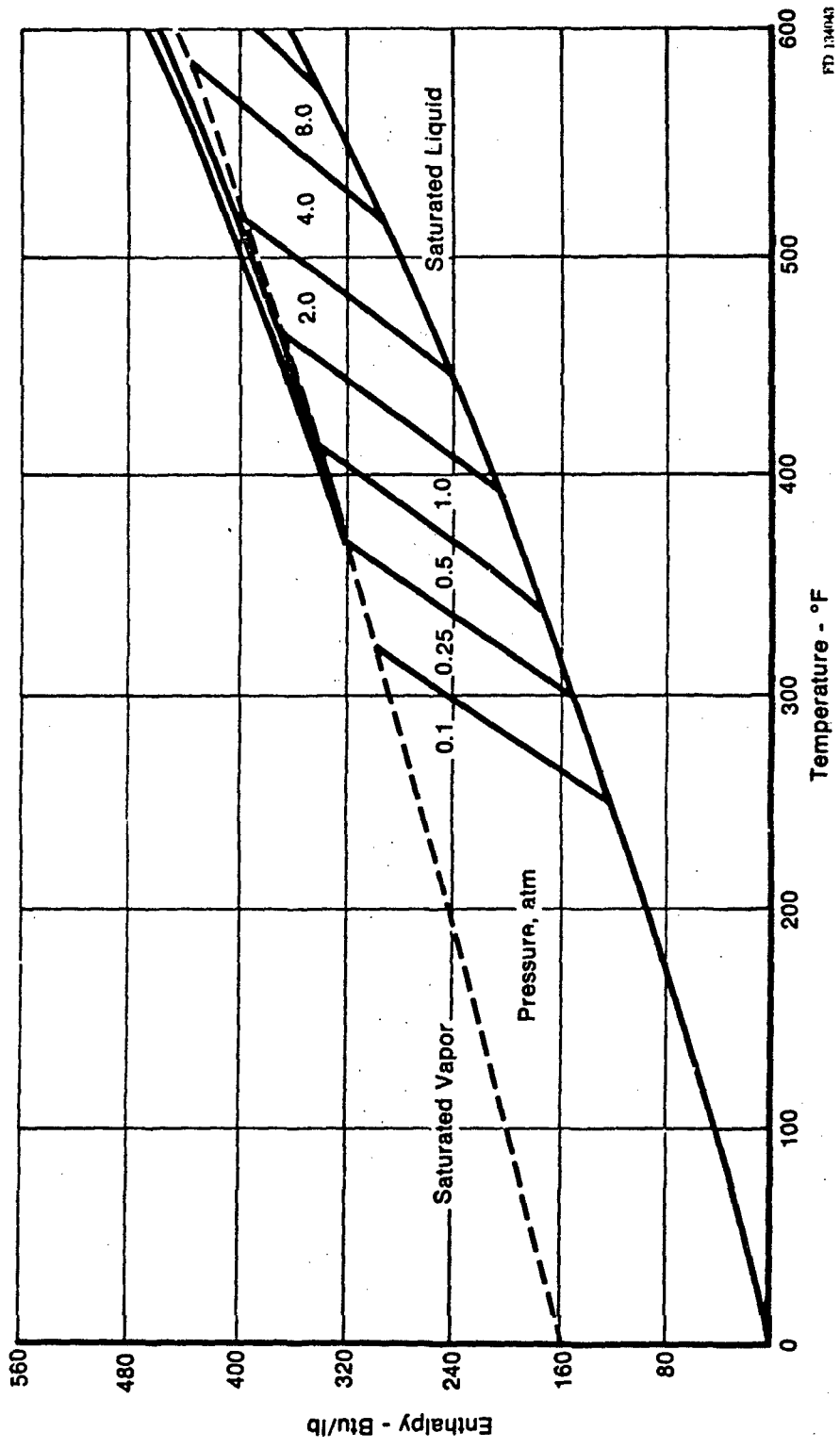
The net amount of heat which is available for sensible heating of the droplet is the net liquid surface flux minus the latent heat required to generate the vapor mass flux:

$$\Delta \dot{q} = \dot{q} - \dot{w}_v \lambda \quad (30)$$



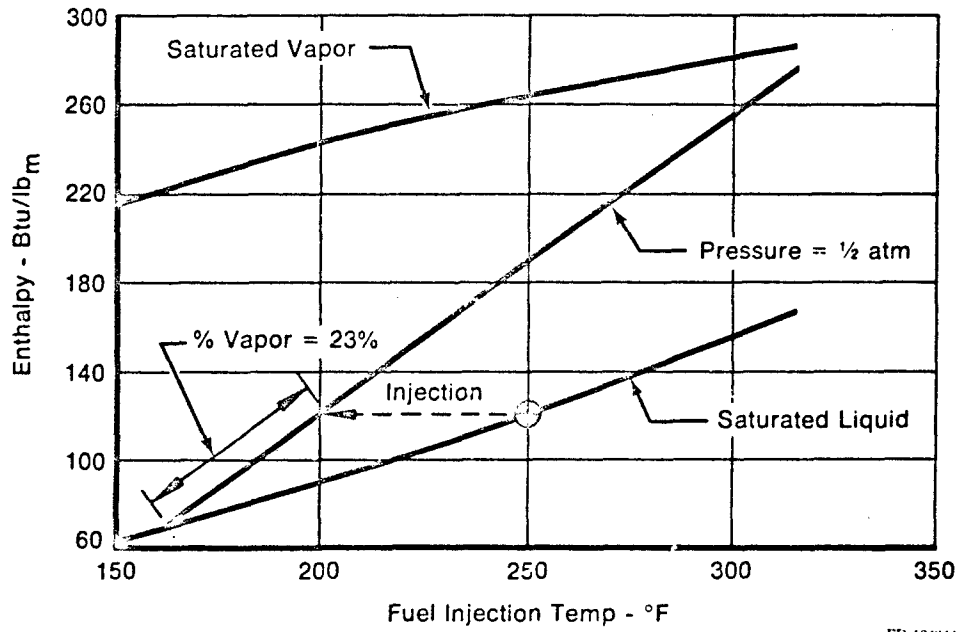
FD 134042

Figure 5. JP-4 Enthalpy Diagram



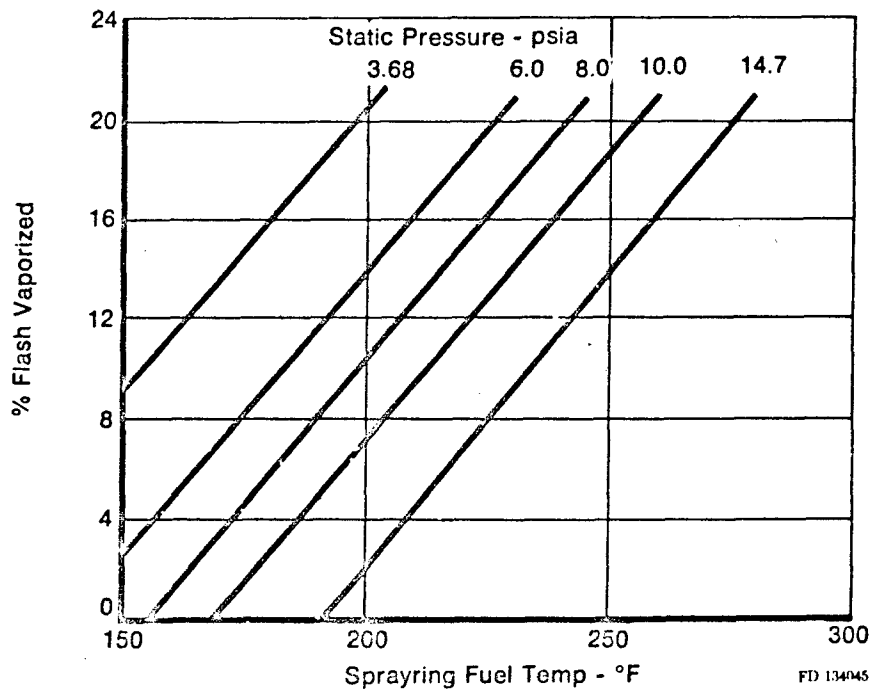
FD 134943

Figure 6. JP-5 Enthalpy Diagram



FD 134044

Figure 7. Constant Enthalpy Fuel Injection of JP-4 Fuel



FD 134045

Figure 8. Throttling Process, % Vaporized vs. Fuel Temperature (JP-4 Fuel)

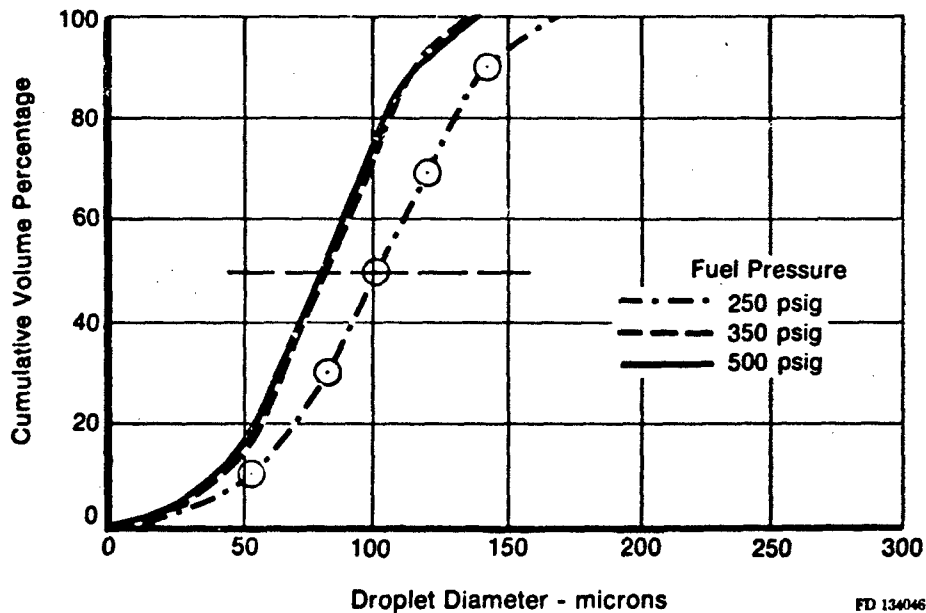


Figure 9. Typical Spray Distribution

This net flux is used to raise the liquid bulk temperature, T , as:

$$\frac{dT}{dt} = \frac{\Delta \dot{q}}{m \cdot C_p} = \frac{\Delta \dot{q}}{4/3 \pi (d./2)^3 \rho_l C_p} \quad (31)$$

This change in T may be positive or negative depending on the relative values of \dot{w} and \dot{q} .

The wet-bulb temperature is defined as that liquid droplet temperature where the thermal net input is just sufficient to generate the mass efflux at that temperature and vapor pressure. As such, it is a function of effective Nusselt number and local static pressure and temperature. Coincident with this transient heating and vaporization, the liquid droplet is being accelerated by the faster free stream gas velocity. The acceleration is evaluated from the standard equation:

$$\frac{dV_l}{dt} = \frac{3}{4} \frac{C_d}{d_l} \frac{\rho_a}{\rho_l} (V_a - V_l)^2 \quad (32)$$

Since the Reynolds number used in the Nusselt number formulation is defined as:

$$Re = \frac{\rho_a d_l (V_a - V_l)}{\mu_a} \quad (33)$$

a simultaneous solution of Equations 31 to 33 is required. In the computer analysis, this is accomplished by a finite difference solution utilizing small time intervals. The ordinary differential equations are rewritten as delta terms, e.g.,

$$\frac{dV_l}{dt}$$

becomes

$$\frac{\Delta V}{\Delta t}$$

For each time increment, the initial values are used to calculate Re , Nu_H , Nu_M , pv , etc. Equations 24 to 31 are solved which yields $\Delta \dot{w}_v$ and ΔT . Equation 32 is solved to yield ΔV . At the end of this step, \dot{w}_v is incremented by $\Delta \dot{w}_v$, T by ΔT and V by ΔV . The average value of V over this Δt yields a delta axial travel distance.

The procedure is repeated in small time steps until either the total axial travel exceeds the spraybar-to-flameholder separation distance or the liquid is fully vaporized. At the start of each new time increment, the input values reset to reflect the effect of the previous step; e.g., ρ_v is evaluated at $T_i + \Delta T$, d is evaluated to reflect less liquid mass, etc.

Some typical results for the vaporization portion of the analysis are presented in Figures 10 to 12. For these results, the droplet acceleration portion of the analysis was deleted to allow solution on a limited size, real-time access computer terminal. Thus, the relative velocity is held constant and the results represent the upper limit on transient heating and mass efflux. Figure 10 shows the transient bulk liquid temperature for a 100 micron droplet in a 400°F, 250 ft/sec gas stream. The decrease in temperature from the initial 80°F injection temperature for the 0.5 atmosphere pressure reflects the fact that the initial mass efflux by convection exceeds the available net heat input. The wet-bulb temperature as a function of gas static pressure and temperature is shown in Figure 11 for the same 100 micron JP-4 droplet.

Corresponding with the wet-bulb temperature, the equilibrium mass efflux for a 100 micron droplet is shown in Figure 12. The effect of pressure and temperature is clearly shown.

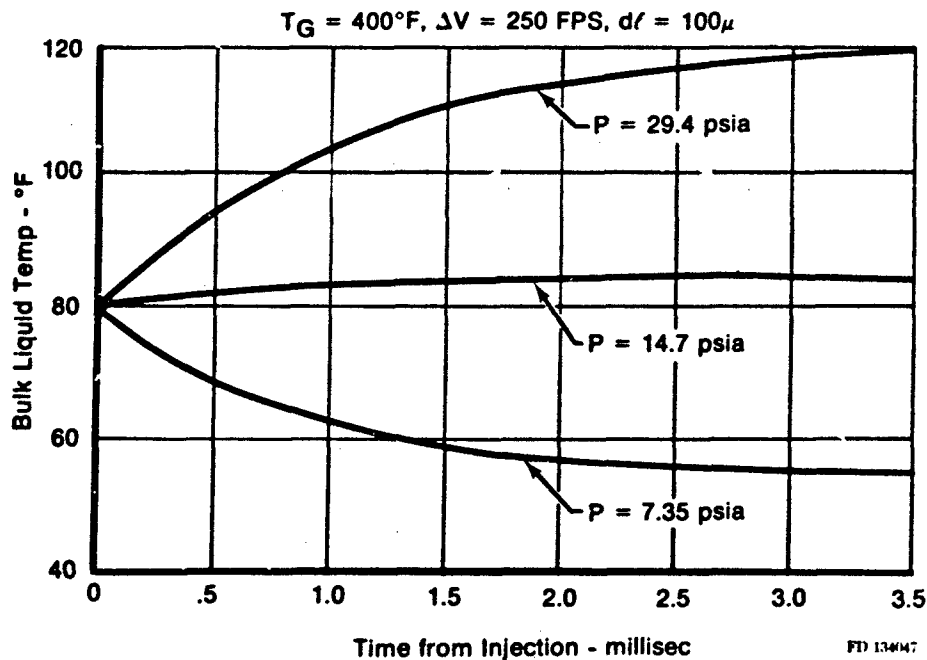


Figure 10. JP-4 Droplet Transient Temperature

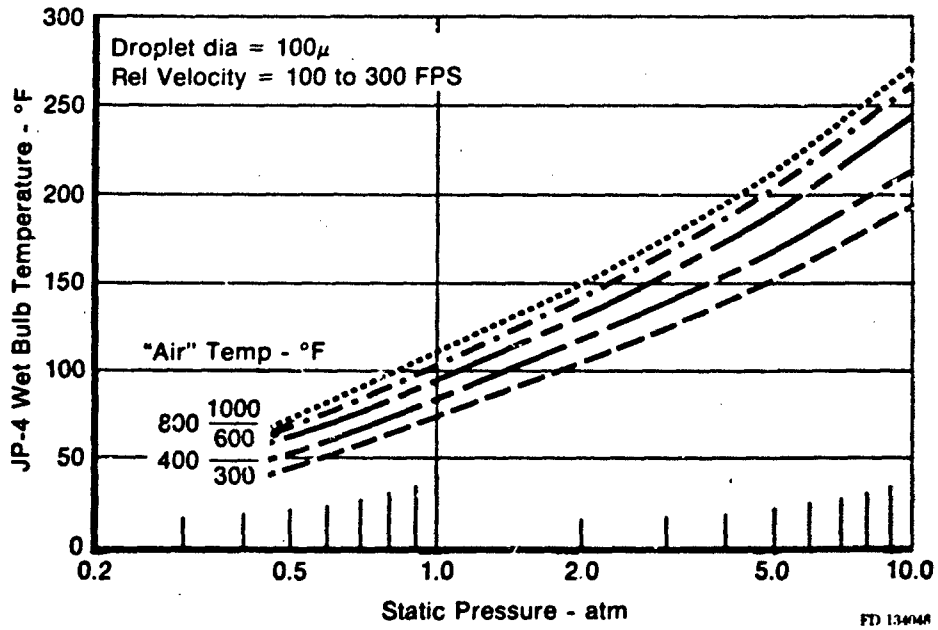


Figure 11. JP-4 Fuel Wet Bulb Temperature vs Pressure and Gas Temperature

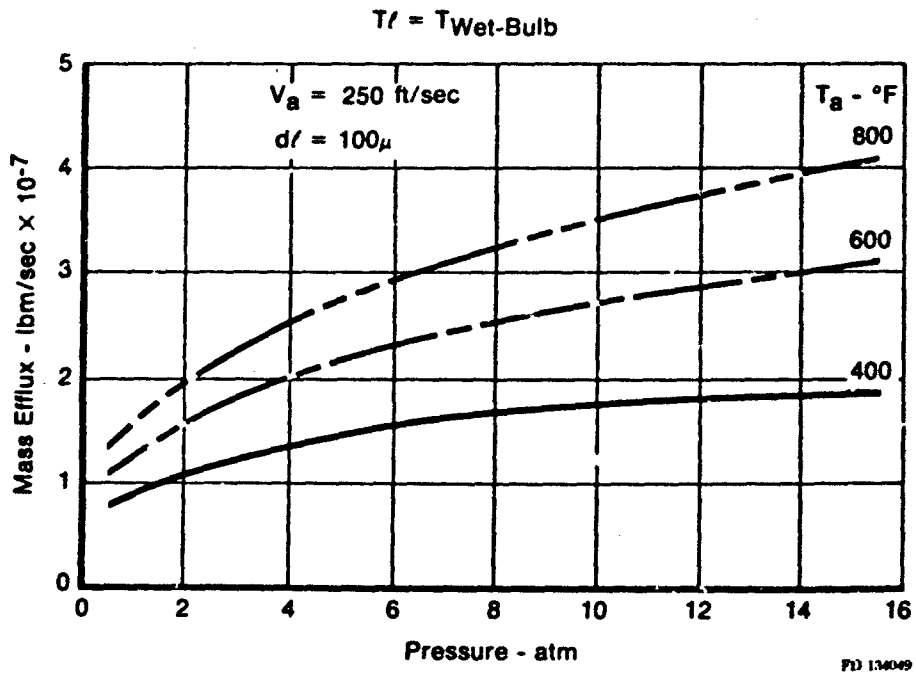


Figure 12. JP-4 Forced Convection Vaporization

For a situation described as follows:

- $V_a = 250$ fps
- $T_a = 275^\circ\text{F}$
- $T_f = 80^\circ\text{F}$
- $P_s = 10$ psia
- $d_i = 25$ to 125 microns.

The amount of JP-4 which will vaporize in a typical distance of 6 inches is shown in Figure 13. These results are typical for fan duct conditions at high altitude and low flight Mach number.

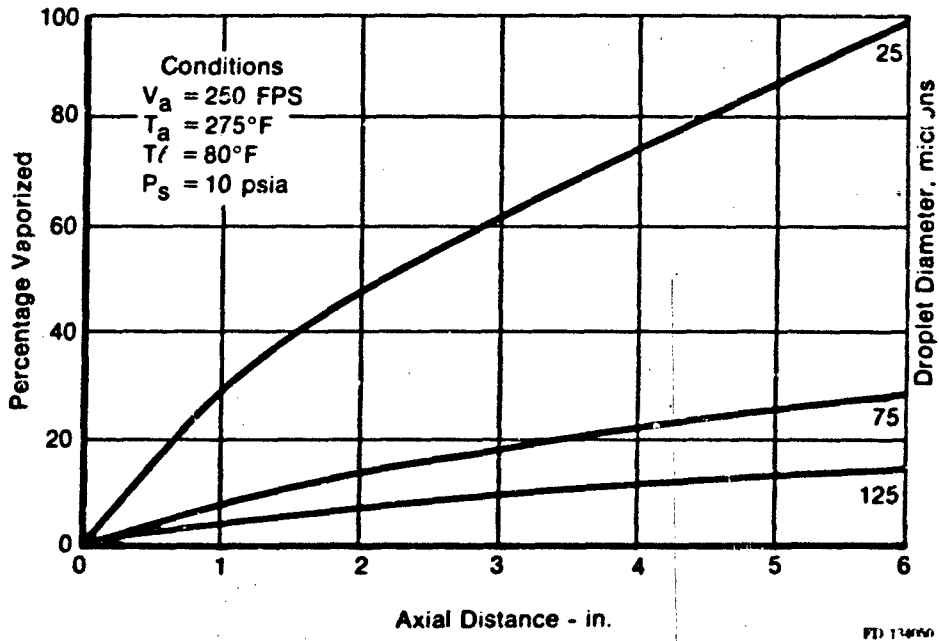


Figure 13. Vaporization of JP-4 Fuel Droplets vs Axial Length

(2) Flameholder Fuel Collection Efficiency

The output from the ACCEL subroutine defines a spray of droplet diameters at a plane with the flameholder leading edge. The diameters are defined from the final step in the forced vaporization analysis as is the droplet axial velocity. The spray field is still assumed to be homogeneous in the transverse direction in terms of size and volume flowrate distribution.

As the flow stream approaches the stabilizer, the suspended droplets are unable to fully follow the divergence of the flow streamlines and a portion of them impinge on the bluff body. The evaluation of this "capture rate" is done in nondimensionalized terms as β_2 :

$$\dot{w}_{lc} = \dot{w}_n \Gamma \beta_2 \quad (34)$$

$$\beta_2 = \frac{\dot{w}_{lc}}{\Gamma \dot{w}_n} \quad (35)$$

where

- \dot{w}_{lc} = fuel liquid capture rate
- \dot{w}_n = fuel liquid flowrate at F/H plane
- Γ = F/H blockage

β_2 is also the ratio of the separation of the droplet capture limit streamlines to the F/H width:

$$\dot{w}_{lc} = \rho_l V_l \delta^* \quad (36)$$

$$\begin{aligned} \dot{w}_n &= \rho_l V_l A \\ &= \rho_l V_l \frac{N}{\Gamma} \end{aligned}$$

Substituting yields:

$$\beta_2 = \frac{\delta^*}{N} \quad (37)$$

where δ^* ~ droplet capture width. This is shown schematically in Figure 14.

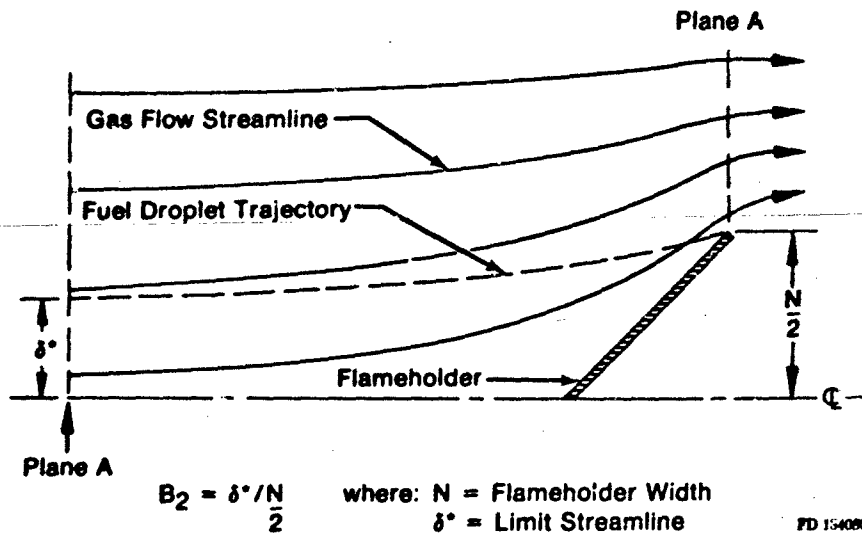


Figure 14. Droplet Capture Schematic

This analysis will be performed once for each size group exiting the vaporization analysis. If 10 groups are used initially, each size represents 10% of the liquid fuel at plane A, since the smaller sizes will have higher vaporization rates between the injection plane and plane A. The overall collection rate is thus:

$$\beta_2 = \frac{1}{m_{1,A}} \sum_{i=1}^{10} m_{1,i} A \beta_{2i} \quad (38)$$

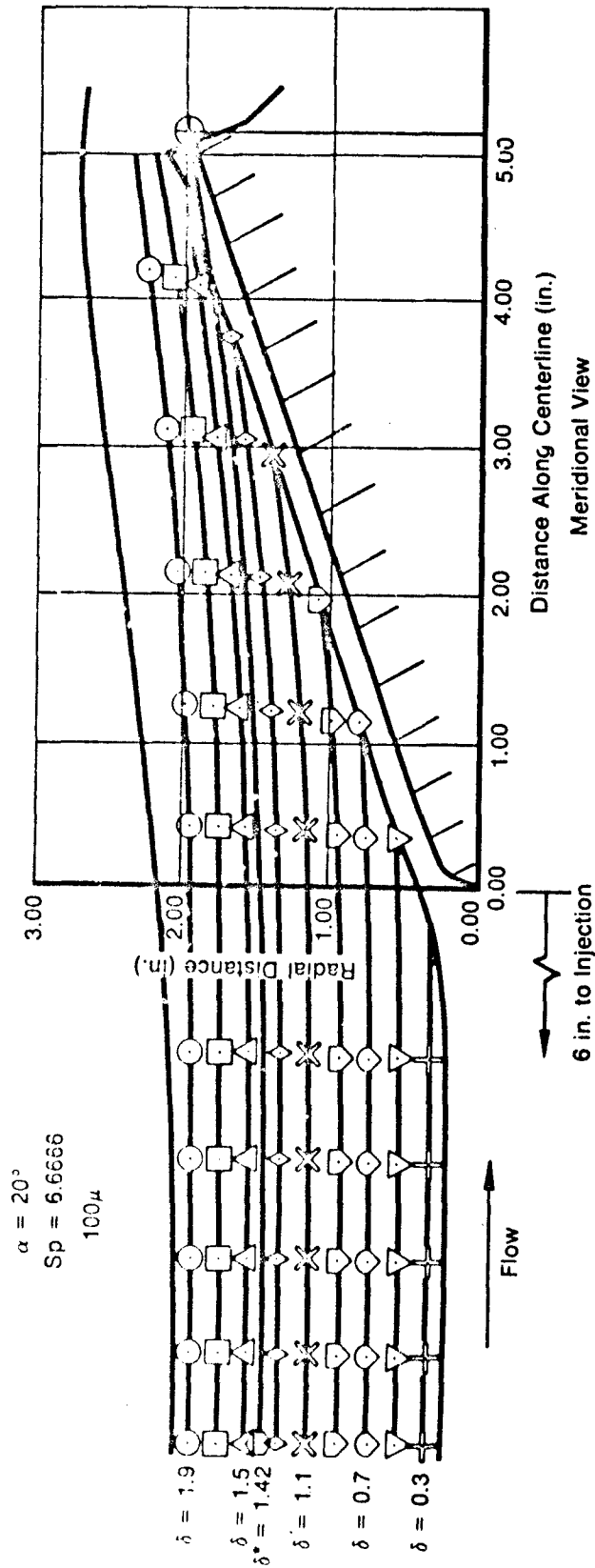
Evaluation of β_2 requires, therefore, evaluation of δ^* for any value of droplet diameter. Additionally, the streamline divergence rate will be a function of the flameholder geometry (apex angle, blockage). The droplet acceleration rate in the x and y directions will be a function of the flow conditions (pressure, temperature, velocity) and initial fuel droplet velocity (output from β_1 subroutine).

An earlier analysis for collection into a cylindrical bar was performed by Langmuir (Reference 4). The collection efficiency was found to be dominated by air velocity and droplet diameter. The influence of diameter is exceptionally strong. Typical results are shown for vee gutter flameholders in Table 1. Going from 25 to 75 micron droplets doubles the collection rate from ~30% to ~70%. A typical streamline result is shown in Figure 15.

The effect reinforces the dependence of the low air temperature stabilization process on the surface film analysis. As the air temperature is reduced, the level of droplet vaporization is also reduced and the droplet diameter at the flameholder is increased. This not only increases the liquid flowrate available for collection but also increases the percentage collected. This doubling effect produces a much greater dependence of the wake fuel-air ratio on the surface film.

TABLE 1
COLLECTION EFFICIENCY VS
DROPLET DIAMETER

Gutter Apex Angle (deg)	Blockage Ratio (%)	Droplet Diameter (microns)	Collection Efficiency (%)
60	15	25	0.35
60	15	50	0.59
60	15	75	0.70
60	15	100	0.76
60	30	25	—
60	30	50	0.65
60	30	75	0.73
60	30	100	0.78
40	30	25	0.30
40	30	50	0.55
40	30	75	0.63
40	30	100	0.71



FD 134081

Figure 15. Typical B, Evaluation Results

(3) Fuel Film Surface Vaporization Evaluation

The liquid droplets which contact the surface of the flameholder are assumed to generate a uniform liquid film. This liquid film experiences heat transfer from the hot wake through the flameholder. This heat is partitioned into forced mass transfer (latent heat) and temperature rise (sensible heat). See Figures 16 and 17.

The liquid film vaporization rate is used to calculate the surface vaporization efficiency, β_s . This efficiency is the percentage of the collected liquid fuel which is vaporized from the flameholder surface and recirculated into the wake reaction.

The controlling parameter becomes a forced diffusion process. The controlling equation may thus be written as:

$$\dot{w}_{rc} = \dot{w}_v + \dot{w}_s + \frac{dm}{dt} \quad (39)$$

$$\dot{w}_v = \text{fcn}(\text{Nu}_m, p_v, A_s) \quad (40)$$

$$p_v = \text{fcn}(T_f) \quad (41)$$

$$T_f \cong T_{rc} + \frac{1}{2} \Delta T_f \quad (42)$$

$$\dot{q} = \dot{w}_v \lambda + \dot{w}_{rc} C_p \Delta T_f \quad (43)$$

$$\dot{q} = \text{fcn}(\text{Nu}_H, T_a, T_v). \quad (44)$$

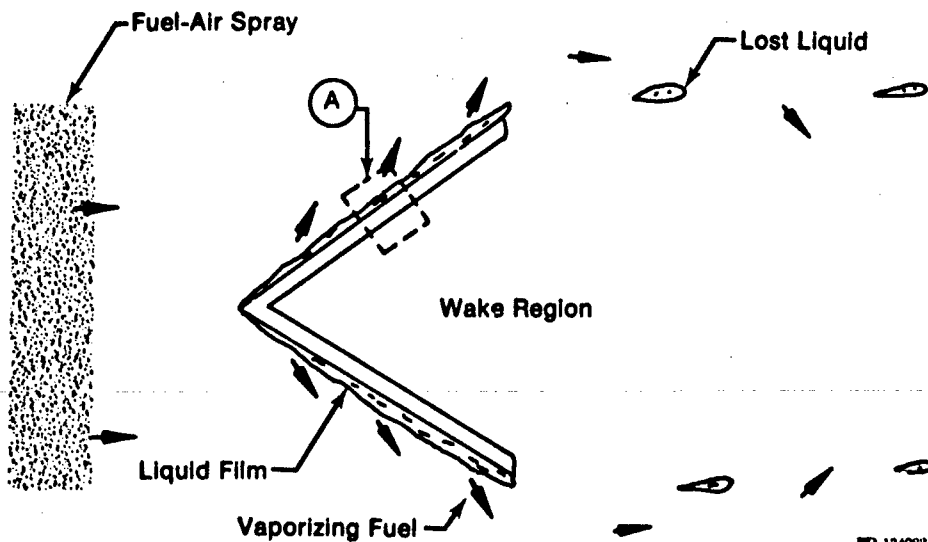
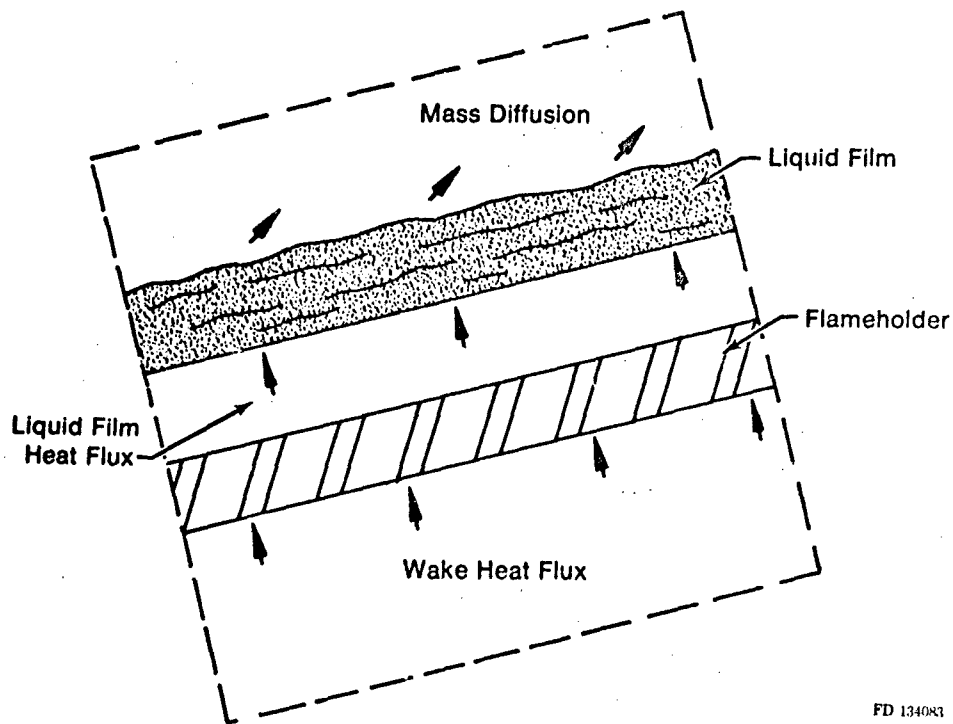


Figure 16. Flameholder Surface Vaporization Schematic



FD 134083

Figure 17. Expanded View of Region A Heat Transfer Mechanisms

In these equations, the collected mass flowrate, $\dot{w}_{r,c}$, is the result of the B2 subroutine. We assume that the liquid film total mass does not change with time unless the entry flowrate alters, i.e.

$$\frac{dm}{dt} = 0.$$

The various film properties are functions of the fuel type and temperature. Suitable curves are used in the program for JP-4 and JP-5 fuel.

This situation is a forced mass transfer from the surface represented by a Nusselt number function driven by the film vapor pressure and a Nusselt number form of heat flux from the wake into the film.

The formulation of the rate of liquid fuel vaporization from the surface of the flameholder has been programmed as a finite element solution to the nonuniform forced diffusion process. The diffusion process is evaluated from the surface Nusselt number for mass transfer:

$$\dot{w}_v = C_1 A_s p_s \ln \left(\frac{p_s}{p_s - p_v} \right) \quad (45)$$

$$C_1 = \frac{Nu_m D_v MW}{R \Delta x T_s} \quad (46)$$

The Nusselt number is functionally identical for heat flux and mass flux when the Prandtl number in the thermal Nusselt number is replaced with the Schmidt number for mass transfer.

The heat flux from the recirculation zone is evaluated directly from a Nusselt number formulation for recirculation wakes behind bluff bodies as:

$$Nu_w = \frac{h_r N}{k_m} = 0.99 Re^{0.5} Pr^{0.33} \quad (47)$$

For a known value of heat flux through the flameholder, the rate of surface vaporization is evaluated by breaking the liquid film into 10 subgroups. In each subgroup, the vaporization process is assumed to be controlled by the vapor pressure corresponding to the mean liquid film temperature within that subgroup (See Figure 18).

The heat flux into each subgroup is responsible for two physical effects. The heat is used to provide the latent heat of vaporization and provide sensible heat to elevate the bulk liquid temperature.

For the initial subgroup, the entrance mass flowrate is the prorated portion of the fuel collection rate. Thereafter, the entry flowrate consists of the prorated collection rate plus the unvaporized liquid fuel from the preceding subgroup.

The entrance fuel temperature for the initial subgroup is the droplet bulk temperature as evaluated in the spray vaporization subroutine. For succeeding subgroups, the initial fuel temperature is evaluated from the mixture of captured fuel at droplet temperature and liquid fuel film at elevated temperature.

The solution in each subgroup for the liquid temperature rise and vaporization rate requires an iteration process. The initial guess on vaporization is evaluated at the fuel entry temperature. The latent heat required to accommodate this vaporization is subtracted from the heat flux and the excess used to increase the bulk film temperature. A new vaporization rate is calculated at a mean fuel temperature between entry and exit. The solutions for vaporization and temperature rise are repeated until convergence occurs.

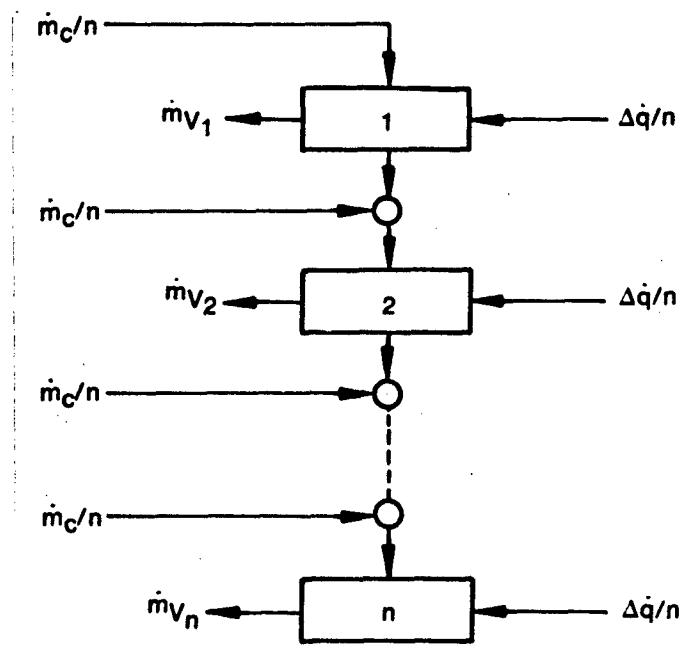
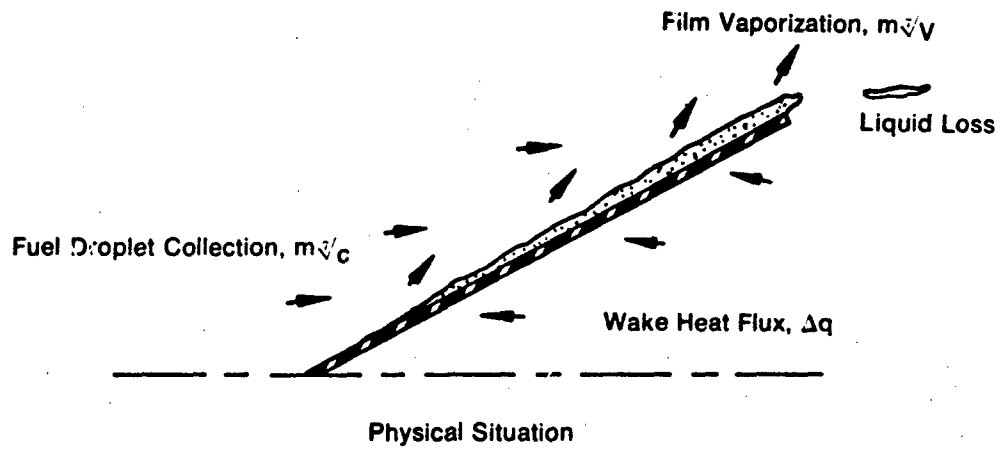
This process of finite element solution, if the subdivisions are fine enough, allows a relatively simple evaluation of the vaporization rate for nonadiabatic walls and a nonuniform liquid film temperature. It may be made as exact as desired by decreasing the subgroup size. This may be very desirable for solutions to multicomponent fuels (such as JP-4) where the latent heat of vaporization and surface vapor pressure are strong functions of the bulk liquid temperature.

The partitioning of the heat flux, Equation 43, and the forced diffusion process, Equations 45 and 46, may be combined to yield:

$$\dot{q} = \dot{w}_{rc} C_p (T_r - T_f) + \lambda \left(\frac{Nu_m D_v MW}{R \Delta_r T_s} \right) A_s p_s \ln \left(\frac{p_s}{p_s - p_v} \right) \quad (48)$$

where C_p , λ and p_v are all functions of T_f .

The functional unknown in this group is T_f , the average film temperature. Once T_f is known, the mass efflux is known from Equation 45. The form of the efflux response to T_f is such that a critical film temperature exists, when $p_v = p_s$, where infinite flux exists. For JP-4 and 10 psia static pressure this is 180°F. A very careful analysis is required to iterate to a successful answer. A typical result is shown in Figure 19 for JP-4 fuel and flow conditions of 250 fps, 275°F, 10 psia.



$$\dot{m}_v = \sum_{i=1}^n \dot{m}_{v_i} \quad \beta_3 = \dot{m}_v / \dot{m}_c$$

FD 134084

Figure 18. Finite Difference Solution Procedure

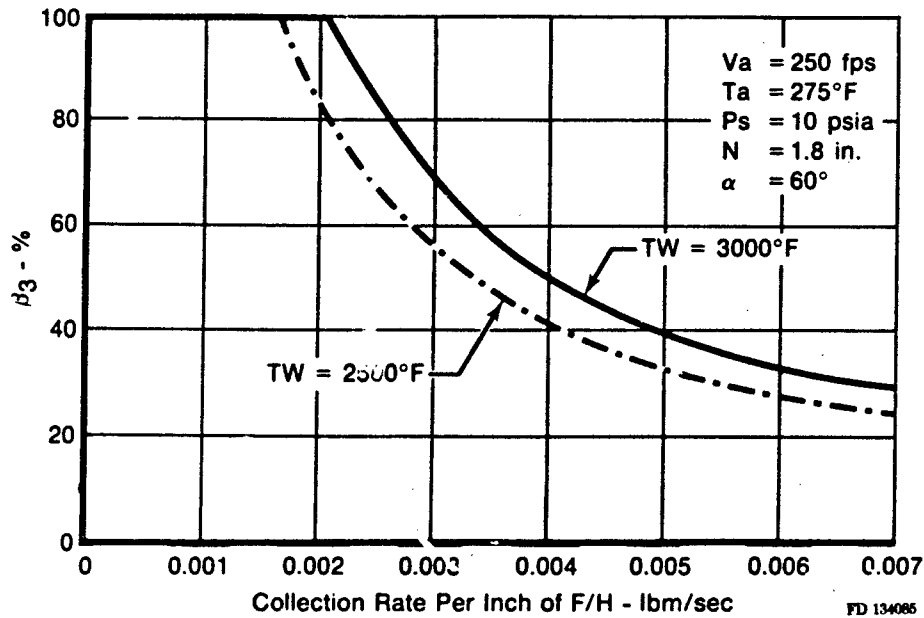


Figure 19. Surface Vaporization vs Fuel Collection Rate for Two Levels of Wake Temperature

(4) Flameholder Wake Recirculation Rate

In a manner analogous to the definition of the collection efficiency, we will define a recirculation efficiency, K_1 . This efficiency relates the mass flowrate into the wake of the flameholder to the mass which flows through the projected blocked area of the flameholder:

$$\dot{w}_{a,r} = \rho_a V_a N K_1 \quad (49)$$

This recirculation flowrate is the mass which is transferred by turbulent diffusion across the free shear layers aft of the flameholder. These layers form the boundaries of the backflow wake aft of the bluff body. If we look at this wake volume as a homogeneous region with mass transfer across the boundaries, the recirculation rate may also be written as:

$$\dot{w}_{a,r} = \frac{\rho_a V_o}{\tau} \quad (50)$$

If the wake volume and residence time may be evaluated as a function of the geometric and flow variables, then the recirculation rate may be evaluated from the known variables without resorting to the much more difficult solution to the effective transport across the shear layers. This approach has been taken by the majority of investigators for wake processes (References 5 through 11).

The approach relates the wake volume and residence time to the controlling aerodynamic and geometric variables, such as:

- Blockage ratio
- Vee gutter apex angle
- Flow Mach number
- Pressure, velocity, temperature.

Once these are known, the recirculation rate calculation proceeds as follows:

$$\dot{w}_{a,r} = \rho_a V_o / \tau \quad (51)$$

$$V_o = C_v(L/D)(B/D)N^2 \quad (52)$$

If we nondimensionalize the residence time with respect to velocity and characteristic dimension, flameholder width, we have:

$$\tau' = \frac{\tau V_a}{N} \quad (53)$$

$$\dot{w}_{a,r} = \frac{V_a}{N} \frac{\rho_a V_o}{\tau'} \quad (54)$$

Now, from Equations 52 and 54, we have:

$$\dot{w}_{a,r} = \frac{\rho_a V_a C_v (L/D)(B/D)N}{\tau'} \quad (55)$$

From this and Equation 49, we may write:

$$K_1 = C_v(L/D)(B/D)(\tau')^{-1} \quad (56)$$

The value of the shape coefficient, C_v , was determined by assuming that the wake was similar to a two-dimensional ellipse which is truncated by the flameholder at its forward edge. The value used is 0.80.

The data presented in References 5 through 11 were reduced to a series of curves which describe the effect of various parameters on recirculation rate. The functional groupings and the corresponding figures are:

L/D	vs Blockage	(Figure 20)
L/D	vs Apex Angle	(Figure 21)
L/D	vs Flow Mach Number	(Figure 22)
B/D	vs Blockage	(Figure 23)
B/D	vs Apex Angle	(Figure 24)
τ'	vs Blockage	(Figure 25)
τ'	vs Air Temperature	(Figure 26)

The only one of these which does not follow directly from the cited references is the temperature dependence of the recirculation zone residence time. The data available were taken over an extremely limited inlet temperature range so that no dependence could be determined.

The shape of this curve was drawn by assuming that the forcing function for the recirculation mass flowrate is the turbulence generated at the recirculation zone boundary. Since the viscosity of the free-stream inhibits this formation, the curve is drawn to follow the increase in viscosity with temperature exhibited by air.

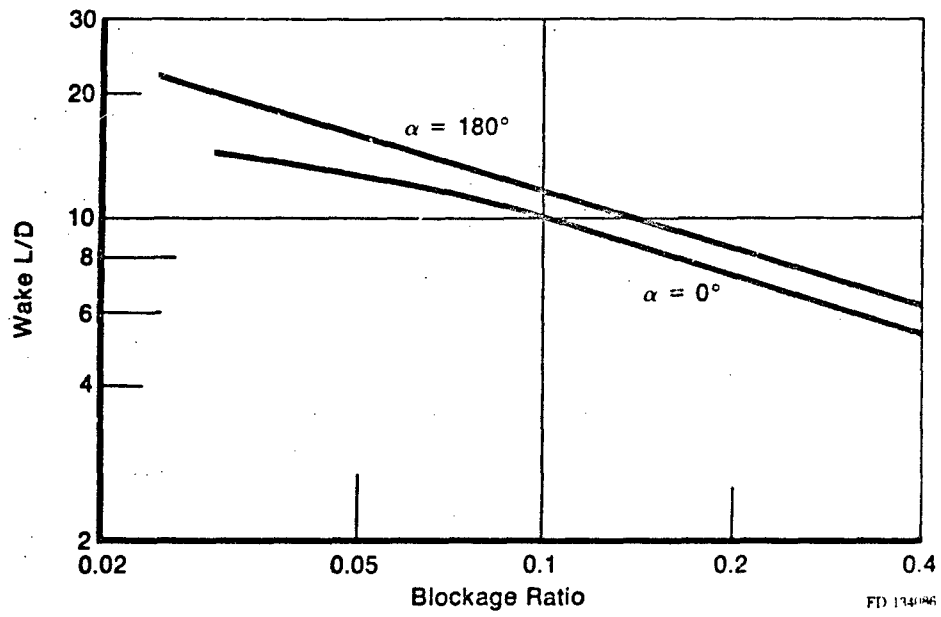


Figure 20. Wake L/D vs Blockage Ratio

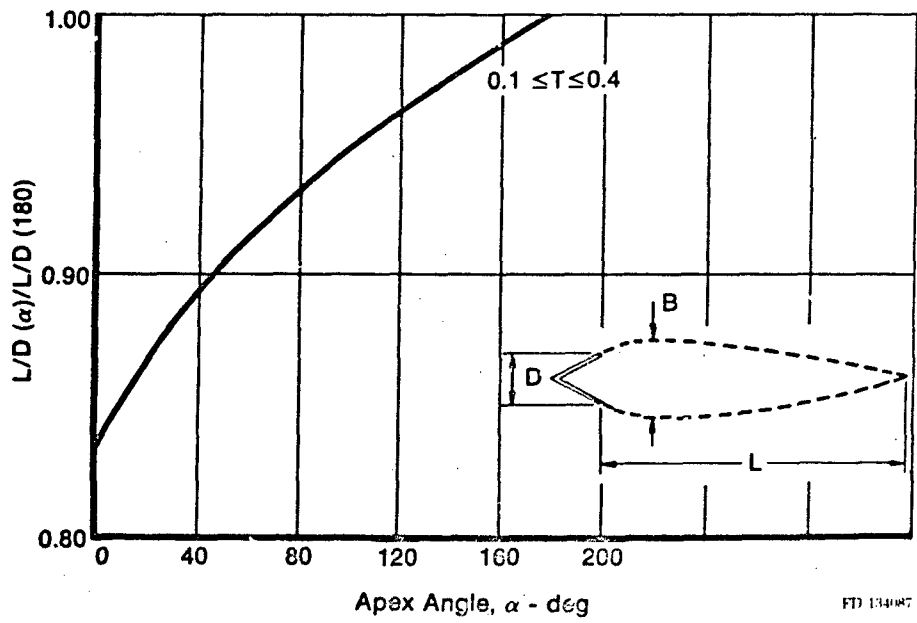


Figure 21. Wake L/D vs Apex Angle

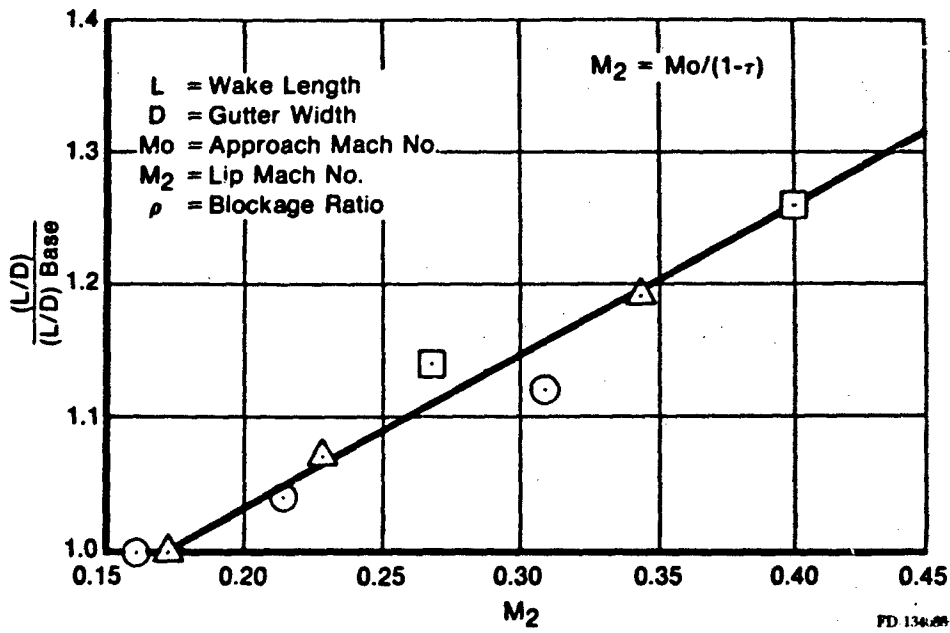


Figure 22. Wake L/D vs Lip Mach Number

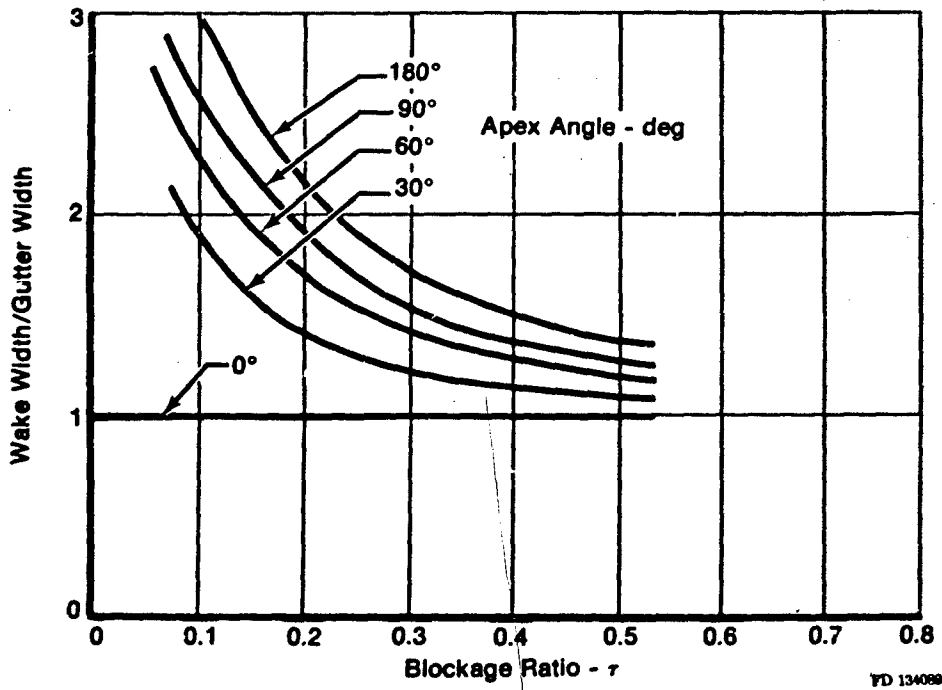


Figure 23. Wake B/D vs Blockage Ratio

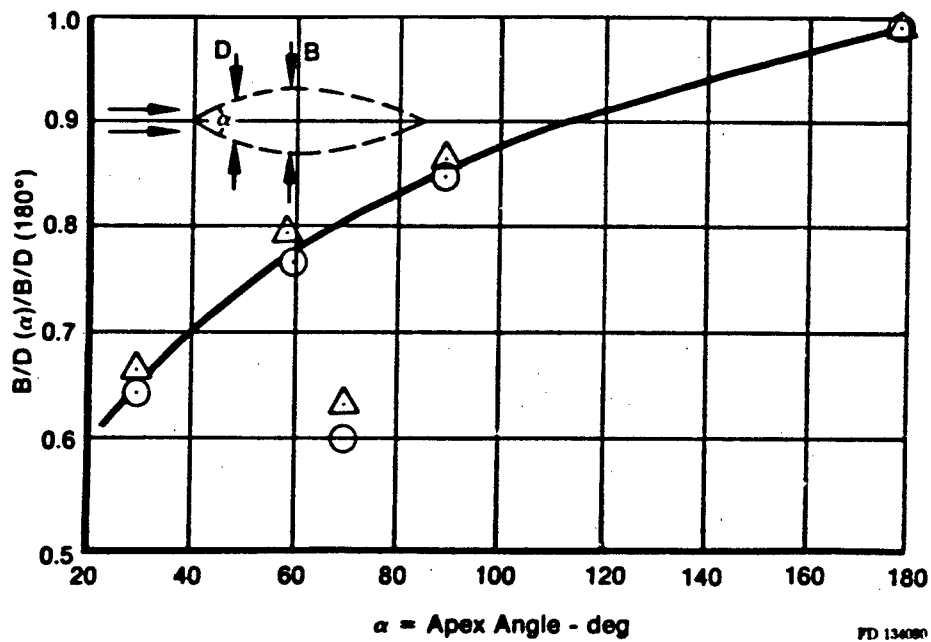


Figure 24. Effect of Apex Angle on Wake B/D

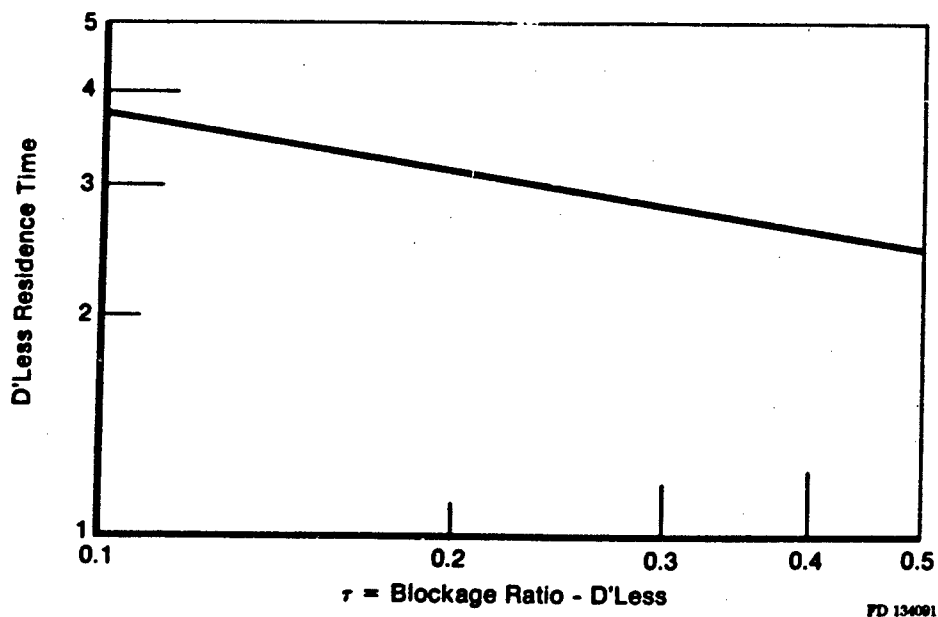


Figure 25. Wake Residence Time vs Blockage Ratio

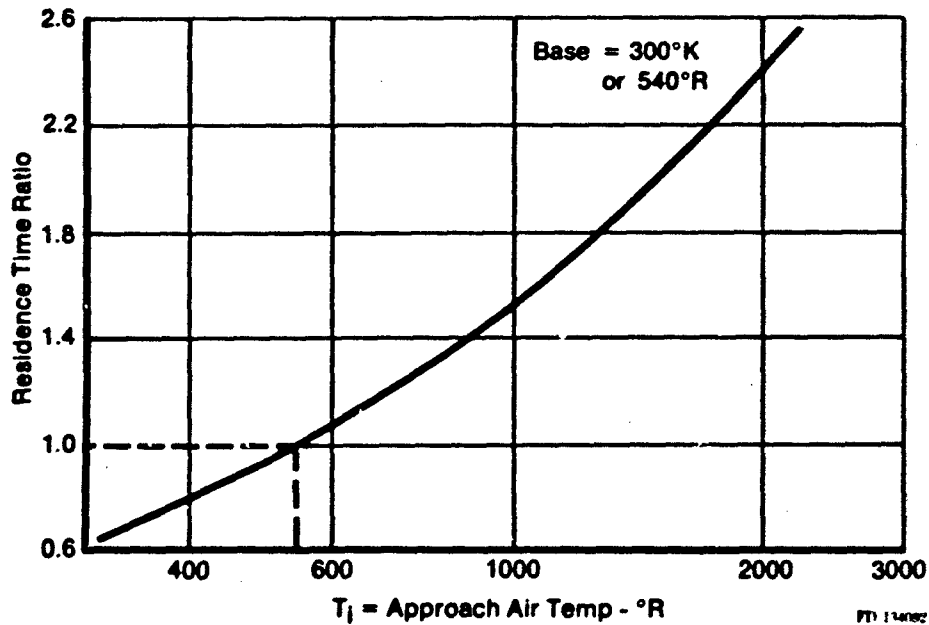


Figure 26. Influence of T_1 on Residence Time

For a typical analysis:

$$\begin{aligned}
 V_a &= 250 \text{ fps} \\
 T_a &= 275^\circ\text{F} \\
 \Gamma &= 0.25 \\
 \alpha &= 60^\circ \\
 \text{Mach No.} &= 0.189
 \end{aligned}$$

we obtain:

$$\begin{aligned}
 L/D &= 7.87 \\
 B/D &= 1.55 \\
 \tau &= 36.9
 \end{aligned}$$

or:

$$K_1 = 0.265.$$

Expressed in direct values, at 10 psia static pressure and with a 2-in. flameholder:

$$\begin{aligned}
 \text{Wake volume} &= 39 \text{ in.}^3 \text{ per inch length} \\
 \text{Recirculation rate} &= 0.034 \text{ lbm/sec per inch length.}
 \end{aligned}$$

The total duct flowrate for this case is 0.51 lbm/sec per inch length. For this case, 6.7% of the free-stream flowrate is recirculated to provide ignition for the remaining 93.3%. The average residence time is 24.6 milliseconds.

Before going on to the reaction kinetics in the wake, a couple of observations are in order here with respect to the applicability of this recirculation approach.

The majority of true gaseous phase stability limit data may be correlated with a dimensional grouping of the form:

$$\frac{V_{max}}{p_o N T_o^{1.5}} = fcn(f/a). \quad (57)$$

An example from Reference 12 is shown in Figure 27.

For gaseous stability analysis, this curve follows a fuel-air function of form similar to the kinetic rate function vs fuel-air ratio. Hence, the limit represents a balance between the recirculation rate and the kinetic mass conversion rate. This then implies that the grouping $V_{max}/p_o N T_o^{1.5}$ represents a grouping for the recirculation rate.

From kinetics, the reaction curve follows a shape related to AN_p^2 for second-order reactions.

For fixed geometry and flow conditions:

$$A = w_a = \frac{\rho_o V_o C_o (L/D)(B/D)N}{\tau} \quad (58)$$

$$V_o = C_o (L/D)(B/D)N^2 \quad (59)$$

$$\rho_o = \frac{p_o}{RT_o} \quad (60)$$

Combining these we have:

$$\frac{A}{V_o p^2} = \frac{p_o}{RT_o} V_a \frac{1}{\tau N} \frac{1}{p_o^2} \quad (61)$$

$$\frac{A}{V_o p^2} = \frac{1}{\tau R} \times \frac{V_a}{p_o N} \quad (62)$$

If we introduce the temperature dependence of τ as $\tau \propto T_o^{1.5}$, we obtain:

$$\frac{A}{V_o p^2} = \text{constant} \times \frac{V_a}{p_o N T_o^{1.5}} \quad (63)$$

This is extremely close to the data correlation and substantiates the functional form of the recirculation analysis.

(5) Recirculation Zone Reaction Kinetics

The recirculation zone wake of the bluff body stabilizer is analyzed by assuming that it behaves similarly to a well-stirred reactor with the volume and mass entry rate known from the results of the RECIRC analyses.

Analyses of well-stirred reactors have been presented by numerous investigators and the analogy to actual combustors and bluff body wakes studied (References 13 through 21). The basic thesis of these studies is that the performance of the reactor may be evaluated from a balance between the mass entry rate and the kinetic conversion rate. For the purpose of these studies, we assume that the entire wake volume is available for reaction and that the mixing is very rapid.

Sym	Flameholder	$\frac{d_e}{d}$	Fuel	Mixture Temp ($^{\circ}$ R)	Pressure (atm)	Notes	Ref
	Disks	1.6	Propane	550	1/3 to 1	Mean Curve;	12
◆	Disks	1.6	Kerosene	1030	~ 1	Wide Data Scatter	22
▲	90° Cones	1.4	Kerosene	1030	~ 1		22
×	Hemispheres	1.1	Kerosene	1030	~ 1		22
◇	60° V-Gutter	1.73	Kerosene	900	~ 1	Approach ϵ ~ 2.5%	5
◇	60° V-Gutter	1.73	Kerosene	900	~ 1	Approach ϵ ~ 10%	5
△	90° V-Gutter	1.86	Kerosene	1390	~ 1		22
⊗	1/4 Round Channel	1.46	Kerosene	1390	~ 1		22
○	Cylinder	1.33	Kerosene	1390	~ 1	Transverse Flow	22

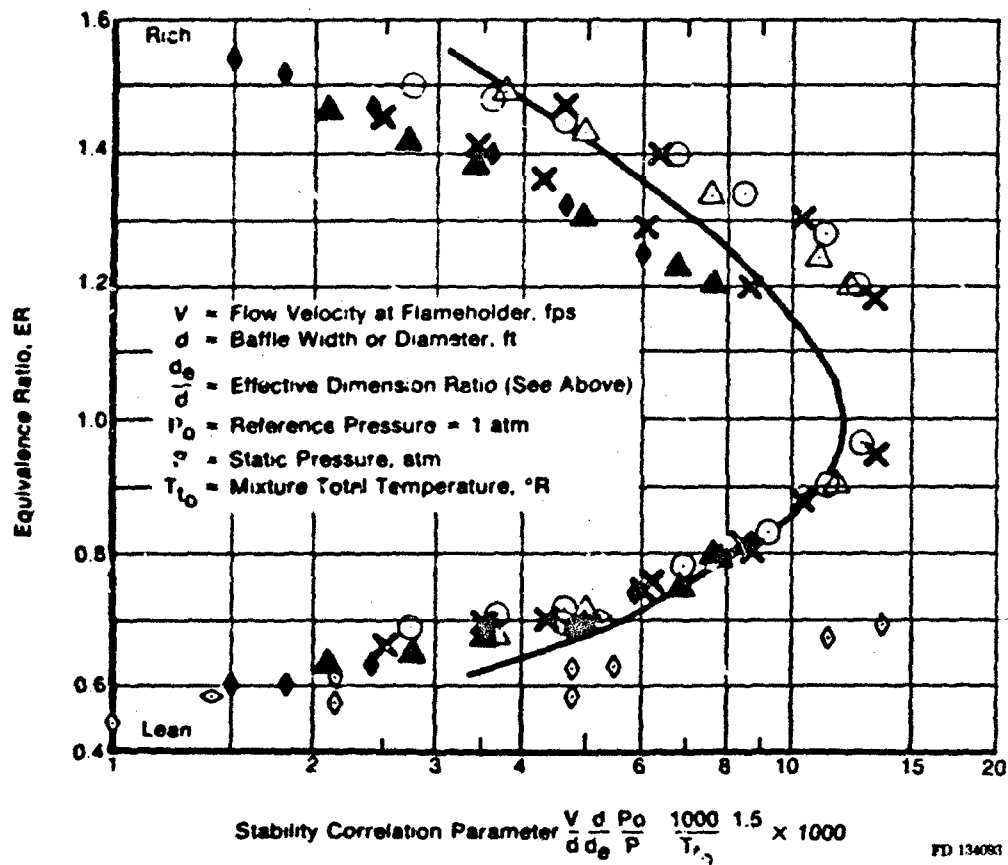


Figure 27. Baffle Stability Correction

These assumptions result in an optimistic evaluation of the kinetic limits which we will correct later.

The following analysis follows the development of Kretschmer and Odgers (Reference 21) for lean wake fuel-air ratios. The general form of the reaction of hydrocarbon fuels proceeds in essentially two major steps. The first is the pyrolysis and partial oxidation of the virgin fuel to form short-lived intermediate species. At the end of this stage, the maximum concentration of carbon monoxide is present. The second stage is the oxidation of carbon monoxide to form carbon dioxide. This latter step is much slower and serves as the rate-controlling process. The slower CO oxidation results in the very close similarity of reaction rates for a wide range of saturated hydrocarbons.

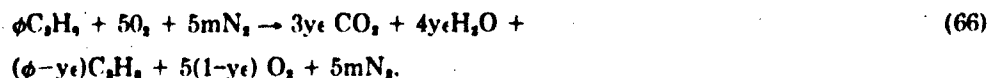
The general form of the conversion equation may be written as:

$$-\frac{dm_o}{dt} = \frac{k}{R_1^n} x_o^a x_i^{n-a} V_o p^n \frac{e^{-C/T}}{T^{n-0.5}} \quad (64)$$

for gaseous flow into a well-stirred reactor, this becomes:

$$\frac{A}{V_o p^n} = \frac{k(m+1)}{R_1^n y \epsilon} x_o^a x_i^{n-a} \frac{e^{-C/T}}{T^{n-0.5}} \quad (65)$$

For the assumed single-step reaction process postulated here, the reaction mass balance is (for propane fuel):



Also, a linear efficiency vs temperature function is assumed:

$$T = T_1 + \epsilon \Delta T. \quad (67)$$

From these equations, the stirred reactor loading capability may be written as:

$$\frac{A}{V_o p^n} = \frac{k(m+1) [5(1-y\epsilon)]^a [\phi - y\epsilon]^{n-a} e^{C/(T_1 + \epsilon \Delta T)}}{R_1^n y \epsilon [5(m+1) + \phi + y\epsilon]^n [T_1 + \epsilon \Delta T]^{n-0.5}} \quad (68)$$

Based on comparison of predicted results with available stirred reactor data, Reference 21 recommends the following values for this reaction:

- n: for $\phi < 1$, $n = 2\phi$
for $\phi > 1$, $n = 2/\phi$
- a: $a = n/2$
- C: $C = E/R$, See Figure 28.

This yields:

$$\frac{A}{V_o p^n} = \frac{1.29 \times 10^{10} (m+1) [5(1-y\epsilon)]^a (\phi - y\epsilon)^a e^{-C/(T_1 + \epsilon \Delta T)}}{(0.08206)^{2a} y \epsilon [5(m+1) + \phi + y\epsilon]^{2a} [T_1 + \epsilon \Delta T]} \quad (69)$$

for lean mixtures.

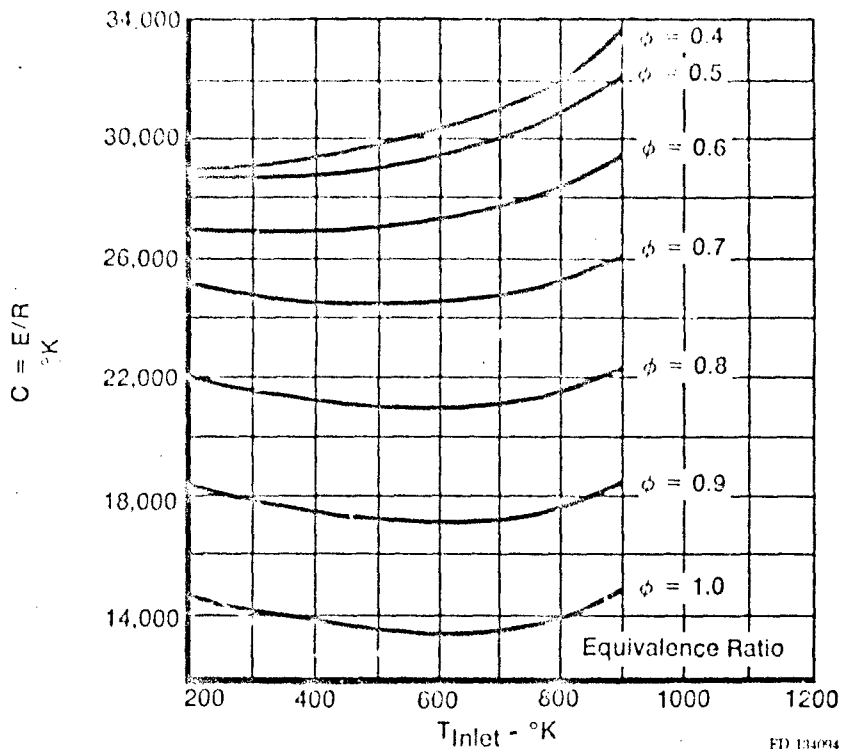


Figure 28. Variation in Activation Energy with Inlet Temperature and Equivalence Ratio

While the results presented above are from one reference, similar results have been obtained by others for the same problem.

Longwell and Weiss (Reference 13) present the following results for lean and rich operation:

Lean:

$$\frac{A}{V_o p^{1.8}} = 430 k_1 \frac{e^{-E/Tr}}{T_r^{1.3}} \frac{[2\phi(1-\epsilon)]^{0.8} (1-\phi\epsilon)}{\phi\epsilon[4.76 + \phi(1.36 - \epsilon)]^{1.8}} \quad (70)$$

Rich:

$$\frac{A}{V_o p^{1.8}} = 430 k_2 \frac{e^{-E/Tr}}{T_r^{1.3}} \frac{(0.080 \phi)^{0.8}}{\epsilon} \left\{ \frac{1-\epsilon}{4.76 - \epsilon + 0.08\phi(1+16\epsilon)} \right\}^{1.8} \quad (71)$$

where

$$\begin{aligned} k_1 &= 1.67 \times 10^{10} \text{ litre}^{0.8}/\text{°K}^{0.8} \text{ gm-mole}^{0.8} \text{ sec} \\ k_2 &= 1.11 \times 10^{11} \text{ litre}^{0.8}/\text{°K}^{0.8} \text{ gm-mole}^{0.8} \text{ sec} \\ E &= 42,000 \text{ gm-cal/g n-mole.} \end{aligned}$$

The solution procedure utilized in the WAKE subroutine utilizes the results of RECIRC as a definition of the entry rate, A, and the zone Volume, V_o , the equivalence ratio is from Equation 20 and the results of B1, B2, B3 and RECIRC. The ideal temperature rise, ΔT , is read from curves of ΔT versus wake fuel-air ratio, inlet temperature, and static pressure for the specified fuel type.

An iterative solution procedure solves for the efficiency, ϵ , where the known value of $A/V_o p^2$ agrees with the predicted value as a function of ϵ . The complexity of Equation 70 or 71 requires this sort of reverse solution.

The behavior of the solution is shown in Figure 29 for inlet temperatures of 300 and 400°K and equivalence ratios of 0.8 and 1.0. The wake efficiency decreases at an increasing rate until the decay slope becomes infinite. At this point, the wake reaction process is said to have blownout. If we plot the locus of the blowout points as $A/V_o p^2$ versus equivalence ratio, we obtain a classical blowout curve. This curve, except for magnitude, represents the classical results for gaseous fuel data from wake-stabilized flames. This is shown in Figure 30.

This analysis tends to overestimate the limits of blowout velocity when compared to available data. To reconcile this, comparisons were made between predicted limits and actual limits for available data (References 22 through 28). The correlating ratio between predicted and actual was 3.55, i.e.:

$$\frac{\left(\frac{A}{V_o p^2}\right)_{\text{max. pred}}}{\left(\frac{A}{V_o p^2}\right)_{\text{max. data}}} = 3.55. \quad (72)$$

In the analysis, the calculated recirculation rate per unit volume is multiplied by this factor before solving for ϵ . In this manner, the predicted limits and available data are numerically equal, and the efficiency response towards blowout follows the theoretical curve.

The reason for this error is most likely either imperfect mixing or lack of full utilization of the wake volume for reaction. The approach used above will account for either one of these.

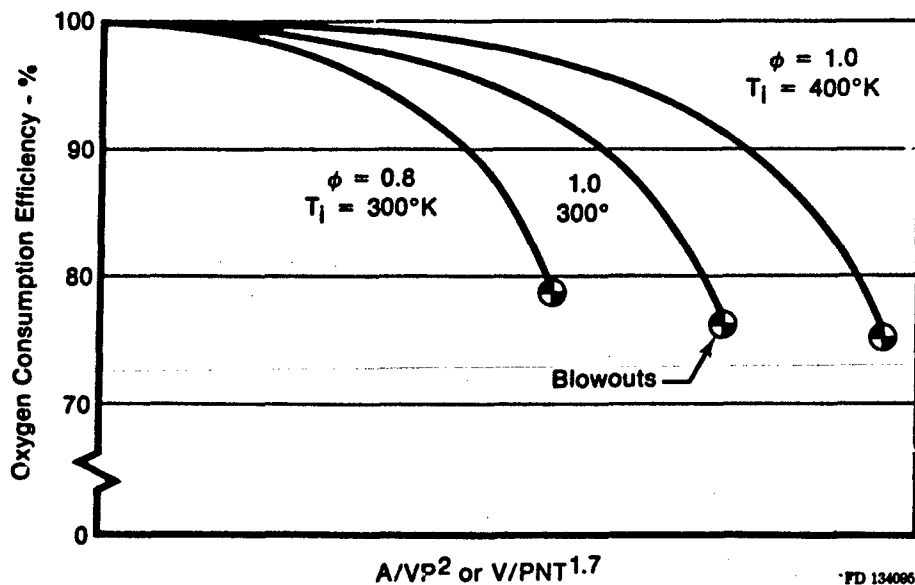
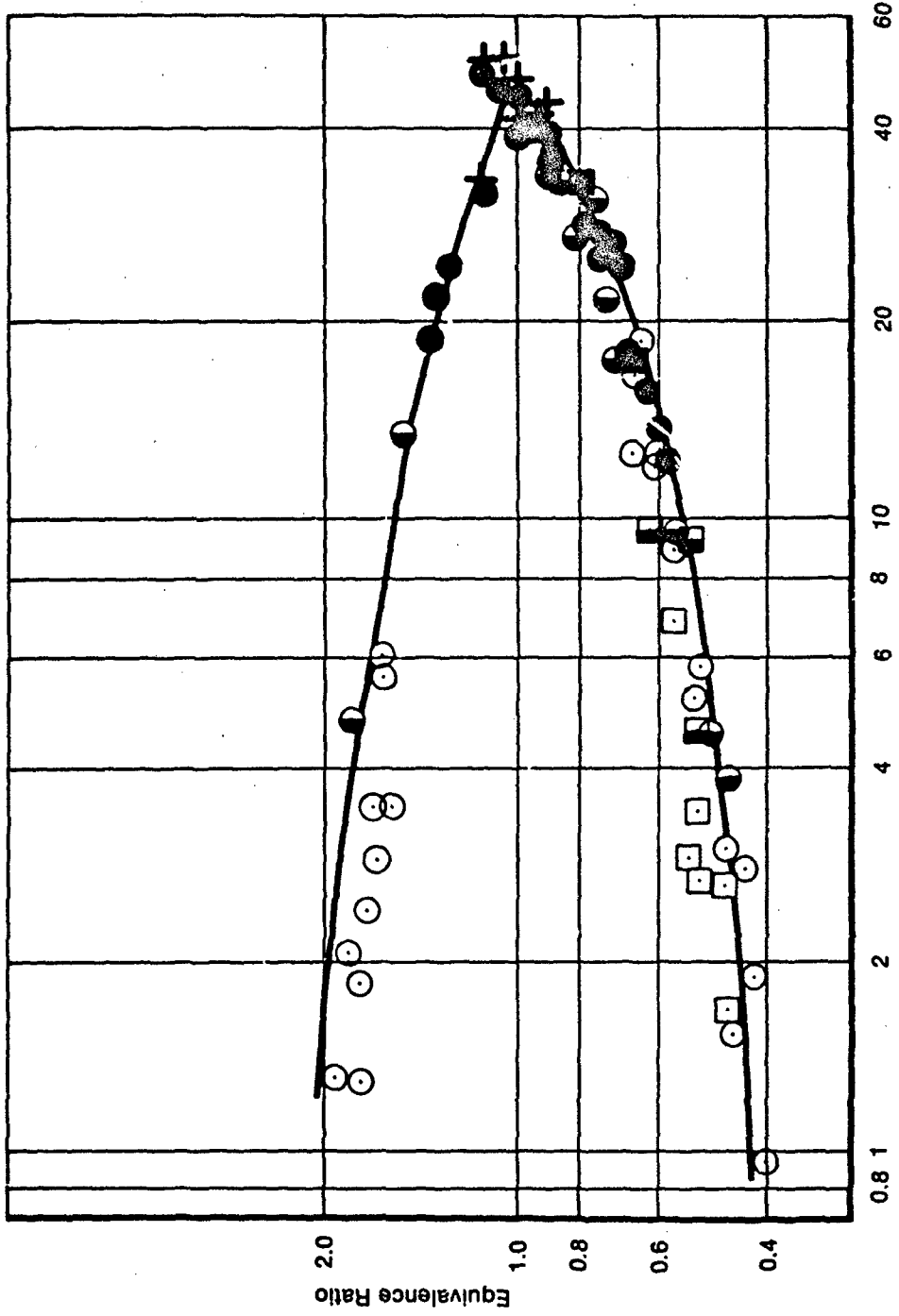


Figure 29. Stirred Reactor Kinetic Efficiency vs Loading Rate



$A/V_{op}^{1.8} = \frac{\text{gm-mole}}{\text{litre-sec-atm}^{1.8}}$

FD 134088

Figure 30. Focus of Stirred Reactor Blowout Limits

(6) Turbulent Flame Spreading Rate

The turbulent flame propagation into the unreacted free-stream is initiated in the shear layers of the wake. The model used (subroutine ST) related the local turbulent flame speed to the local aerothermodynamic conditions and performs a finite difference integration of the flame front penetration starting in the wake and proceeding to the exhaust nozzle.

For the purposes of current analysis, the following assumptions were made:

1. Uniform airflow profiles
2. Uniform fuel-air ratio
3. Incompressible acceleration of free air velocity by the flameholder blockage with no induced profile
4. Known wake size and reaction efficiency
5. Two-dimensional ducted flame.

The schematic of the situation which is analyzed is shown in Figure 31.

The approach flow, at known levels of pressure, temperature, velocity and fuel-air ratio, is accelerated by the blockage of the flameholder to velocity U , where:

$$U = \frac{V_a}{(1-\Gamma)} \quad (73)$$

where:

- U ~ Velocity at flameholder tip
- V_a ~ Approach velocity
- Γ ~ Blockage ratio.

At this point, Station 1 of Figure 31, an induced turbulence level is calculated from:

$$\epsilon_o = \left[\left\{ C_d \Gamma + \left(\frac{\Gamma}{1-\Gamma} \right)^2 \right\} \frac{1}{6} \right]^{1/2} \quad (74)$$

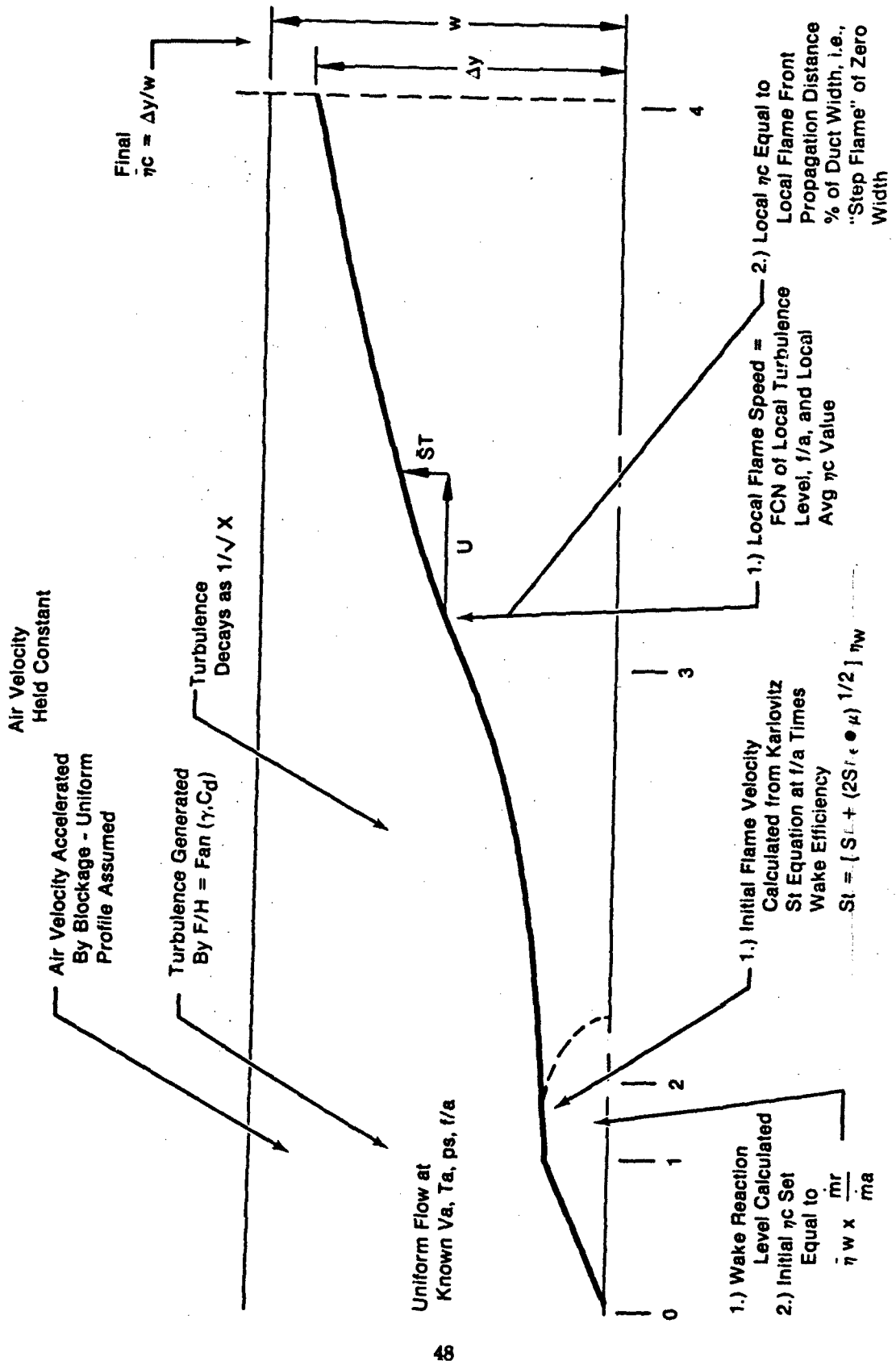
This equation (Reference 12) relates the turbulence intensity, ϵ_o , to the blockage ratio and the flameholder zero blockage drag coefficient, C_d .

At this location, the turbulent flame velocity calculations are initiated. The equation used for the local flame speed is the Karlovitz equation (Reference 22):

$$St = S_l + (2u'S_l)^{1/2} \quad (75)$$

where:

- St ~ Turbulent flame speed, ft/sec
- S_l ~ Laminar flame speed, ft/sec
- u' ~ RMS turbulence velocity, ft/sec.



FD 134987

Figure 31. Schematic of Flame Spreading Analysis

The value of u' is:

$$u' = \epsilon_0 U.$$

An additional term is required to relate the resultant flame speed to the level of recirculation zone reaction efficiency. As the wake efficiency and temperature decrease, local areas in the flame sheet appear where ignition does not occur. Since the model assumes a continuous flame sheet, we model these local areas of no ignition by reducing the overall flame speed. A reduced flame speed results in lower overall combustion efficiency which is similar to the effect of locally zero ignition. The model uses the following equation:

$$St' = St \cdot \eta_w. \quad (77)$$

The initial value for the augmentor efficiency is the wake reaction level on a mass weighted basis. Expressed as an equation this is:

$$\eta_{c_0} = \eta_w \cdot \frac{\dot{m}_r}{\dot{m}_a} \quad (78)$$

where:

- $\eta_{c_0} \sim$ Initial efficiency
- $\eta_w \sim$ Wake efficiency
- $\dot{m}_r \sim$ Wake mass flowrate
- $\dot{m}_a \sim$ Total duct flowrate.

The type of flame utilized in this model is a zero thickness flame which separates a region of unreacted propellants from a region of completely reacted products. From this set up the average local augmentor efficiency is simply the ratio of the transverse flame penetration, Δy , to the duct width, W , (see Figure 31).

To be consistent, the transverse location of the flame front at the initial calculation station is taken to be:

$$\Delta y_0 = \eta_{c_0} \cdot W \quad (79)$$

This value is assigned to the first axial station, which is assumed to occur halfway down the length of the recirculation zone. From visual observations of wake-stabilized flames, this is the approximate location of transverse flame initiation.

From this location down stream to the exhaust nozzle, the flame front transverse location is calculated by a finite difference integration of the local flame speed. Several axial profiles are introduced as the integration proceeds. These are:

- The turbulence intensity is decayed from the value generated at the aft flameholder lip (Equation 74) at a rate inversely proportional to the square root of axial distance over an effective jet length. The final value is set at the initial turbulence level. The effective jet length is set at $10 L/D$ where the D is the open area distance between adjacent flameholders.
- The velocity of the unreacted fuel-air mixture is retained at the level generated at the flameholder lip. Measured profiles from several ducted flame test rigs support this assumption.

- A term is introduced which relates the local flame speed to the local average duct combustion efficiency, peaking at 50%. This treats the counteracting influences of reduced heat loss as efficiency increases and the reduced free oxygen concentration. Local rates which follow roughly a sine wave function have been reported from duct data.

An additional term is added to account for the reduction in flame speed of a fuel spray compared to a premixed flame. This term relates the ratio of effective flame speed to premixed laminar flame speed following the results of Reference 30. It accounts for the complicated interactions during flame spreading in an evaporating spray in a simplified manner. The effect of the liquid droplet diameter is shown in Figure 32. The droplet diameter utilized in the analysis will be the mean diameter as it exists at the flameholder trailing edge.

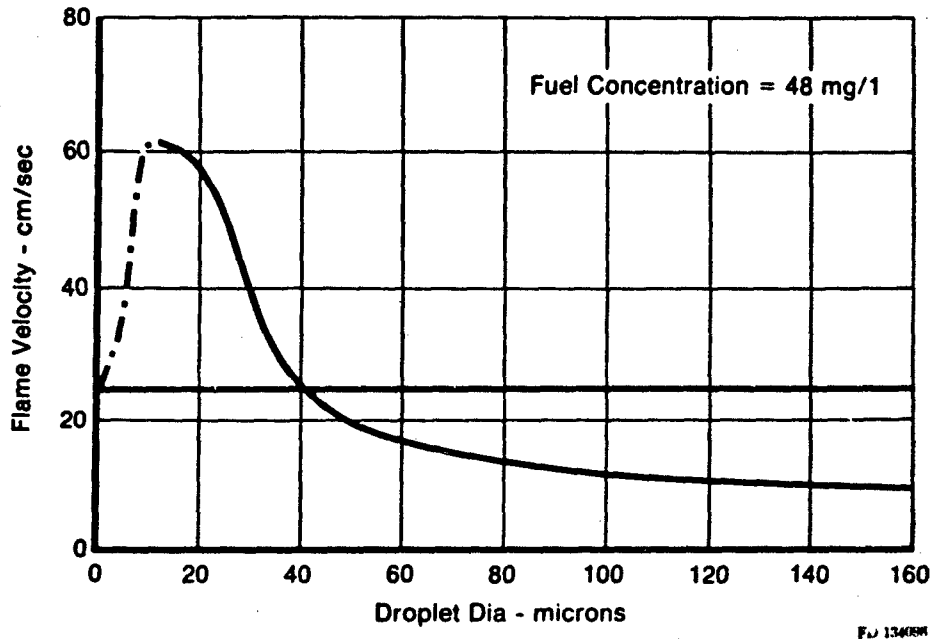


Figure 32. Flame Speed for Monodisperse Tetralin Spray

Analysis of the terms utilized for evaluation of the laminar flame speed term, S_l , has resulted in the following (Reference 23):

$$S_l = S_l(\phi) \left(\frac{T_a}{540} \right)^{1.5} \left(\frac{x_{O_2}}{0.21} \right)^0 \quad (80)$$

where:

- S_l = laminar flame speed at 1 atm and 540°
- ϕ = equivalence ratio
- T_a = air temperature, °F
- x_{O_2} = oxygen mole fraction.

The influence of pressure is indeterminate at this time and has been incorporated as $\sqrt{\rho}$ for subatmospheric data and no influence for pressures above 1 atmosphere.

Several results have been generated from this model in its current stage of evaluation. The first is shown in Figure 33 for a 60-in. duct, 2-in. flameholder, and 25% blockage at 250 ft/sec entrance velocity. The curve shows a significant rate of increase in efficiency between 0.050 and 0.060 fuel-air ratio and a steep decline past 0.090 f/a.

Figure 34 shows the local values of efficiency versus axial length for a fixed duct width and various flameholder widths. For this case, the blockage is proportional to the width. The interacting effects of increased lip velocity and increased induced turbulence are such that the net effect is reduced overall efficiency as the blockage is increased. Since in this case complete wake reaction efficiency is assumed, some of this effect will be reduced by the decreased wake efficiency as the flameholder size is reduced. This blockage effect is in agreement with results from the experimental portion of this program.

The effect of free-stream turbulence is shown in Figure 35. The anticipated effect of increased flame speed generated by the higher turbulence was verified.

The effect of reduced wake reaction level on the overall efficiency is shown in Figure 36. The relationship is such that near the peak flame speed levels, a unit reduction in wake efficiency results in less than a unit reduction in overall efficiency. This implies a reduced sensitivity of the overall efficiency to oscillations of the wake efficiency relative to what was previously assumed.

A companion program to this, Contract F33615-76-C-2024, utilized a correlation for augmentor efficiency called the "Beta Correlation." Since this correlation represents a fairly large body of test data, comparison of the results of this subroutine with the Beta Correlation is a quick way of comparing the model to test results. Two comparisons are shown in Figure 37. As shown, good agreement is achieved.

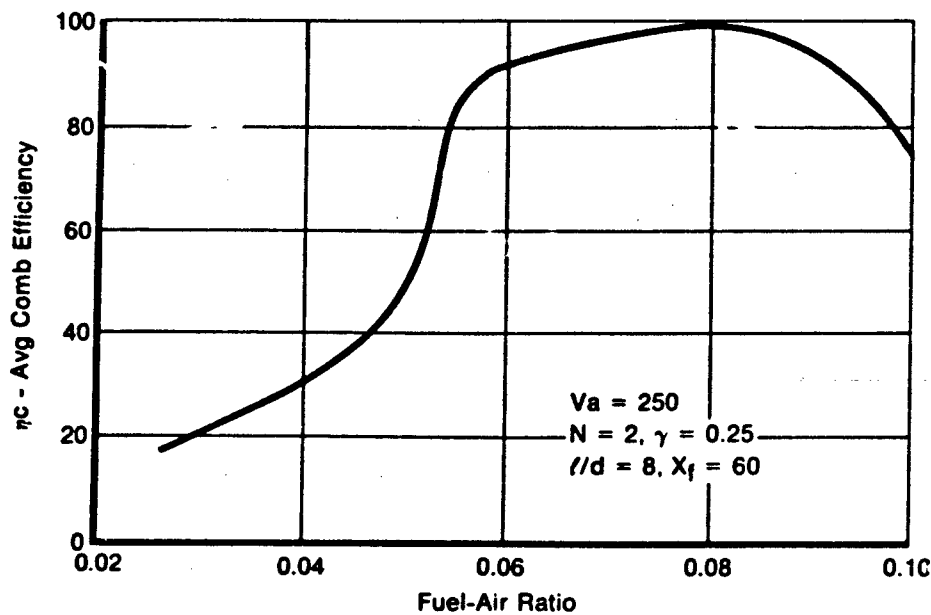


Figure 33. Average Efficiency vs Fuel Air Ratio

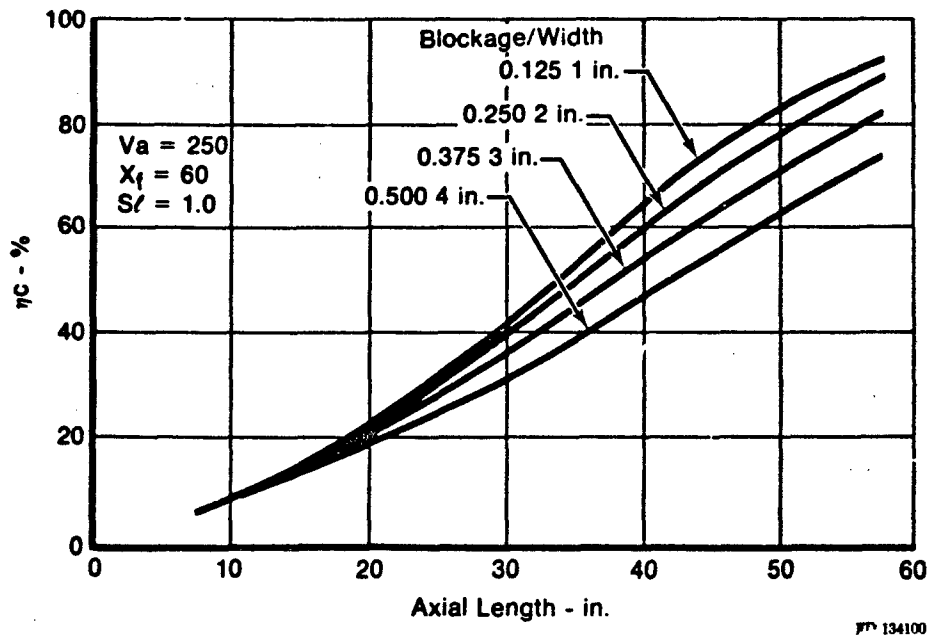


Figure 34. Axial Efficiency at Various F/H Widths for 8-in. Duct

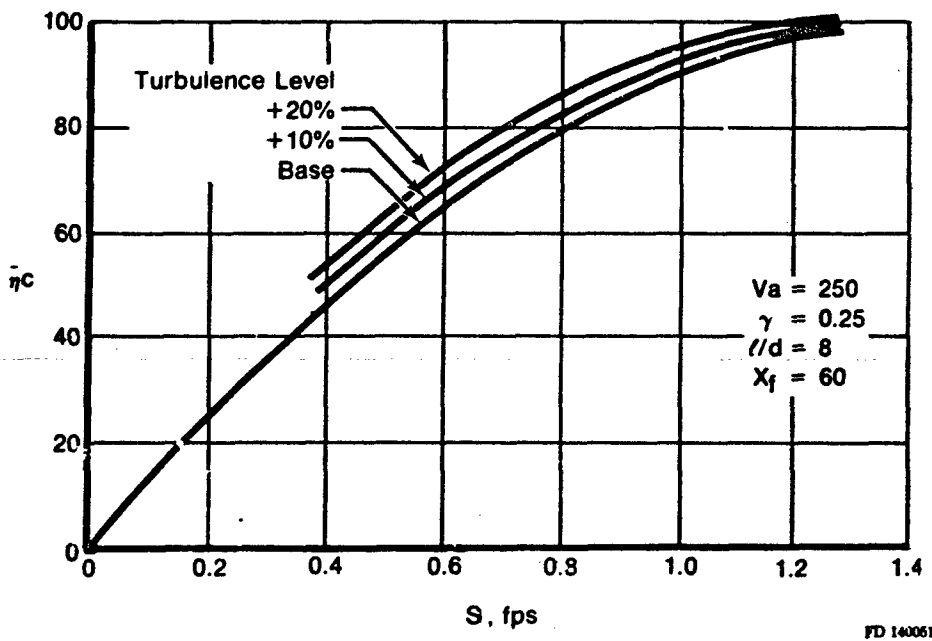


Figure 35. Effect of Turbulence

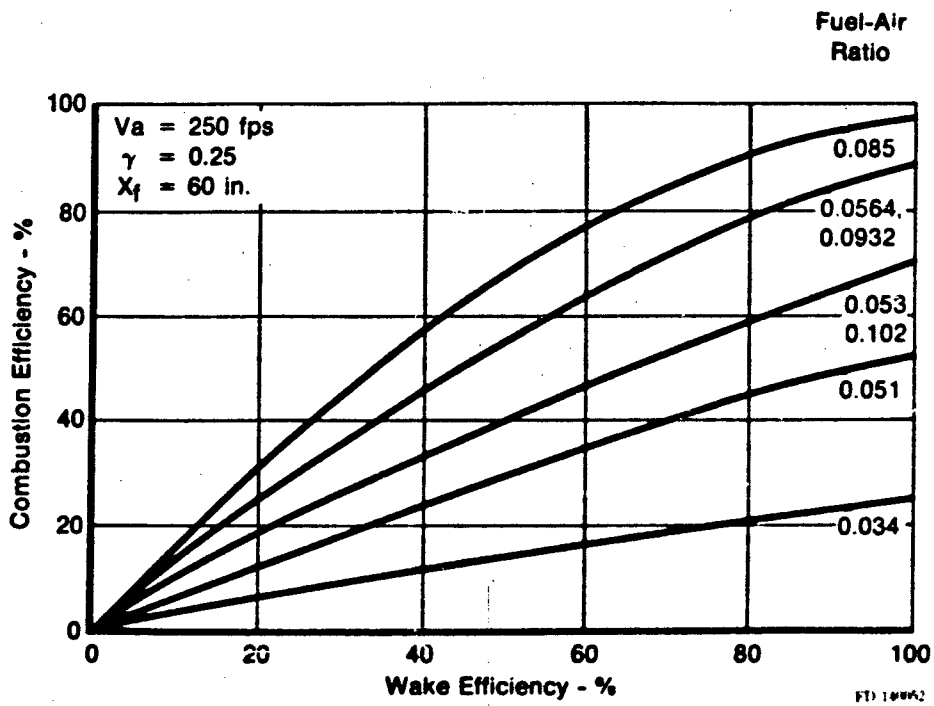


Figure 36. Effect of Wake Reaction Level on Duct Combustion Level

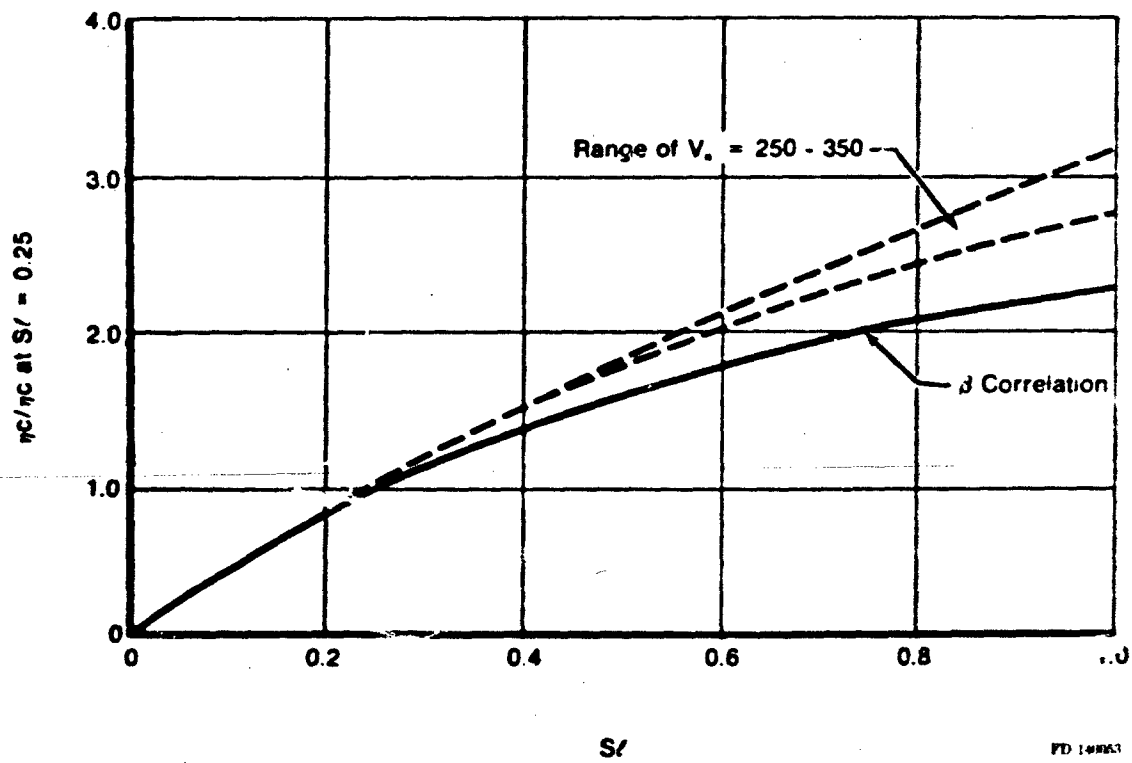
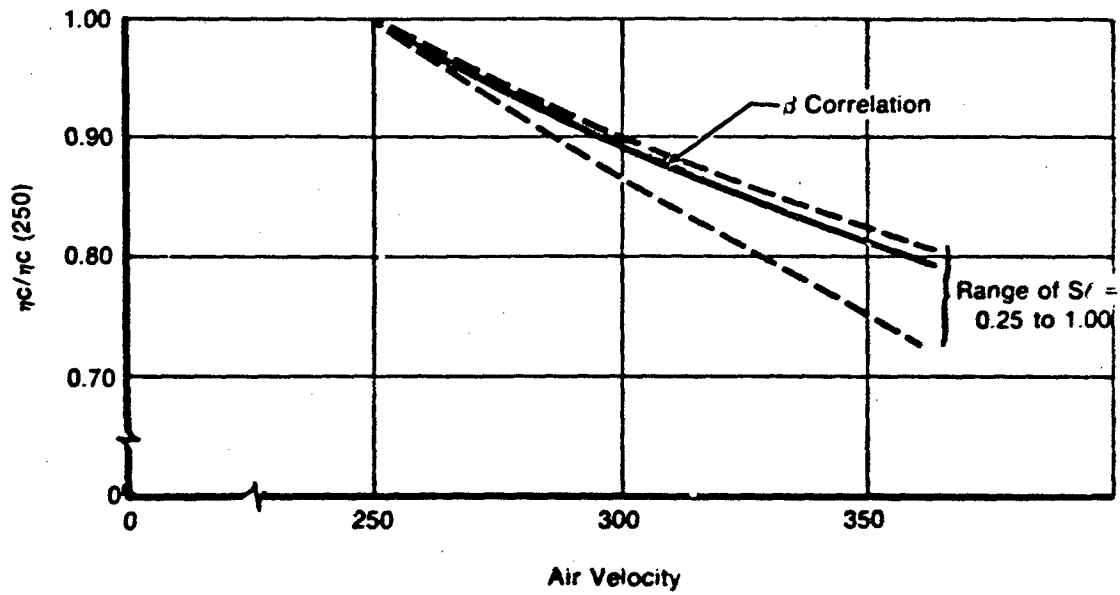


Figure 37. Comparison of Flame Model with Beta Correlation

2. EXPERIMENTAL INVESTIGATION

a. Test Apparatus

The study experiments were conducted in a (boiler plate) combustion system in which the pressure, temperature, gas flow and flameholder instability in an augmentor were simulated. The circular cross-sectional rig was designed and built under an independent Pratt & Whitney Aircraft Group research program. The simulator was designed so that various configuration changes including flameholders, spraybars, and distances between reflective points could be easily made for diagnostic evaluation.

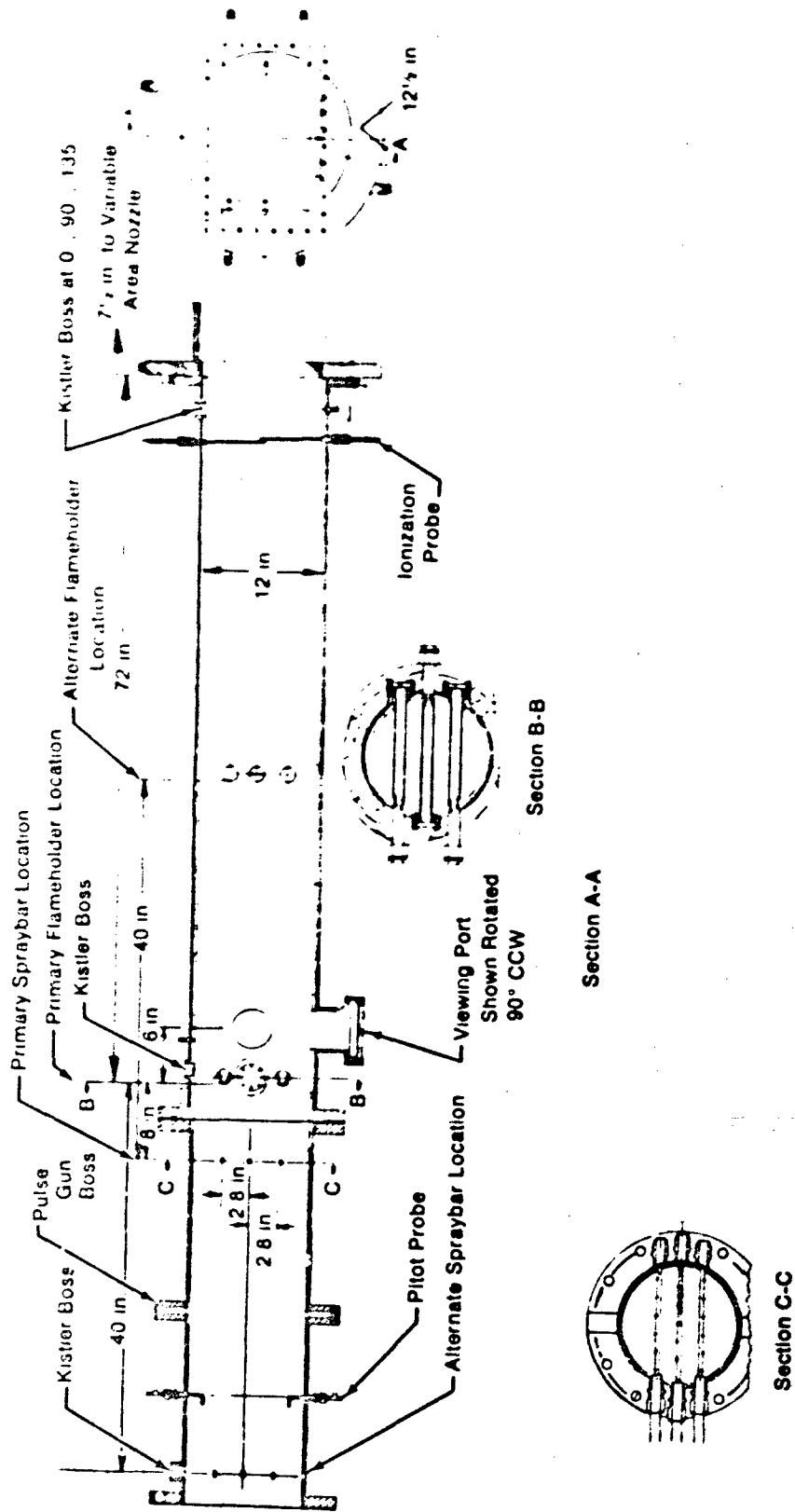
A drawing of the test rig is shown in Figure 38. The rig is made up of an inlet reflective orifice plate, inlet case, fuel injection case, combustion case, transition flange, and a variable area exhaust nozzle. Photographs of the test hardware are shown in Figures 39 through 47.

The orifice plate (Figure 39) provides the system upstream reflective point. The overall system length can be varied from 162.4 to 119.4 inches by the location chosen for the orifice plate. It can be placed at the entrance or exit of the inlet case. The inlet case (Figure 40) is 39.9 inches long. When inlet temperatures above 600°F are desired, the inlet case is replaced with a heater burner that consists of a burner can and fuel nozzle cluster mounted in a boiler plate housing. All high temperature (600 to 1300°F) testing was done with a system length of 119.4 inches.

The uncooled fuel injection section (Figure 41) is 39.4 inches long and has two injection planes which can be fitted with either three liquid fuel or three gaseous fuel spraybars. Typical liquid and gaseous spraybars are shown in Figure 42. The primary and secondary injection planes are located 8 and 40 inches, respectively, upstream of the primary flameholder location. The zone 1 spraybar is located on the rig centerline. The zone 2 and zone 3 spraybars are located 2.8 inches outboard of the rig centerline. The location and the spray direction of the liquid fuel zones are shown in Figure 43. The injection direction for each zone was the same for the gas spraybars.

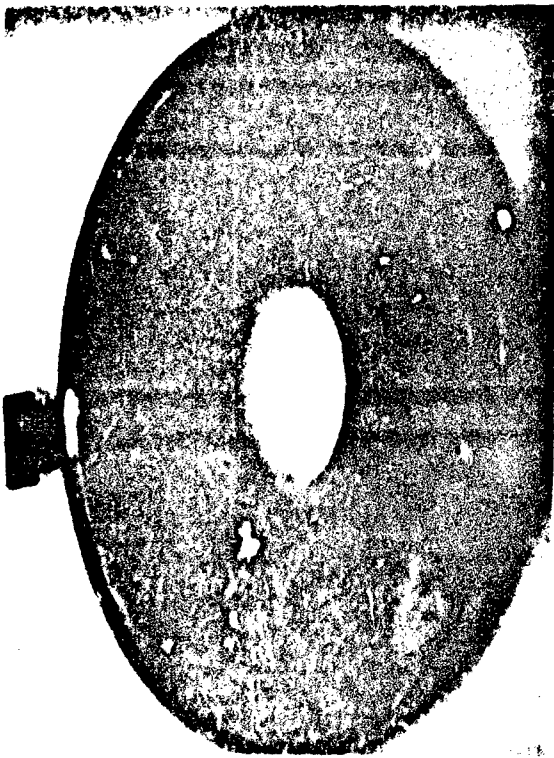
The combustion section (Figure 44) is a water cooled duct 12 inches in diameter, 76.6 inches long and has a primary and secondary flameholder location. The primary flameholder location is 79.5 inches from the nozzle exit plane and the secondary location is 47.5 inches from the nozzle exit plane. Either position can be fitted with three "V" gutter flameholders of 35 and 52% blockage, 1:1 and 2:1 length to width, and draft angles of 22.5 and 45°. An oxy-acetylene pilot burner is mounted in the recirculation zone of the center flameholder. This burner can provide a continuous ignition source and was used to supply the variations in heat addition. The various flameholders configurations are shown in Figure 45. The centerline of the three flameholder zones are aligned with the centerline of the respective fuel spraybar zones.

The water cooled transition flange (Figure 46) changes the rig flowpath from circular to rectangular to match the variable area nozzle. The exhaust nozzle assembly is designed to permit continuous variation of exit area over a wide range of choked operating conditions. The nozzle assembly consists of (1) two remotely actuated cylindrical water-cooled rods, 4 1/2 inches in diameter on one end and 1 1/4 inches in diameter on the other, (2) two semicylindrical side wall plugs, and (3) two flat plate sidewalls. Moving the rods in and out of the duct, with and without the side wall plugs, results in a geometric area change ranging from 16.1 to 112.9 in.² Figure 47 shows the possible geometric area extremes. The rods have been provided with total pressure ports on the upstream side and static pressure taps on the sides of the rods, so that at any rod position there is a minimum of five total pressure and four static pressure pickups per rod in the duct. As shown in Figure 48, each rod is driven independently by a linear actuator powered by a 24 volt dc motor.

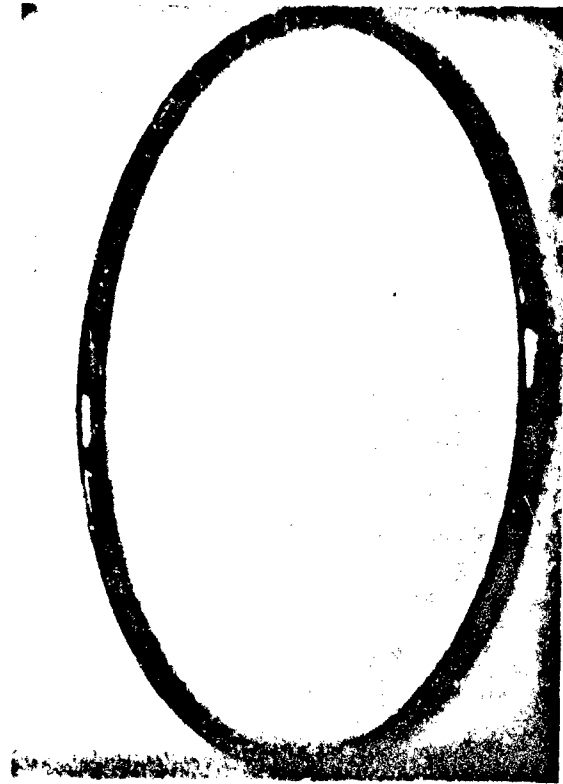


FD 11472

Figure 38. Flameholder Instability Study Test Rig



Orifice Plate



Ring Joint Gasket



Target Probe



Flameholder Blank-Off

FD-1001A

Figure 39. Rig Hardware

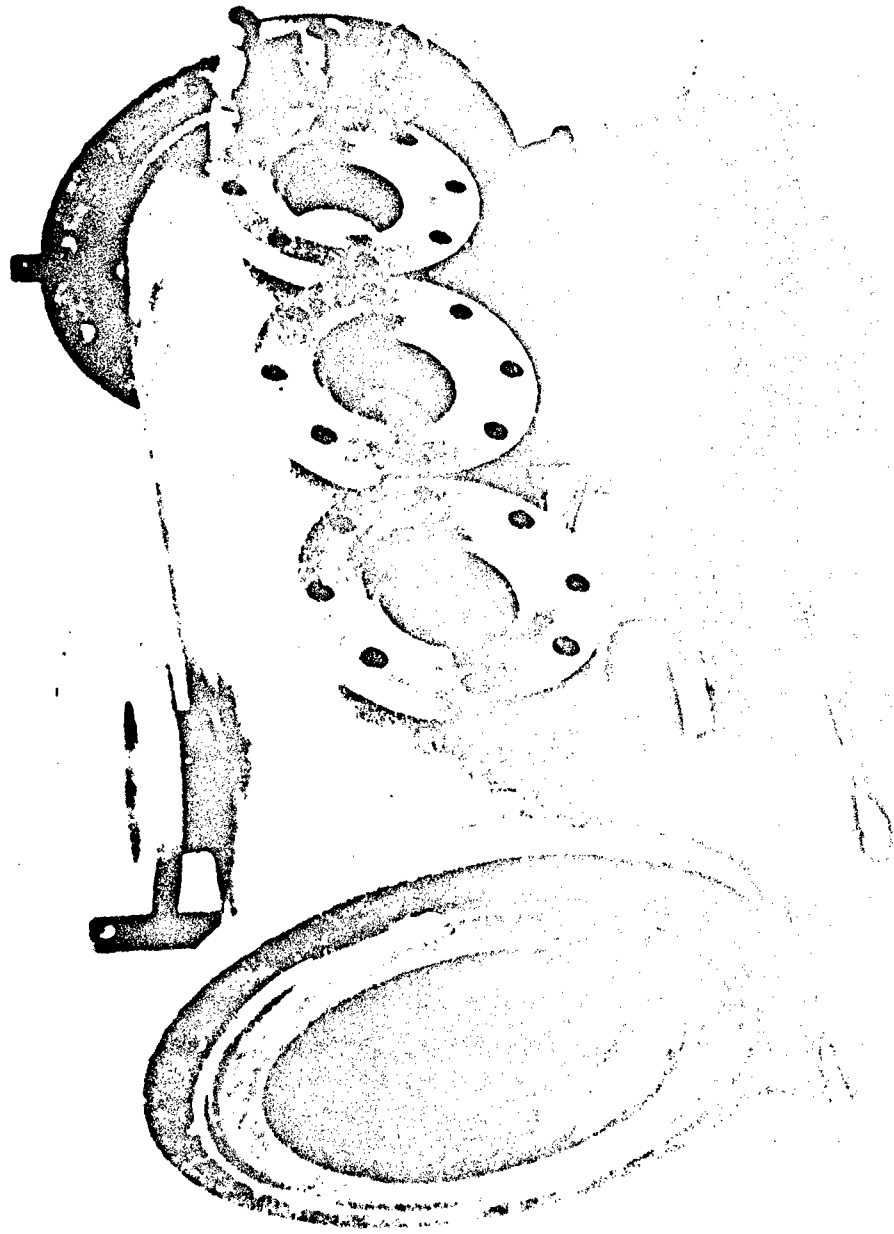
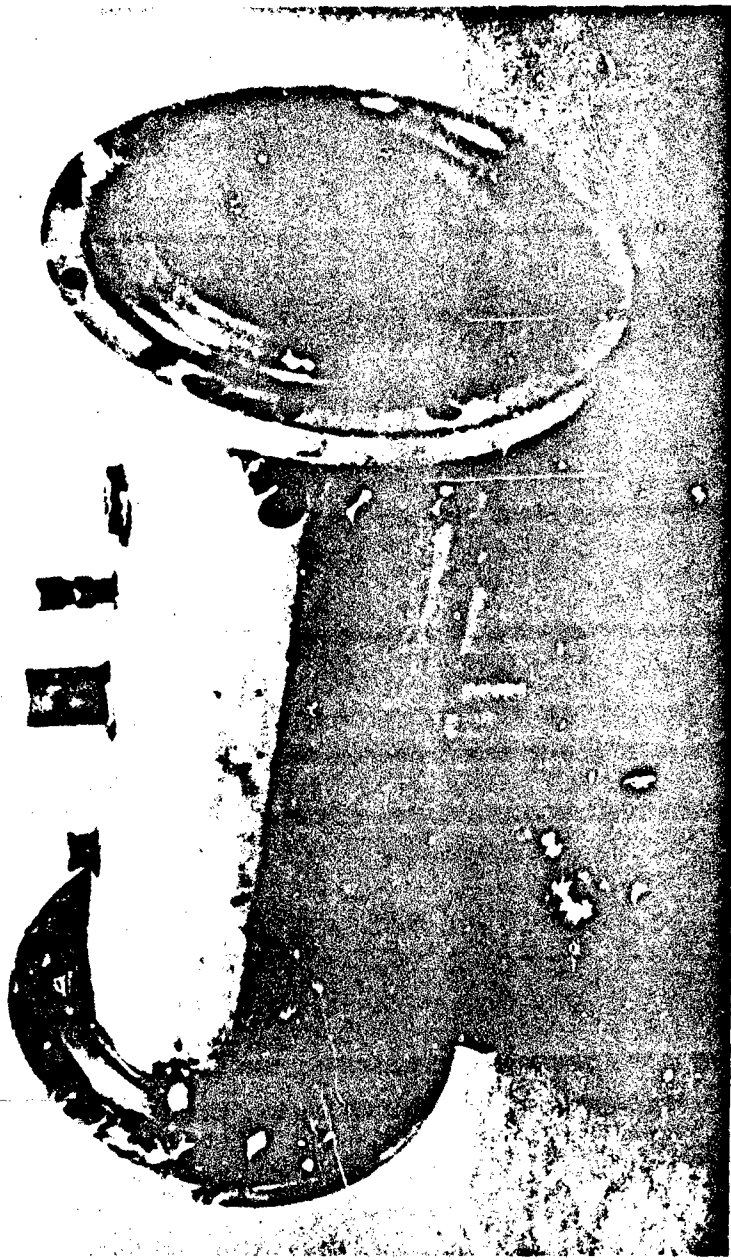
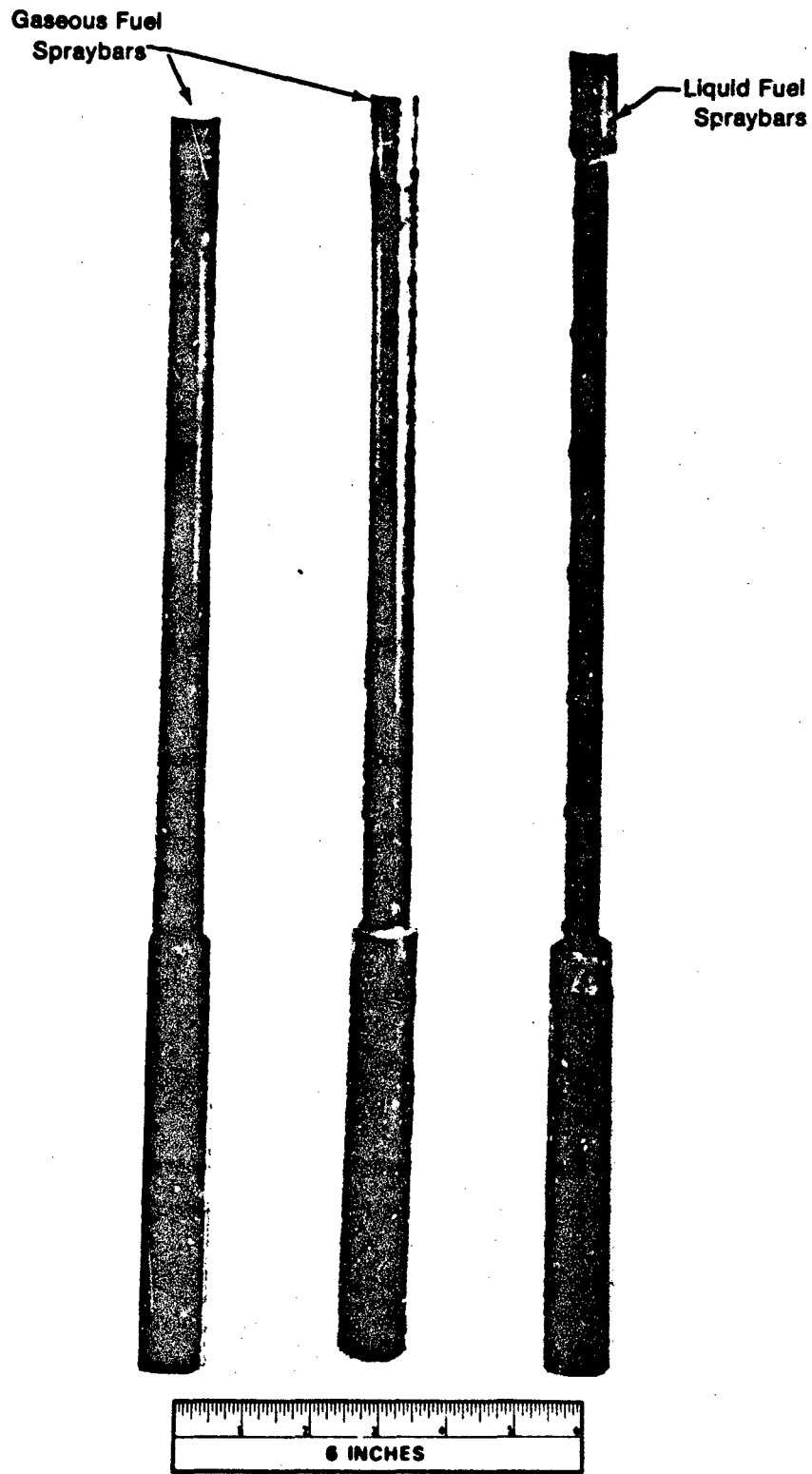


Figure 40. Inlet Case



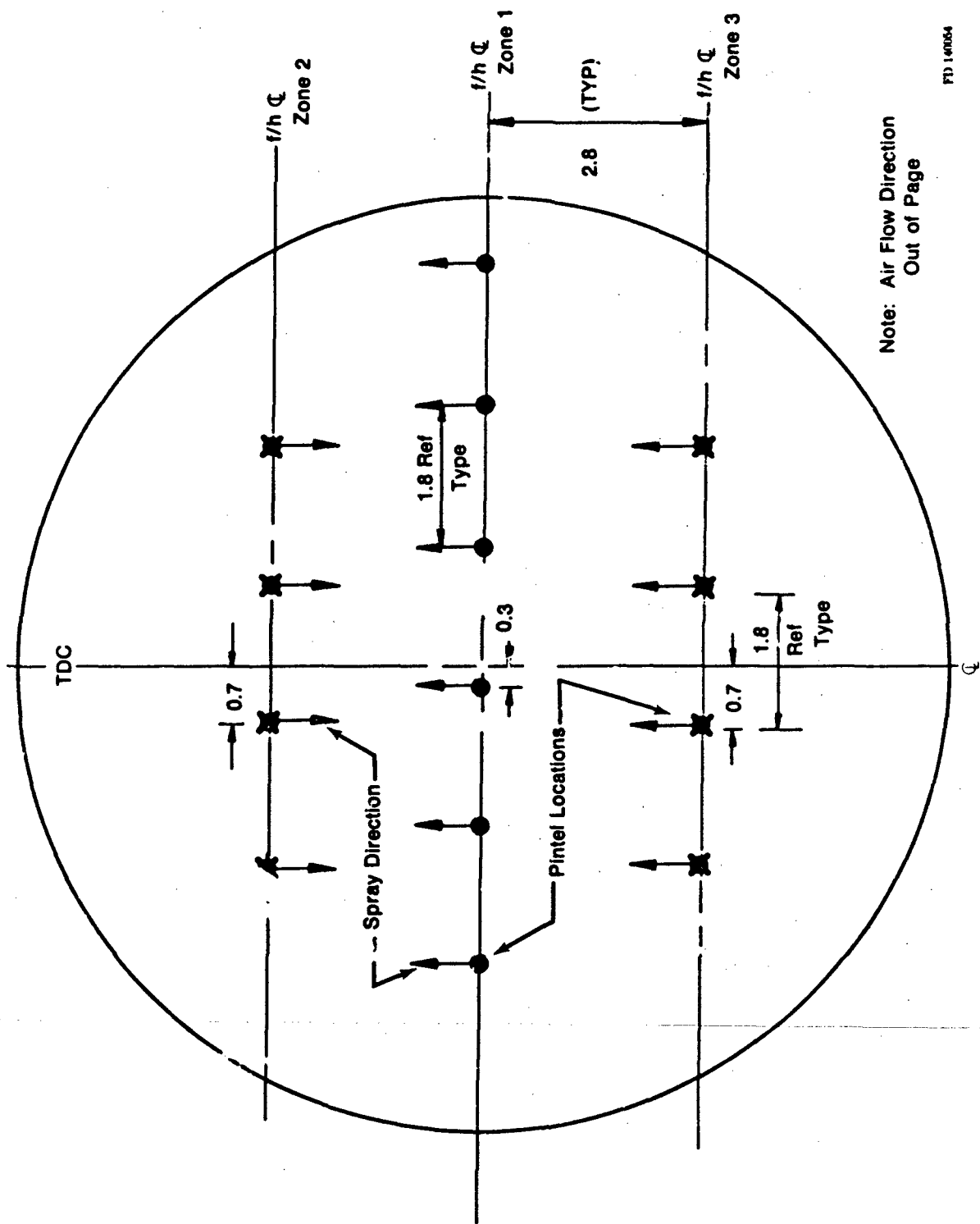
FD-140130

Figure 41. Fuel Injection Case



FD 140117

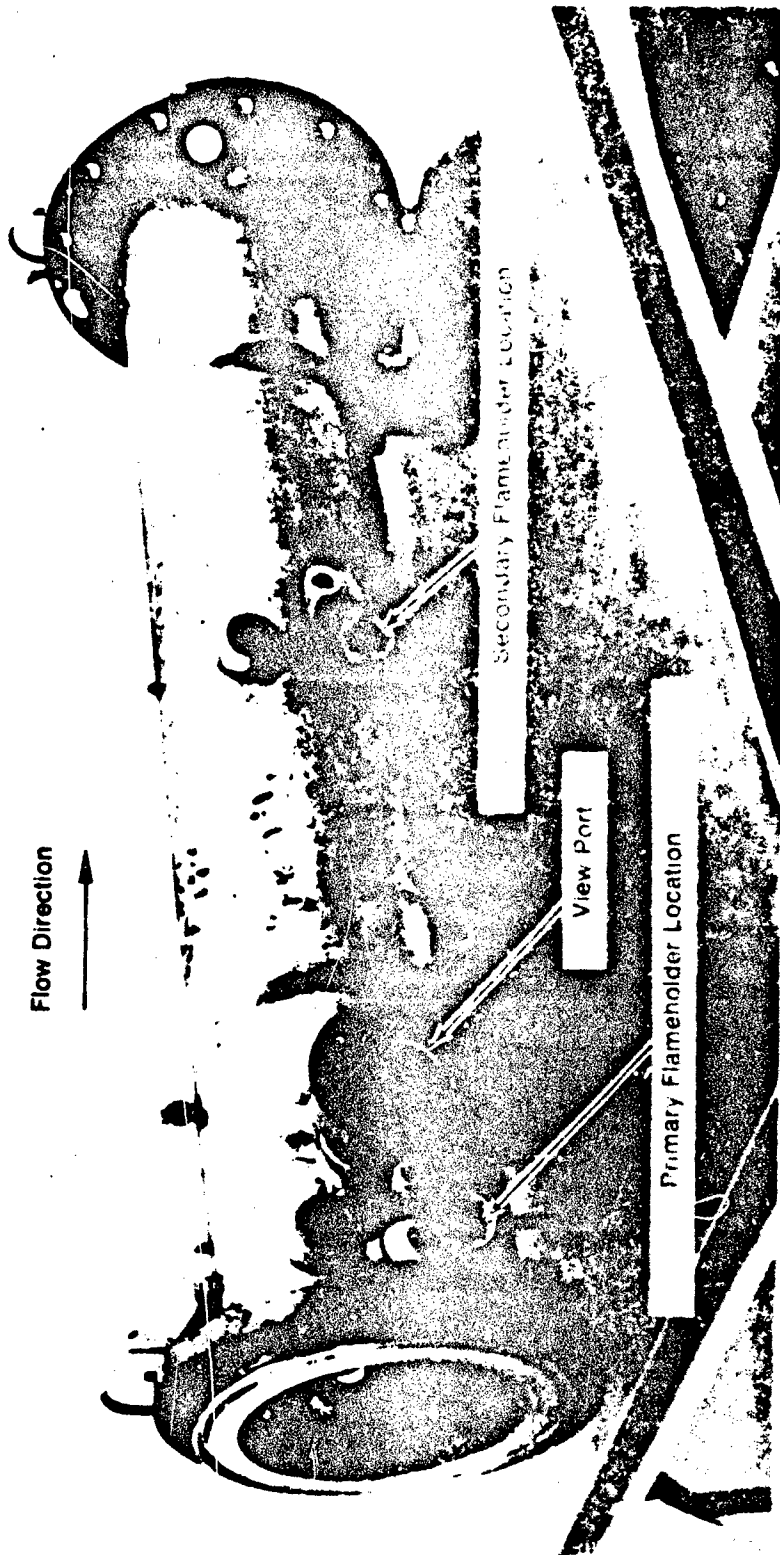
Figure 42. Fuel Spraybars



Note: Air Flow Direction
Out of Page

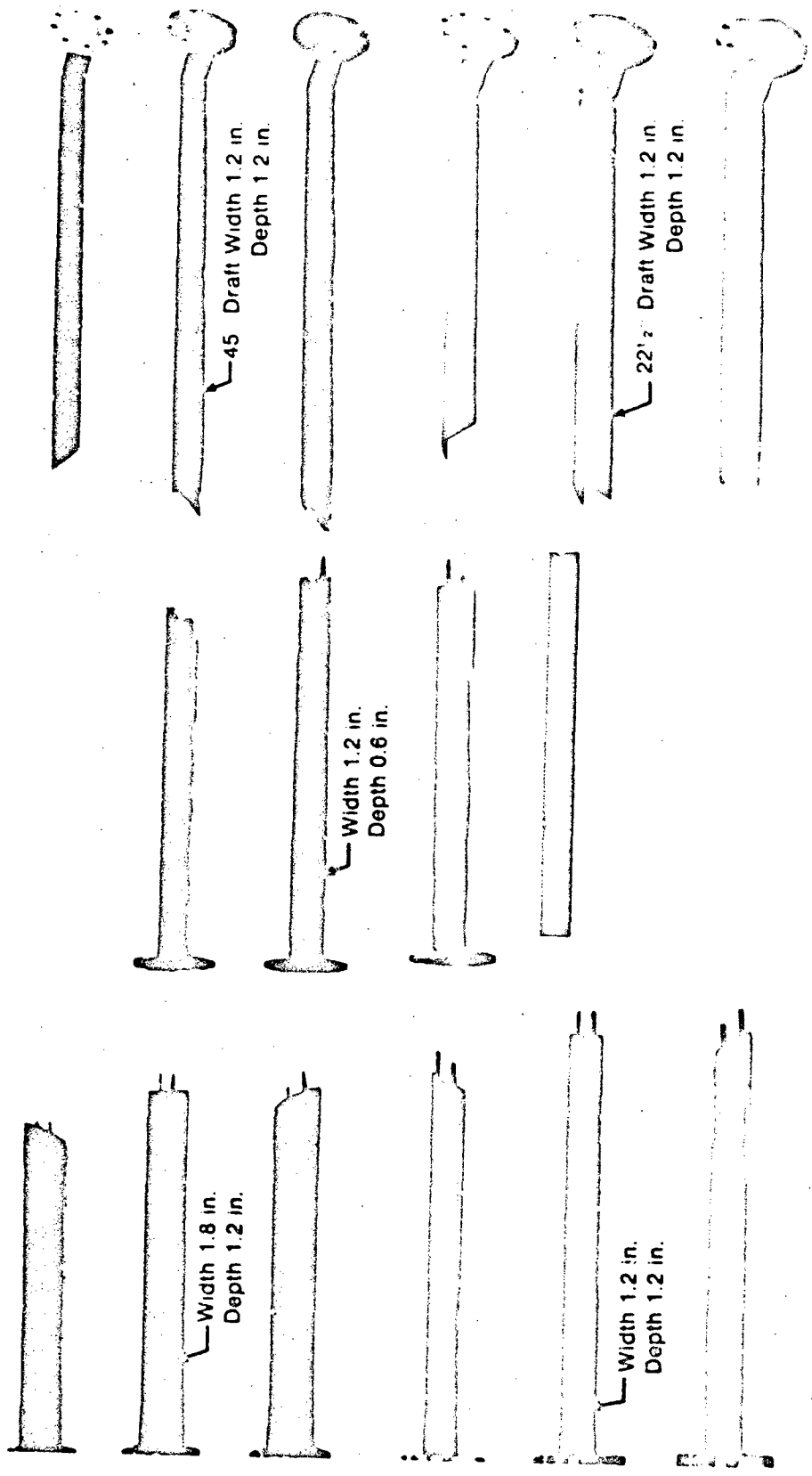
FD 14054

Figure 43. Spray Direction and Pintel Location with Liquid Fuel Injectors



FD 140116

Figure 44. Combustion Chamber



FD 14015

Figure 45. Flamelolders

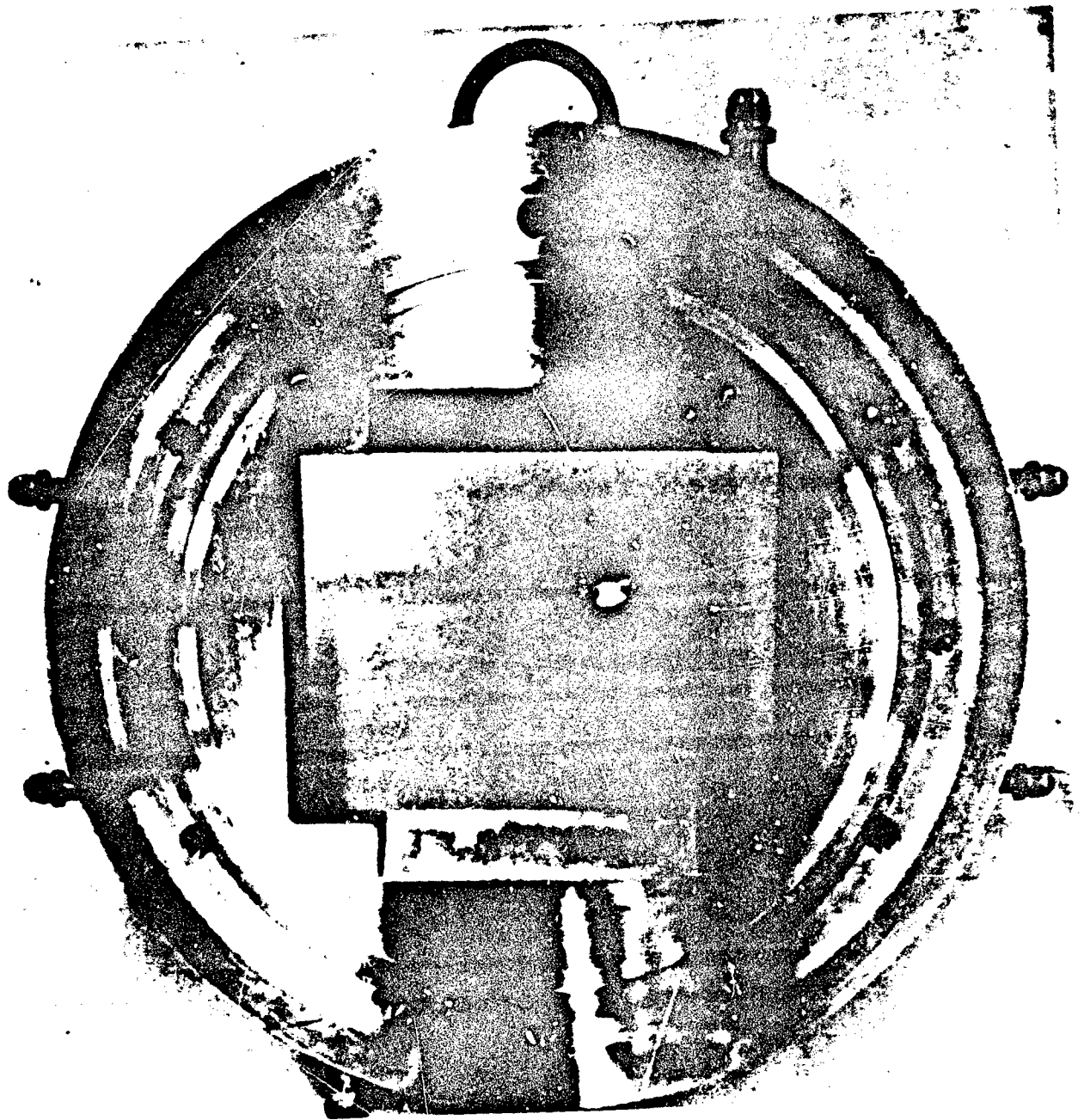
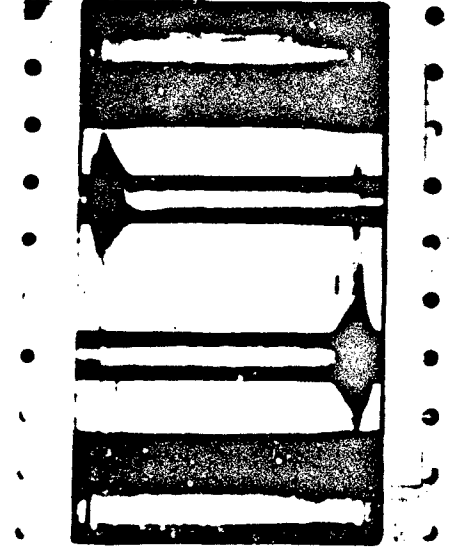
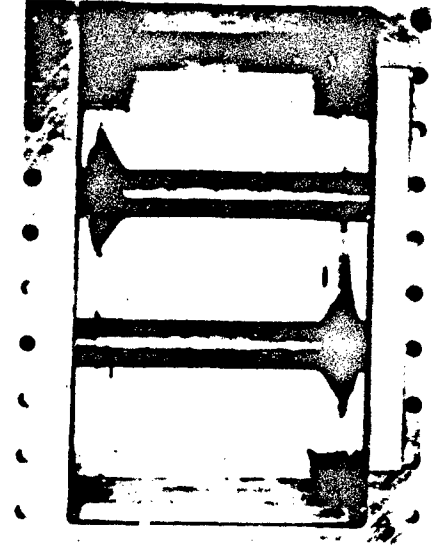


Figure 46. Transition Flange



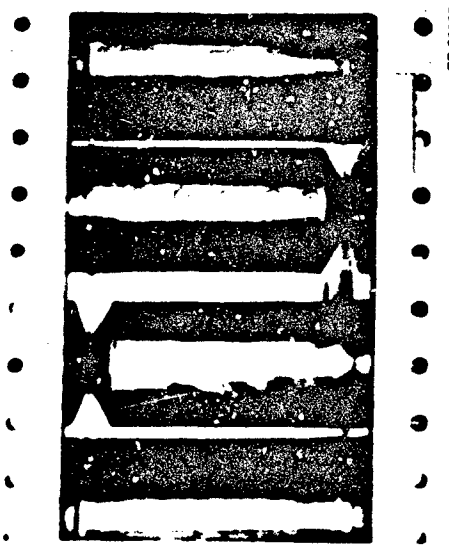
FE 89376

a. Minimum Nozzle Area With Sidewall Plugs



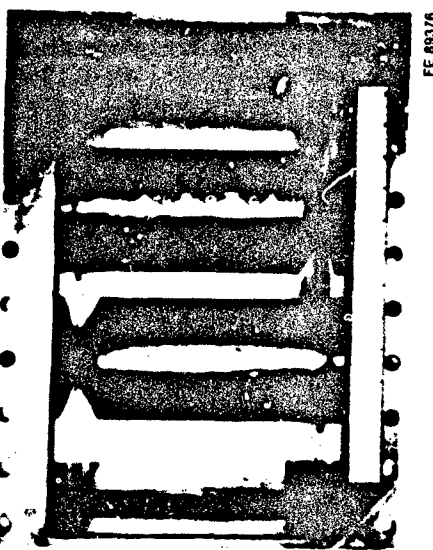
FE 89377

b. Maximum Nozzle Area With Sidewall Plugs



FE 89380

c. Minimum Nozzle Area With Sidewall Plugs

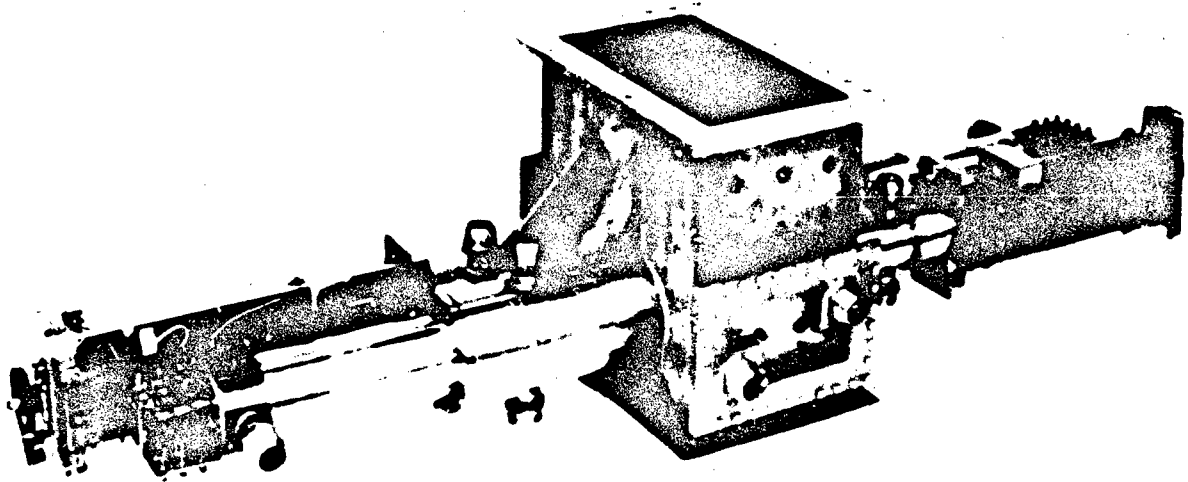


FE 89376

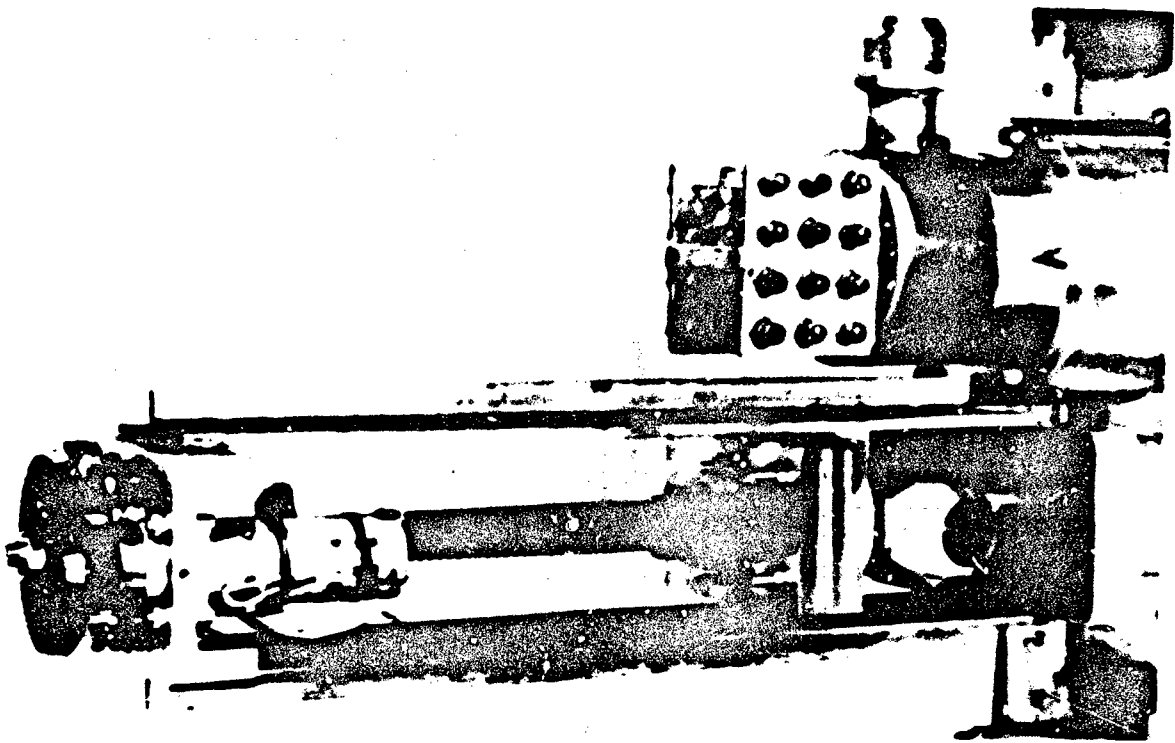
d. Minimum Nozzle Area Without Sidewall Plugs

FD 14011A

Figure 47. Geometric Nozzle Area Extremes



a. Variable Area Nozzle Actuator Assembly



b. Nozzle Actuator Assembly

Figure 48. Nozzle Actuator Assemblies

b. Instrumentation

The instrumentation, listed in Table 2 was used to monitor the following test parameters:

- Airflow
- Fuel flow
- Rig inlet total pressure and temperature
- Combustor inlet total pressure and temperature
- Combustor exit total pressure
- Combustor pressure oscillations
- Fuel temperature, flowrate, and pressure
- Velocity changes in duct
- Temperature changes in combustor
- Flameholder skin temperatures
- Pilot burner oxygen and acetylene flow rates
- Fuel air ratio upstream of the flameholder and in the flameholder wake

The data were recorded by an automatic data recording system and reduced through the IBM 370-168 computer system.

Special test items unique to this program are discussed in the following paragraphs.

The combustor was instrumented with five high-response Kistler Model 605A pressure transducers (Figure 49) to determine both the frequency and type of wave occurring during combustion instability. The axial and angular locations for each of the Kistlers are shown in Figure 38. The phase relationship and relative amplitude of the oscillations, sensed by the transducers located at intervals down the rig, provided the necessary information to identify the wave pattern and amplitude gains during rumble operation.

An oxy-acetylene pilot torch was mounted in the recirculation zone of the center flameholder. This torch provided continuous ignition and simulated piloting by wake heat addition.

The center flameholder position, zone 1, was instrumented with two skin thermocouples. They were attached to the upstream side of the "V" gutter on the 1.8 × 1.2, 1.2 × 1.2, and 1.2 × 0.6 flameholder configurations. A typical thermocouple location is shown in Figure 50.

Two four-inch diameter view glass viewing ports were located 180° apart at the trailing edge of the primary flameholder so that high speed color motion pictures could be made during steady-state and rumble operations to provide comparative data on flow dynamics and combustion. Two air-cooled ionization probes (Figure 38) are used to determine gas temperature increase or decrease. The temperature changes are correlated with velocity changes detected by a strain gage attached to a target probe upstream of the flameholders. The correlation between local temperature and velocity changes provide additional data on the rumble mechanism.

The fuel vaporization probe is located just upstream of the flameholder and can be traversed across the flameholder (Figure 38). The purpose of this probe is to sample the fuel-air mixture just upstream of the flameholder and provide a means of quantifying the amount of liquid and vaporized fuel present.

TABLE 2
FLAMEHOLDER COMBUSTION INSTABILITY STUDY RIG INSTRUMENTATION DESCRIPTION

<i>Item</i>	<i>Location</i>	<i>Sensors</i>	<i>Indication</i>
1. Orifice-Venturi	Upstream of Test Rig	Two Total Pressure Probes Two Static Pressure Taps (upstream) Two Static Pressure Taps (downstream)	Two 150-psi Gages for Control Room Monitoring. Automatic Data Recording System.
2. Inlet Total Pressure	Fuel Injection Case	Two Total Pressure Probes	Automatic Data Recording System.
3. Inlet Static Pressure	Fuel Injection Case	Two Static Pressure Probes	Automatic Data Recording System.
4. Inlet Total Temperature	Fuel Injection Case	Two Wall Static Pressure Taps Chromel-Alumel Thermocouples (Two Locations)	Direct Reading Potentiometer for Control Room Monitoring. Automatic Data Recording.
5. Combustor Exit Temperature Profile	Slightly Upstream of Exhaust Nozzle Plane	Total Pressure Ports in the Exhaust Nozzle Rods	Oxygen Concentration Meter.
6. Combustor Exit Total Pressure	Exhaust Nozzle Plane	Twelve Total Pressure Ports Located in Water-Cooled Exhaust Nozzle Rods (Six in each rod)	Two 50-psi Gages for Control Room Monitoring. Automatic Data Recording.
7. Combustor Exit Static Pressure	Exhaust Nozzle Plane	Sixteen Taps Located in the Sides of the Water-Cooled Nozzle Rods. (Six in each rod)	Two 50-psi Gages for Control Room Monitoring. Automatic Data Recording.
	Combustor Case	Two Wall Static Pressure Taps	Automatic Data Recording System.

TABLE 2
 FLAMEHOLDER COMBUSTION INSTABILITY STUDY RIG INSTRUMENTATION DESCRIPTION (Continued)

Item	Location	Sensors	Indication
8. Combustor Pressure Oscillations	Inlet Case, Fuel Injection Section and Combustor Section	Eight High Response Dynamic Pressure Sensors	Oscilloscope for Control Room Monitoring. Automatic Data Recording.
9. Fuel Flowrate	Fuel Supply Line (each zone)	Turbine Flowmeter	Electronic Counter for Control Room Monitoring. Automatic Data Recording.
10. Fuel Temperature	(1) Fuel Line Near Flowmeter (2) Fuel Line Near Sector	Thermocouple	Direct-Reading Potentiometer for Control Room Monitoring. Automatic Data Recording.
11. Fuel Pressure	Fuel Line Near Test Rig	Static Taps 0.05 in. Diameter	Two 500-psi Gages for Control Room Monitoring. Automatic Data Recording.
12. Velocity Changes	Fuel Injection Case — 7 in. Upstream of Primary Fuel Injection Plane	Strain Gage — Target Probe	Oscillograph for Control Room Monitoring Automatic Data.
13. Temperature Changes	Combustor Case — 14 and 69 in. from Nozzle Exit Plane	Two Ionization Probes	Oscillograph for Control Room Monitoring Automatic Data.
14. Fuel Vaporization	Combustor Case — 2 in. Downstream of Primary Flameholder Exit Plane	Fuel Vaporization Probe	Hookman Model 402 on Line Gas Monitoring. Digital Display in Control Room.
15. Flameholder Temperature	Upstream Wall of Center Flameholder	Skin Thermocouple	Direct-Reading Potentiometer for Control Room Monitoring. Automatic Data Recording.

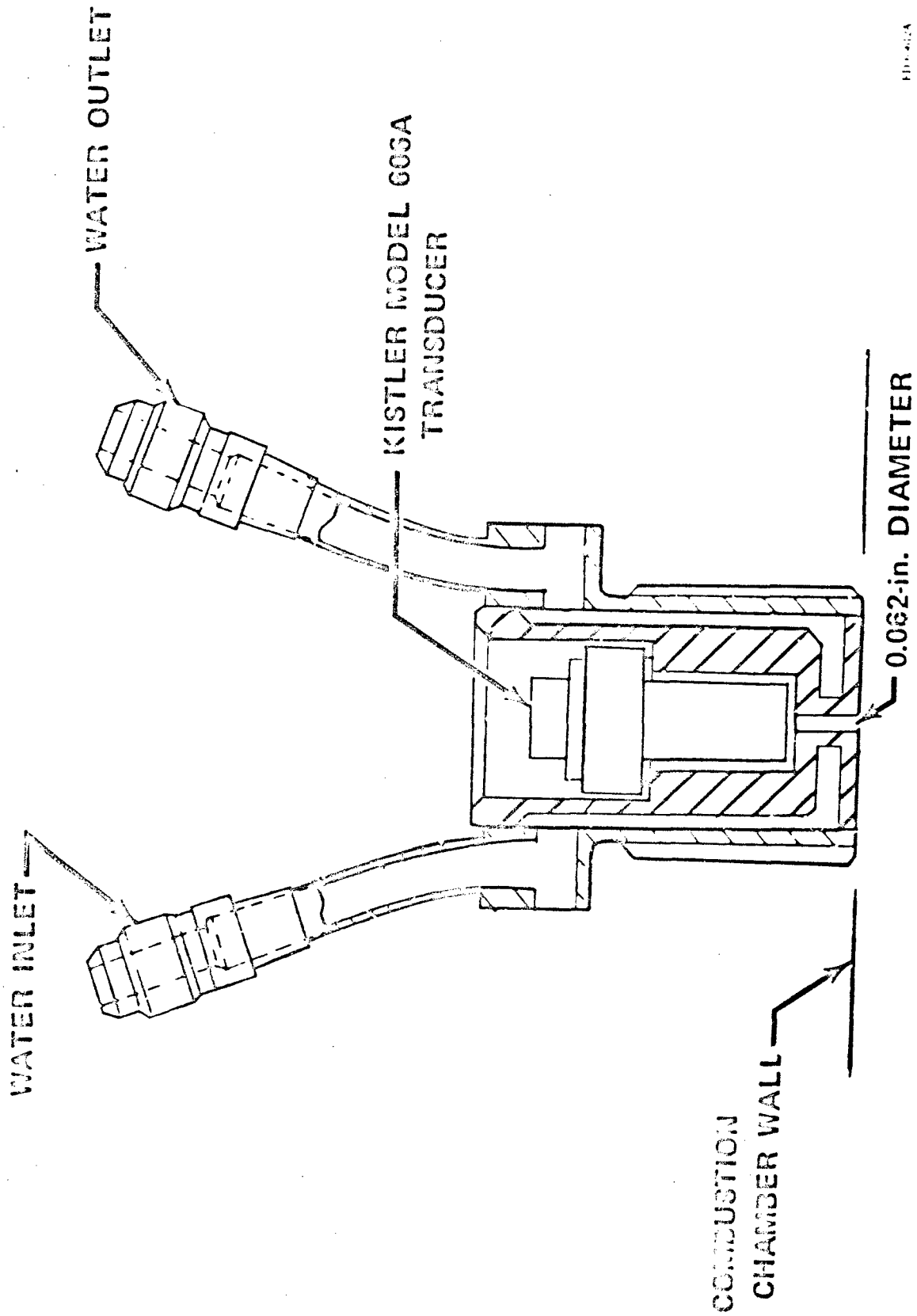
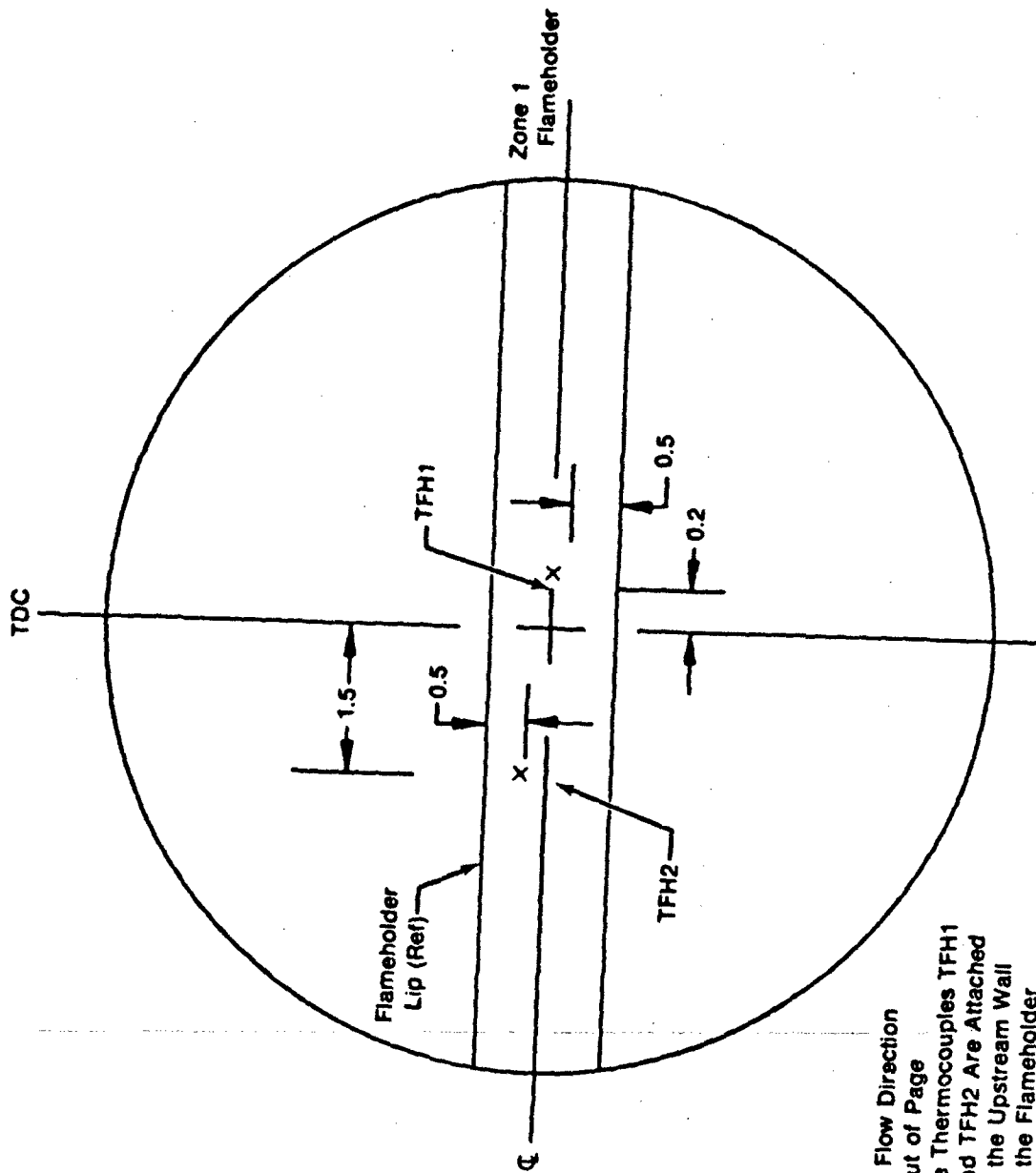


FIG. 49A

Figure 49. Cross-Sectional View of Kistler Model 606A Installed in a Water Cooled Adapter



FD 140065

- Note: 1. Air Flow Direction
Out of Page
2. The Thermocouples TFH1
and TFH2 Are Attached
to the Upstream Wall
of the Flameholder

Figure 50. Flameholder Skin Thermocouple Locations

c. Test Program

Concurrent with Task 1 analytical studies, an experimental program was conducted to verify the analytical model and to determine values for portions of the flame stabilization model. Studies were conducted over a range of fuel-air ratios to evaluate the influence of gutter geometry and blockage, pressure, temperature, velocity, and fuel vaporization level. Additional tests were made to evaluate the influence of heat addition to the wake and the influence of inclined flameholder gutters.

Planned test series (Figure 51) were designed to cover a range of inlet conditions typical of augmentors, especially the conditions which simulate the effect of the cold, fan duct airstream in turbofan engines. Particular emphasis was placed on the cold air influence, since turbofan augmentor experience at Pratt & Whitney Aircraft has shown that rumble may be reduced or eliminated by alterations to the cold-stream flameholder alone.

The test matrix included varying the fuel-air ratio, blockage ratio, flameholder geometry, inlet temperature, pressure, fuel distribution and vaporization. For each sequence of test variables, a sampling probe was installed to measure the local total and vapor phase fuel-air ratios upstream of the flameholder. For several tests, two sampling tubes were mounted in the downstream wall of the center flameholder for measurements inside the near wake region. A Beckman Model 402 hydrocarbon analyzer was used to measure on line the data from the upstream probe and the wake tubes.

After completion of the first test series, the test program was modified. The revised test program shown in Figure 52 was a composite program combining the test requirements of both the Flameholder Combustion Instability Study and the companion system model, Contract F33615-76-C-2024, into a single test program to cost effectively gather the most data. The test matrix was not significantly changed from the original program, i.e., most of the original items to be investigated were still included. The only item deleted was the effect of fuel injection system stiffness because (1) a consensus of the investigators believed its impact on the program was minimal, and (2) more test time could be allocated to the other suspected mechanisms. Most of the test program changes were reflected in the test operating conditions. In the original test matrix, bands of pressure, temperatures, duct Mach numbers, and fuel-air ratios were given. The Series I test results, however, specifically defined the test conditions of interest within the capabilities of the system. The resultant test conditions are shown in Table 3.

d. Experimental Program Problems

(1) Series I Testing

The primary purpose of the Series I testing was to determine stability characteristics of the test rig, which would serve as a baseline for the Series II test program. A secondary purpose of the Series I testing was to evaluate the test rig hardware and instrumentation which, for the most part, had not undergone previous testing.

Series	Test Cond. No.	Flamholders		Fuel Type	Orifice to Nozzle Distance	Sprocket to Flamholder Distance	Flamholder to Nozzle Distance	Test Conditions			Test Purpose		
		Number	Width					Inlet Pressure	Inlet Temp.	Inlet Mach No.		Post-Air Ratio	
I	1	3	1.2	35	JP-4	163	9	78	6.5	200	0.12-0.25	.065-.15	Map system low frequency stability characteristics of the experimental apparatus. High speed motion pictures will be filmed during "rumbles".
	2	3	1.2	35	JP-4	163	9	78	10	400	0.12-0.25	.065-.15	
	3	3	1.2	35	JP-4	163	9	78	10	1300	0.12-0.25	.065-.15	
	4	3	1.8	52	JP-4	163	9	78	10	700	0.12-0.25	.065-.15	
	5	3	1.8	52	JP-4	163	9	78	10	400	0.12-0.25	.065-.15	
II	6	3	1.8	52	JP-4	163	42	78	10	1300	0.12-0.25	.065-.15	Determine the effect of fuel vaporization on system stability.
	7	3	1.8	52	JP-4	163	42	78	10	700	0.12-0.25	.065-.15	
	8	3	1.8	52	JP-4	163	42	78	10	400	0.12-0.25	.065-.15	
III	9	3	1.8	52	CH ₄	163	42	78	10	1300	0.12-0.25	.065-.15	Determine the effect of system length on system stability.
	10	3	1.8	52	CH ₄	163	42	78	10	700	0.12-0.25	.065-.15	
	11	3	1.8	52	CH ₄	163	42	78	10	400	0.12-0.25	.065-.15	
IV	12	3	1.8	52	JP-4	163	9	78	10	1300	0.12-0.25	.065-.15	Determine the effect of turbulence at the flameholders and spraybars on system stability. (1)
	13	3	1.8	52	JP-4	163	9	78	10	700	0.12-0.25	.065-.15	
	14	3	1.8	52	JP-4	163	9	78	10	400	0.12-0.25	.065-.15	
V	15	3	1.8	52	JP-4	163	9	78	10	1300	0.12-0.25	.065-.15	Determine the effect of injection point ΔP on system stability. (2)
	16	3	1.8	52	JP-4	163	9	78	10	700	0.12-0.25	.065-.15	
	17	3	1.8	52	JP-4	163	9	78	10	400	0.12-0.25	.065-.15	
VI	18	3	1.8	52	JP-4	163	42	78	10	1300	0.12-0.25	.065-.15	Determine the effect of combustion efficiency oscillations on system stability.
	19	3	1.8	52	JP-4	163	42	78	10	700	0.12-0.25	.065-.15	
	20	3	1.8	52	JP-4	163	42	78	10	400	0.12-0.25	.065-.15	
VII	21	3	1.8	52	JP-4	163	9	78	10	1300	0.12-0.25	.065-.15	Determine the effect of flamholder recirculation energy on system stability. (3)
	22	3	1.8	52	JP-4	163	9	78	10	700	0.12-0.25	.065-.15	

NOTES:

- (1) Geometry of test conditions 7 through 22 will be based on the stability limits determined in test conditions 1 through 6.
- (2) Exact test conditions will depend on stability limits determined during test conditions 1 through 6.
- (3) Two different orifice sizes will be tested. Both orifices will be 1/32 inches from the nozzle.
- (4) Two different spraybar ΔP's at the same flowrate will be tested.
- (5) Energy will be added by use of an Orin-acetylene burner at the flamholder.

Figure 51. Low-Frequency Augmentor Instability Investigation Test Matrix

Test Point	Flameholder Configuration	Fuel Type	Special Test Instrumentation	Test Condition	Test Purpose
1	1.8X1.2 50% blockage	JP4	None	Repeat Baseline at 200° and 400°F inlet temperature at 10 psi and 0.1, 0.15 Mach number	Repeat Series I baseline tests to checkout system
2	Same as 1	JP4	Iso-kinetic probe wake f/a probe flameholder T/C's	Test matrix. Torch flowrate variation at 200° and 400°F inlet	Characterization of approach and wake fuel-air ratio as a function of velocity, pressure, temperature and flameholder geometry
3	1.2X1.2 35% blockage	JP4	Wake f/a probe Flameholder T/C's	Same as 2	Same as 2
4	1.2X0.6 35% blockage	JP4	Same as 3	Same as 3	Same as 2
5	1.2X1.2 35% blockage 22½° draft	JP4	None	Same as 1	Evaluate the effect of flameholder drafting on rumble and combustion efficiency
* 6	1.2X1.2 35% blockage 45° draft	JP4	None	Same as 5	Same as 5
7	1.8X1.2 50% blockage	JP4	Flameholder T/C's, two turbulence screens	Same as 1	Evaluate the effect of turbulence
8	Same as 2	CH4	Flameholder T/C's	Same as 1	Evaluation of gaseous fuel on efficiency and stability limits
9	Same as 2	JP4	Flameholder T/C's	Relocate fuel injectors	Evaluate the effect of increased fuel injector to flameholder distance
10	Same as 2	JP4	Flameholder T/C's	Relocate flameholders	Evaluate the effect of reduced augmentor length
11	Same as 3	JP4	Flameholder T/C's	Relocate flameholders to nominal position, 1300°F inlet condition	Simulate core stream effects. Evaluate the effect of Augmentor Length -shorten cold duct

* Did not test at this point

Figure 52. Flameholder Model Rig Tests

TABLE 3
REVISED TEST CONDITIONS

Test Number	Inlet Pressure (psia)	Inlet Temperature (°F)	Equivalence Ratio ϕT	Duct Mach Number
A	10	*200	0.5, 1.0, 1.5	0.088
B	10	200	0.5, 1.0, 1.5	0.155
C	10	*400	0.5, 1.0, 1.5	0.088
D	10	400	0.5, 1.0, 1.5	0.155
E	15	*400	0.5, 1.0, 1.5	0.088
F	15	400	0.5, 1.0, 1.5	0.155
G	15	400	0.5, 1.0, 1.5	0.238

* Run 2 or 3 torch flowrate variations at the completion of the iso-kinetic and wake f/a data acquisition.

The overall test rig condition after Series I testing, was very good. No major damage was incurred. The target probes, ionization probes, viewing window, and a total pressure probe, however, were damaged during the course of the testing. The damaged probes were repaired with slight modifications incorporated to improve durability before additional testing. The set of vycor glass viewing windows was destroyed early in the first series of tests. It was not replaced during the remainder of the Series I program because more valuable visual data could be obtained during later testing after the stability characteristics of the test rig were known. Another problem area uncovered during the Series I testing was the upstream orifice. The orifice, which had been installed to provide a known reflective location, was sending a jet of airflow throughout the burner system at high airflow rates (10 to 13 lbm/sec). This jet was apparently not attached to any wall surface for the entire length of the burner system. To remedy the problem, prior to Series II testing, the orifice plate was reworked by plugging the large single hole and rematching to include sixteen (16) smaller holes to maintain the same open area. Since combustion efficiency could not be determined from the data with an unchoked nozzle, the sidewall plugs, discussed earlier (Figure 47), were installed in the nozzle before Series II testing to ensure that choked flow could be maintained and combustion efficiency determined over the full range of operating conditions. The two-phase sampling probe was not operational during the first series of testing.

(2) Series II Testing

Some minor problems were also encountered during the Series II testing. The test facility ejector system was not operating at specified efficiency and would have required major repairs to correct the deficiencies. Since combustion efficiency measurements were desired, choked flow at the exhaust nozzle was required. To maintain choked flow, the lowest rig pressure was limited to approximately 14 psia and the rig duct Mach number to 0.12 compared to a planned rig pressure of 10 psia and duct Mach number of 0.155. It was determined that these revised conditions would provide the required input for the model and the test program was modified accordingly.

Upon completion of the test program, it was determined that the target probe, which had been modified at the conclusion of the Series I testing, was often vibrating at frequencies between 200 and 600 Hz when the airflow dynamic pressure measurements were 55 Hz. It was also determined that the ionization probes were occasionally grounded due to dampness that resulted in a 60-cycle, high-gain signal. Because the test program had been completed when these two discrepancies were determined, and the elimination of these two pieces of instrumentation would have only a minor impact on the model input, the data was disregarded. It was felt that disregarding all of the data would be more prudent than drawing conclusions from data that may or may not be correct.

The final problem area of Series II testing involved the zone 3 spraybar. After completion of the testing with turbulence screens, it was determined that the spraybar had been partially plugged with teflon tape that had been used to seal the fuel system fittings. The tape was removed and the spraybar recalibrated prior to resuming the test program, but the data from the previous test sequence involving zone 3 fuel flow was disregarded. This problem also had a minor impact on the model input.

3. EXPERIMENTAL PROGRAM RESULTS

a. Overall Comments and Results

The experimental program was structured to evaluate the impact on the combustion process of the following major variables:

- Fuel-air ratio
- Spray vaporization

- Fuel distribution
- Heat addition to the wake
- Combustion length
- Inlet conditions, pressure, temperature, velocity
- Flameholder geometry and blockage
- Inclined flameholders.

The test matrices presented in Section II-2 included a fuel-air ratio excursion at several pressures, temperatures and flow velocities for each major configuration change. Several of these were run with and then without an oxyacetylene torch mounted to provide heat addition to the wake of the central flameholder.

The major results of the test program may be summarized as follows:

- It was not possible to maintain a stable combustion process in the system at approach flow Mach numbers above approximately 0.12 at inlet temperatures of 200 to 400°F.
- The test data at these lower temperatures exhibited a large scatter and a lack of definitive repeatability with regard to efficiency. As such, the recorded efficiencies should be interpreted as accurate only to about $\pm 10\%$ absolute.
- A definite correlation was observed between the recorded metal temperature of the flameholder and the overall combustion efficiency. The correlation varied from one system configuration to another but was fairly good for each system.
- The onset of rumble and the decline in combustion efficiency occurred at the same time, reinforcing the combustion efficiency-driven oscillation concept.

Before going further into the data analysis a test case will be examined to substantiate the applicability of the two-phase fuel model concept.

The data here are from the first run of Series II after modifications to the variable area exhaust nozzle. This run, 7.01, utilized a 52% blockage flameholder with 1.8-in. wide gutters. The separation between flameholders and spraybars was 8 in. The measured overall combustion efficiency and rumble amplitude are shown versus fuel-air ratio in Figures 53 and 54. The results indicate significant deviations from premixed behavior in that peak efficiencies occur at less than stoichiometric fuel-air ratios.

The two-phase fuel wake composition equation:

$$\frac{\phi}{\delta} = \beta_1 + (1 - \beta_1) \frac{\beta_2 \beta_3}{K_1} \quad (81)$$

allows for the existence of a wake vapor fuel-air ratio which is on the rich side of stoichiometric ($\phi > 1.0$) even when the injected fuel-air ratio is lean ($\theta < 1.0$). As the injected fuel-air ratio was increased, the wake also increased and, being rich, the wake reaction efficiency decreased. Thus, the overall efficiency would exhibit a peak value while the injected fuel-air ratio was lean. For the conditions of Run 7.01 (i.e., 400°F inlet temperature, near ambient pressure and 150 fps velocity) the calculated value of β_1 is 32%. The droplet averaged collection efficiency, β_2 , is calculated at 85%. The wake recirculation rate, K_1 , for the 52% blockage is 23%. The percentage of the surface film which vaporizes, β_3 , is calculated to be about 40% for a fuel-air ratio of 0.050.

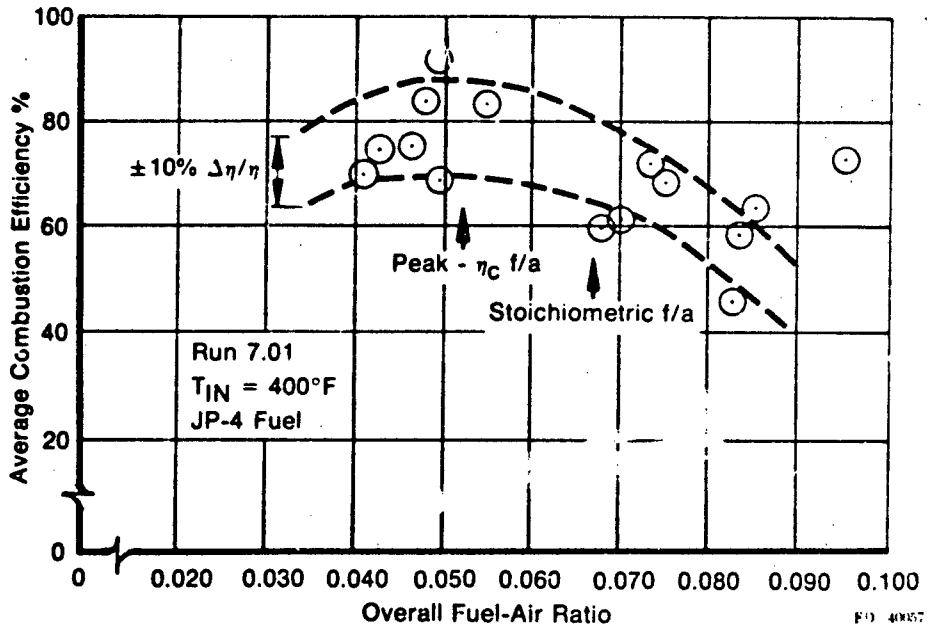


Figure 53. Rumble Rig Combustion Efficiency vs Total Fuel-Air Ratio Peak η_c Lean

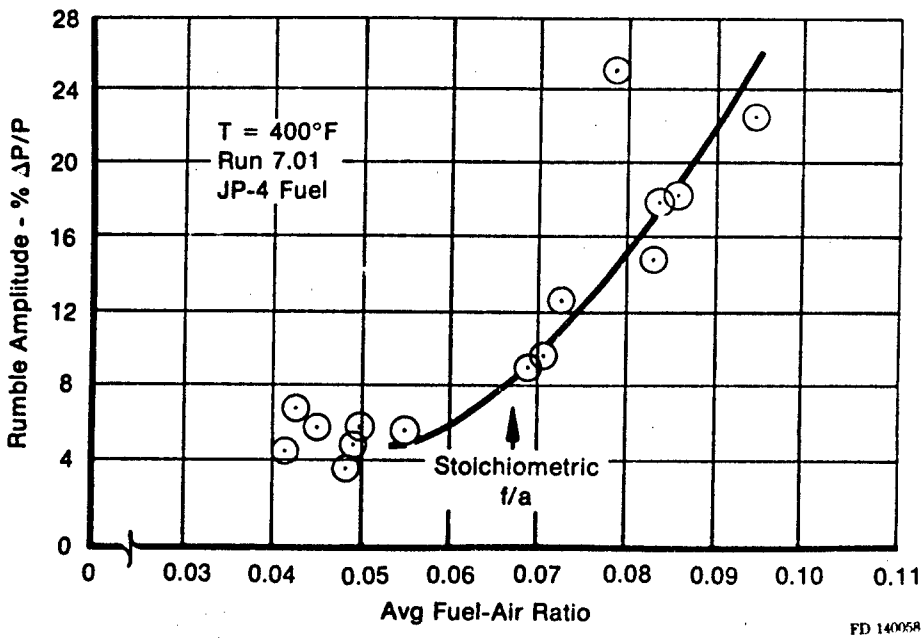


Figure 54. Rumble Break Point Occurs at Predicted Point of Rich Wake Transfer

Factoring these into equation 81 yields:

$$\frac{\phi}{\theta} = (0.32) + (0.68) \frac{(0.85)(0.4)}{(0.23)} = 1.325 \quad (82)$$

or a wake fuel-air ratio of 0.066 at the inlet fuel-air ratio of 0.050.

As the overall fuel-air ratio increases, the wake fuel-air ratio continues to pace it at 32% greater value. At 0.070 overall fuel-air ratio, the wake is at 0.092. Due to the very rapid decrease in wake reaction capability as the fuel-air ratio exceeds stoichiometric, the overall system efficiency decreases as we go from 0.050 to 0.070 overall fuel-air ratio.

The data from Run 7.01 indicate peak efficiency at approximately a 0.052 f/a. A premixed system would produce a peak value at about 107% stoichiometric, or 0.0728 f/a. This ratio is 1.399 and is very close to the predicted wake enrichment ratio of 1.32. These results confirm the anticipated results of the predictions.

The influence of the fuel vaporization level on the efficiency was studied by two ways. A purely gaseous fuel case was run utilizing natural gas (98% CH₄) rather than the liquid JP-4, and a test was run with liquid fuel and the spraybar to flameholder separation increased from 8 to 40 in. This latter shift would increase the level of fuel droplet vaporization from 32 to 64% at the 400°F inlet condition. This shifts the enrichment ratio (equation 81) from 1.32 to 1.17. This test was Run 9.01 and the 400°F results are shown in Figure 55. For this case the pronounced peak at fuel-air ratios below stoichiometric is absent. The model predicts the peak efficiency fuel-air ratio to be 0.062.

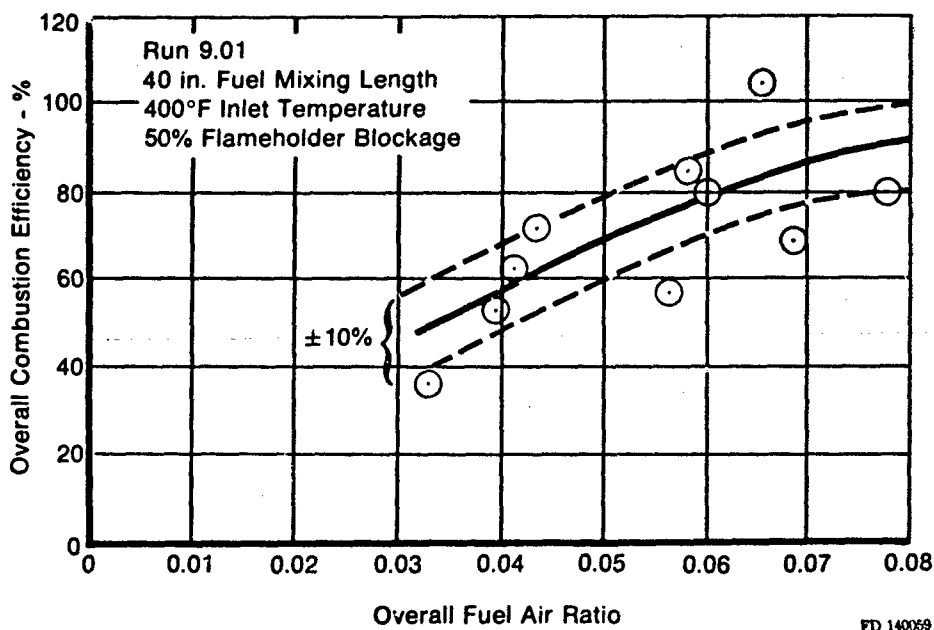


Figure 55. Overall Combustion Efficiency vs Fuel-Air Ratio

The longer mixing and vaporization length test produced larger data scatter and higher rumble amplitudes. It is felt that these results are due to the increased time delay between injection and stabilization. The longer time delay allows any gas velocity oscillations to produce greater oscillations in the droplet velocity through the drag terms. These liquid velocity oscillations generate fuel-air oscillations at the flameholder which are ultimately seen as efficiency oscillations, or rumble.

The largest problem which exists with the data as taken is the rather severe fuel distribution errors which were present. The location of the flameholders and the flow characteristics of the spraybars resulted in the center flameholder being run at a fuel-air ratio several times greater than the outer ones. This distribution requires that analyses over the overall efficiency data be done on a multiple streamtube basis.

The flameholders are shown in Figure 56 for the 52% blockage flameholder (1.8-in. wide). The open area distribution, from top to bottom, is 15.1, 11.6, 11.6, 15.1 sq in.. As a percentage this is 28, 22, 22, 28. For the three 1.8-in. wide flameholder gutters, assuming that the flow streamlines split between adjacent gutters on an equal basis, the effective blockages are 47.6, 65, 47.6. The airflow distributions assigned to the three gutters becomes 39, 22 and 39 of the total airflow.

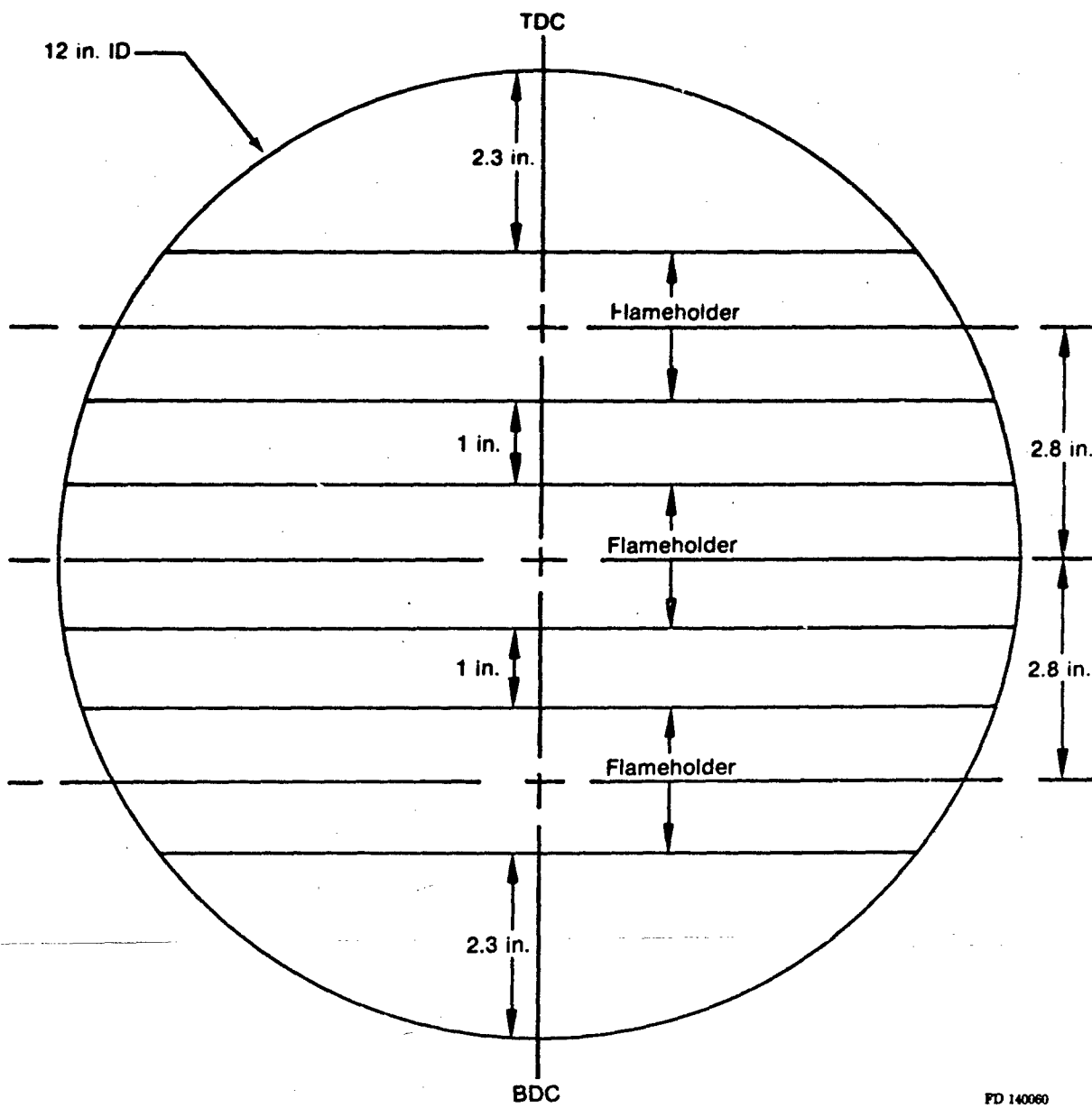
Concurrent with this, the fuel flowrate from the three spraybars was such that the centerline spraybar was producing about twice the fuel flow of either of the other two spraybars. For a fuel flowrate distribution of 25, 50, 25 and an overall fuel fuel-air ratio of 0.050, the local fuel-air ratios, top to bottom, become 0.032, 0.113 and 0.032. The central element is thus operating in a very rich mode. This wide distribution requires that analysis of the overall combustion efficiency must be performed as a multiple streamtube analysis.

Utilizing this approach, the 400°F inlet temperature data from Run 9.01 were analyzed. Figure 57 presents the results of this study. The predicted results are in good agreement with the test data with regard to the peak efficiency fuel-air ratio and the trend of efficiency versus f/a . The predicted values are lower than the test data, however. The major problem in making these predictions is the low value of the flame speeds at the fuel-air ratio extremes generated by the fuel-air distribution problem. As a result, the results are quite sensitive to the value of laminar flame speed.

This value is currently read from data similar to Figure 58. For a typical data point of Run 9.01, the fuel-air ratios are calculated to be:

<u>Zone</u>	<u>f/a</u>	<u>Equivalence Ratio</u>
Overall	0.060	0.882
Top F/H	0.037	0.544
Center F/H	0.140	2.059
Lower F/H	0.039	0.573

From Figure 58, the values of flame speed for the outer two zones are at the lower end of the available data, but the central zone value requires an educated guess. Since this one zone comprises 22% of the airflow in the test rig, the error produced by this one zone may swing the results by easily 10% η .



FD 140060

Figure 56. Flameholder Geometry

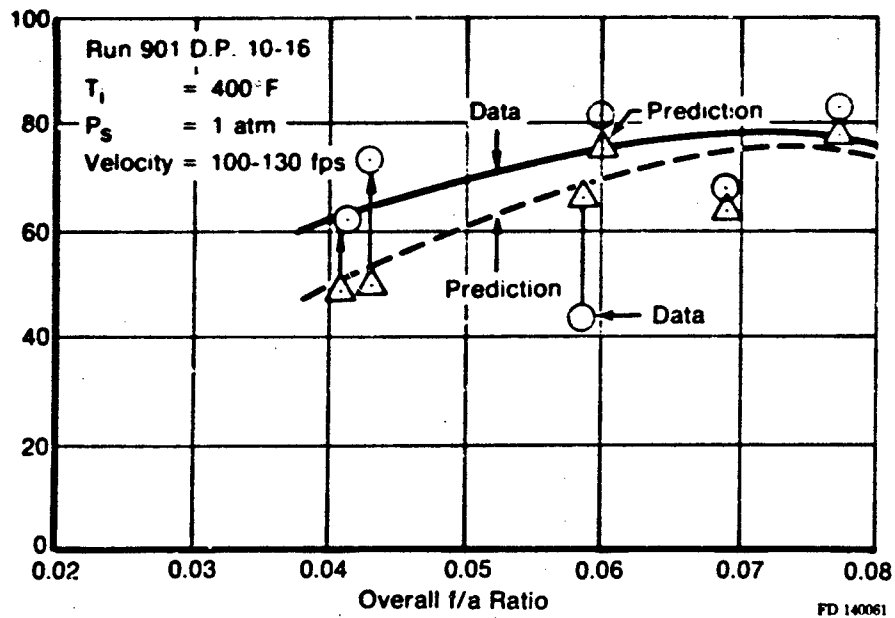


Figure 57. Combustion Efficiency Data vs Prediction

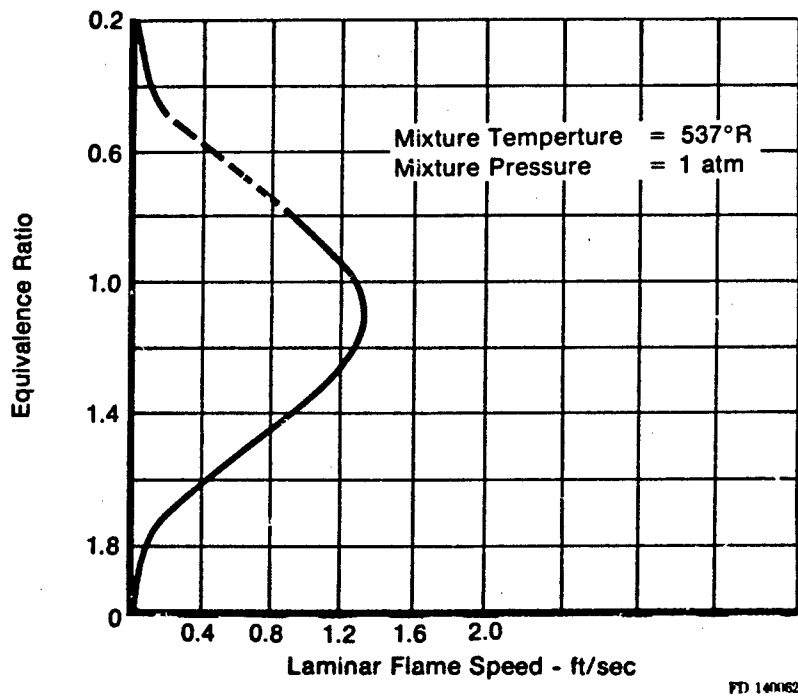


Figure 58. Laminar Flame Speed for Propene-Air

For some other data points the reverse situation is true, and the outer two zones have very lean values, and the local equivalence ratios are in the 0.3 to 0.4 range. Again, the flame speed values require estimates. For example:

<u>Zone</u>	<u>Local f/a</u>	<u>Equivalence Ratio</u>
Overall	0.041	0.602
Top F/H	0.025	0.367
Center F/H	0.105	1.544
Lower F/H	0.021	0.313

The results of Figure 57 were generated by a three streamtube analysis of the data, extending the flame speed curve down to 0.2 equivalence ratio and up to 2.0. A symmetric behavior of the flame speed versus fuel air ratio curve about a 1.1 equivalence ratio was used.

A similar result is shown in Figure 59 for the data from Run 7.01 at 400°F inlet and 120 to 140 fps approach velocity. The comments drawn are similar to those from Run 9.01.

This section has demonstrated the agreement between the major tenets of the model and the experimental results of the test program. Good quantitative agreement was observed for predicted and observed combustion efficiency data, including the capability to predict the results of fuel distribution changes. This latter effect is observed by the agreement between the results of Run 7.01 and the predictions.

b. Specific Results

The following sections will address the specific evaluations of geometric and aerothermodynamic variations which were performed during the test program. The effects of fuel distribution and overall fuel-air ratio have been discussed. As in the previous section, this report will be concerned with the effects on overall combustion efficiency. The analysis of the impact on rumble amplitudes is presented in the report on the Lo-Frequency Augmentor Instability Study, Contract F33615-76-C-2024.

(1) Heat Addition to the Wake

The wake reaction model predicts an increase in wake efficiency and a decrease in rumble gain factor if heat is artificially added to the wake. This is caused by an increase in the effective kinetic reaction rate. On the test rig this was provided by an oxyacetylene torch which was mounted to feed the wake of the central flameholder.

A problem arose during this test in that a limitation on the available torch flowrate prevented achieving the levels of heat addition which were desired. The torch heat rate of 0.8 Btu/sec to the wake is equivalent to a 15°F rise in effective inlet temperature or a 3% increase in reactor efficiency at a 400°F nominal inlet temperature. At this level of heat addition, the data scatter normal to efficiency measurements exceeds the level of anticipated improvements. However, several data points were run during the baseline tests with the 52% blockage and the 35% blockage flameholders where back-to-back effects were noted at zero and full torch flowrate. These results are shown in Table 4. Figure 60 shows the results over a fuel-air ratio excursion for 35% blockage (Run 11.02). In general, the torch resulted in a small but positive gain in efficiency.

This result is significant in that, although small, it is consistent and correct in direction and magnitude with the projected effect. Unfortunately, the direct impact on rumble amplitude could not be determined with this slight heat addition.

TABLE 4
EFFECT OF WAKE HEAT ADDITION ON EFFICIENCY

Run No.	Data Point	Inlet Temp (°F)	Mach No.	Fuel-Air Ratio	Torch On	Overall Efficiency
7.01	21	410	0.087	0.0851	Yes	0.618
7.01	22	408	0.088	0.0833	No	0.589
7.01	23	413	0.096	0.0829	No	0.577
7.01	29	396	0.132	0.0406	No	0.687
7.01	30	396	0.127	0.0422	Yes	0.752
11.02	40	394	0.059	0.057	No	1.040
11.02	41	402	0.058	0.058	Yes	1.000
11.02	42	408	0.060	0.096	Yes	1.000
11.02	43	410	0.059	0.097	No	1.100
11.02	44	402	0.090	0.036	No	0.888
11.02	45	405	0.090	0.037	Yes	0.898
11.02	48	410	0.090	0.075	No	0.807
11.02	49	411	0.089	0.076	Yes	0.840
11.02	57	397	0.100	0.038	No	0.811
11.02	58	398	0.098	0.038	Yes	0.839
11.02	59	398	0.101	0.050	Yes	0.790
11.02	60	398	0.103	0.049	No	0.771
11.02	61	400	0.101	0.061	No	0.709
11.02	62	401	0.101	0.062	Yes	0.709
11.02	63	398	0.102	0.079	Yes	0.736
11.02	64	398	0.103	0.079	No	0.721

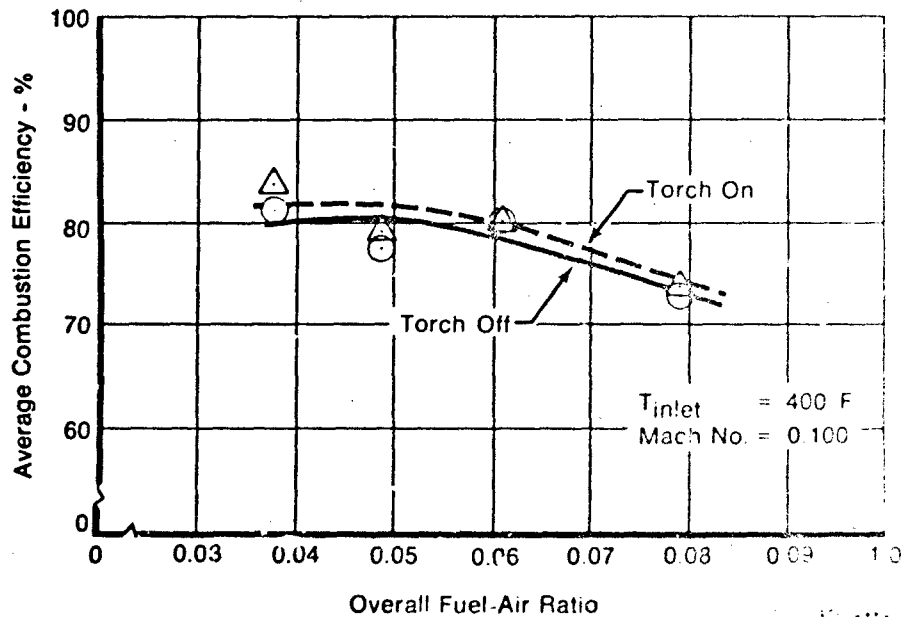


Figure 60. Effect of Heat Addition on Overall Combustion Efficiency Run 11.02, 35% Blockage Flameholder

(2) Effect of Available Combustion Length

The effect of the available axial length after the flameholders was examined by two runs. Run 9.01 had about 80 in. available for post-flameholder reaction and Run 10.01 reduced this to about 48 in. These tests were run with a 52% blockage flameholder and a 40-in. fuel mixing length at 200 and 400°F inlet temperatures. During this test sequence, the fuel was observed to be trapped by the volume of the ports to the observation windows, and flameholding occurred at that location as well as the normal flameholder.

Additionally, the shortened available combustion zone length produced severe sensitivity, and rumble or unsteady combustion was prevalent over the majority of the test sequence. As a result of these problems, no useful information could really be obtained with regard to efficiency.

The combustion model predicts that a shorter length results in a steeper axial temperature gradient near the nozzle inlet and lower overall efficiency. The steeper gradient should have resulted in an increased sensitivity of the average inlet temperature to pressure and velocity oscillations. The gross system behavior certainly agreed with this qualitative prediction.

(3) Effect of Inlet Conditions

The effects of inlet static pressure, temperature and approach velocity are shown in Figures 61 through 63. The effect of inlet temperature, Figure 61, is essentially in agreement with predictions. The degree of increase in efficiency is lower than was expected, partially due to the manner of the tests where a fixed level of inlet flow Mach number was set. The fixed Mach number resulted in a 14% increase in absolute velocity at a fixed Mach number between 200 and 400°F which reduces the gain due to the increased reaction rates at the elevated temperature. The remainder is unexplained at present.

Although the data is sparse for a fuel-air ratio effect, there did not appear to be any significant effects due to the 400 versus 200°F inlet temperature. Analysis of the variations in the droplet and collected film vaporization rates predicted only about a 10% shift in vaporization rate.

The inlet velocity effect, Figure 62, is also in the anticipated direction. The increase in velocity reduces the effective flameholder wake reaction efficiency and the effective flame spreading angle. These effects are modeled in this manner in the analysis, and the results appear to be of the correct magnitude.

The pressure effect, Figures 63 and 64, is interesting. Although the data are quite scattered, the general trend is a reduction of several percent in overall efficiency when the pressure is raised from 15 to 21 psia. This trend is reversed over several data points of Run 8.01 in Figure 64.

The predicted effect of pressure variation on the fan duct combustion process has offsetting parts. The vaporization potential at fixed liquid temperature is reduced as the static pressure is increased, but the convective heat flux increases which raises the liquid temperature. This increase in liquid temperature partially or completely offsets the increased pressure effect of reduced vaporization potential for these test data. The predicted effect is a slight increase in the overall efficiency. The data show a slight decrease, which may be scatter, but is not understood.

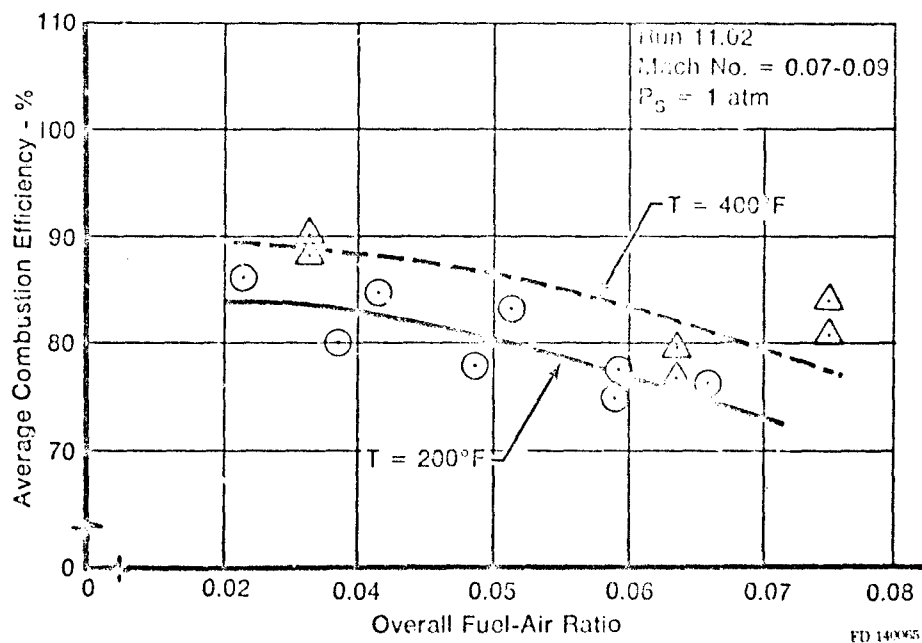


Figure 61. Effect of Inlet Temperature on Efficiency

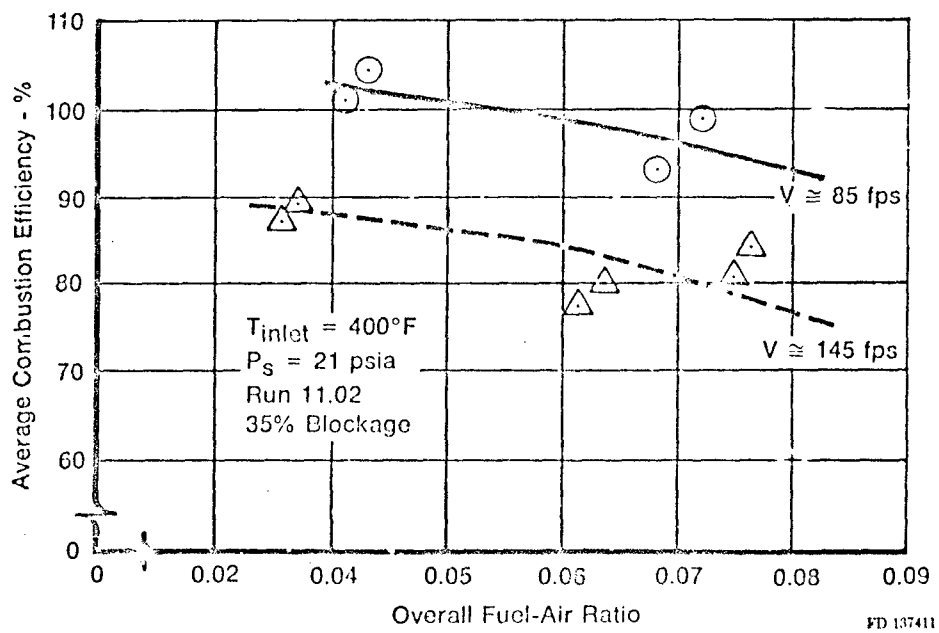


Figure 62. Effect of Velocity on Efficiency

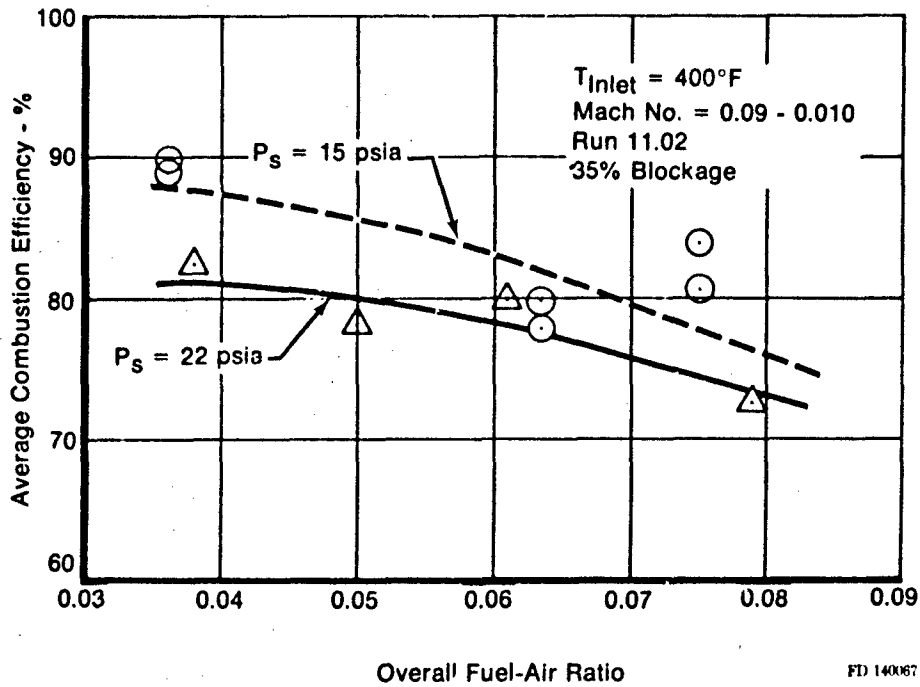


Figure 63. Effect of Inlet Static Pressure on Efficiency

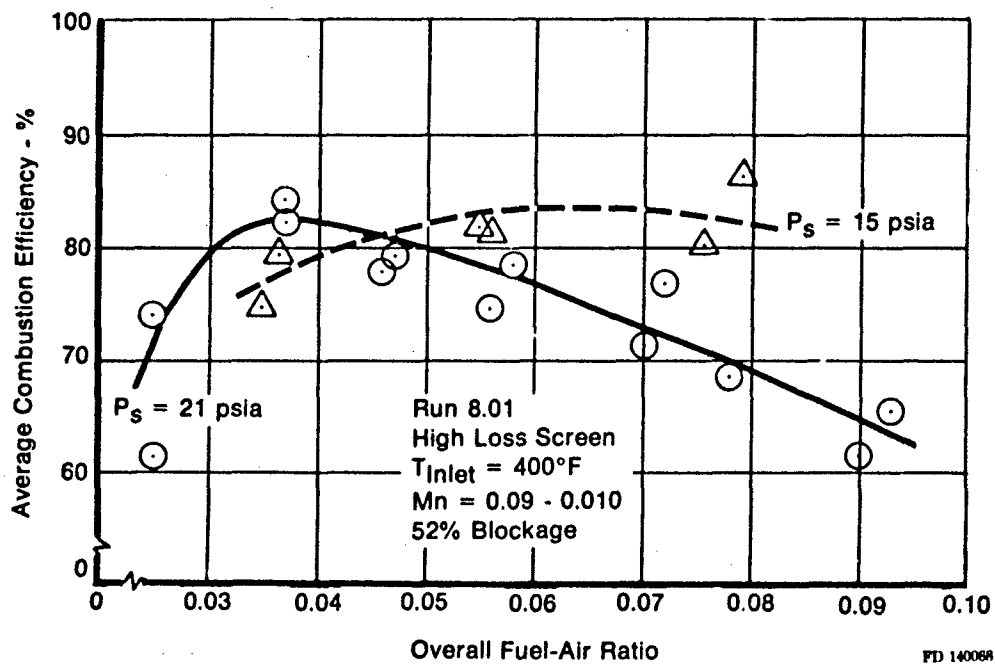


Figure 64. Effect of Static Pressure on Efficiency

(4) Effect of Flameholder Width and Blockage

The structure of the test apparatus did not allow an independent variation in flameholder width and blockage, i.e., there is a fixed total flow area and number of flameholders. This coupling of width and blockage produces offsetting effects. The increased width produces an increased wake volume but also increases the recirculation rate. The increased blockage ratio generates a higher turbulence level at the flameholder lip and, hence, increased flame speed, but also increases the flameholder lip velocity which reduces the transverse flame spreading rate.

The predicted overall efficiency as a function of width and blockage was shown in Figure 34. This showed a decrease in efficiency of about 10% for an increase from 37.5% blockage to 50%. The test data, Figure 65, shows about 10% reduction in η_c for 35% blockage to 52% blockage ratio. Although the amount measured is slightly lower than predicted, the agreement is felt to be excellent. This section of the model is felt to be in an accurate form.

(5) Effect of Flameholder Apex Angle

The geometric variation of flameholder apex angle was evaluated at the 35% blockage level. The standard apex angle design is 1.20-in. wide and 1.20-in. for a 53 deg apex angle. The increased angle design was 1.20-in. wide and 0.60-in. deep for a 90 deg included angle. This manner of altering the apex angle holds width and blockage constant but reduces the flameholder surface area by 38%. This change will thus alter the rate of surface vaporization. The increased apex angle also slightly increases the rate of fuel collection onto the surface and the rate of gaseous recirculation into the wake and the wake volume.

The test results are shown in Figure 66 for 400°F inlet temperature and 0.07 approach flow Mach number. The results are very interesting in that the 90 angle flameholder efficiencies do not exhibit the peak well below stoichiometric that was observed with the 53 angle design. Also, the overall levels of efficiency appear lower than with the smaller apex angle. Comparison of Run 11.02 and 12.01 at 22 psia static pressure shows that the peak efficiencies are very close although Run 11.02 was at a higher approach velocity and should have been lower.

Analysis of the effect of the reduced available surface area produces about 40% surface vaporization for the 53 deg angle and 25% for the 90 deg angle. The air recirculation constant, K_1 , increases from 23 to 25%, and the collection constant increases from 85 to 87%. The resultant effect on the wake fuel-air ratio, for 32% preflameholder vaporization becomes:

$$\frac{\phi}{\theta} = \beta_1 + (1-\beta_1) \frac{\beta_2 \beta_3}{K_1} \quad (83)$$

$$53 \text{ deg angle: } \frac{\phi}{\theta} = (0.32) + (0.68) \frac{(0.85)(0.4)}{(0.23)} = 1.325 \quad (84)$$

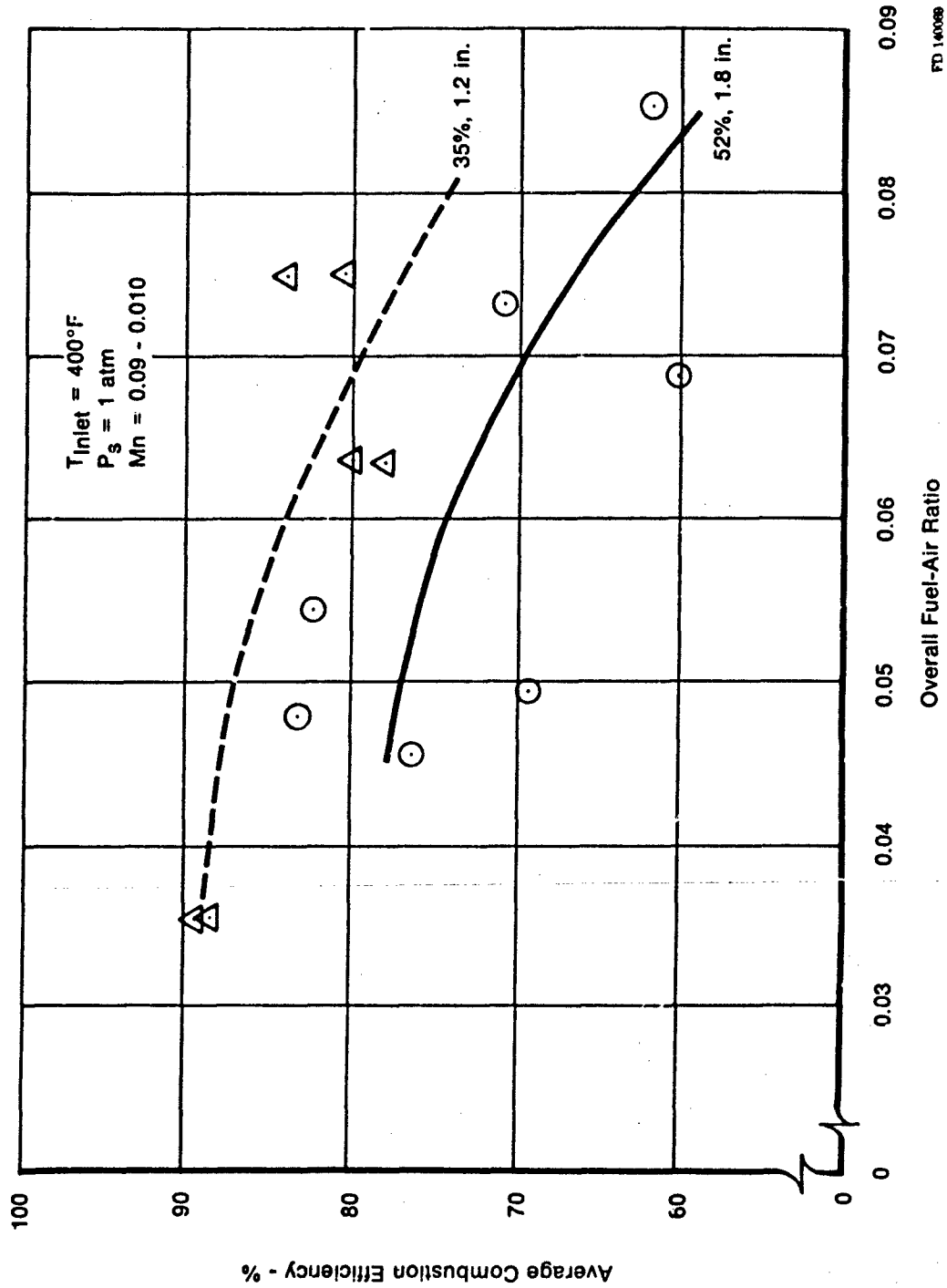
$$90 \text{ deg angle: } \frac{\phi}{\theta} = (0.32) + (0.68) \frac{(0.87)(0.25)}{(0.25)} = 0.912 \quad (85)$$

The predicted approach fuel-air ratios for peak wake reaction are thus:

$$53 \text{ deg angle: } f/a = 0.051$$

$$90 \text{ deg angle: } f/a = 0.076$$

In Figure 66 this shift was definitely observed.



FD 140089

Figure 65. Effect of Flameholder Width and Blockage Ratio on Combustion Efficiency

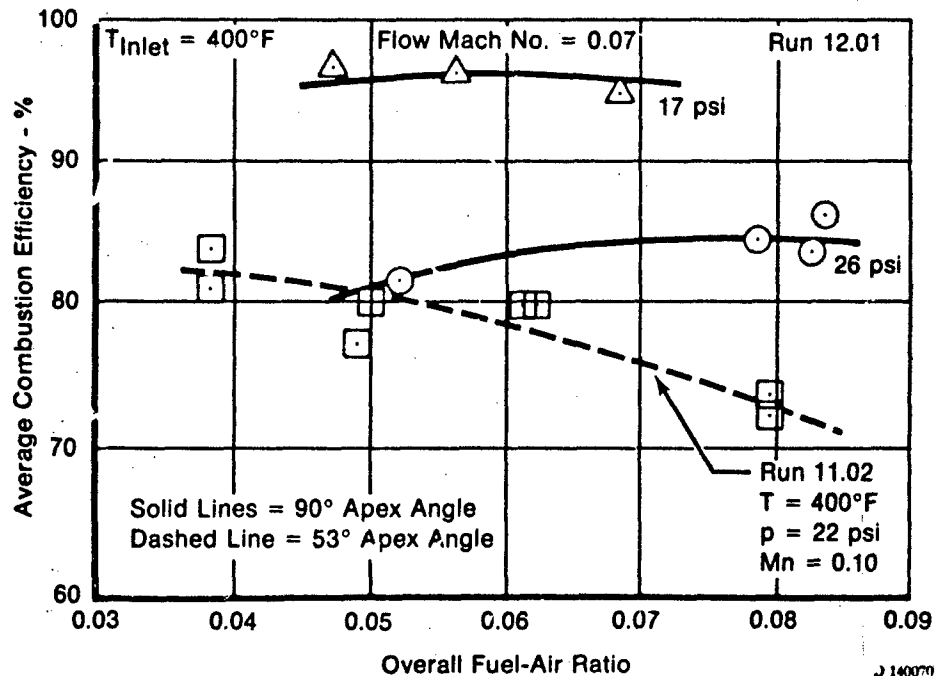


Figure 66. Effect of Apex Angle on Efficiency

The reduction in peak efficiency level is not in agreement with the predictions, which expected a small gain. This error is most likely due to the effect on the larger amount of nonvaporized fuel which leaves the flameholder.

The static pressure influence may be observed again: as in earlier comments.

(6) Effect of Free-Stream Turbulence Level

The impact of the turbulence level on the efficiency level was evaluated by the use of turbulence generating screens placed upstream of the fuel injector spraybars. This screen generated turbulence of a small scale suitable for interaction with the recirculation zone shear layers and the downstream flame propagation rate.

The increased turbulence level produces two basic results within the framework of the current model. The increased turbulence level produces a higher effective recirculation zone shear layer mass exchange rate. This increases the effective unit aerodynamic loading and should reduce the wake reaction efficiency. The turbulence also increases the effective turbulent flame propagation rate downstream of the flameholder.

The test results are shown in Figure 67 for 400°F inlet temperature and 20-22 psia static pressure. The increased turbulence level produced an apparent increase of 7 to 10% in overall efficiency. Apparently, the effect of increased flame spreading rate is dominant over the wake efficiency reduction in controlling overall efficiency.

Earlier analysis of the impact of free-stream turbulence was presented in the model development section. The trends are in general agreement with the test results. For example, in Figure 35, an increase of 20% in turbulence i.e., 4 to 4.8%, resulted in an increase in efficiency from 70 to 76%. The test data at 0.055 overall fuel-air resulted in an efficiency increase from 70 to 78%. These cases were selected to yield the same base efficiency, and only the differences are meaningful.

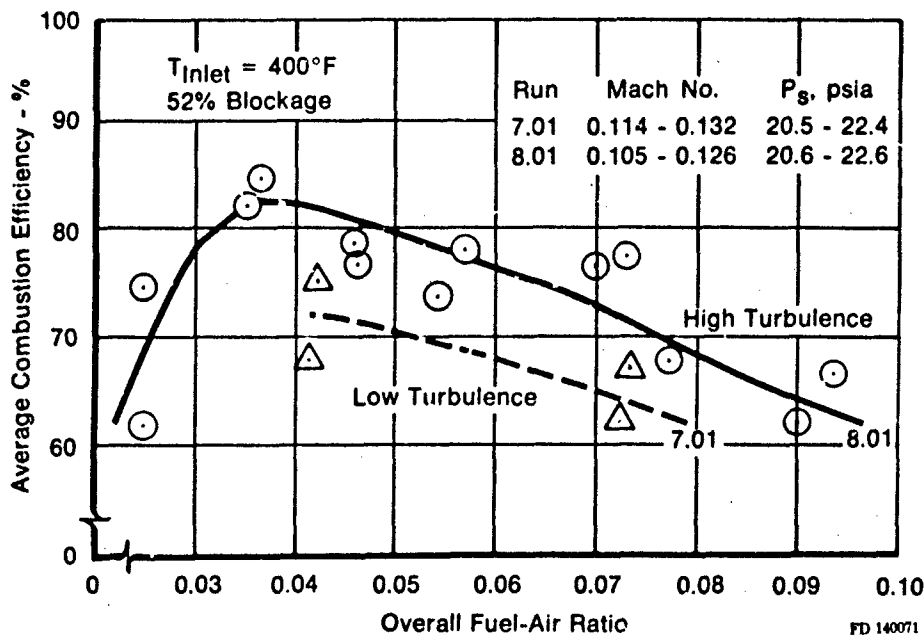


Figure 67. Effect of Turbulence Level on Efficiency

The analysis assumed that no decrease in wake efficiency occurred. In reality the wake decreases due to the higher mass recirculation rate which should result in a lower efficiency increase. However, the screens also produced a turbulence increase greater than the 20% relative increase used in this analysis. Thus, the match between data and predictions is quite good.

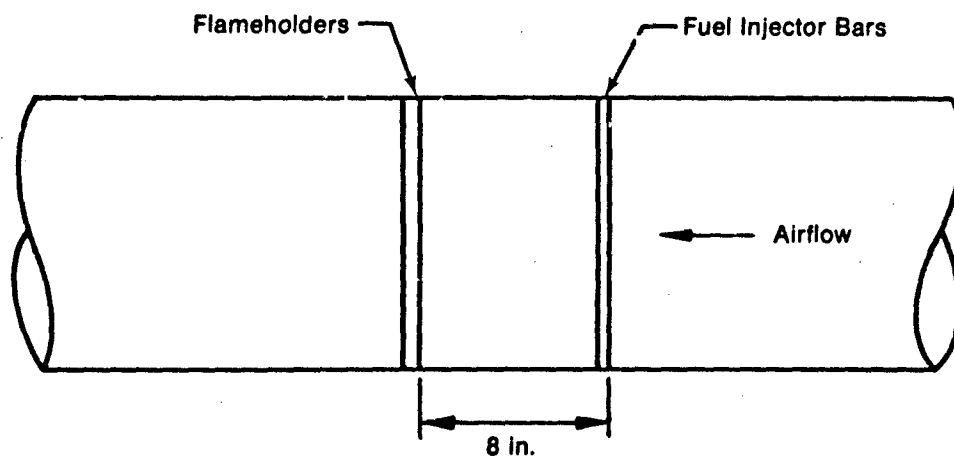
(7) Effect of Inclined (Drafted) Flameholders

The effect of inclined flameholders was evaluated on Run 13.01 with 12-in. wide gutters which were angled aft at a 22½ deg angle relative to the spraybars. Due to the construction of the test apparatus, the three flameholders were not parallel but rather staggered, since the attachment port for the central flameholder was on one side of the duct while the upper and lower flameholder ports were on the opposite side. The stagger is shown in Figure 68.

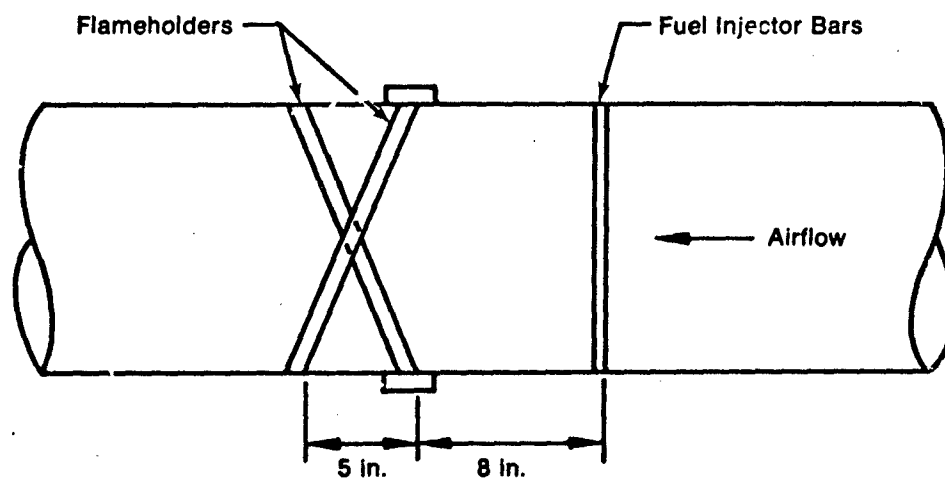
The flameholder array had a projected blockage of 35% and 1.2-in. gutter width. The swept ends were displaced 5 in. downstream resulting in 13-in. maximum fuel preparation distance.

Several theories have been advanced for why drafted gutters should or should not improve performance. Two major theories are:

1. Sweeping the tips of the flameholder gutters downstream, without moving the fuel injector spraybars, increased the physical separation distance between injection and the flameholder. This will result in a higher level of fuel vaporization and, thus, less dependence on the surface vaporization. Based on the analysis of the controlling processes, reduced surface vaporization should reduce the wake fuel-air ratio and extend the rich limit. For the change in distance as tested here, the difference is small.
2. The drafting causes reduced aerodynamic blockage which generates reduced turbulence and reduced wake aerodynamic loading. The previous test results for reduced geometric blockage showed this to result in increased combustion efficiency.



Top View - Normal Location



Top View - Inclined Location

FD 140072

Figure 68. Inclined Flameholders vs Normal Location

The test results, Figure 69, show a gain of 5 to 6% in overall combustion efficiency. However, the comparison data from Run 11.62, also 35% blockage, are at a slightly higher approach velocity which should reduce its efficiency slightly. From these data the conclusion is that drafting, by itself, has little effect on efficiency.

A three point test was run at $T = 400^{\circ}\text{F}$ and 15 psia to evaluate the efficiency fall-off with approach velocity. The test results are shown in Figure 70. The severe fall in efficiency with velocity is as the analysis predicts. The equivalent data from the undrafted gutters are shown for comparison. No discernible effect is noted which suggests that the wake efficiency versus flame speed trade is equal. Unfortunately, a velocity blowout limit was not run to isolate the influences.

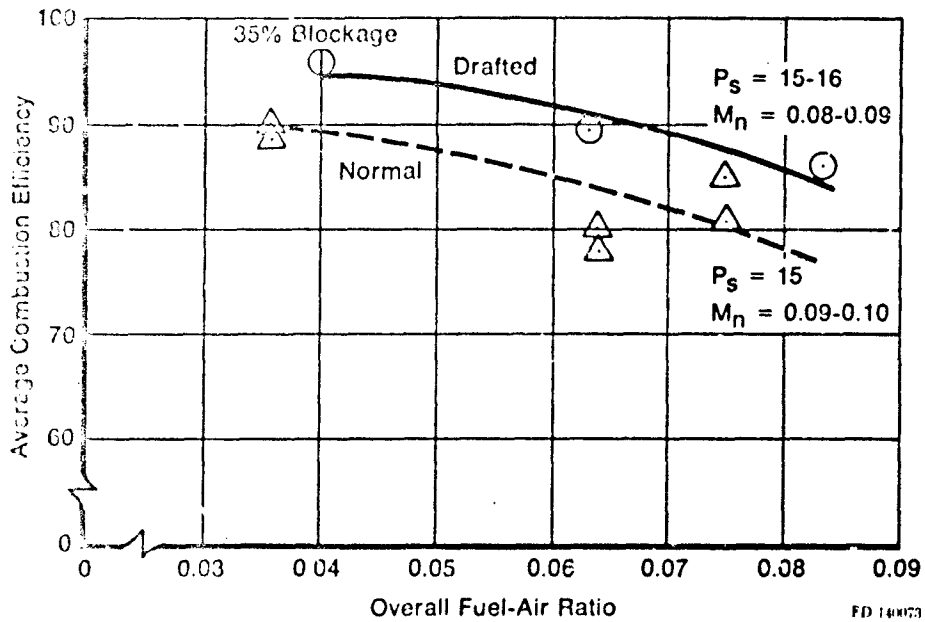


Figure 69 Drafted Flameholders Efficiency

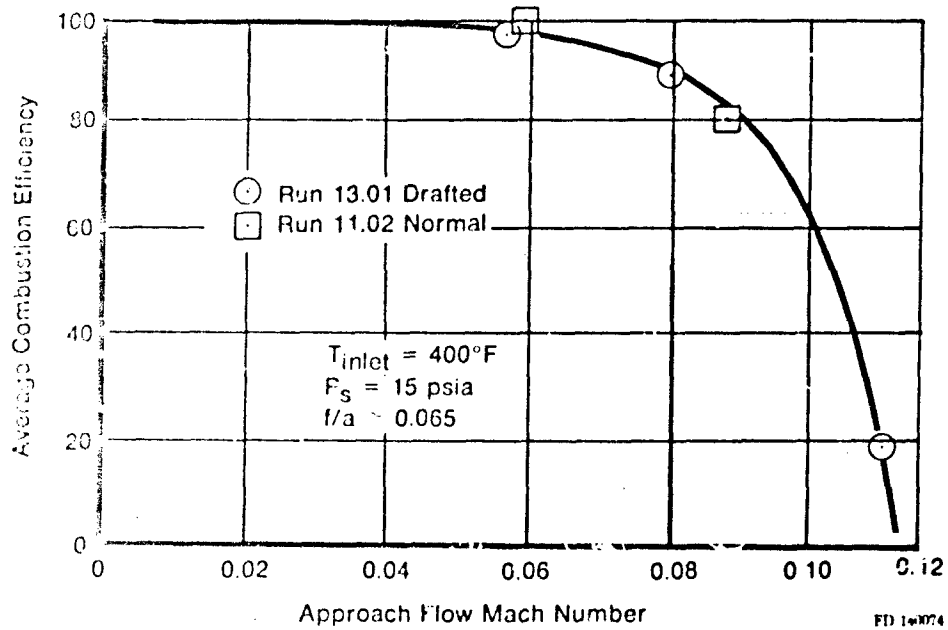


Figure 70. Effect of Approach Mach Number on Drafted Flameholder Efficiency

c. Conclusions

The agreement with the experimental results which the two-phase fuel combustion model has generated is very encouraging. The major conclusions from the experimental program are as follows:

- The major thesis of the two-phase fuel model has been verified.
- External piloting is required to maintain combustion at flow Mach numbers beyond 0.12 at 200 to 400°F with liquid JP fuels. The turbofan engine does this by transferring core engine hot gases to the wake of the fan stream gutters.
- Fuel vaporization processes have a major impact on the combustion process.
- Rumble is not uniquely tied to the flameholder near-wake but is influenced by it insofar as the near-wake influences the flame spreading rate.
- Rumble tendencies follow the classic lines of combustion instability behavior. That is, any change which reduces the velocity or pressure sensitivity of the combustion process or increases the system damping factor will reduce the instability.
- The largest rumble producing influence which is not predicted by the combustion portion of the model is the separation distance effect of flameholder to fuel injector. This influence is a result of the dynamics of liquid fuel oscillations versus air oscillations and the time delay between injection and stabilization.
- The multistreamtube approach to modeling fuel distribution effects produces reasonable results. The analysis of the test rig based on three streamtubes agreed fairly well.

d. Experimental Mechanisms

The specific conclusions regarding rumble drivers are:

- Rumble is an oscillation in the overall heat release rate of the augmentor produced by variations in the flame propagation rate.
- The downstream flame propagation rate is dependent on the flameholder wake reaction efficiency. Changes which alter this efficiency produce alterations in overall heat release rate, and sensitivity of the process to velocity or pressure oscillations.
- A fuel-air ratio distribution other than uniform is destabilizing.
- Any change which reduces the flame spreading rate is generally destabilizing:

- Increased velocity
- Reduced temperature
- Reduced wake size (residence time)
- Rich wake fuel-air ratio.

- The following postulated mechanisms were rejected:

- Fuel injector flowrate oscillations
- Wake vortex shedding
- Fuel-air ratio oscillations.

4. PHASE II — MODEL EVALUATION

a. Task I — Comparison of Model

The efforts under this task were essentially grouped into two categories:

- Computerization of Model
- Comparison with other Models and Data.

The two tasks were performed simultaneously as the computer analysis was refined and predictions compared with available data.

(1) Computerization of the Model

The analyses performed during Phase I were assembled into a cohesive computer program which is capable of analyzing either the core or fan duct stream of a conventional mixed-flow turbofan augmentor. The program requires as input, a description of the geometry of the augmentor stream and a description of the physical operating conditions to be analyzed.

The operational logic is such that each case run represents a single geometry and operating point. The program will generate a curve of the axial average combustion efficiency and final augmentor section performance.

The program operational logic is shown in Figure 71, and the subroutines are defined in Table 5.

In addition to the augmentor duct axial efficiency curve, the program evaluates the wake conditions for fan stream flameholders. Based on the technical development previously discussed, the duct flameholder wake composition is defined as:

$$\frac{\phi}{\theta} = \beta_1 + (1 - \beta_1) \cdot \frac{\beta_2 \beta_3}{K_1} \quad (86)$$

The computer code evaluates these coefficients as well as the degree of wake reaction efficiency, η_w , at the wake fuel-oil ratio, ϕ , and the wake aerodynamic loading, A/V_{∞}^2 .

The solution procedure for the droplet vaporization and collection onto the flameholder proceeds directly. The recirculation rate solution is also accomplished easily. A problem arose with the solution for the surface vaporization rate, β_2 , and the wake reaction efficiency, η_w . The problem was due to the interdependent nature of β_2 and η_w . The vaporization depends strongly on the wake temperature which is a function of the wake fuel-air ratio and aerodynamic loading. Since the wake fuel-air ratio is a function of β_2 , a direct explicit solution is not possible.

Attempts to write an explicit algorithm for the solution did not produce the desired results. This failure was primarily due to the nature of the wake kinetics equations which are also implicit functions of the aerodynamic loading in terms of wake efficiency and fuel-air ratio, e.g.

$$\frac{A}{V_{\infty}^2} = \text{fcn}(\phi, \eta_w) \quad (87)$$

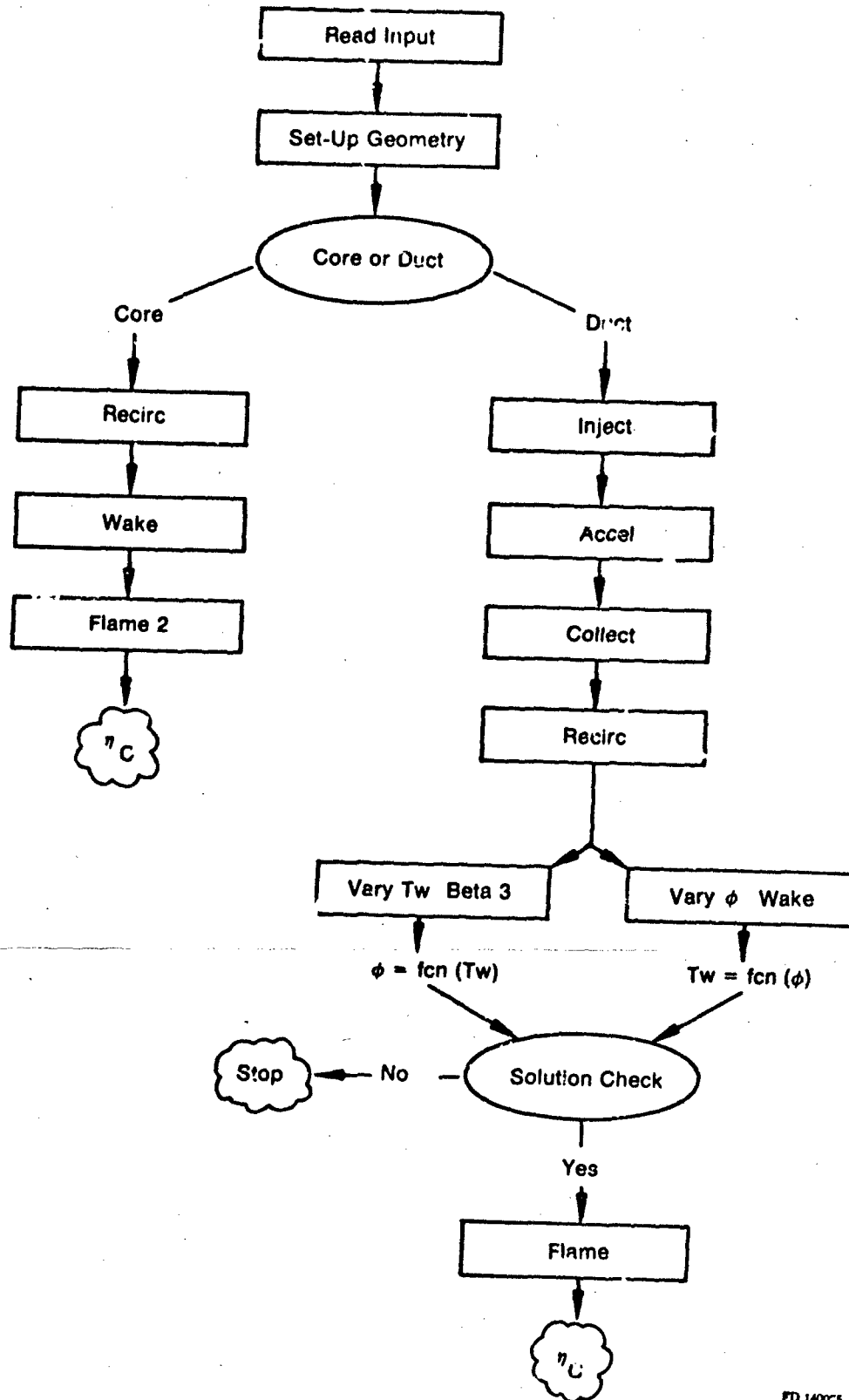


Figure 71. Basic Computer Program Logic Diagram

FD 14005

TABLE 5
PROGRAM SUBROUTINE DESCRIPTION

Subroutine	Major Operations
Inject	Sets up droplet size groups Injection vaporization level
Accel	Droplet vaporization and acceleration from spraying to flameholder
Collect	Droplet collection onto flameholder surface
Recirc	Wake recirculation rate and aerodynamic load- ing
Beta 3	Liquid vaporization rate from surface film
Wake	Wake kinetics solution
Flame	Two-phase fuel flame speed
Flame 2	Gaseous flame speed

The resultant equation set which must be solved is thus:

$$\phi = \theta\beta_1 + \theta(1-\beta_1) \frac{\beta_2\beta_3}{K_1} \quad (88)$$

$$\beta_3 = \text{fcn}(T_w, \beta_2, \theta) \quad (89)$$

$$T_w = T_a + \eta_w \Delta T_{\text{ideal}} \quad (90)$$

$$\Delta T_{\text{ideal}} = \text{fcn}(T_a, \phi) \quad (91)$$

$$\eta_w = \text{fcn}(T_a, \phi, A/V_{op}^2) \quad (92)$$

Where the η_w function has the form shown earlier in equation 87.

The known quantities are $\theta, \beta_1, \beta_2, K_1, T_a, A/V_{op}^2$, and the ΔT_{ideal} function. The solution should yield T_w, ϕ, η_w . The required flexibility of the analysis should also be able to recognize the possibility that a solution does not exist. For example, over the range of wake fuel-air ratios, a maximum value of kinetic capability exists. The analysis must recognize an input set which produces an aerodynamic loading in excess of this value as an augmentor blowout.

Another failure might occur when the compositional solution (Equation 88) does not yield a wake fuel-air ratio which is possible from the kinetics solution (Equation 87). Typically, this occurs as a rich blowout. Both of these failures are a direct consequence of the input values. The program is written to analyze a situation which exceeds the physical limits for that particular geometry and flow field.

(2) Computer Program Description

The computer code is currently set to analyze a conventional turbofan augmentor with vee-gutter flameholders. The generalized geometry which is analyzed is shown in Figure 73. The liquid fuel is injected through a spraybar located a specified distance upstream of the flameholder. The combustion process is stabilized by the bluff body recirculation zone, and a turbulent flame sheet propagates into the approach fuel-air mixture. The geometry is two-dimensional and would represent one streamtube of a multiple stream augmentor system.

The various analyses which were developed previously and referenced in the following paragraphs are written as subroutines in the computer program. This results in a modular program with a supervisory MAIN executing subroutines as required. This approach allows easy modification of the various analyses without disturbing the overall program operational logic.

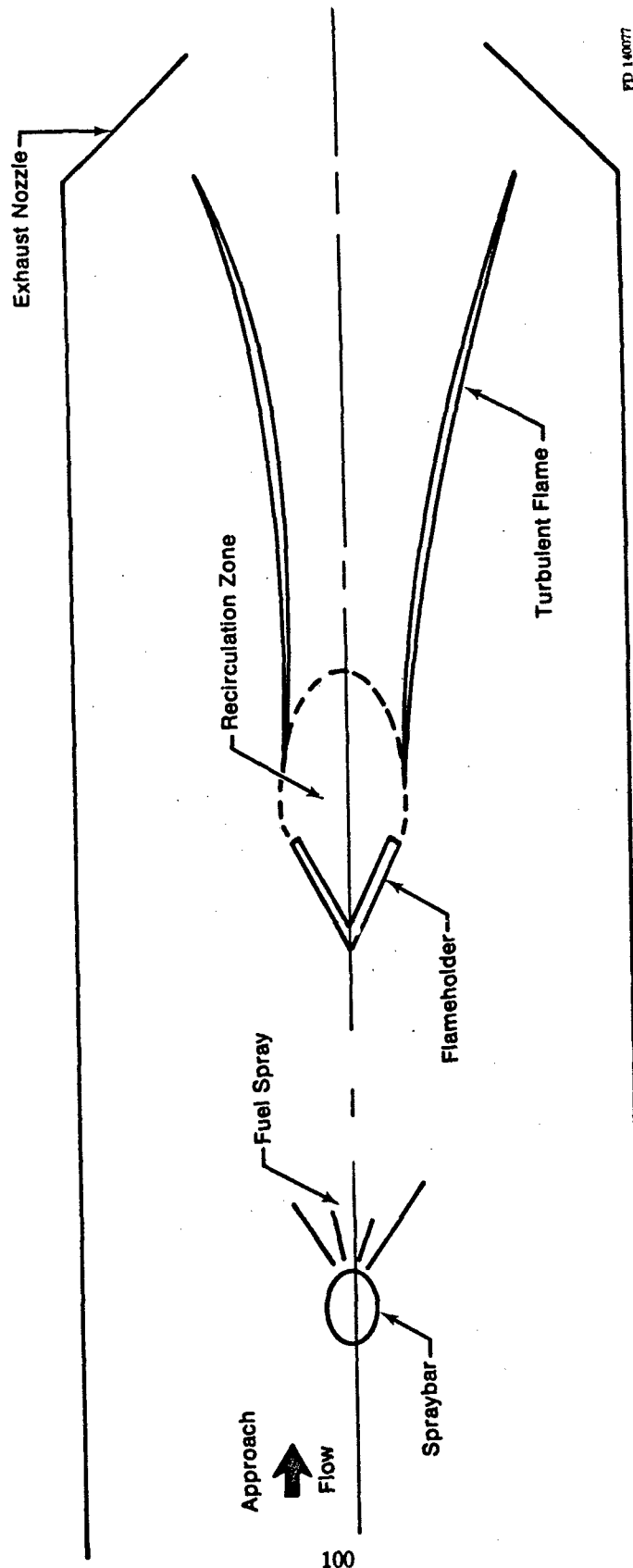
The program first reads the input in NAMELIST format. From the input the two-dimensional model format is set up. Total air and fuel flowrates are calculated and the core stream or duct stream option is exercised. The following description details the duct stream analysis procedure.

From the fuel conditions in the spraybar and the flow field conditions in the duct, the degree of flash vaporization which occurs during injection is calculated. This percentage of fuel is allocated to the initial vapor phase.

The fuel which remains liquid is assigned to five equal mass flowrate groups. These groups are each assigned a mean droplet diameter. The droplet diameters generated by the program represent the spray formation characteristics of a variable area pintle spraybar. The controlling size parameter is the fuel injection pressure drop. These data are empirical from Pratt & Whitney Aircraft data. These five groups thus represent the flowrate versus size distribution unique to this spraybar type. If a different type of injector is to be analyzed, the droplet sizing subroutine must be rewritten.

The program then performs a finite difference solution to the droplet acceleration and vaporization equations by selecting a small time step and solving for the deltas of liquid velocity, temperature and a delta vaporized from the drag and vaporization/heating equations. The axial travel of the liquid droplet during this time increment is calculated from the initial and final liquid velocities. The analysis continues this small time step solution until the axial distance value equals the spraybar to flameholder separation distance. The acceleration/vaporization model assumes that the isolated droplet vaporization rate exceeds the rate in spray clouds by a factor of two. The calculation sums the amount of fuel which vaporizes from all the droplet size groups and adds this to the amount of fuel vaporized during injection. The sum of these represents the total term in the wake compositional equation.

The analysis next calculates the percentage of each of these size groups which is collected by impingement onto the flameholder surface. The collection rate is calculated for each size group individually utilizing the droplet diameter which exists for each group after the vaporization calculations. The total collected liquid flowrate is summed from the collection efficiency for each group and the liquid flowrate which exists in each group after the vaporization calculations. The collection rate calculation for each droplet size group is evaluated from droplet trajectory analyses which were performed and correlated against the geometric variables of the flameholder system. The details of this were presented in the earlier Phase I results.



FD 140077

Figure 73. Combustion Model Generalized Geometry

The wake recirculation rate is next evaluated, again following the earlier reported analyses. The influence curves were reduced to a series of equations or curve reading routines within the RECIRC subroutine. This subroutine evaluates the aerodynamic loading of the idealized recirculation zone based on the empirical data earlier presented. The recirculation coefficient, K_1 , is calculated, and the loading is stored for transfer to the wake kinetics subroutine.

At this point the solution proceeds along the parallel paths of exercising the flameholder surface vaporization subroutine, BETA 3, and the wake kinetics subroutine.

For the solution of BETA 3, values of wake temperature are assumed for every 200°F increment from 1000 to 5000°F. For each of these values, the heat flux from the recirculation zone through the flameholder into the liquid film is calculated. The surface vaporization is calculated utilizing a 20-step finite difference solution to the forced convection vaporization problem. The solution technique is the same as presented earlier. A 20-step solution was found necessary for convergence of numerical accuracy and to assure a smooth evaluation as the vaporization rate passes through to 100%. A check is made in the calculation for the ratio of heat flux to the liquid latent heat at collection conditions. Whenever the ratio exceeds unity, the vaporization is set at 100%.

For each value of wake temperature, the calculated vaporization rate is used in conjunction with the previous compositional coefficients to define a wake vapor phase fuel-air ratio. This temperature versus fuel-air ratio array is stored for later use.

The program transfers next to the WAKE subroutine for the kinetics solution utilizing the recirculation rate from RECIRC and the Longwell reactor model presented earlier. The subroutine is exercised over a range of fuel-air ratios. The fuel-air ratios are started at 0.020 and increased by 0.0045. The solution is stored in an array of efficiency and wake temperature versus wake fuel-air ratio between the lean and rich limits.

These limits are evaluated at the level of aerodynamic loading for the case being analyzed. The lean limit is the first fuel-air ratio where a kinetic solution is found. The rich limit is found by a fine grid search backwards from the first fuel-air ratio which fails to produce a solution on the rich side. The increased accuracy of definition of the rich limit was found necessary since the rich blowout is the significant failure mode of duct flameholders.

Once this array is generated, the program searches for array intersection between the BETA 3 and WAKE results. If none is found, appropriate failure messages are printed and execution stops. If intersection is found, the convergent results of the wake compositional solution are printed.

The next subroutine, FLAME, performs the finite difference solution to the two-dimensional flame propagation problem presented earlier. The flame speed base value is altered by the level of wake reaction efficiency and by the percentage of liquid fuel which is sloughed from the flameholder trailing edge. This influence accounts for two real effects in the augmentor transferred to the pseudo-two-dimensional analysis. The wake efficiency is assumed uniform and continuous as is the flame sheet. In reality, as the efficiency decreases, local regions are generated where flame initiation in the shear layer fails. Decreasing the transverse speed of the idealized flame sheet is a method of describing this effect to account for the requirement of flame propagation normal to the duct into these unignited regions.

Similarly, the sloughed fuel serves to quench local regions of ignition in the shear layers which also require more normal flame penetration. The inclusion of a vaporization/sloughing term accounts for this in a two-dimensional analysis.

Once the flame is initiated, the subroutine performs a finite difference solution to the transverse propagation into the free-stream allowing for the axial variations in velocity, turbulence, etc. This continues until the exhaust nozzle is reached.

For the analysis of a core stream segment the procedure is simplified greatly due to the complete fuel vaporization. The program sets the wake fuel-air ratio equal to the total fuel-air ratio and performs the wake kinetics solution at this value and the calculated value of recirculation. A gaseous phase turbulent flame is initiated, corrected by wake efficiency, and evaluated downstream as before.

(3) Model Comparison With Other Models and Data

The model for the stabilization of two-phase fuel at low inlet temperatures did not employ analog data. This model was evaluated against the available literature references. The analysis of the high inlet temperature core stream stabilization and propagation model was performed by comparison with the currently used turbojet augmentor efficiency correlations as well as the available body of gaseous fuel stabilization literature.

The two-phase stabilization model is based on the pioneering research efforts of Marion in 1952 (Reference 31). In his studies, Marion generated the basic concept of flame stabilization under conditions of flameholder surface vaporization. The testing and analysis were performed for low volatility fuels (primarily diesel fuel) but the qualitative behavior of the situation is comparable.

The major consequence of reduced vapor pressure fuels on the process of surface vaporization is in the location of the equilibrium solution to the wake vapor-phase fuel-air ratio. For the reduced volatility diesel fuel employed in Marion's studies two compositional intersections were calculated. One on the lean side was rejected as a solution due to its lack of stability. The solution on the rich side was stable, however. The solutions for the more volatile JP fuels produce a single intersection of wake formative and reaction. This solution lies on vaporization coefficient less than 1.0. The value may be on the lean side, if the surface vaporization is 100%, and still be stable.

Figure 72 is a typical compositional result generated by Marion. Figure 74 is a similar result from the model generated here. The variation in the intersection behavior is the result of the variations in surface vaporization rates for given wake heat transfer caused by fuel volatility differences.

Another study on wake flame stabilization with liquid fuels was performed by R. M. Gross (References 32 and 33). In this study the liquid fuel was injected on the upstream side of a semi-porous cylindrical flameholder. Two interesting results from this study confirm critical sections of the analysis.

First, Gross' experimental program confirmed the behavior of the surface vaporization phenomenon as predicted by this study. The experimental efforts employed wake compositional sampling at various flowrates of the surface liquid film. The observed wake behavior, Figures 75 and 76, show a plateau in composition. This was observed to coincide with the onset of liquid sloughing from the surface as the fuel flowrate was increased. Essentially, this implies that the vaporization rate maximum value is controlled by the available heat flux from the wake. Any excess fuel is merely lost. This effect is not linear due to the heat transferred to the sensible heat of the lost liquid. In fact, the data may be read as exhibiting a slight recurvature.

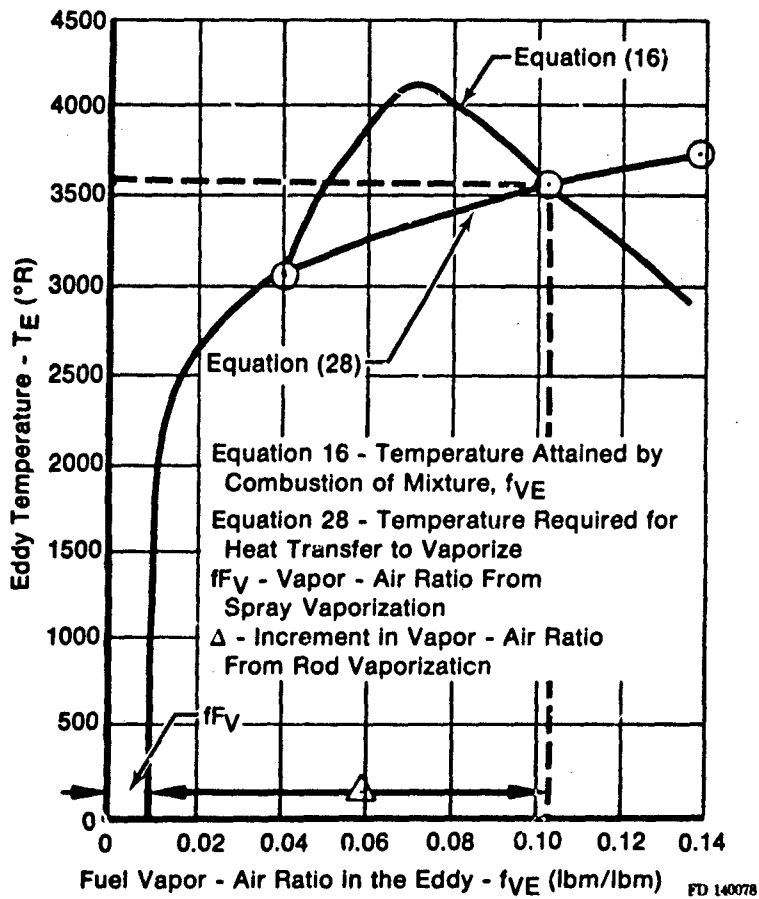


Figure 74. Flame Stability Criteria

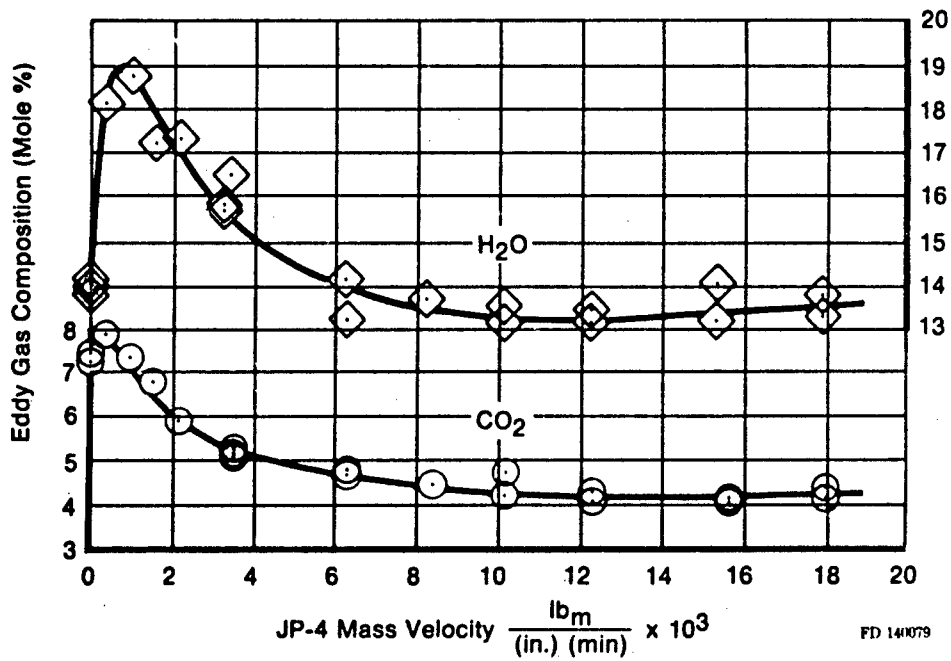


Figure 75. The Effect of the JP-4 Mass Velocity on the Eddy Gas Composition for the Natural Gas ($\theta = 0.620$) — JP-4 Flame: H₂O and CO₂ Concentration Profiles

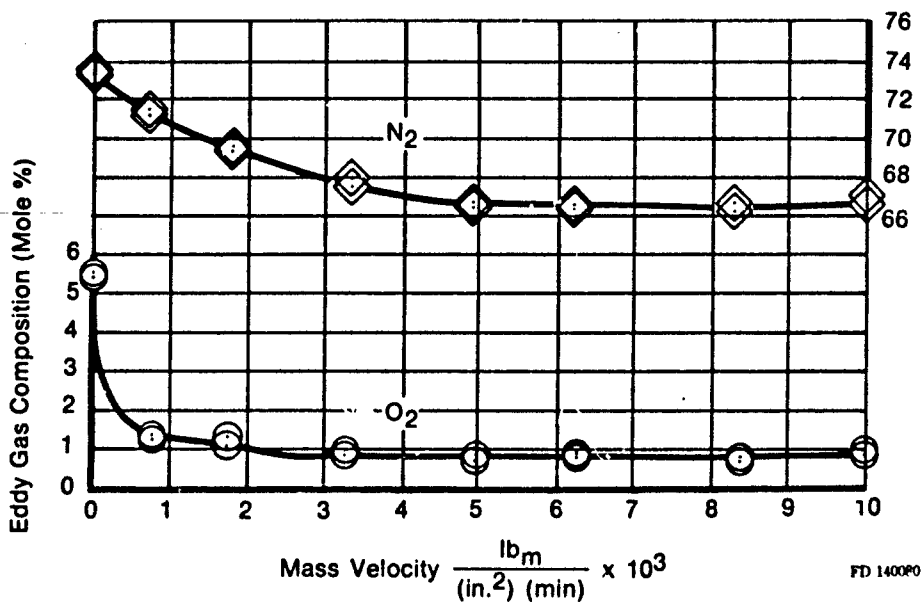


Figure 76. The Effect of the Kerosene Mass Velocity on the Eddy Gas Composition for the Natural Gas ($\theta = 0.620$) — Kerosene Flame: N₂ and O₂

The effect, as predicted by the rumble combustion model, was shown in Figure 19 as the effect of fuel collection rate on the surface vaporization rate. The decrease in percentage as the total fuel flowrate is increased will yield the same behavior as seen by Gross. The quantitative shift is due to the lower air velocities used by Gross which result in lower mass effect rates due to the reduced mass transfer Nusselt number.

The second major point of the model, which was confirmed by Gross' test results, is the influence of the approach air velocity on the wake composition (Figure 77). There is little or no influence at low velocities but a very rapid increase in unreacted composition as the blowout limit is reached. The sharp oxygen concentration increase is primarily due to the rapid fall-off in reaction kinetic efficiency. The comparison results (Figure 78) show a sharp decrease in CO₂ at the same time. The CO concentration shows an increase at first, due to the failure of the relatively slow CO oxidation reaction and a fall-off near blowout due to the failure of the CO formation kinetics. This data tends to confirm the kinetic model of the wake as the controlling parameter as did Longwell's original analysis (Reference 13) used in this model.

The augmentor model was exercised against development experience on a mixed flow turbofan engine. Predictions were made for the fan duct and core stream efficiencies as a function of altitude at a fixed subsonic flight Mach number. The influence of heat addition to the wakes of the fan duct flameholders was also predicted, since this was studied on the engine and produced significant gains in the rumble onset altitude.

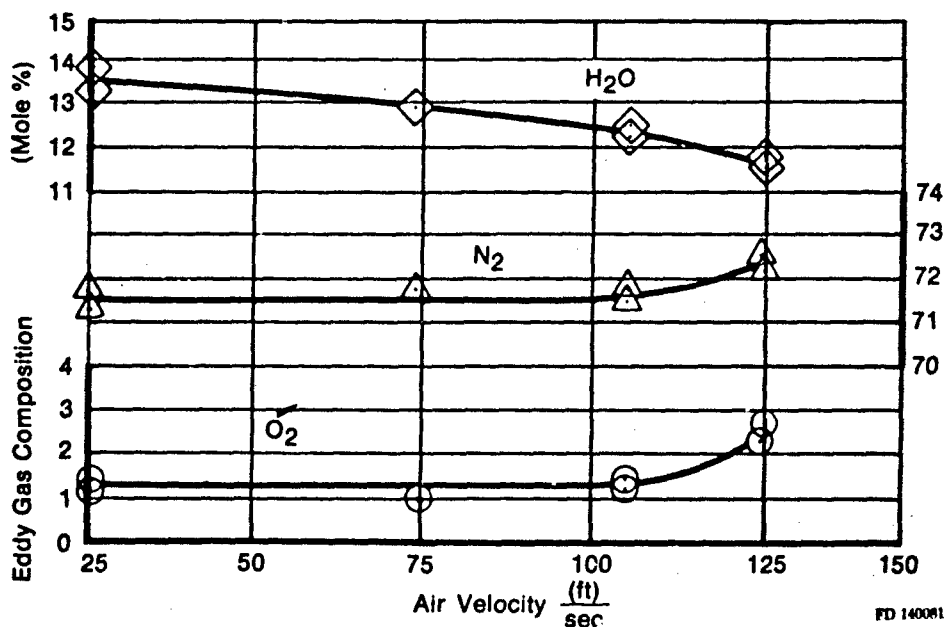
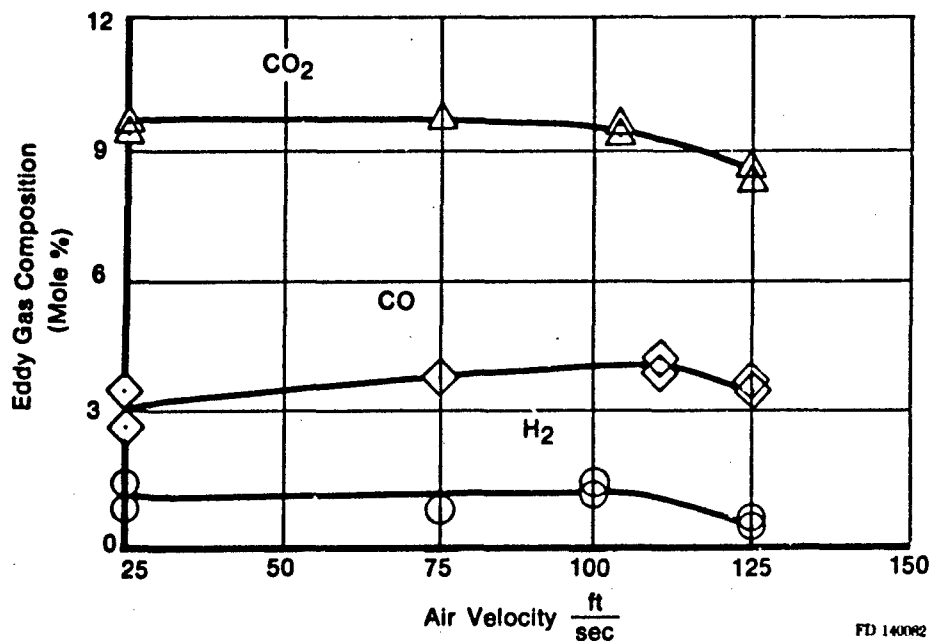


Figure 77. The Effect of the Entrance Air Velocity on the Eddy Gas Composition for the 18×10^{-3} lbm/(in.)² (min.) JP-4 Wake Flame: H₂O, N₂, and O₂ Concentration Profiles



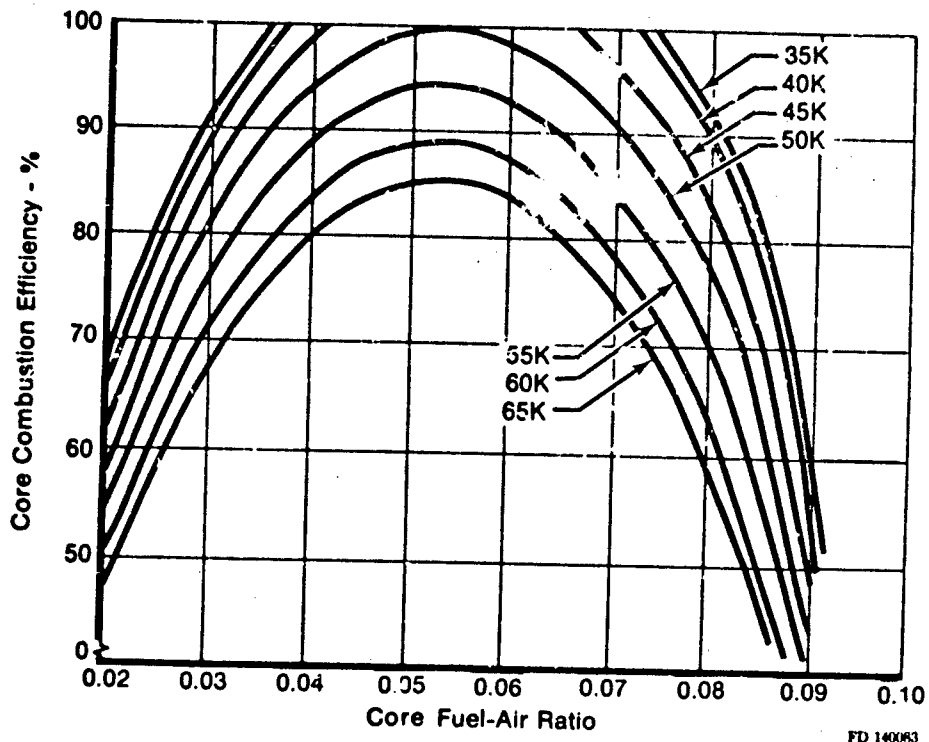
FD 140082

Figure 78. The Effect of the Entrance Air Velocity on the Eddy Gas Composition for the 18×10^{-3} lbm/(in.) (min.) JP-4 Wake Flame: CO₂, CO, and H₂ Concentration Profiles

The results for the core stream are shown in Figure 79. The behavior follows the classic curve of efficiency versus fuel-air ratio for gaseous fuels. The peak efficiency fuel-air ratio does not occur at stoichiometric (0.068 for JP-4) but rather at about 0.055. This shift is caused by the vitiation of the turbine exit flow due to main burner combustion. For the cases analyzed, the core stream efficiency is quite good up to very high altitudes. This would be expected at this level of approach temperature.

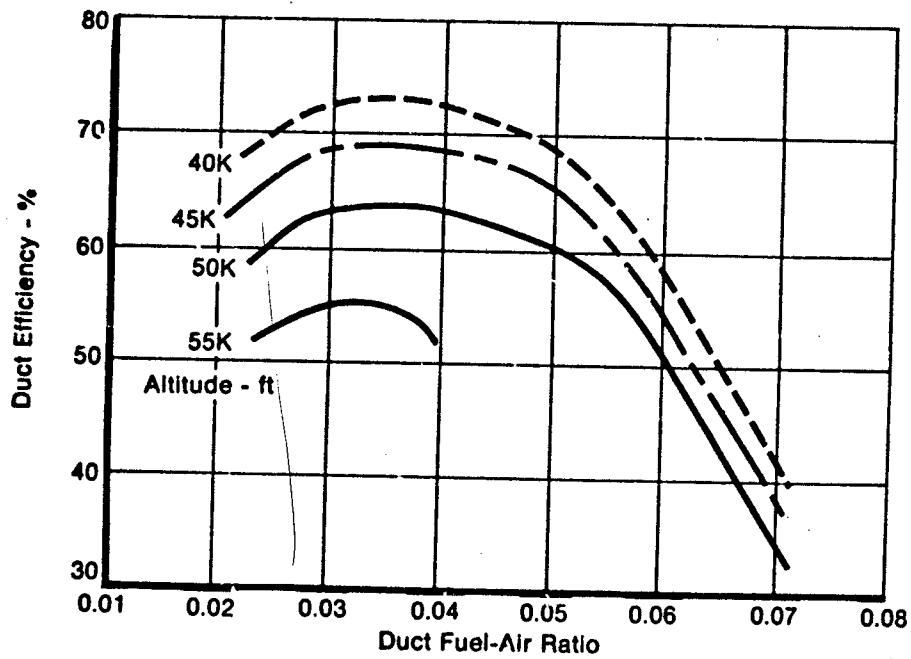
The analysis for the fan duct stream resulted in quite different behavior. The efficiency (Figure 80) shows a sharp climb from the lean limit and a plateau of efficiency for some range of fuel-air ratios followed by a sharp fall towards rich blowout. Also, significant decline occurs above 50,000 feet at the anaerobic flight Mach number.

The peak efficiency fuel-air ratio is approximately 0.035. This is due partly to the relative wake enrichment from the two-phase fuel concept and partly to the loss of some combustion airflow diverted for liner cooling. The sharp decline past the 0.050 fuel-air ratio is due to the wake nearing its rich limit. This is accompanied by a rapid decline in reaction capability with increasing fuel-air ratio.



FD 140063

Figure 79. F100 Core Stream Efficiency Prediction



FD 140064

Figure 80. F100 Fan Duct Stream Efficiency

Two factors contribute to the rapid decline in efficiency from 50,000 to 55,000 feet. The reduced static pressure in the augmentor increases the rate of fuel vaporization from the surface of the flameholder for a given level of wake heat flux. Also, the reduced pressure results in a decrease in the wake rich limit fuel-air ratio. Thus, a richer wake with a leaner rich limit yields earlier blowouts at higher altitudes. This region is shown in more detail in Figure 81. This region is the same altitude region where the development engine experienced rumble instability at fuel-air ratios above 0.050. The predictions are shown below:

<u>Altitude</u>	<u>Rumble Limit f/a</u>
51,000	0.060
53,000	0.058
54,000	0.052
55,000	0.038

The extreme sensitivity of this limit underscores a recurring development engine problem. During evaluation testing for rumble limit altitudes or fuel-air ratios, severe data scatter is continuously encountered. The fan duct behavior is such that small shifts in the test engine trim or fuel schedule within normally allowable error bands will generate large changes in the limit points.

The predicted behavior of the engine is right in the development engine data range under these conditions of flight Mach number. The total augmentor efficiency versus fuel-air ratio at 50,000 feet altitude is shown in Figure 82. These predictions agree fairly well with the engine behavior at this flight point. Again the severe decrease above about 0.050 fuel-air ratio is evident. At these conditions, the general experience rumble limit was in the 0.052 range, which agrees well with the predictions.

The influence of wake heat addition is shown in Figure 83. A significant increase in the limit fuel-air ratio is predicted as well as a slight gain in overall efficiency at lower fuel-air ratios. The dramatic increase in limit f/a at the higher altitudes is primarily due to the increase in the allowable rich limit wake f/a. The heat addition greatly increases the wake kinetic capability which expands the rich limit.

Two data comparisons are possible. First, the data from the experimental program run for this study showed an increase of 2 to 4% in augmentor efficiency with direct wake heat addition. The model predicts about 4 to 5% gain for the engine at similar conditions. Second, the engine development experience was an altitude increase of 5000 to 10,000 feet, at 0.055 f/a, in rumble limit altitude. The model predicts approximately 7000 feet. This heat addition on the development engine resulted in problems not related to this study which precluded its use.

The basic portions of the model were previously compared to the test data from the experimental program and also compared to a generalized turbojet engine efficiency correlation with good results. These comparisons were presented in the earlier section of this report. Typical results are repeated in Figure 84.

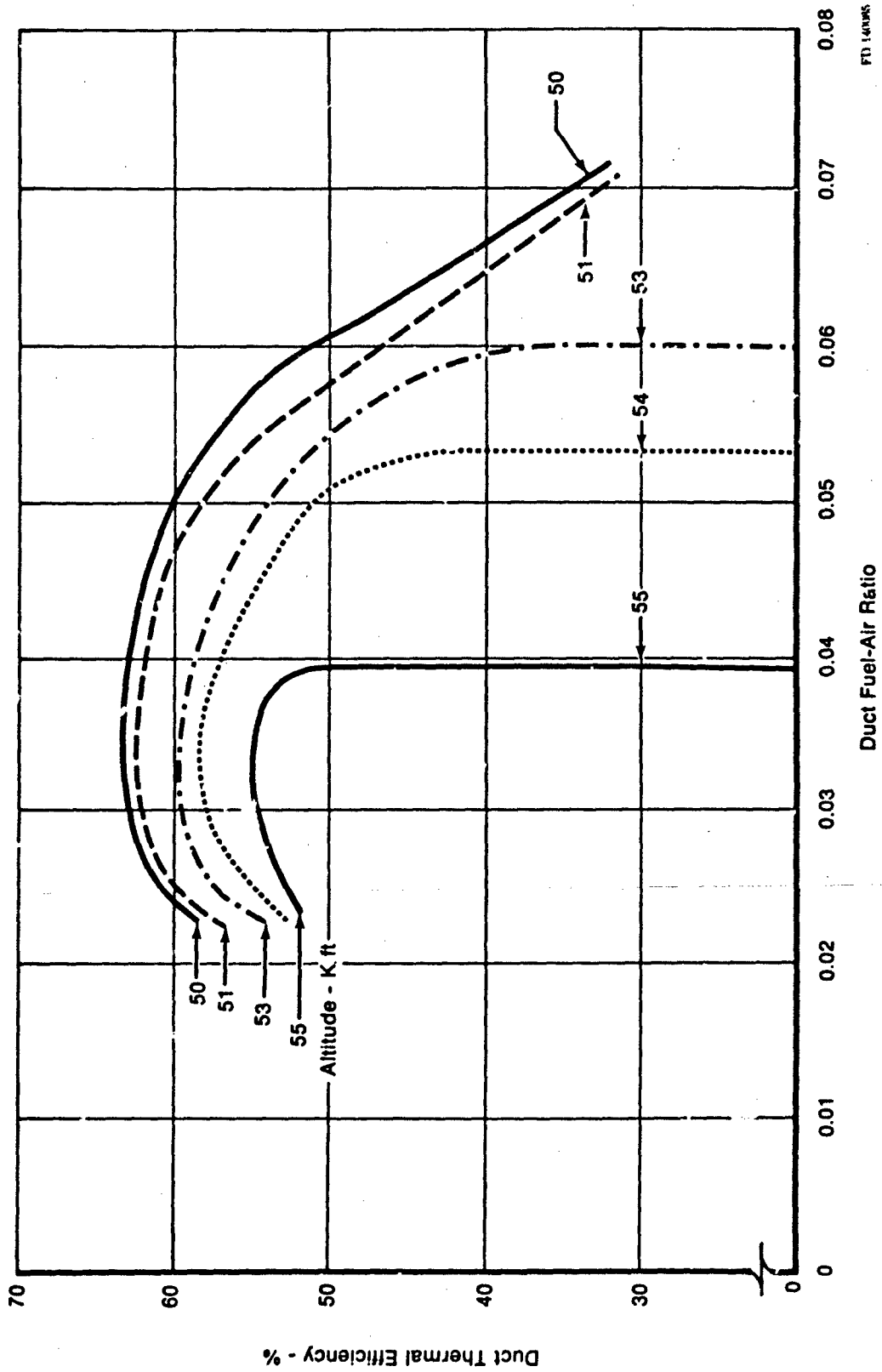


Figure 81. Fan Duct Efficiency Near the Blowout Limit

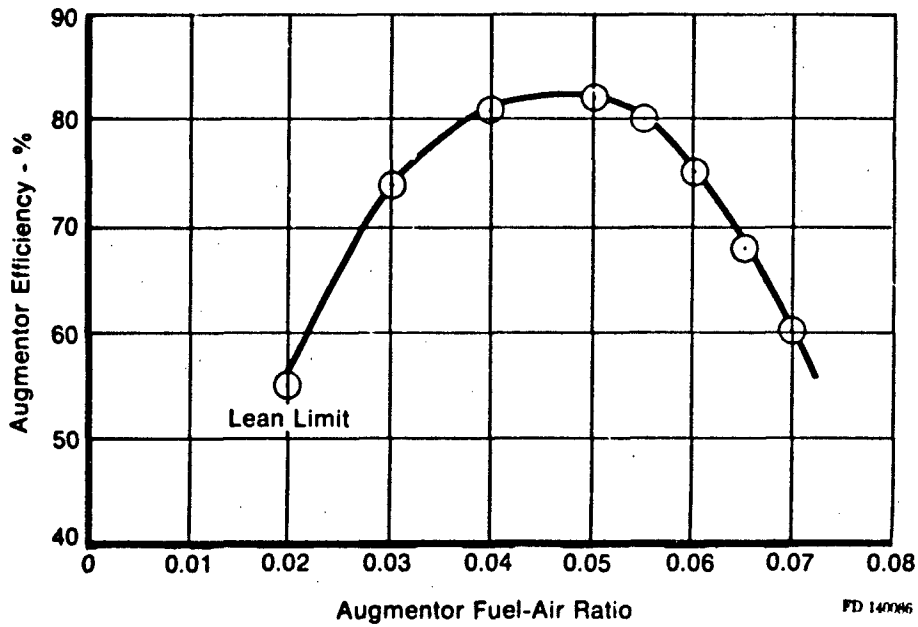


Figure 82. F100 Augmentor Predicted Efficiency vs Fuel-Air Ratio

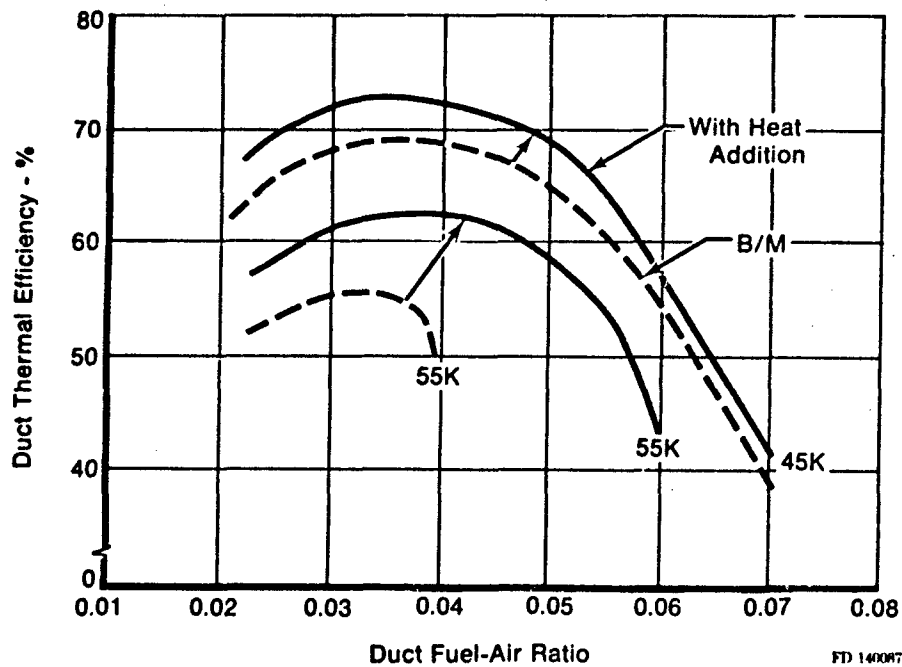
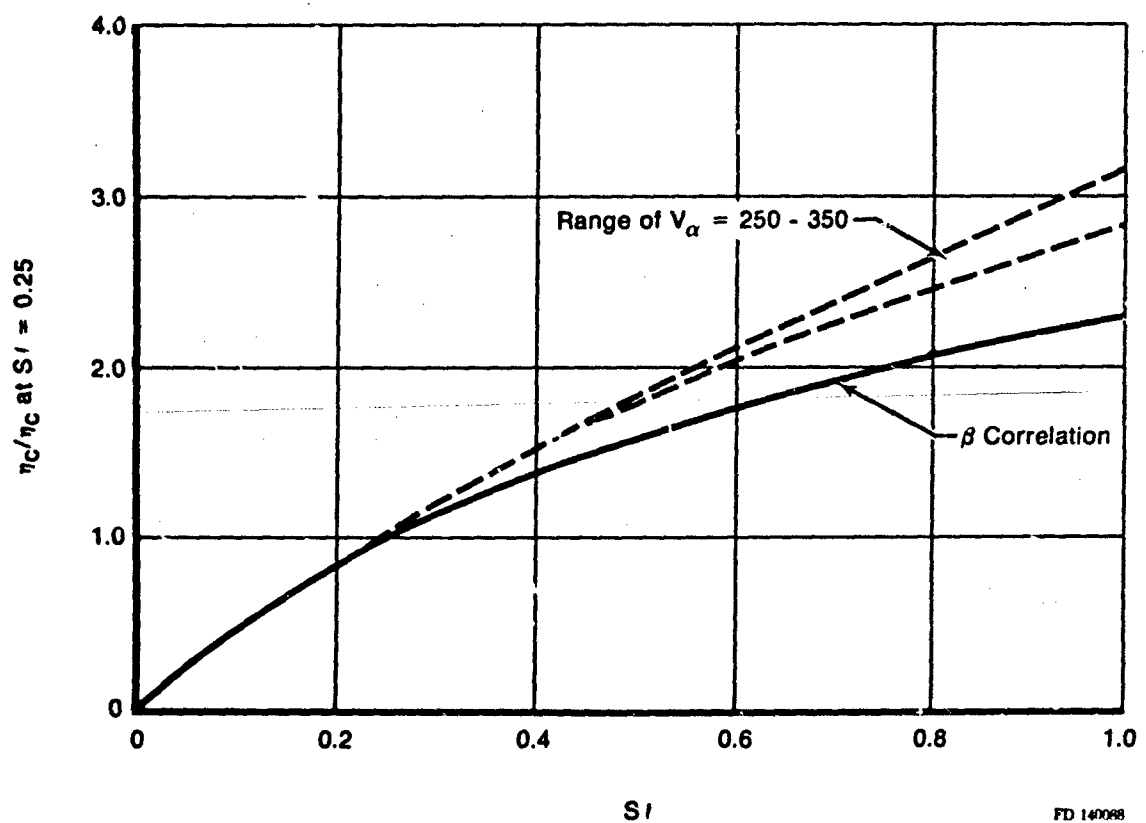
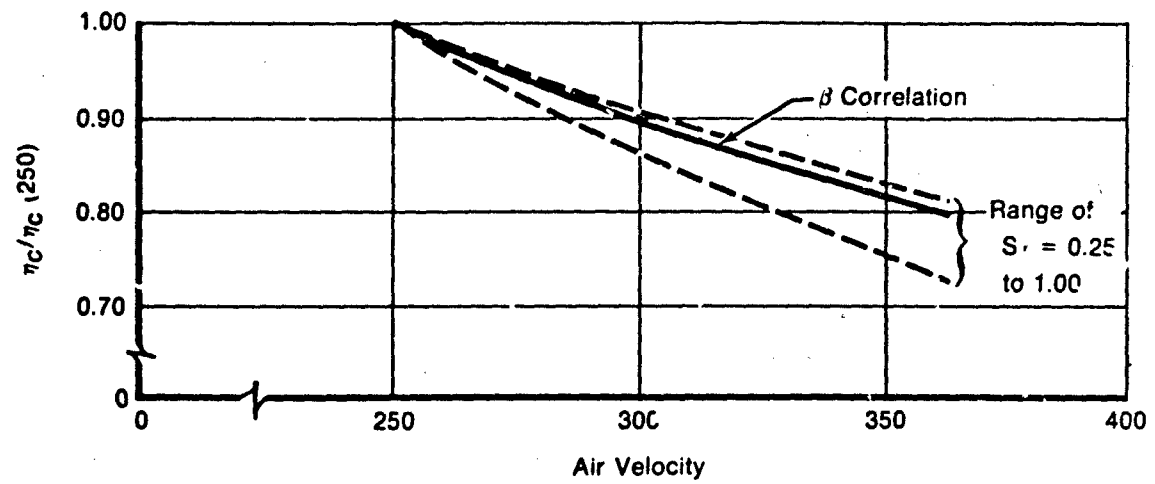


Figure 83. Effect of Heat Addition on Duct Efficiency



FD 140088

Figure 84. Comparison of Flame Model with Beta Correlation

b. Task II — Recommend Improved Designs

This task involved two related elements involving extension of the model's results into the area of augmentor rumble elimination. These elements were:

- Extend the model to other concepts
- Predict the stability of these concepts.

This task was a relatively minor part of the total program in terms of expended activity but important in terms of identification of directions for improved turbofan augmentor technology.

The model formulated was derived specifically for the conventional bluff body stabilized turbofan augmentor with normal turbulent flame propagation controlling the ultimate level of augmentor efficiency. The primary cause of rumble is the dynamic response of these processes to fluctuations in either inlet conditions or fuel-air ratio.

This similar augmentor response logic was used for defining two advanced augmentation concepts. The analyses for these concepts are less rigorous than for the conventional augmentor for two reasons:

- Considerably less effort was expended
- Less is known about the controlling processes than for the conventional case.

The two concepts examined here are the swirling flow augmentor and the VORPIX augmentor. In both of these concepts there is an attempt to provide a "hard" pilot rather than the "soft" flameholder wake region and to reduce the dependence of the downstream transverse flame penetration rate on the fuel-air ratio. Both of these changes will serve to reduce the augmentor efficiency response and will generate increased stability limits.

The swirling flow augmentor concept generates an increased flame speed by implementation of the concept of buoyant penetration in centrifugal force fields. The basic concepts are presented in Reference 34 and subscale rig test experience in Reference 35. The essential elements of an augmentor utilizing swirling flow consist of inlet flow swirl vanes, an outer diameter annular pilot with its own fuel system and zoned circumferential fuel sprayings.

The outer pilot provides a circumferentially uniform flame initiation. The transverse flame propagates via centrifugally enhanced turbulent flame speed into the swirling approach flow. The flame speeds achieved by this mechanism are many times greater than from normal turbulent flame penetrations. In addition, the driving potential for the flame speed is the buoyant force caused by density differences between the burned and unburned gases rather than turbulent-kinetic transport. Thus, the variation due to fuel-air ratio excursions is much less.

Figure 85 compares the predicted variation in flame speed versus fuel-air ratio for a swirling flow and a conventional design. The curves are both normalized to 1.0 at the maximum flame speed fuel-air ratio. The dramatic difference is evident. This degree of change will reduce the variational influence of fuel-air ratio excursions on total augmentor efficiency.

The results of the subscale rig testing tended to verify the improved combustion efficiency over a wider fuel-air ratio range. It also underscored the very strong influence of the fuel distribution on the augmentor performance. Typical results are shown in Figure 86. This test apparatus utilized four zones of fuel injection with zone 1 feeding the annular pilot and zones 2, 3 and 4 located more toward the centerline. The largest efficiency values were obtained by maintaining as nearly as possible locally stoichiometric conditions.

The effect of inlet velocity during testing was considerably less than conventional flameholders as shown in Figure 87. The variation with fuel-air ratio is shown in Figures 88 and 89 at two different augmentor lengths. The insensitive nature is clearly seen.

The anticipated behavior of an augmentor design utilizing the swirl concept would be an extremely stable configuration. However, there are several qualifying factors; the major ones are delineated.

- The fuel distribution should be designed to produce local stoichiometry as nearly as possible. The data clearly show that local richness will produce efficiency declines severe enough to drive rumble instabilities
- The variational effect of pressure on the flame speed needs experimental evaluation
- The pilot must be sized to eliminate any significant airflow dynamic response. If the pilot responds, the effect will be the same as if the flameholder wake is forced near blowout
- More research is required on the fundamental processes involved, particularly the effect of liquid fuel concentration which at present is virtually unknown.

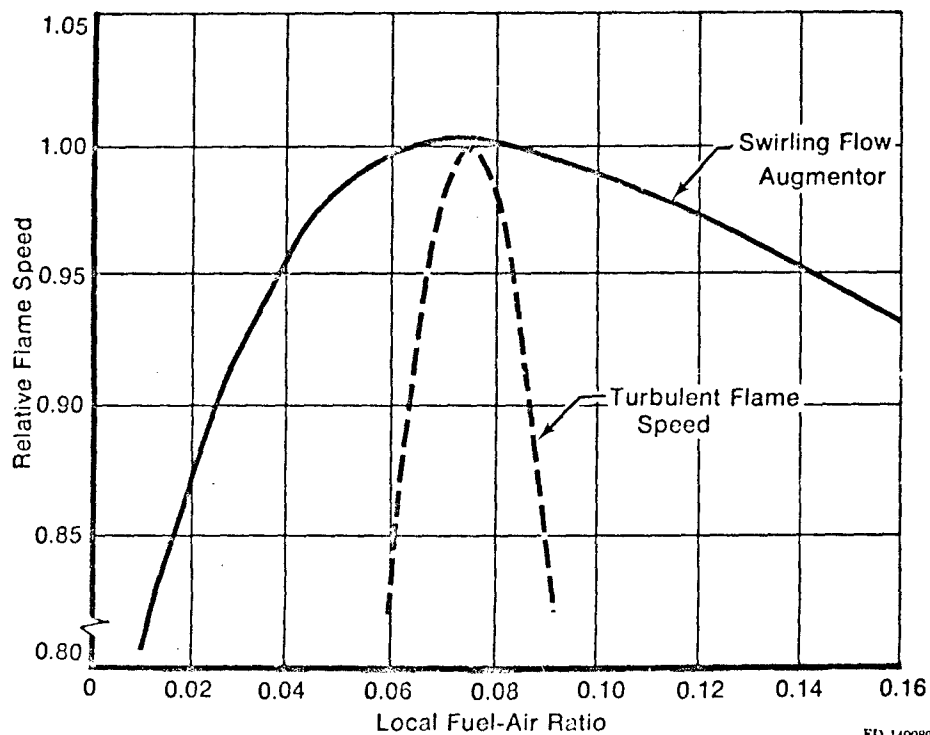
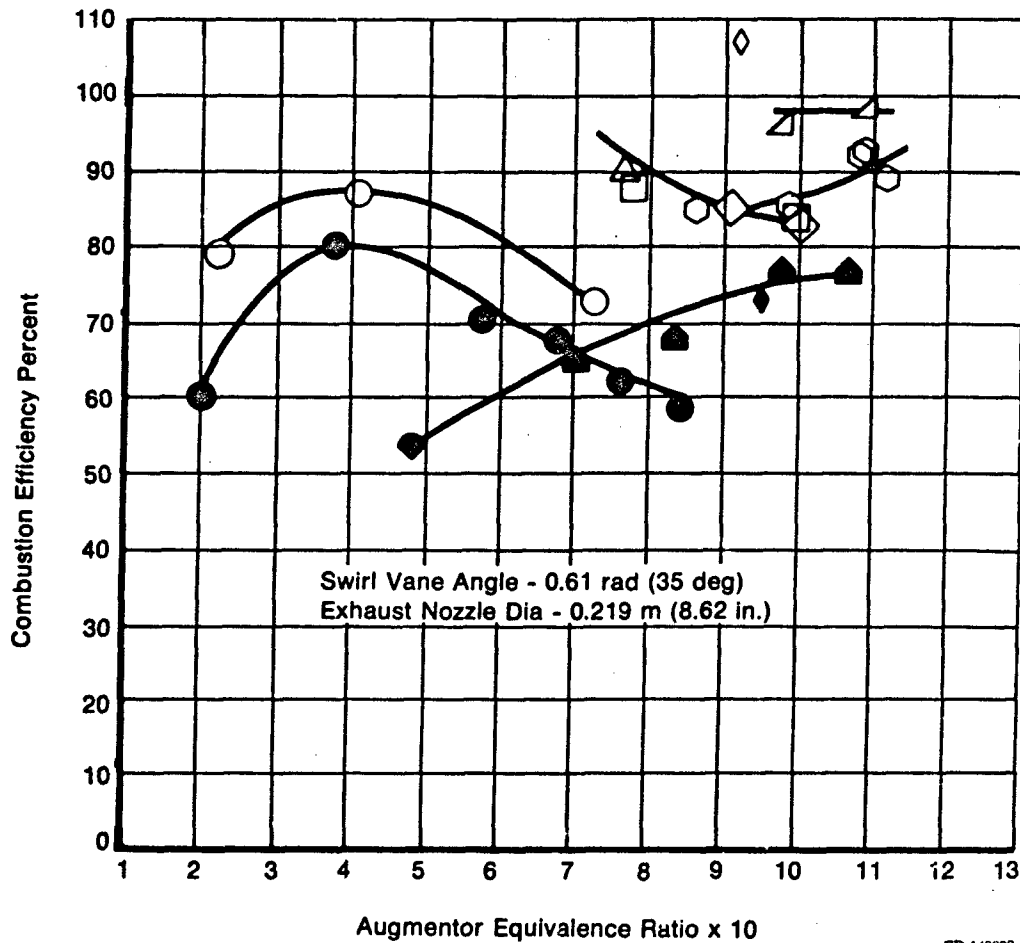


Figure 85. Swirling Flow Flame Speed vs Conventional Flame Speed

Open Symbols - L/D = 1.414; Closed Symbols - L/D = 0.914

- - Zone 2 Only
- - Zone 2 $\phi = 0.175$; Zone 3 ϕ Varied
- ◇ - Zone 2 $\phi = 0.339$; Zone 3 ϕ Varied
- △ - Zone 2 $\phi = 0.518$; Zone 3 $\phi = 0.134$
- ▴ - Zone 2 $\phi = 0.328$; Zone 3 $\phi = 0.335$; Zone 4 ϕ Varied
- ◊ - Zone 2 $\phi = 0.397$; Zone 3 $\phi = 0.167$; Zone 4 $\phi = 0.339$
- ⊙ - Zone 2 $\phi = 0.699$; Zone 4 ϕ Varied
- ◆ - Zone 2 $\phi = 0.463$; Zone 3 $\phi = 0.432$
- ▲ - Zone 2 $\phi = 0.486$; Zone 4 ϕ Varied
- - Zone 2 $\phi = 0.286$; Zone 4 $\phi = 0.168$



FD 140090

Figure 86. Effect of Augmentor L/D on Combustion Efficiency

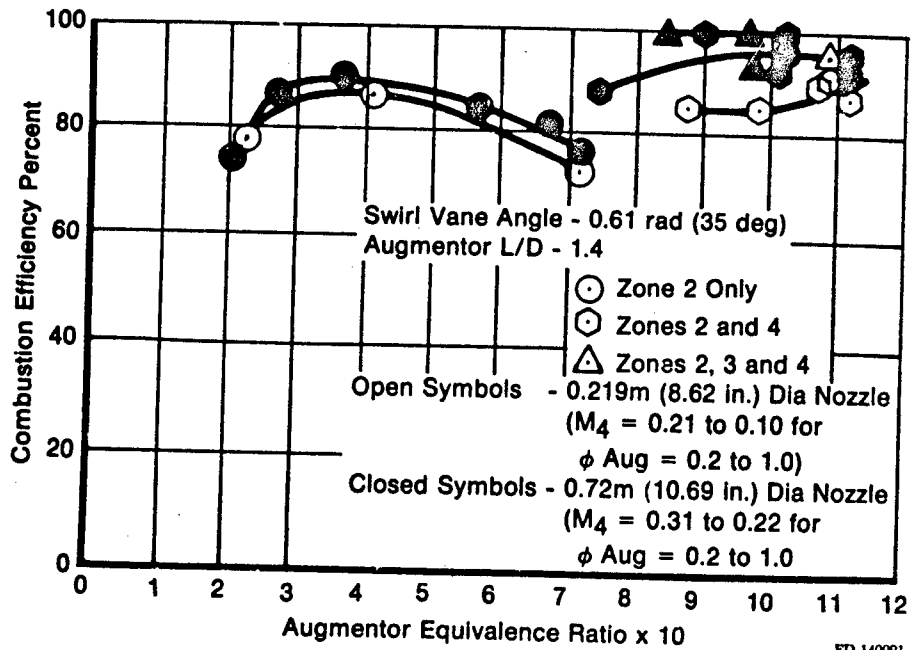


Figure 87. Effect of Mach Number on Combustion Efficiency

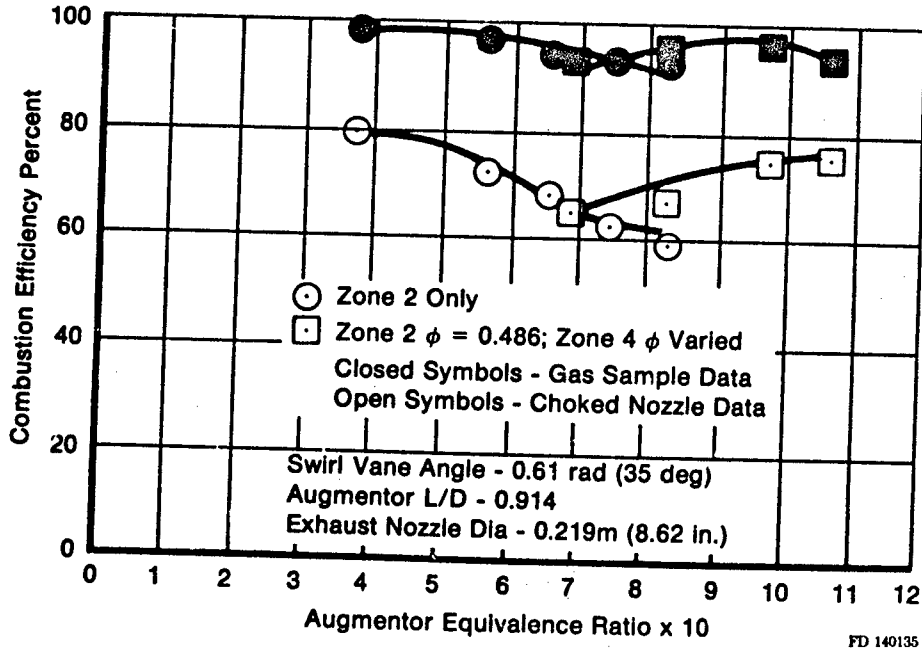


Figure 88. Comparison of Gas Sample and Choked Nozzle Calculated Efficiencies

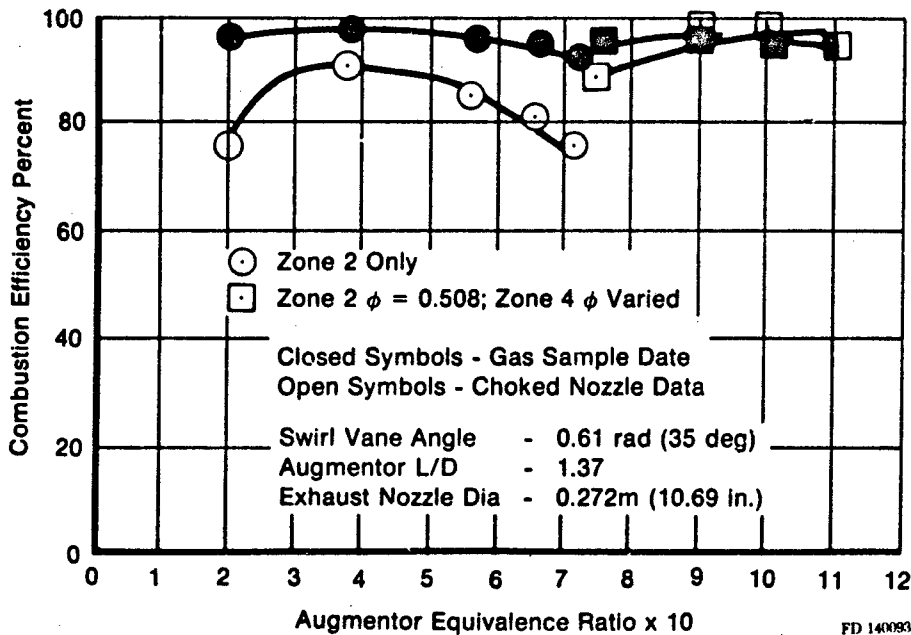


Figure 89. Comparison of Gas Sample and Choked Nozzle Calculated Combustion Efficiencies

The alternative augmentor design to which the rumble model concepts were applied is the P&WA VORBIX augmentor. This augmentor concept (Reference 36) relies on a pilot burner fed by high-temperature engine stream airflow. The main fuel injection is into the pilot discharge flow where vaporization occurs. This fuel rich vapor cloud is penetrated later by vortices of the fan duct and engine airflows which are driven by mechanical swirling devices. This produces a central spinning core of cooler air surrounded by hot fuel rich vapor.

This situation produces flow instability where the cooler spinning air attempts to penetrate the hot pilot exhaust gases. This forces intimate contact between the fuel vapor and the available oxygen at temperatures sufficient for auto ignition. The rate of combustion is primarily driven by the aerodynamic forced mixing rather than locally turbulent flame speed. Although the reaction proceeds in a fuel rich gas, the significant kinetics are controlled by the interfacial composition between the fuel vapor cloud and the air core of the vortices.

The subscale test data are typically represented by Figure 90. The system is sensitive to the secondary air swirler angle since the angle establishes the strength of the penetrating vortex. The system is, however, quite insensitive to the overall fuel-air ratio.

Similar tests were run with a different form of vortex generator in the fan duct stream. These data are shown in Figure 91. Although slightly more decrease in efficiency is observed with increased fuel-air ratio, the decrease is insufficient to drive rumble.

From the results available at this time, the VORBIX augmentor should exhibit rumble-free operation at a significantly higher altitude than the conventional system. The model cannot be developed much beyond this point without more detailed information on the basic processes.

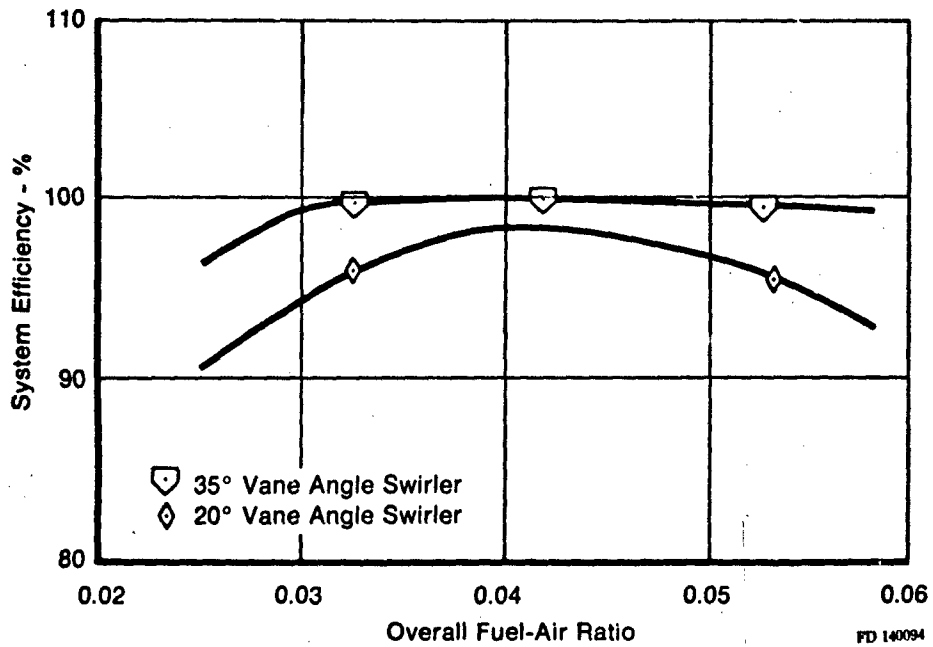


Figure 90. System Efficiency of the Mechanical Swirler Configuration

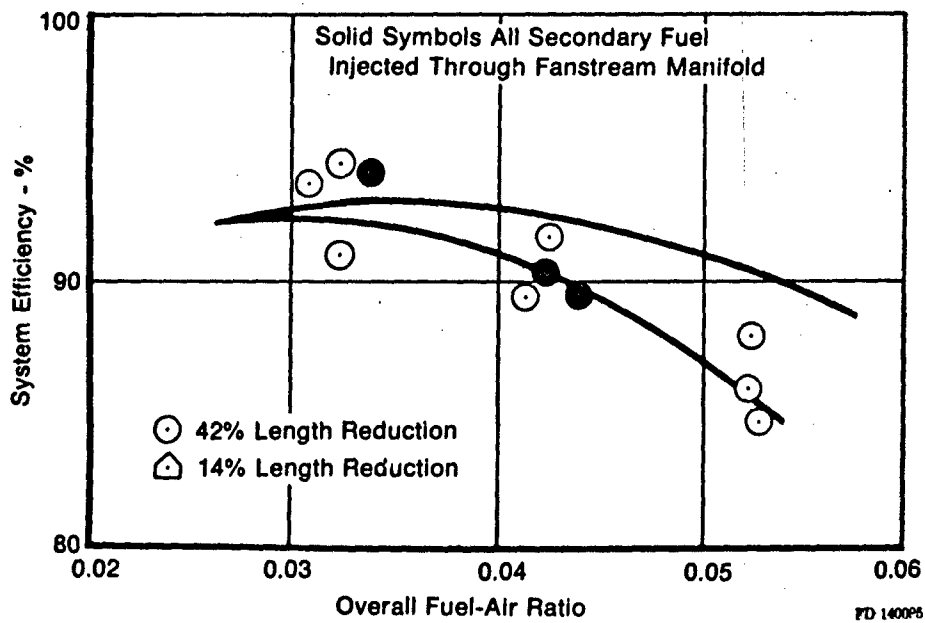


Figure 91. System Efficiency Characteristics of the Final Large Pilot Vorbix Augmentor

The following comments apply to a correctly designed swirl on VORBIX augmentor:

- The controlling mechanism on relative flame speed has been decoupled from a direct fuel-air ratio dependence
- The piloting region has been made dynamically stiffer than a bluff body recirculation zone
- The effect of poor fuel vaporization has been reduced or eliminated.

All of these factors generate reduced efficiency response to dynamic variations in fuel-air ratio, pressure, velocity, or airflow, which in turn causes lower rumble gain factors and improved stability.

5. CONCLUSIONS AND RECOMMENDATIONS

As a result of the exploratory efforts performed under this study, the major drivers of rumble instability in turbofan augmentors have been identified. The response for a turbofan augmentor of mixed flow configuration with conventional bluff body flameholders has been quantified and the major limitations identified. A computer program has been written which predicts the combustion efficiency of a conventional turbofan augmentor and has been evaluated successfully against development experience on a current engine. The possible improvements with advanced augmentation concepts have been explored.

As a result of the analytical and experimental efforts of this study with regard to flame stabilization and rumble, the following major conclusions have been reached.

- Rumble is driven by oscillations in overall augmentor efficiency caused by the response of the combustion process to variations in fuel-air ratio, pressure, velocity, or temperature. These are important in this order.
- Consideration of the physical processes which control flame stability in a two-phase fuel spray has resulted in the identification of surface vaporization from the flameholder as a major parameter in the stability and rumble limits.
- The flame stability requirements ultimately control the response of the overall augmentation process through the nature of the turbulent flame initiation process in the flameholder wake shear layers.
- Rumble instabilities are initially driven by a severe decline in the fan duct flameholding capability as the wake fuel-air ratio approaches the rich limit. Due to the nature of the two-phase fuel stability equations, this decline occurs at total fuel-air ratios well below the rich limit overall.
- Local modifications to the stability level of the fan duct wakes through flameholder alterations or external heat addition can greatly improve the rumble onset limits.

- Rumble response may be reduced by isolating the flame speed from local reaction rate or piloting strength and by improving the "hardness" of the piloting source. Two novel augmentor concepts offer the promise of increased altitude capability without rumble. The VORBIX offers the greater capability.
- The conventional flameholder concept in a mixed flow turbofan augmentor offers limited improvement unless more control over the wake composition is obtained or methods are employed to increase the wake reaction rate.

The augmentor model as currently developed presents a reasonable representation of the combustion process in the turbofan augmentor. For an increased rumble limit conventional design, the following guidelines are recommended:

- The fuel system and flameholder design should be specifically tailored to the augmentor inlet profile to eliminate locally rich fuel-air regions and operate at a uniform level of wake aerodynamic loading. These profiles should be realistic engine data as experience has shown that these are rarely periodic or symmetric.
- A high level of wake reaction speed should be maintained by direct engine stream mixing or heat addition to the wakes.
- The fuel system should be as closely coupled to the wake as feasible and consistent with acceptable lean limits to reduce excessive wake enrichment.
- The fuel atomization should be as great as possible (small droplets) for the same reasons.
- Methods of decoupling the flame speed from the local fuel-air ratio offer the most significant areas of future augmentor design.
- The predictions of this model should be verified on full-scale engine evaluation.

APPENDIX A

TEST DATA

This appendix contains the tabulated and plotted experimental rig data. The following symbols are used:

T	air temperature upstream of the flameholders	°F
P	rig pressure upstream of the flameholders	psia
M	Mach number upstream of the flameholder	
η	combustion efficiency	%
TFH1, TFH2	center flameholder metal temperatures	°F
Amp	peak-to-peak pressure amplitude at flameholders	%
Freq	frequency read from o-graph	Hz

Included with this tabulation are the transfer functions for the various pressure probes. The following symbols are used to define the transfer functions:

$P_{21}, P_{31}, P_{42}, P_{43}, P_{44}$ - ratio of pressure amplitude at the subscript location to the amplitude at the flameholder.

$\phi_{21}, \phi_{31}, \phi_{42}, \phi_{43}, \phi_{44}$ - phase difference between the pressure at the subscript location and the flameholder.

$f_{21}, f_{31}, f_{42}, f_{43}, f_{44}$ - transfer function frequency.

TABLE A-1
EXPERIMENTAL STUDY RIG DATA

TEST POINT 1 & 2
TEST CONDITION Baseline
IMP SOURCE 7.01

POINT	Rig Condition										Transfer Functions															
	T	P	H	F/A	AMP	PHAS	P21	P22	P23	P24	P31	P32	P33	P34	P35	P41	P42	P43	P44	P45	P46	P47	P48	P49	P50	
18	410	13.0	.084	.085	6.6	-	-	-	-	-	-	-	-	-	-	-	-	-	-	-	-	-	-	-	-	-
19	407	13.0	.081	.078	5.4	-	-	-	-	-	-	-	-	-	-	-	-	-	-	-	-	-	-	-	-	-
20	409	13.02	.087	.083	3.8	-	-	-	-	-	-	-	-	-	-	-	-	-	-	-	-	-	-	-	-	-
21	412	13.03	.087	.118	18.0	40	-	-	-	-	-	-	-	-	-	-	-	-	-	-	-	-	-	-	-	-
22	408	13.14	.048	.114	17.6	60	1.13	63	80	1.52	45	70	1.4	60	1.35	60	1.4	60	1.4	60	1.4	60	1.4	60	1.4	60
23	413	13.01	.086	.116	15.6	60	2.4	69	80	1.5	63	70	1.5	63	1.4	63	1.4	63	1.4	63	1.4	63	1.4	63	1.4	63
24	409.8	13.03	.048	.143	22.3	80	2.3	65	85	1.55	44	70	1.35	60	1.35	60	1.35	60	1.35	60	1.35	60	1.35	60	1.35	60
25	410	14.8	.103	.078	5	-	2.25	70	100	1.4	50	80	1.3	60	1.3	60	1.3	60	1.3	60	1.3	60	1.3	60	1.3	60
26	414	14.5	.093	.081	5.5	-	1.1	180	20	1.1	180	20	1.1	180	20	1.1	180	20	1.1	180	20	1.1	180	20	1.1	180
27	414	15.4	.098	.098	9.1	60	1.05	120	30	1.05	120	30	1.05	120	30	1.05	120	30	1.05	120	30	1.05	120	30	1.05	120
28	410.8	13.76	.091	.105	12.6	50	2.35	50	100	1.4	48	95	1.3	72	1.35	72	1.35	72	1.35	72	1.35	72	1.35	72	1.35	72
29	396	20.5	.132	.082	6.4	-	2.25	50	85	1.4	45	80	1.2	70	1.2	70	1.2	70	1.2	70	1.2	70	1.2	70	1.2	70
30	398	20.3	.117	.065	6.4	150	1.9	45	80	1.2	65	85	1.35	85	1.35	85	1.35	85	1.35	85	1.35	85	1.35	85	1.35	85
31	397.2	21.45	.123	.112	9.7	50	1.6	60	140	1.3	140	160	1.3	140	1.3	140	1.3	140	1.3	140	1.3	140	1.3	140	1.3	140
32	600	22.4	.114	.118	23	100	1.85	50	110	1.0	30	90	1.5	55	1.5	55	1.5	55	1.5	55	1.5	55	1.5	55	1.5	55
33																										
34	234	19.0	.082	.080	3	-	-	-	-	-	-	-	-	-	-	-	-	-	-	-	-	-	-	-	-	-
35	235	18.0	.083	.077	3.7	30	2.4	42	115	1.4	44	83	1.4	44	1.4	44	1.4	44	1.4	44	1.4	44	1.4	44	1.4	44

TABLE A-1
EXPERIMENTAL STUDY RIG DATA (CONT.)

TEST NO. 1.6.3
TEST CONDITION Baseline
RIG IMPACT 7.01

POINT	RIG Condition										Transfer Function																																																																																																																																																																																																																																																																																																																																																																																																																																																																																																																																																																																																																																																																																																																																																																																																																																																																																																																																																																																																																																																																																																																																																																																																																																																																																																																																																																																																																																																																																																																						
	T	P	H	P/A	AMP	FRQ	P21	P22	P23	P24	P25	P26	P27	P28	P29	P30	P31	P32	P33	P34	P35	P36	P37	P38	P39	P40	P41	P42	P43	P44	P45	P46	P47	P48	P49	P50	P51	P52	P53	P54	P55	P56	P57	P58	P59	P60	P61	P62	P63	P64	P65	P66	P67	P68	P69	P70	P71	P72	P73	P74	P75	P76	P77	P78	P79	P80	P81	P82	P83	P84	P85	P86	P87	P88	P89	P90	P91	P92	P93	P94	P95	P96	P97	P98	P99	P100	P101	P102	P103	P104	P105	P106	P107	P108	P109	P110	P111	P112	P113	P114	P115	P116	P117	P118	P119	P120	P121	P122	P123	P124	P125	P126	P127	P128	P129	P130	P131	P132	P133	P134	P135	P136	P137	P138	P139	P140	P141	P142	P143	P144	P145	P146	P147	P148	P149	P150	P151	P152	P153	P154	P155	P156	P157	P158	P159	P160	P161	P162	P163	P164	P165	P166	P167	P168	P169	P170	P171	P172	P173	P174	P175	P176	P177	P178	P179	P180	P181	P182	P183	P184	P185	P186	P187	P188	P189	P190	P191	P192	P193	P194	P195	P196	P197	P198	P199	P200	P201	P202	P203	P204	P205	P206	P207	P208	P209	P210	P211	P212	P213	P214	P215	P216	P217	P218	P219	P220	P221	P222	P223	P224	P225	P226	P227	P228	P229	P230	P231	P232	P233	P234	P235	P236	P237	P238	P239	P240	P241	P242	P243	P244	P245	P246	P247	P248	P249	P250	P251	P252	P253	P254	P255	P256	P257	P258	P259	P260	P261	P262	P263	P264	P265	P266	P267	P268	P269	P270	P271	P272	P273	P274	P275	P276	P277	P278	P279	P280	P281	P282	P283	P284	P285	P286	P287	P288	P289	P290	P291	P292	P293	P294	P295	P296	P297	P298	P299	P300	P301	P302	P303	P304	P305	P306	P307	P308	P309	P310	P311	P312	P313	P314	P315	P316	P317	P318	P319	P320	P321	P322	P323	P324	P325	P326	P327	P328	P329	P330	P331	P332	P333	P334	P335	P336	P337	P338	P339	P340	P341	P342	P343	P344	P345	P346	P347	P348	P349	P350	P351	P352	P353	P354	P355	P356	P357	P358	P359	P360	P361	P362	P363	P364	P365	P366	P367	P368	P369	P370	P371	P372	P373	P374	P375	P376	P377	P378	P379	P380	P381	P382	P383	P384	P385	P386	P387	P388	P389	P390	P391	P392	P393	P394	P395	P396	P397	P398	P399	P400	P401	P402	P403	P404	P405	P406	P407	P408	P409	P410	P411	P412	P413	P414	P415	P416	P417	P418	P419	P420	P421	P422	P423	P424	P425	P426	P427	P428	P429	P430	P431	P432	P433	P434	P435	P436	P437	P438	P439	P440	P441	P442	P443	P444	P445	P446	P447	P448	P449	P450	P451	P452	P453	P454	P455	P456	P457	P458	P459	P460	P461	P462	P463	P464	P465	P466	P467	P468	P469	P470	P471	P472	P473	P474	P475	P476	P477	P478	P479	P480	P481	P482	P483	P484	P485	P486	P487	P488	P489	P490	P491	P492	P493	P494	P495	P496	P497	P498	P499	P500	P501	P502	P503	P504	P505	P506	P507	P508	P509	P510	P511	P512	P513	P514	P515	P516	P517	P518	P519	P520	P521	P522	P523	P524	P525	P526	P527	P528	P529	P530	P531	P532	P533	P534	P535	P536	P537	P538	P539	P540	P541	P542	P543	P544	P545	P546	P547	P548	P549	P550	P551	P552	P553	P554	P555	P556	P557	P558	P559	P560	P561	P562	P563	P564	P565	P566	P567	P568	P569	P570	P571	P572	P573	P574	P575	P576	P577	P578	P579	P580	P581	P582	P583	P584	P585	P586	P587	P588	P589	P590	P591	P592	P593	P594	P595	P596	P597	P598	P599	P600	P601	P602	P603	P604	P605	P606	P607	P608	P609	P610	P611	P612	P613	P614	P615	P616	P617	P618	P619	P620	P621	P622	P623	P624	P625	P626	P627	P628	P629	P630	P631	P632	P633	P634	P635	P636	P637	P638	P639	P640	P641	P642	P643	P644	P645	P646	P647	P648	P649	P650	P651	P652	P653	P654	P655	P656	P657	P658	P659	P660	P661	P662	P663	P664	P665	P666	P667	P668	P669	P670	P671	P672	P673	P674	P675	P676	P677	P678	P679	P680	P681	P682	P683	P684	P685	P686	P687	P688	P689	P690	P691	P692	P693	P694	P695	P696	P697	P698	P699	P700	P701	P702	P703	P704	P705	P706	P707	P708	P709	P710	P711	P712	P713	P714	P715	P716	P717	P718	P719	P720	P721	P722	P723	P724	P725	P726	P727	P728	P729	P730	P731	P732	P733	P734	P735	P736	P737	P738	P739	P740	P741	P742	P743	P744	P745	P746	P747	P748	P749	P750	P751	P752	P753	P754	P755	P756	P757	P758	P759	P760	P761	P762	P763	P764	P765	P766	P767	P768	P769	P770	P771	P772	P773	P774	P775	P776	P777	P778	P779	P780	P781	P782	P783	P784	P785	P786	P787	P788	P789	P790	P791	P792	P793	P794	P795	P796	P797	P798	P799	P800	P801	P802	P803	P804	P805	P806	P807	P808	P809	P810	P811	P812	P813	P814	P815	P816	P817	P818	P819	P820	P821	P822	P823	P824	P825	P826	P827	P828	P829	P830	P831	P832	P833	P834	P835	P836	P837	P838	P839	P840	P841	P842	P843	P844	P845	P846	P847	P848	P849	P850	P851	P852	P853	P854	P855	P856	P857	P858	P859	P860	P861	P862	P863	P864	P865	P866	P867	P868	P869	P870	P871	P872	P873	P874	P875	P876	P877	P878	P879	P880	P881	P882	P883	P884	P885	P886	P887	P888	P889	P890	P891	P892	P893	P894	P895	P896	P897	P898	P899	P900	P901	P902	P903	P904	P905	P906	P907	P908	P909	P910	P911	P912	P913	P914	P915	P916	P917	P918	P919	P920	P921	P922	P923	P924	P925	P926	P927	P928	P929	P930	P931	P932	P933	P934	P935	P936	P937	P938	P939	P940	P941	P942	P943	P944	P945	P946	P947	P948	P949	P950	P951	P952	P953	P954	P955	P956	P957	P958	P959	P960	P961	P962	P963	P964	P965	P966	P967	P968	P969	P970	P971	P972	P973	P974	P975	P976	P977	P978	P979	P980	P981	P982	P983	P984	P985	P986	P987	P988	P989	P990	P991	P992	P993	P994	P995	P996	P997	P998	P999	P1000	P1001	P1002	P1003	P1004	P1005	P1006	P1007	P1008	P1009	P1010	P1011	P1012	P1013	P1014	P1015	P1016	P1017	P1018	P1019	P1020	P1021	P1022	P1023	P1024	P1025	P1026	P1027	P1028	P1029	P1030	P1031	P1032	P1033	P1034	P1035	P1036	P1037	P1038	P1039	P1040	P1041	P1042	P1043	P1044	P1045	P1046	P1047	P1048	P1049	P1050	P1051	P1052	P1053	P1054	P1055	P1056	P1057	P1058	P1059	P1060	P1061	P1062	P1063	P1064	P1065	P1066	P1067	P1068	P1069	P1070	P1071	P1072	P1073	P1074	P1075	P1076	P1077	P1078	P1079	P1080	P1081	P1082	P1083	P1084	P1085	P1086	P1087	P1088	P1089	P1090	P1091	P1092	P1093	P1094	P1095	P1096	P1097	P1098	P1099	P1100	P1101	P1102	P1103	P1104	P1105	P1106	P1107	P1108	P1109	P1110	P1111	P1112	P1113	P1114	P1115	P1116	P1117	P1118	P1119	P1120	P1121	P1122	P1123	P1124	P1125	P1126	P1127	P1128	P1129	P1130	P1131	P1132	P1133	P1134	P1135	P1136	P1137	P1138	P1139	P1140	P1141	P1142	P1143	P1144	P1145	P1146	P1147	P1148	P1149	P1150	P1151	P1152	P1153	P1154	P1155	P1156	P1157	P1158	P1159	P1160	P1161	P1162	P1163	P1164	P1165	P1166	P1167	P1168	P1169	P1170	P1171	P1172	P1173	P1174	P1175	P1176	P1177	P1178	P1179	P1180	P1181	P1182	P1183	P1184	P1185	P1186	P1187	P1188	P1189	P1190	P1191	P1192	P1193	P1194	P1195	P1196	P1197	P1198	P1199	P1200	P1201	P1202	P1203	P1204	P1205	P1206	P1207	P1208	P1209	P1210	P1211	P1212	P1213	P1214	P1215	P1216	P1217	P1218	P1219	P1220	P1221	P1222	P1223	P1224	P1225	P1226	P1227	P1228	P1229	P1230	P1231	P1232	P1233	P1234	P1235	P1236	P1237	P1238	P1239	P1240	P1241	P1242	P1243	P1244	P1245	P1246	P1247	P1248	P1249	P1250	P1251	P1252	P1253	P1254	P1255	P1256	P1257	P1258	P1259	P1260	P1261	P1262	P1263	P1264	P1265	P1266	P1267	P1268	P1269	P1270	P1271	P1272	P1273	P1274	P1275	P1276	P1277	P1278	P1279	P1280	P1281	P1282	P1283	P1284	P1285	P1286	P1287	P1288	P1289	P1290	P1291	P1292	P1293	P1294	P1295	P1296	P1297	P1298	P1299	P1300	P1301	P1302	P1303	P1304	P1305	P1306	P1307	P1308	P1309	P1310	P1311	P1312	P1313	P1314	P1315	P1316	P1317	P1318	P1319	P1320	P1321	P1322	P1323	P1324	P1325	P1326	P1327	P1328	P1329	P1330	P1331	P1332	P1333	P1334	P1335	P1336	P1337	P1338	P1339	P1340	P1341	P1342	P1343	P1344	P1345	P1346	P1347	P1348	P1349	P1350	P1351	P1352	P1353	P1354	P1355	P1356	P1357	P1358	P1359	P1360	P1361	P1362	P1363	P1364	P1365	P1366	P1367	P1368	P1369	P1370	P1371	P1372	P1373	P1374	P1375	P1376	P1377	P1378	P1379	P1380	P1381	P1382	P1383	P1384	P1385	P1386	P1387	P1388	P1389	P1390	P1391	P1392	P1393	P1394	P1395	P1396	P1397	P1398	P1399	P1400	P1401	P1402	P1403	P1404	P1405	P1406	P1407	P1408	P1409	P1410	P1411	P1412	P1413	P1414	P1415	P1416	P1417	P1418	P1419	P1420	P1421	P1422	P1423	P1424	P1425	P1426	P1427	P1428	P1429	P1430	P1431	P1432	P1433	P1434	P1435	P1436	P1437	P1438	P1439	P1440	P1441	P1442	P1443	P1444	P1445	P1446	P1447	P1448	P1449	P1450	P1451	P1452	P1453	P1454	P1455	P1456	P1457	P1458	P1459	P1460	P1461	P1462	P1463	P1464	P1465	P1466	P1467	P1468	P1469	P1470	P1471	P1472	P1473	P1474	P1475	P1476	P1477	P1478	P1479	P1480	P1481	P1482	P1483	P1484	P1485	P1486	P1487

TABLE A-1
EXPERIMENTAL STUDY RIG DATA (CONT.)

TABLE A-1
EXPERIMENTAL STUDY RIG DATA (CONT.)
RIG CONDITION

TEST POINT 3
TEST CONDITION 3
Flange/Seal Damage Change
RIG NUMBER 11-01

• SEE FIGURE 11-51

POINT	T	P	W	F/A	AMP	PRSQ	7	TRM1	TRM2
23	238	15.1	.060	.032	8.0	50	88.4	289	335
26	247	15.1	.060	.032	8.9	50	87.6	300	305
27	249	14.3	.053	.094	13.3	60	95.3	340	443
28	250	13.9	.037	.648	9.4	50	80.6	34*	380
29	254	14.1	.053	.074	9.3	50	87.4	432	318
30	255	15.5	.09*	.032	8.3	55	84.2	215	197
31	251	14.3	.041	.039	12.2	55	80.3	261	187
32	254	14.2	.079	.041	9.2	55	85.3	210	197
33	251	17.0	.075	.049	13.1	55	78.9	222	202
34	254	17.0	.071	.051	14	55	83.2	218	206
35	252	17.4	.071	.040	11.4	55	74.3	245	279
36	252	17.4	.072	.059	14.2	55	74.4	252	238
37	252	18.0	.044	.065	14.4	50	80.0	289	280
38	255	13.8	.041	.044	11.4	40	77.2	233	211
39	254	8.74	.143	.060		40	18.3	203	218
40	284	15.3	.058	.057	8.8	40	104	330	373
41	402	15.4	.058	.038	9.7	58	109	449	542
42	408	15.5	.040	.094	12.9	57	106	345	443
43	410	15.3	.038	.097	10	55	110	343	411
44	402	13.3	.082	.034	2.3	45	84.8	344	345
45	405	15.5	.090	.037	11.4	45	89.8	344	370
46	405	15.7	.090	.042	12.7	45	78	391	373
47	402	15.7	.084	.044	10.8	45	80	344	341
48	410	13.3	.090	.071	4.3	140	80.7	344	370
49	411	15.4	.083	.034	7.4	45	84	392	349

TABLE A-1
EXPERIMENTAL STUDY RIG DATA (CONT.)

TEST POINT 3
TEST CONDITION Flambolite Slabage Change
REV. NUMBER 11-01

POINT	Rig Conditions									
	T	P	H	V/A	AMP	PRSD	η	TR91	TR92	TR93
50	437	21.5	.060	.041	15.3	85	101	375	375	375
51	408	21.4	.059	.047	15.0	60	103.8	445	410	410
52	411	21.4	.058	.072	9.1	60	96.4	505	382	382
53	409	21.5	.060	.043	14.8	90	11.3	318	317	317
54	408	21.4	.060	.101	9.7	60	-	375	435	435
55	411	21.5	.058	.103	10.2	45	-	338	342	342
56	410	21.4	.060	.175	19	30	-	390	474	474
57	397	22.0	.10	.038	10	65	81.1	381	354	354
58	398	21.3	.098	.038	10.3	70	81.9	382	335	335
59	398	22.0	.101	.050	10.3	70	78.0	318	367	367
60	398	22.0	.103	.048	9.1	10	72.1	318	366	366
61	400	22.2	.101	.041	7.2	70	78.3	377	368	368
62	401	21.1	.101	.042	6.8	70	78.3	378	367	367
63	408	22.2	.102	.078	11.3	80	73.8	378	331	331
64	398	22.1	.103	.078	11.5	55	71.1	39	380	380

TABLE A-1
EXPERIMENTAL STUDY RIG DATA (CONT.)

TEST POINT 5
TEST CONDITION Drilled Pipeholder (22.9°)
REV NUMBER 13.01

POINT	T	P	N	P/A	AMP	FREQ	τ	TPL1	TPL2
1	142	14.8	.055	.058	3	-	100	-	-
2	209	14.5	.061	.051	6	-	103	-	-
3	207	15.2	.063	.037	3	-	88.1	-	-
4	214	18.8	.070	.053	3	-	81.6	-	-
5	196	15.8	.051	.049	10	53	103.3	-	-
6	195	15.5	.056	.044	5.8	60	98.3	-	-
7	199	9.8	.110	.065	3	-	19.3	-	-
8	411	13.3	.090	.040	4	63	65.8	-	-
9	415	16.5	.080	.065	8.5	65	89.0	-	-
10	417	16.0	.085	.083	10	60	86.5	-	-
11	418	21.4	.075	.075	11.2	60	74.2	-	-
12	422	21.2	.073	.061	11.8	61	81.8	-	-
13	423	20.8	.074	.085	10.4	60	64.0	-	-

TABLE A-1
EXPERIMENTAL STUDY RIG DATA (CONT.)

TEST POINT* 7
TEST CONDITION Turbulent Stream (SS)
RIG NUMBER 8-01

Point	Rig Condition										Transfer Function													
	T	ρ	M	P/A	AMP I	PRUQ	P21	f21	Q21	P31	f31	Q31	P42	f42	Q42	P43	f43	Q43	P44	f44	Q44	η	TPM1	TPM2
45	385	14.1	0.76	0.58	4.3	-	-	-	-	-	-	-	-	-	-	-	-	-	-	-	-	-	-	-
46	386	14.5	0.76	0.81	11.7	80	2.0	50	1.5	56	51	1.4	56	345	1.32	56	350	1.45	56	345	31.8	490	510	
47	388	14.3	0.76	1.17	13.2	80	2.05	61	1.5	46	20	1.3	52	335	1.2	52	335	1.2	55	340	28.4	556	608	
48	387	13.9	1.02	0.92	8.4	50	-	-	-	-	-	-	-	-	-	-	-	-	-	-	-	-	-	-
49	400	14.1	1.12	0.95	7.1	180	-	-	-	-	-	-	-	-	-	-	-	-	-	-	-	-	-	-
50	405	14.8	1.08	0.98	15.5	50	-	-	-	-	-	-	-	-	-	-	-	-	-	-	-	-	-	-
51	403	14.5	1.12	0.95	12.4	55	-	-	-	-	-	-	-	-	-	-	-	-	-	-	-	-	-	-
52	402	14.2	1.02	0.78	20.1	70	1.5	50	1.2	50	70	1.1	50	340	1.03	50	340	1.15	50	340	80.1	419	472	
53	394	13.1	0.78	0.90	3.7	-	-	-	-	-	-	-	-	-	-	-	-	-	-	-	-	-	-	-
54	394	14.5	0.77	0.76	11	80	1.25	55	1.2	55	50	1.45	57	340	1.35	55	340	1.40	55	340	57.3	250	265	
55	393	14.3	0.79	1.21	14	55	-	-	-	-	-	-	-	-	-	-	-	-	-	-	-	-	-	-
56	391	13.3	0.79	1.18	6.5	-	-	-	-	-	-	-	-	-	-	-	-	-	-	-	-	-	-	-
58	384	14.8	1.06	0.94	14.9	200	-	-	-	-	-	-	-	-	-	-	-	-	-	-	-	-	-	-
59	386	14.6	1.12	0.93	11.7	150	-	-	-	-	-	-	-	-	-	-	-	-	-	-	-	-	-	-
60	384	14.5	1.16	0.93	5	180	-	-	-	-	-	-	-	-	-	-	-	-	-	-	-	-	-	-
61	384	14.6	1.16	0.93	5	150	-	-	-	-	-	-	-	-	-	-	-	-	-	-	-	-	-	-
62	387	14.9	1.18	0.94	4.1	-	-	-	-	-	-	-	-	-	-	-	-	-	-	-	-	-	-	-
63	389	15.1	1.13	0.94	5.1	-	-	-	-	-	-	-	-	-	-	-	-	-	-	-	-	-	-	-
64	385	14.9	1.05	0.92	10.1	50	-	-	-	-	-	-	-	-	-	-	-	-	-	-	-	-	-	-
65	385	14.8	1.19	0.92	14.2	50	-	-	-	-	-	-	-	-	-	-	-	-	-	-	-	-	-	-

TABLE A-1
EXPERIMENTAL STUDY RIG DATA (CONT.)

TEST POINT^a 7
TEST CONDITION Turbulent Screen (T)
AIR SPEED 8.01

POINT	Rig Condition									
	T	P	H	V/A	AMP	PLSD	η	TR1	TR2	
81	337	13.3	.086	.038	3.8	-	-	370	337	
82	339	14.8	.080	.073	8.8	60	60.7	427	582	
83	404	14.5	.087	.084	13.3	80	84.3	679	848	
84	No Data									
85	407	14.0	.083	.143	8.6	50	-	405	433	
86	389	13.0	.110	.046	4.7	-	-	302	381	
87	321	15.9	.117	.062	7.5	60	69.4	346	407	
88	390	13.6	.106	.093	8.3	65	59.4	338	385	
89	391	16.6	.109	.083	9.6	80	45.3	343	373	
90	239	13.5	.089	.032	4.4	-	-	178	232	
91	238	14.9	.070	.062	4.7	-	-	244	300	
92	238	13.0	.069	.023	2.0	50	60.4	713	595	

TABLE A-1
EXPERIMENTAL STUDY RIG DATA (CONT.)

TEST POINT 6
TEST CONDITION Gascon Fuel
RIG NUMBER 11.01

POINT	T	P	M	P/A	AMP	PERQ	γ	TR11	TR12
1	230	14.0	.055	.057	6.2	507/180	-	150	295
2	230	15.7	.051	.061	6.5	-	-	1000	710
3	249	15.6	.052	.111	2	-	-	1100	760
4	250	15.7	.054	.123	2	-	-	1100	765
5	255	15.8	.051	.131	3.4	-	-	1102	783
6	252	15.5	.052	.129	7.7	55/170	-	1102	790
7	209	20.7	.054	.054	5.8	60/180	86.4	350	230
8	209	18.1	.062	.061	11.	51/180	91	382	271
9	208	17.4	.072	.078	3.6	140	81	817	507
10	208	17.3	.072	.082	4.0	-	84	853	506
11	203	25.1	.035	.057	6	54/180	-	580	500
12	202	25.7	.033	.078	2	-	-	1060	845
13	202	25.7	.038	.105	7	50/180	-	1235	930
14	205	25.7	.031	.124	3	-	-	1220	960
15	397	15.4	.042	.078	3	130	-	720	624
16	401	15.4	.055	.084	3.9	-	-	1025	720
17	403	15.4	.054	.127	3	-	-	1187	835
18	407	15.4	.048	.150	3.2	-	-	1198	838
19	385	18.5	.075	.052	17.3	200	87.4	445	311
20	389	18.1	.082	.084	12.4	180	74.2	617	354
21	386	15.2	.093	.077	6	-	87.5	895	385
22	389	24.1	.050	.062	6.6	60	-	640	385
23	388	24.6	.048	.080	2	-	-	1200	840
24	369	24.3	.047	.096	6.5	-	-	1240	917

TABLE A-1
EXPERIMENTAL STUDY RIG DATA (CONT.)

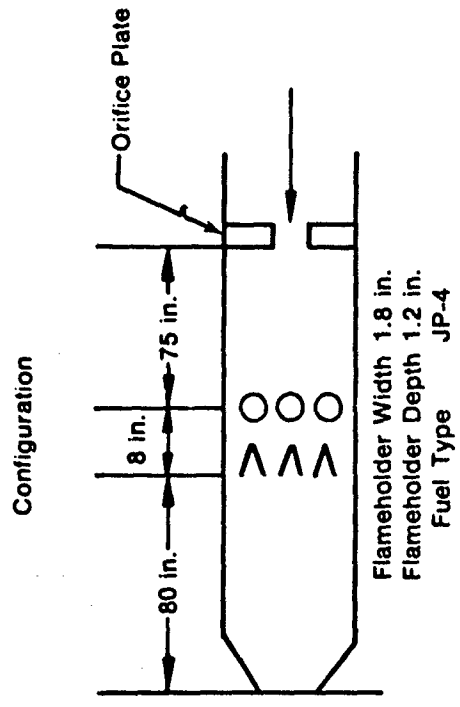
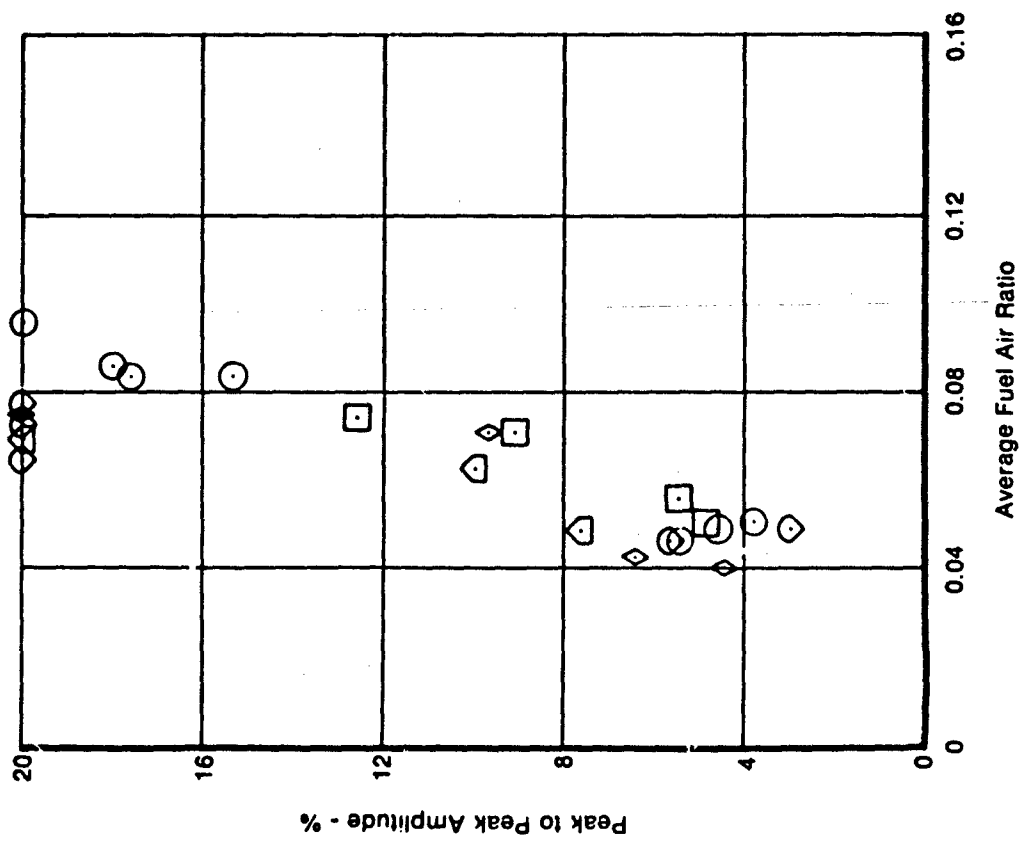
TEST POINT 9
TEST CONDITION Selected Fuel Spraybars
RIG NUMBER 9.01

POINT	RIG Condition									
	I	P	H	F/A	AMP	FREQ	7	7PH1	7PH2	
1	237	14.7	.065	.046	6.8	-	89.3	-	535	
2	240	15.3	.093	.044	-	-	36.5	-	510	
3	227	16.6	.096	.050	-	-	65.5	-	670	
4	226	16.7	.118	.032	34	60	41.9	-	360	
5	225	21.2	.082	.033	4.5	-	58.0	-	480	
6	225	23.2	.059	.049	5.6	70	96.3	-	706	
7	226	23.2	.062	.046	4.8	-	30.2	-	215	
8	226	23.9	.061	.049	6.3	60	90.6	-	752	
9	219	23.0	.055	.062	3.6	80	95.3	-	780	
10	417	16.9	.082	.041	10	52	61.7	-	659	
11	604	15.2	.077	.043	12	60	21.5	-	760	
12	415	16.1	.069	.059	19.8	60	67.5	-	2160	
13	426	8.2	.028	.124	-	-	-	-	1140	
14	428	16	.083	.039	17.3	60	41.7	-	1023	
15	353	13.6	.121	.040	13.2	45	32.4	-	633	
16	353	16.5	.092	.060	6	-	80	-	390	
17	396	18.8	.107	.058	20	60	26.2	-	890	
18	398	21.0	.097	.061	7	60	52.5	-	1270	
19	396	20.3	.085	.064	5	60	106	-	1200	
20	398	18.2	.111	.031	14.5	60	36	-	210	
21	393	21.3	.103	.038	6.6	55	64.8	-	950	
22	391	22.6	.098	.078	15.5	60	60.1	-	1230	

TABLE A-1
EXPERIMENTAL STUDY RIG DATA (CONT.)

TEST POINT* 10
TEST CONDITION Balanced Plumbhairs
NEW ARRIVES 10.01

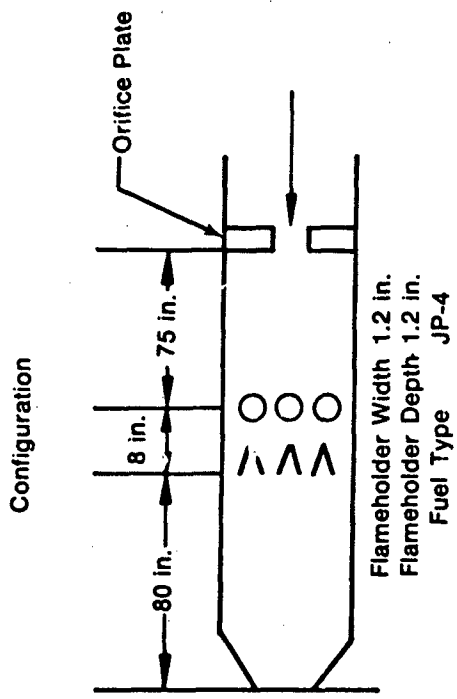
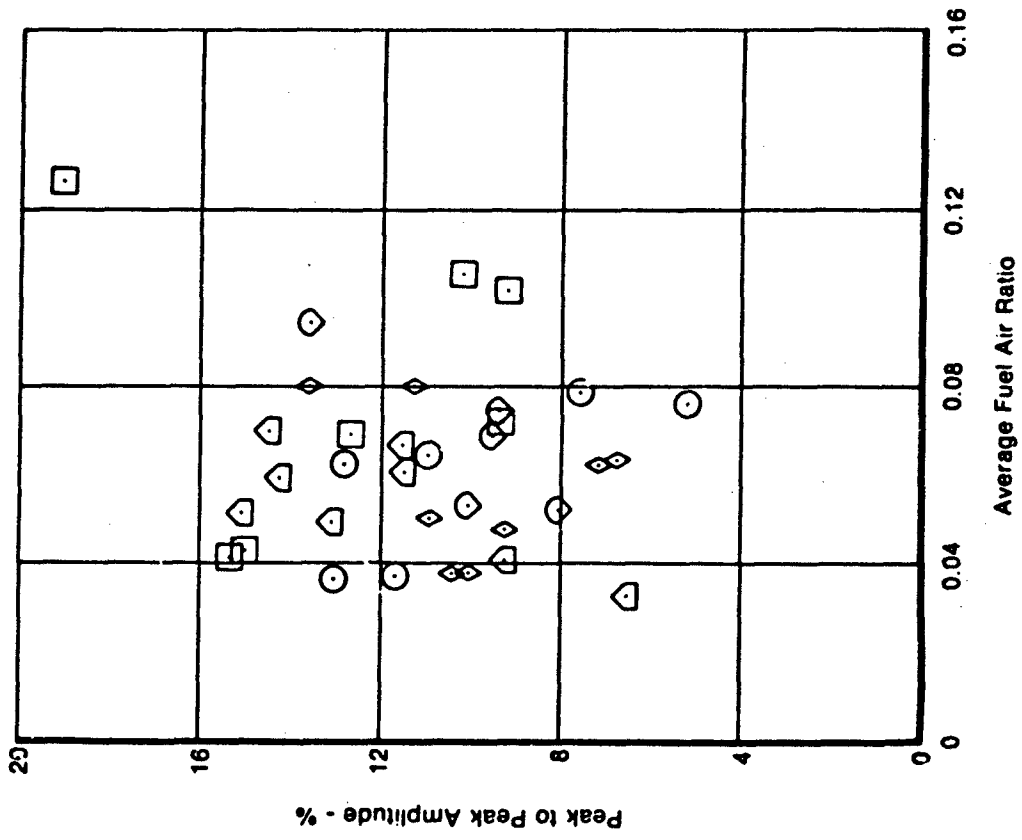
POINT	T	P	H	V/A	AMP	FREQ.	T	TTL	TPL
21	100	13.3	.064	.064	7.7	33	87.1	350	813
22	100	14.2	.058	.063	7.8	40	76.7	1170	840
23	115	14.7	.065	.058	7.7	50	76.5	140	890
24	20	8.1	.128	.059	1	-	14.4	-	-
27	201	13.1	.055	.060	9.4	60	61.1	1120	530
28	185	14.1	.078	.078	18	80	70.9	-	-
29	212	15.3	.053	.061	6.8	-	107	-	-
30	217	14.1	.048	.062	7.5	80	117	1210	775
31	290	13.6	.100	.019	2	-	41.5	-	-
32	251	14.3	.079	.061	6.2	60	84.3	-	-
33	284	14.5	.055	.030	1	60	87.7	610	530
34	284	14.4	.048	.050	4.2	30	112	1220	1090
35	288	17.4	.064	.064	1	-	113	1540	1433
36	286	18.2	.066	.075	17	55	91.7	2920	1490
37	284	21.7	.063	.067	10	-	102	2020	1150



Sym	T °F	P psia	Mach No.	Stability Parameter V/NPT 1.7 x 10 ⁵
⊙	239	14.4	0.083	6.1
⊙	203	16.6	0.093	6.3
⊙	410	13.0	0.089	5.2
⊙	411	13.7	0.091	5.4
⊙	397	21.5	0.123	4.7

FD 140123

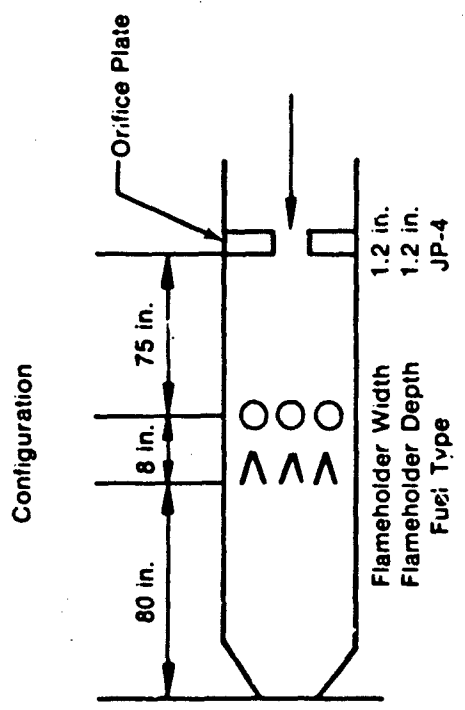
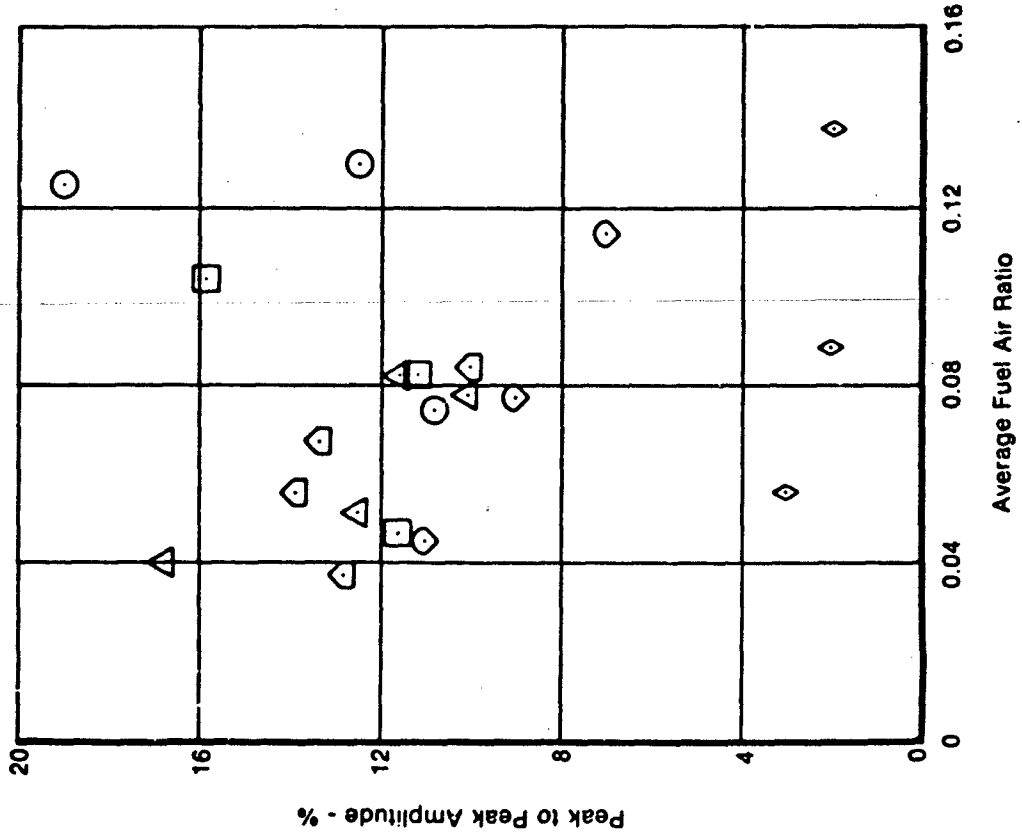
Figure A-1. Rumble Data for Test Point Number 1 and 2 --- Test Number 7.01



Sym	T °F	P psia	Mach No.	Stability Parameter V/NPT ^{1.7} x 10 ⁵
◇	248	15.7	0.057	5.6
○	213	16.8	0.076	7.5
△	407	15.6	0.090	7.0
□	409	21.5	0.059	3.3
◇	398	22.1	0.101	5.6

FD 140126

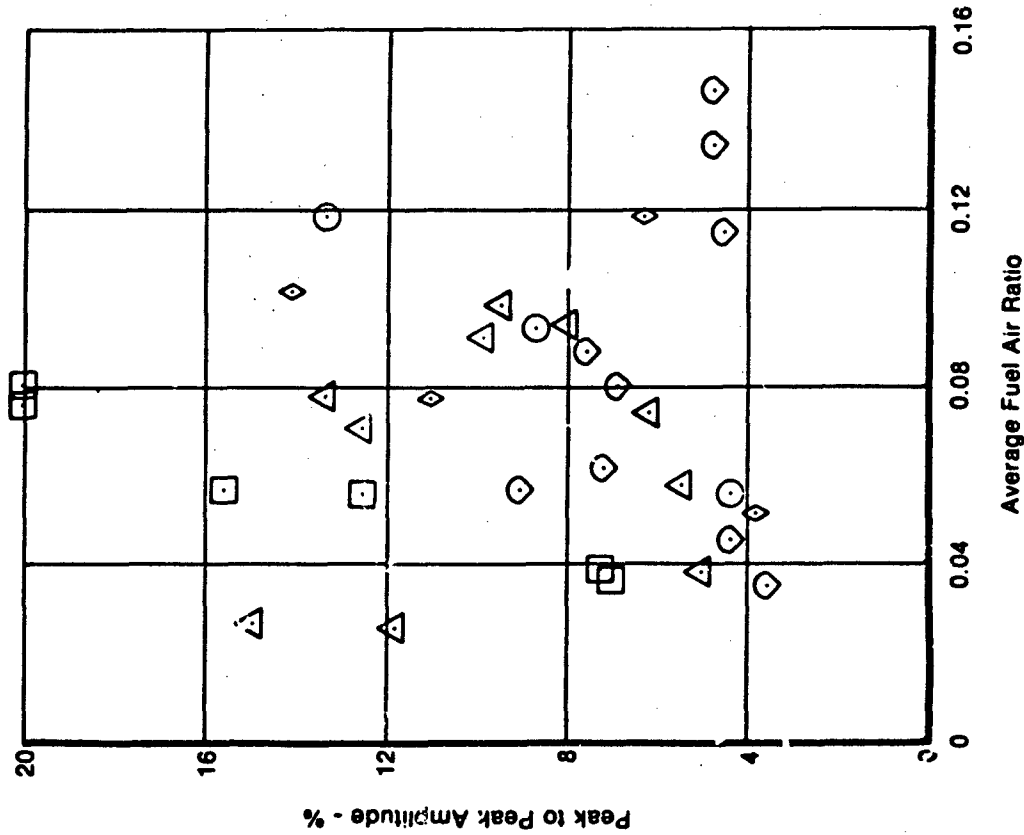
Figure A-2. Rumble Data for Test Point Number 3 — Test Number 11.01



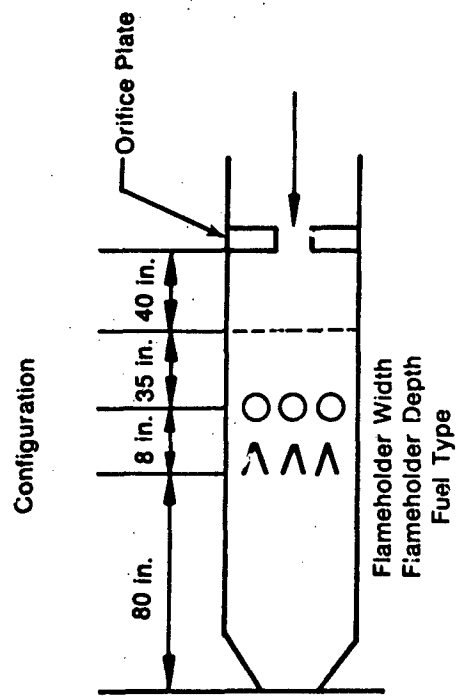
Sym	T °F	P psia	Mach No.	Stability Parameter V/NPT ^{1.7} x 10 ⁵
○	207	17.5	0.042	4.0
○	195	18.8	0.061	5.5
○	410	16.3	0.044	3.3
○	394	17.5	0.068	4.8
○	397	23.6	0.042	2.2
○	398	28.4	0.070	3.0

FD 140127

Figure A-3. Rumble Data for Test Point Number 4 — Test Number 12.01

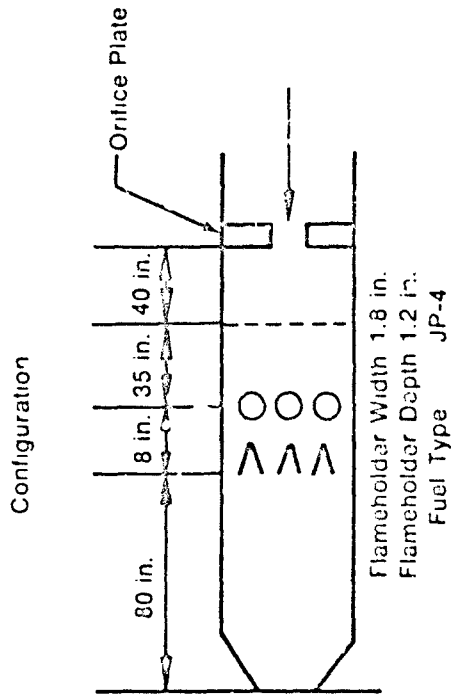
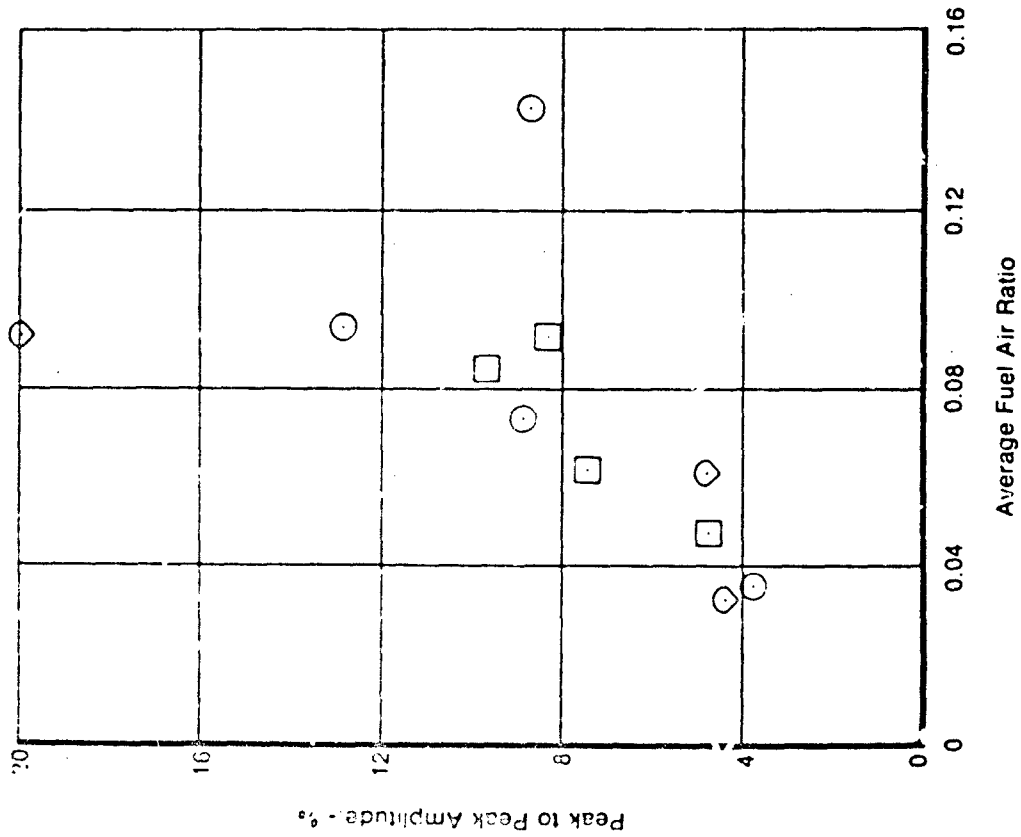


FD 140122



Sym	T °F	P psia	Mach No.	Stability Parameter V/NPT ^{1.7} x 10 ⁵
◇	232	15.4	0.070	4.8
△	228	13.4	0.068	5.4
○	386	14.1	0.082	4.5
□	403	14.8	0.106	5.8
◇	394	14.1	0.078	4.6
△	396	21.9	0.116	4.4

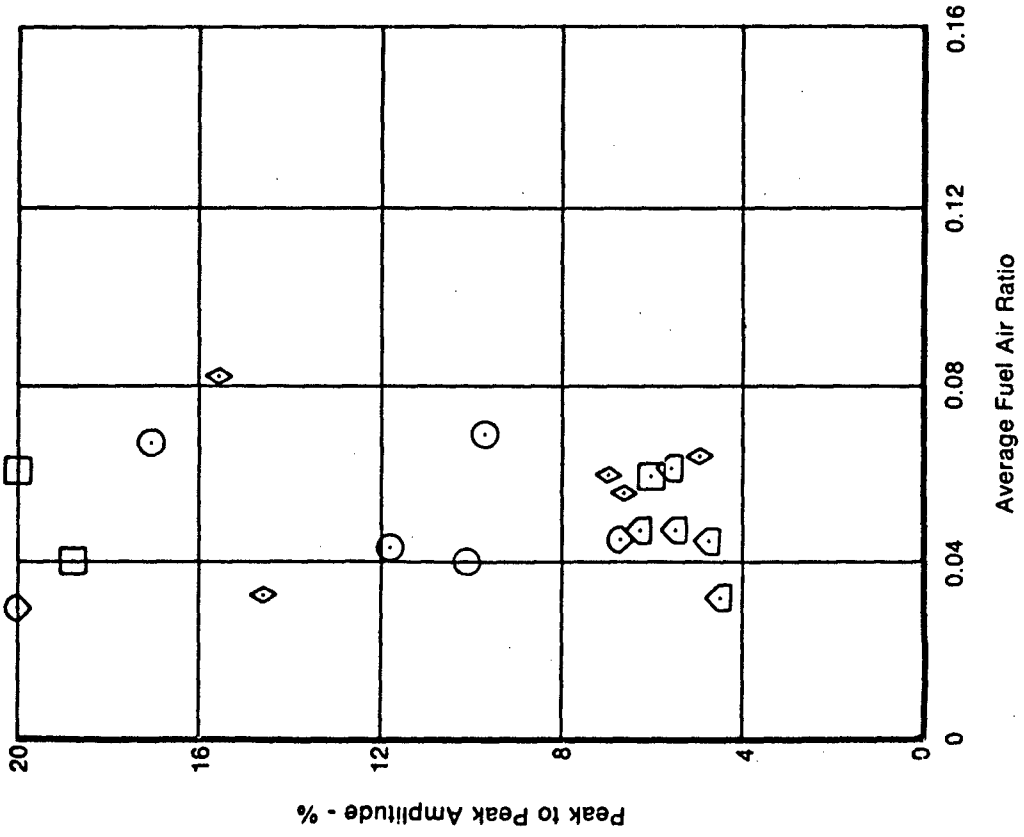
Figure A-4. Rumble Data for Test Point Number 4 — Test Number 8.01



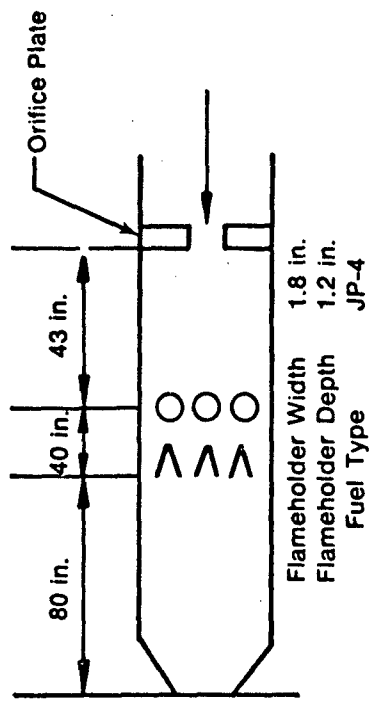
Sym	T °F	P psia	Mach No.	Stability Parameter V/NPT 1.7 x 10 ⁵
◇	239	14.5	0.076	5.5
○	402	14.2	0.082	4.7
□	390	15.8	0.110	5.8

FD 140124

Figure A-5. Rumble Data for Test Point Number 1 — Test Number 8.01



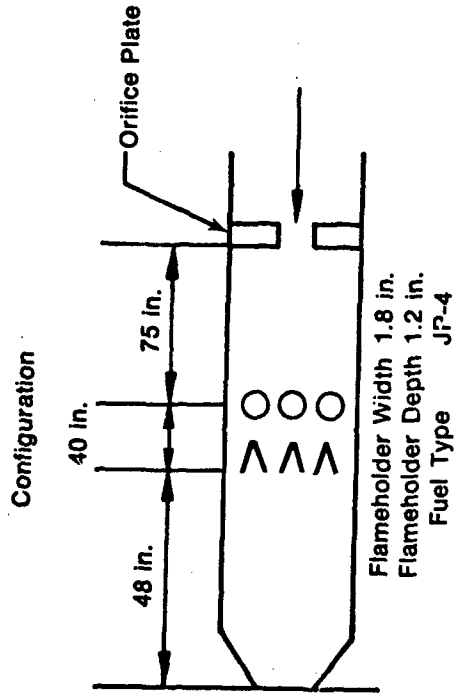
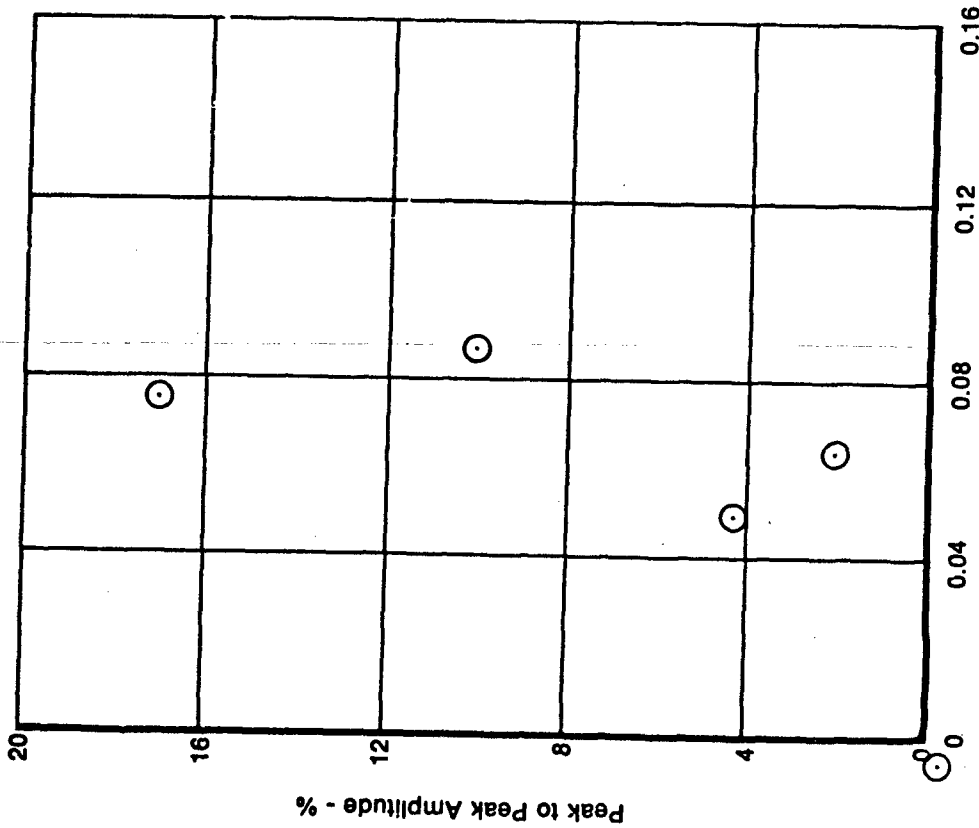
Configuration



Sym	T °F	P psia	Mach No.	Stability Parameter V/NPT ^{1.7} × 10 ⁵
◇	242	15.0	0.078	8.1
△	226	23.5	0.064	2.9
○	418	14.3	0.077	4.3
□	395	16.3	0.107	5.4
◇	395	20.9	0.093	3.7

FD 140125

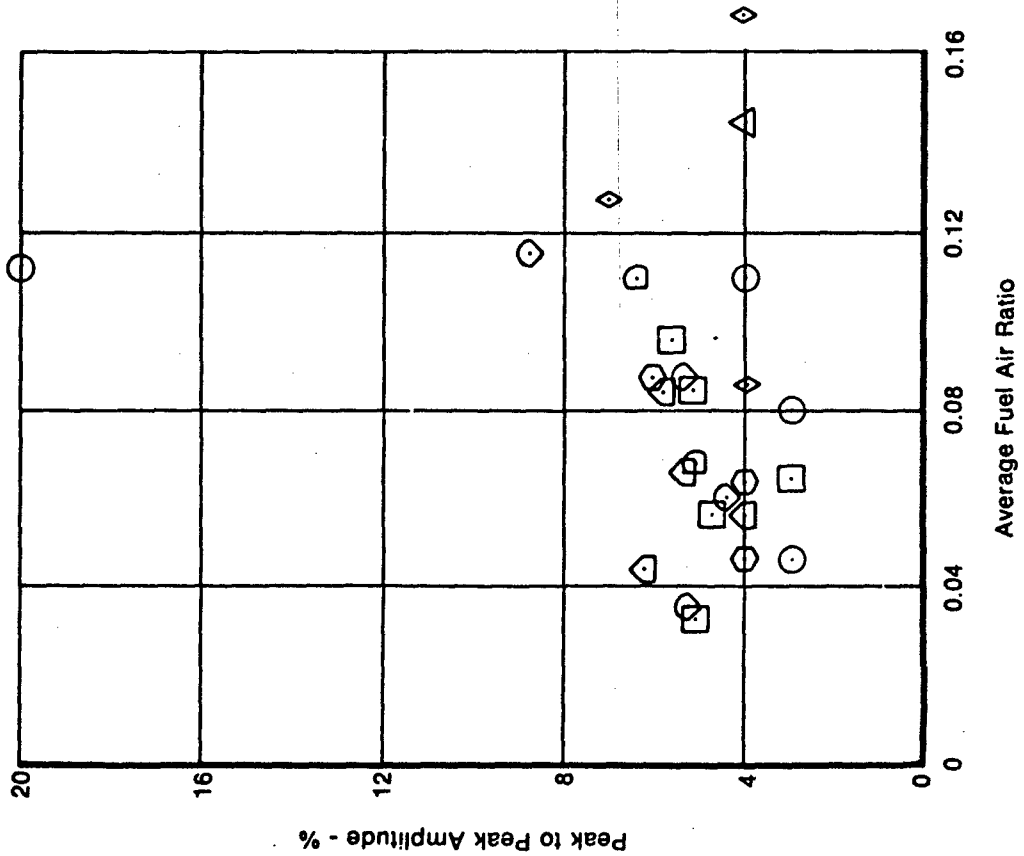
Figure A-7. Rumble Data for Test Point Number 9 — Test Number 9.01



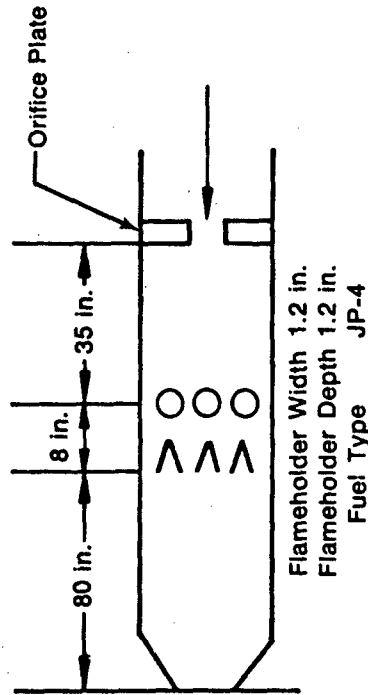
Sym	T °F	P psia	Mach No.	Stability Parameter
Q	229	27.7	0.045	V/NPT 1.7 x 10 ⁵
				1.8

Average Fuel Air Ratio

Figure A-8. Rumble Data for Test Point Number 10 — Test Number 10.01



Configuration



Sym	T °F	P psia	Mach No.	Stability Parameter V/NPT ^{1.7} X 10 ⁵
◇	255	15.2	0.076	6.2
○	213	16.2	0.074	7.5
□	397	16.7	0.047	3.5
△	407	15.9	0.082	6.3
○	407	25.6	0.046	2.2
□	1307	13.5	0.080	3.0
△	1297	12.8	0.129	5.2

Figure A-9. Rumble Data for Test Point Number 11 — Test Number 14.01

APPENDIX B EQUATIONS

The equations which are referred to in the text are presented here for reference.

$$\dot{w}_{t_v} = \beta_{1_T} \dot{w}_t \quad \text{B-1}$$

$$\dot{w}_{t_v} = \beta_{1_E} (1 - \beta_{1_T}) \dot{w}_t \quad \text{B-2}$$

$$\dot{w}_{t_v} = \beta_1 \dot{w}_t \quad \text{B-3}$$

$$\dot{w}_a = \rho_a VA \quad \text{B-4}$$

$$\dot{w}_{t_T} = \theta \dot{w}_a \quad \text{B-5}$$

$$\dot{w}_{t_v} = \beta_1 \dot{w}_{t_T} = \beta_1 \theta \dot{w}_a \quad \text{B-6}$$

$$\dot{w}_{t_l} = \dot{w}_{t_T} - \dot{w}_{t_v} = (1 - \beta_1) \theta \dot{w}_a \quad \text{B-7}$$

$$\dot{w}_{a_\Gamma} = \Gamma \dot{w}_a = \Gamma \rho_a VA \quad \text{B-8}$$

$$\dot{w}_{t_{l\Gamma}} = (1 - \beta_1) \theta \dot{w}_a \Gamma \quad \text{B-9}$$

$$\dot{w}_{t_{v\Gamma}} = \beta_1 \theta \dot{w}_a \Gamma \quad \text{B-10}$$

$$(f/a)_v \frac{\dot{w}_{t_{v\Gamma}}}{\dot{w}_a \Gamma} = \frac{\beta_1 \theta \dot{w}_a \Gamma}{\dot{w}_a \Gamma} = \beta_1 \theta \quad \text{B-11}$$

$$(f/a)_l = (1 - \beta_1) \theta \quad \text{B-12}$$

$$\dot{w}_{t_{lc}} = \beta_2 \dot{w}_{t_{l\Gamma}} = \beta_2 (1 - \beta_1) \theta \dot{w}_a \Gamma \quad \text{B-13}$$

$$\dot{w} = \beta_2 \dot{w}_{t_{lc}} = \beta_2 \beta_2 (1 - \beta_1) \theta \dot{w}_a \Gamma \quad \text{B-14}$$

$$\dot{w} = \dot{w}_{t_{v\Gamma}} K_1 = \beta_1 \theta \dot{w}_a \Gamma K_1 \quad \text{B-15}$$

$$\dot{w}_{t_{vw}} = \beta_1 \theta \dot{w}_a \Gamma K_1 + (1 - \beta_1) \beta_2 \beta_2 \theta \dot{w}_a \Gamma \quad \text{B-16}$$

$$\dot{w}_{a_w} = \dot{w}_a \Gamma K_1 \quad \text{B-17}$$

$$\phi = \frac{\dot{w}_{t_{vw}}}{\dot{w}_{a_w}} \quad \text{B-18}$$

$$\phi = \beta_1 \theta + (1 - \beta_1) \theta \frac{\beta_2 \beta_2}{K_1} \quad \text{B-19}$$

$$\frac{\phi}{\theta} = \beta_1 + (1 - \beta_1) \frac{\beta_2 \beta_2}{K_1} \quad \text{B-20}$$

EQUATIONS (Continued)

$$\beta_1 = \beta_{1T} + (1 - \beta_{1T})\beta_{1E} \quad \text{B-21}$$

$$\text{Nu}_H = 2 + 0.6 \text{Re}^{1/2} \text{Pr}^{1/3} \quad \text{B-22}$$

$$\text{Nu}_M = 2 + 0.6 \text{Re}^{1/2} \text{Sc}^{1/3} \quad \text{B-23}$$

$$\dot{w} = K A_s p_s \ln \left(\frac{p_s}{p_s - p_v} \right) \quad \text{B-24}$$

$$K = \frac{\text{Nu} D_v \text{MW}}{R d_i T_s} \quad \text{B-25}$$

$$h_i = \frac{k \text{Nu}_H}{d_i} \quad \text{B-26}$$

$$q = h_i A_s (T_s - T_i) \beta \quad \text{B-27}$$

$$\beta = \frac{z}{e^z - 1} \quad \text{B-28}$$

$$z = \text{Cp}_v \dot{w} / \pi k d_i \text{Nu}_H \quad \text{B-29}$$

$$\Delta \dot{q} = \dot{q} - \dot{w}_v \lambda \quad \text{B-30}$$

$$\frac{dT_i}{dt} = \frac{\Delta \dot{q}}{m_i \text{Cp}_i} = \frac{\Delta \dot{q}}{4/3 \pi (d_i/2)^3 \rho_i \text{Cp}_i} \quad (31)$$

$$\frac{dV_i}{dt} = \frac{3}{4} \frac{C_d}{d_i} \frac{\rho_a}{\rho_i} (V_a - V_i)^2 \quad \text{B-32}$$

$$\text{Re} = \frac{\rho_a d_i (V_a - V_i)}{\mu_g} \quad \text{B-33}$$

$$\dot{w}_{rc} = \dot{w}_{ri} \Gamma \beta_2 \quad \text{B-34}$$

$$\beta_2 = \frac{\dot{w}_{rc}}{\Gamma \dot{w}_R} \quad \text{B-35}$$

$$\dot{w}_{rc} = \rho V_i \delta^* \quad \text{B-36}$$

$$\begin{aligned} \dot{w}_r &= \rho V_i A \\ &= \rho V_i \frac{N}{\Gamma} \end{aligned}$$

$$\beta_2 = \frac{\delta^*}{N} \quad \text{B-37}$$

EQUATIONS (Continued)

$$\beta_2 = \frac{1}{m_{1,1} A} \sum_{i=1}^{10} m_{1,i} A \beta_{2i} \quad \text{B-38}$$

$$\dot{w}_{tc} = \dot{w}_v + \dot{w}_s + \frac{dm}{dt} \quad \text{B-39}$$

$$\dot{w}_v = \text{fcn}(\text{Nu}_m, p_v, A_s) \quad \text{B-40}$$

$$p_v = \text{fcn}(T) \quad \text{B-41}$$

$$T \cong \dot{T}_c + 1/2 \Delta T \quad \text{B-42}$$

$$q = \dot{w}_v \lambda + \dot{w}_{tc} C_p \Delta T \quad \text{B-43}$$

$$= \text{fcn}(\text{Nu}_H, T_s, T_w) \quad \text{B-44}$$

$$\dot{w}_v = C_1 A_s p_s \ln \left(\frac{p_s}{p_s - p_v} \right) \quad \text{B-45}$$

$$C_1 = \frac{\text{Nu}_m D_v \text{MW}}{R \Delta x T_s} \quad \text{B-46}$$

$$\text{Nu}_w = \frac{h_r N}{k_m} = 0.99 \text{Re}^{0.6} \text{Pr}^{0.33} \quad \text{B-47}$$

$$\dot{q} = \dot{w}_{tc} C_p (T_r - T_c) + \lambda \left(\frac{\text{Nu}_m D_v \text{MW}}{R \Delta x T_s} \right) A_s p_s \ln \left(\frac{p_s}{p_s - p_v} \right) \quad \text{B-48}$$

$$\dot{w}_{s,r} = \rho_s V_s N K_1 \quad \text{B-49}$$

$$\dot{w}_{s,r} = \frac{\rho_s V_s}{\tau} \quad \text{B-50}$$

$$\dot{w}_{s,r} = \rho_s V_o / \tau \quad \text{B-51}$$

$$V_o = C_v (L/D) (B/D) N^2 \quad \text{B-52}$$

$$\tau' = \frac{\tau V_s}{N} \quad \text{B-53}$$

$$\dot{w}_{s,r} = \frac{V_s}{N} \frac{\rho_s V_o}{\tau'} \quad \text{B-54}$$

$$\dot{w}_{s,r} = \frac{\rho_s V_s C_v (L/D) (B/D) N}{\tau'} \quad \text{B-55}$$

$$K_1 = C_v (L/D) (B/D) (\tau')^{-1} \quad \text{B-56}$$

EQUATIONS (Continued)

$$\frac{V_{\max}}{p_a N T_a^{1.5}} = \text{fcn}(f/a) \quad \text{B-57}$$

$$A = \dot{w}_{a,r} = \frac{\rho_a V_a C_v (L/D)(B/D)N}{r} \quad \text{B-58}$$

$$V_a = C_v (L/D)(B/D)N^2 \quad \text{B-59}$$

$$\rho_a = \frac{p_a}{RT_a} \quad \text{B-60}$$

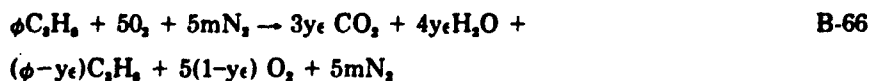
$$\frac{A}{V_a p^2} = \frac{p_a}{RT_a} V_a \frac{1}{rN} \frac{1}{p_a^2} \quad \text{B-61}$$

$$\frac{A}{V_a p^2} = \frac{1}{rR} \times \frac{V_a}{p_a N} \quad \text{B-62}$$

$$\frac{A}{V_a p^2} = \text{constant} \times \frac{V_a}{p_a N T_a^{1.5}} \quad \text{B-63}$$

$$-\frac{dm_o}{dt} = \frac{k}{R_1^n} x_o^a x_r^{n-a} V_a p^n \frac{e^{-C/T}}{T^{n-0.5}} \quad \text{B-64}$$

$$\frac{A}{V_a p^n} = \frac{k(m+1)}{R_1^n y \epsilon} x_o^a x_r^{n-a} \frac{e^{-C/T}}{T^{n-0.5}} \quad \text{B-65}$$



$$T = T_1 + \epsilon \Delta T \quad \text{B-67}$$

$$\frac{A}{V_a p^n} = \frac{k(m+1) [5(1-y\epsilon)]^a [\phi - y\epsilon]^{n-a} e^{-C/(T_1 + \epsilon \Delta T)}}{R_1^n y \epsilon [5(m+1) + \phi + y\epsilon]^n [T_1 + \epsilon \Delta T]^{n-0.5}} \quad \text{B-68}$$

$$\frac{A}{V_a p^{2.5}} = \frac{1.29 \times 10^{10} (m+1) [5(1-y\epsilon)]^a (\phi - y\epsilon)^{n-a} e^{-C/(T_1 + \epsilon \Delta T)}}{(0.08206)^{2.5} y \epsilon [5(m+1) + \phi + y\epsilon]^{2.5} [T_1 + \epsilon \Delta T]} \quad \text{B-69}$$

$$\frac{A}{V_a p^{1.5}} = 430 k_1 \frac{e^{-E/T_1}}{T_1^{1.5}} \frac{[2\phi(1-\epsilon)]^{n.5} (1-\phi\epsilon)}{\phi \epsilon [4.76 + \phi(1.36 - \epsilon)]^{1.5}} \quad \text{B-70}$$

$$\frac{A}{V_a p^{1.5}} = 430 k_2 \frac{e^{-E/T_1}}{T_1^{1.5}} \frac{(0.080 \phi)^{n.5}}{\epsilon} \left\{ \frac{1-\epsilon}{4.76 - \epsilon + 0.08\phi(1+16\epsilon)} \right\}^{1.5} \quad \text{B-71}$$

$$\frac{\left(\frac{A}{V_a p^2} \right)_{\text{max, pred}}}{\left(\frac{A}{V_a p^2} \right)_{\text{max, data}}} = 3.55 \quad \text{B-72}$$

EQUATIONS (Continued)

$$U = \frac{V_s}{(1-\Gamma)} \quad \text{B-73}$$

$$\epsilon_o = \left[\left\{ C_d \Gamma + \left(\frac{\Gamma}{1-\Gamma} \right)^2 \right\} \frac{1}{6} \right]^{1/2} \quad \text{B-74}$$

$$St = S_f + (2u'S_f)^{1/2} \quad \text{B-75}$$

The Value of u' is:

$$u' = \epsilon_o U \quad \text{B-76}$$

$$St' = St \cdot \eta_w \quad \text{B-77}$$

$$\eta_{c_o} = \eta_w \cdot \frac{m_r}{m_a} \quad \text{E-78}$$

$$\Delta y_o = \eta_{c_o} \cdot W \quad \text{B-79}$$

$$S'_f = S_f (\phi) \left(\frac{T_a}{540} \right)^{1.5} \left(\frac{X_{O_2}}{0.21} \right)^2 \quad \text{B-80}$$

$$\frac{\phi}{\theta} = \beta_1 + (1-\beta_1) \frac{\beta_2 \beta_3}{K_1} \quad \text{B-81}$$

$$\frac{\phi}{\theta} = (0.32) + (0.68) \frac{(0.85)(0.4)}{(0.23)} = 1.325 \quad \text{B-82}$$

$$\frac{\phi}{\theta} = \beta_1 + (1-\beta_1) \frac{\beta_2 \beta_3}{K_1} \quad \text{B-83}$$

$$53^\circ \text{ angle: } \frac{\phi}{\theta} = (0.32) + (0.68) \frac{(0.85)(0.4)}{(0.23)} = 1.325 \quad \text{B-84}$$

$$90^\circ \text{ angle: } \frac{\phi}{\theta} = (0.32) + (0.68) \frac{(0.87)(0.25)}{(0.25)} = 0.912 \quad \text{B-85}$$

$$\frac{\phi}{\theta} = \beta_1 + (1-\beta_1) \cdot \frac{\beta_2 \beta_3}{K_1} \quad \text{B-86}$$

EQUATIONS (Continued)

$$\frac{A}{V_o p^2} = \text{fcn} (\phi, \eta_w) \quad \text{B-87}$$

$$\phi = \theta \beta_1 + \theta (1 - \beta_1) \frac{\beta_w \beta_s}{K_1} \quad \text{B-88}$$

$$\beta_s = \text{fcn} (T_w, \beta_1, \theta) \quad \text{B-89}$$

$$T_w = T_a + \eta_w \Delta T_{\text{ideal}} \quad \text{B-90}$$

$$\Delta T_{\text{ideal}} = \text{fcn} (T_a, \phi) \quad \text{B-91}$$

$$\eta_w = \text{fcn} (T_a, \phi, A/V_o p^2) \quad \text{B-92}$$

LIST OF SYMBOLS

<i>English</i>	
a	Reaction order for oxygen (eqn. 64)
A	Duct flow area
A	Stirred reactor mass loading, gm-mole/sec
A_s	Surface area for heat or mass flux
B/D	Wake width/flameholder width
C	Kinetic activation constant = E/R
C_d	Drag coefficient
C_w	Wake shape factor (eqn. 52)
C_p	Specific heat
C₁	Surface mass efflux parameter (eqn. 46)
D_v	Binary diffusion coefficient
ϕ	Liquid fuel droplet diameter
E	Activation energy
f/a	Fuel-air ratio
h_f	Film coefficient for heat flux
k	Film thermal conductivity
K	Mass efflux parameter (eqn. 25)
k₁, k₂	Frequency factor for kinetic collision theory
K₁	Wake recirculation coefficient (eqn. 17)
L/D	Wake length/flameholder width
m	Ratio of diluent to oxygen mole fraction
m	Mass quantity
m_w	Mass of oxygen in wake
MW	Molecular weight

LIST OF SYMBOLS (Continued)

n	Overall reaction order
N	Flameholder width
Nu_H	Nusselt number for heat flux
Nu_M	Nusselt number for mass flux
Pr	Prandtl number
P	Pressure
\dot{q}	Heat flux
R, R_g	Gas constant
Re	Reynold's number
Sc	Schmidt number
S	Laminar flame speed
S_t	Turbulent flame speed
t	Time
T	Temperature
T_f	Flame temperature (eqn. 70)
u	RMS turbulence velocity
U	Accelerated air velocity (eqn. 73)
V	Velocity
V_o	Reactor volume
\dot{w}	Flowrate
W	Duct width
x	Axial distance
y	Reactor flow factor; = ϕ if $\phi < 1$ and = 1 if $\phi > 1$
z	Blocking coefficient (eqn. 29)

LIST OF SYMBOLS (Continued)

Greek

α	Flameholder apex angle
β_1	Pre-flameholder vaporization coefficient (eqn. 3)
β_2	Fuel collection coefficient (eqn. 13)
β_3	Surface vaporization coefficient (eqn. 14)
β_{17}	Throttling process vaporization coefficient (eqn. 1)
β_{18}	Droplet vaporization coefficient (eqn. 2)
β	Blocking coefficient (eqn. 28)
Γ	Blockage ratio
δ^*	Capture streamline (eqn. 36)
ϵ	Wake oxygen consumption efficiency
ϵ	Turbulence intensity at flameholder lip
η	Wake reaction efficiency
θ	Overall fuel-air ratio
λ	Latent heat of vaporization
μ	Viscosity
χ_0	Oxygen molal concentration
χ_1	Fuel molal concentration
ϕ	Wake fuel-air ratio
τ	Residence time
τ	Non-dimensional residence time
ρ	Density

LIST OF SYMBOLS (Continued)

Subscripts

a	Air
f	Fuel
l	Liquid phase fuel
v	Vapor phase fuel; vaporized portion
t	Total
c	Collected on flameholder
f	Pertaining to flameholder area
w	Into the wake of the flameholder
s	Static, surface, sensible
o	Initial or injection conditions
i	Initial or stepping notation
r	Recirculated

Operational Notes

Δ	Finite difference
d	Differential operation
α	Partial differential operation
=	Average value

REFERENCES

1. Ranz, W. E., W. R. Marshall, J., "Evaporation from Drops," Part I., Eng Prog., Vol. 48, No. 3, pp 141-146, March 1952.
2. Preim, R. J., and M. F. Heidmann, "Propellant Vaporization as a Design Criteria for Rocket-Engine Combustion Chambers," NASA TR R-67, 1960.
3. Stahle, W.C., "Forced Convection Droplet Evaporation With Finite Vaporization Kinetics and Liquid Heat Transfer," *Int'l Jnl of Heat and Mass Transfer*, Vol. 15, p 2077, 1972.
4. Langmuir, I., and K. Blodgett, Report No. 5418, USAF, Air Material Command, Wright-Patterson AFB, 19 February 1946.
5. Winterfeld, G., "On Processes of Turbulent Exchange Behind Flame Holders," Tenth Symposium (International) on Combustion, p 1265, 1965.
6. Bovina, T. A., "Studies of Exchange Between Re-Circulation Zone Behind the Flame-Holder and Outer Flow," Seventh Symposium (International) on Combustion, p 692, 1959.
7. Lefebvre, A. H., et al, "Factors Affecting Fresh Mixture Entrainment in Bluff-Body Stabilized Flames," *Combustion and Flame*, Vol 10, September 1966.
8. Wright, F. H., "Bluff-Body Flame Stabilization: Blockage Effects," *Combustion and Flame*, Vol 3, p 319, 1959.
9. Cornell, W. G., "The Flow in a Vee-Gutter Cascade," Transactions of the ASME, p 573, April 1956.
10. Davies, T. W., and J. M. Beer, "Flow in the Wake of Bluff-Body Flame Stabilizers," Thirteenth Symposium (International) on Combustion, p 631, 1971.
11. Loblich, K. R., "Semitheoretical Consideration on Scaling Laws in Flame Stabilization," Ninth Symposium (International) on Combustion, p 949, 1963.
12. Ozawa, R. I., "Survey of Basic Data on Flame Stabilization and Propagation for High-Speed Combustion Systems," AFAPL-TR-70-81, November 1970.
13. Longwell, J. P., and M. A. Weiss, "High Temperature Reaction Rates in Hydrocarbon Combustion," *Industrial and Engineering Chemistry*, 47, 8, p 1634, 1955.
14. Longwell, J. P., E. E. Frost, and M. A. Weiss, "Flame Stability in Bluff-Body Re-Circulation Zones," *Industrial and Engineering Chemistry*, 45, 8, p 1629, 1953.
15. Herbert, M. V., "A Theoretical Analysis of Reaction Rate By Controlled Systems: Part II," Eighth Symposium (International) on Combustion, p 970, 1960
16. Clarke, A. E., A. J. Harrison, and J. Odgers, "Combustion Stability in a Spherical Combustor," Seventh Symposium (International) on Combustion, p 664, 1959.
17. Clarke, A. E., J. Odgers and Ryan, "Further Studies of Combustion Phenomena in a Spherical Combustor," Eighth Symposium (International) on Combustion, p 982, 1960.

REFERENCES (Continued)

18. Weiss, M. A., J. C. Rohrer, and J. P. Longwell, "Some Effects on Fuel Reactivity and Heat Loss on Flame Stabilization," Sixth Symposium (International) on Combustion, p 439, 1956.
19. Odgers, J., and C. Carrier, "Modeling of Gas Turbine Combustors: Considerations of Combustion Efficiency and Stability," *Journal of Engineering for Power*, p 105, April 1973.
20. Clarke, A. E., et al. "Combustion Processes in a Spherical Combustor," Tenth Symposium (International) on Combustion, p 1151, 1965.
21. Kretschmer, D., and J. Odgers, "Modeling of Gas Turbine Combustors — A Convenient Reaction Rate Equation," *Journal of Engineering for Power*, p 173, July 1972.
22. NACA Report 1300, "Basic Considerations in the Combustion of Hydrocarbon Fuels With Air," 1959.
23. Polymerapoulos, C., "Combustion Science and Technology," Vol 9, pp 197-207, 1974.
24. Longwell, J. P., "Flame Stabilization by Bluff-Bodies and Turbulent Flames in Ducts," Fourth Symposium, p 90.
25. Pein, R., H. Pischel, and F. Fetting, "Re-Circulation Zone Concentrations and Temperatures of Bluff-Body Stabilized Turbulent Flames," *Combustion Science and Technology*, Vol 1, p 327, 1970.
26. Khitrin, L. N., and S. A. Goldenberg, "The Influence of the Initial Temperature of a Combustible Mixture and of Ambient Pressure on the Stabilization Limits," Sixth Symposium on Combustion, p 448, 1956.
27. Williams, G. C., and C. W. Shipman, "Some Properties of Rod-Stabilized Flames of Homogenous Gas Mixtures," Fourth Symposium on Combustion, p 773.
28. Filippi, F., and L. Fabbroich — Mazza, "Control of Bluff-Body Flameholder Stability Limits," Eighth Symposium on Combustion, p 956, 1962.
29. Herbert, M. V., "A Theoretical Analysis of Reaction Rate Controlled Systems — Part I," AGARDograph No. 115, Combustion Researches and Reviews, p 76, 1957.
30. Spalding, D. B., "Some Fundamentals of Combustion," Butterworths, p 157-205, 1955.
31. Marion, C. P., "Flame Stabilization in Volatile Fuel Sprays," Ph. D. Thesis, MIT, 1952.
32. Gross, R. M., "Bluff-Body Flame Stabilization With Liquid Fuel Present on the Flameholder," MS Thesis, Univ. of Utah, 1972.
33. Gross, R. M., A. D. Baer, and N. W. Ryan, "Flame Stabilization on Fuel-Wetted Cylinders," *Combustion and Flame*, 25, pp 121-128, 1975.
34. Lewis, G. D., et al, "Swirling Flow Combustion," *Journal of Energy*, Vol I, No. 4, July 1977.

REFERENCES (Continued)

35. Clements, T. R., "Effect of Swirling Flow on Augmentor Performance — Final Report," NASA CR-134639, November 1974.
36. Reilly, R. S., and S. J. Markowski, "Vortex Burning and Mixing (VORBIX) Augmentation System," AIAA/SAE 12th Propulsion Conference, 27 July 1976.